공학박사학위논문

Experimental Study on Flame Structure and Combustion Dynamic Characteristics in a Low NOx Model Gas Turbine Combustor

저 NOx 모형 가스터빈 연소기에서 화염구조 및 연소동특성에 대한 실험적 연구

2016년 2월

서울대학교 대학원
기계항공공학부
김민기

ABSTRACT

Experimental Study on Flame Structure and Combustion Dynamic Characteristics in a Low NOx Model Gas Turbine Combustor

Min-Ki Kim

School of Mechanical and Aerospace Engineering

The Graduate School

Seoul National University

There has been increased demand in recent years for low NOx gas turbines to meet stringent emissions goals by operating in a lean, premixed combustion and an advanced combustion system for aero gas turbine engine such as the Rich-Burn, Quick-Mix, Lean-Burn (RQL) combustor. Unfortunately, detrimental combustion instabilities are often excited within the combustor when it operates under lean and rich equvalence ratio conditions, degrading performance and reducing combustor life. To eliminate the onset of these combustion instabilities and develop effective approaches for their control, the mechanisms responsible for their combustion oscillation chartacteristics and jet spray mechanism of secondary quick mix zone must be understood. The main objective of this study was conducted to identify the secondary spray jet mechanism for the turbulent quick mixing zone and combustion instability characteristics in a swirl-stabilized and partially premixed model gas turbine combustor, with the attention focused on the effect of the various fuel-air mixing section geometries, fuel-air mixture velocities and effect of the formation of recirculation zones and vortex interaction on the combustion instability characteristics. Lastly, for the confirmed the this experimental study and analyzed mechanisms, we investigated an optimized operating strategy and developed a

combustion tuning methodology for the GE 7FA+e DLN-2.6 (DLN : Dry Low NOx) ground state gas turbine engine used for power generation operated by Korea Western Power Co. Ltd. at Seo-Incheon power plant, Incheon, Republic of Korea.

The flame recirculation zone is very important, as it can modulate the fuel flow rate and may be the source of instability, plus its flame structure has a major impact on heat release rate oscillation and flame stabilization. This study addresses structural characteristics of natural gas flames in a lean premixed swirl-stabilized combustor with attention focused on the effect of the formation of recirculation zones and vortex interaction on the combustion instability. To improve our understanding of the role of the recirculation zone and vortex combustion instability, the flame structure was investigated for various mixture velocities, equivalence ratios and swirl numbers. The optically accessible combustor allowed for the laser diagnostics of Particle Image Velocimetry (PIV) measurement, while OH chemiluminescence was used to characterize the flow structure under both cold flow conditions and hot flow combustion conditions. and heat release oscillation rate with the use of a high-speed ICCD camera under both stable and unstable flame conditions. Multi-channel dynamic pressures were also measured at the same time to investigate characteristics of the combustion phenomenon. We also observed fundamental longitudinal type of combustion instability characteristics related to the instability of thermo-acoustics. The result suggests that the formation of the recirculation zone is strongly related to the occurrence of combustion instabilities.

The effect of fuel-air mixture velocity on combustion instability characteristics have been investigated by measuring the flame structure, dynamic pressure mode and phase. The swirling CH_4 - air flame was investigated with an overall equivalence ratio of 1.2 to lean blowout limit and dump plane velocity of 30 ~ 70 m/s. Phase locking analysis was performed to identify structural changes at each phase of the reference dynamic pressure sensor under conditions of instability. At an unstable condition, flame root size varies a lot compared to stable condition which is because of air and fuel mixture flow rate changes due to combustor pressure modulation. After this structural change, local extinction and re-ignition occur and it can generate a feedback loop for combustion instability. This analysis suggests that pressure fluctuation of combustion causes

deformation of flame structure and variation of flame has a strong effect on combustion instability. In this section, we observed two types of combustion instability characteristics related to the instability of both the thermo-acoustics and flame vortex interaction mode.

To investigate the instability characteristics of combustor geometry. The combustor and inlet mixing section length was varied in order to have different acoustic resonance characteristics from 800 to 1680 mm of the combustor and 470, 550 and 870 mm of the inlet mixing section. In this study, we observed two dominant instability frequencies. Lower instability frequencies were obtained around 240 ~ 380 Hz, which were associated with a fundamental longitudinal mode of combustor length. Higher frequencies were observed around 410 ~ 830 Hz. These were related to the secondary longitudinal mode in the combustion chamber and the secondary quarter wave mode in the inlet mixing section. These second mode instability frequency characteristics are coupled with the conditions of the combustor and inlet mixing section acoustic geometry. Also, these higher combustion instability characteristics include dynamic pressure oscillation of the inlet mixing section part, which was larger than the combustor section. As a result, combustion instability was strongly affected by the acoustically coupling characteristics of the combustor and inlet mixing section geometry, which is called the plenum.

The effects of variable angled injection characteristics for quick mixing zone such as liquid column trajectory and breakup length has been experimentally studied in liquid jets injected into subsonic crossflow. With water as fuel injection velocity and injection angle were varied to provide of jet operation conditions. The pulsed shadowgraph photography with highly resolution and PLLIF (Planar Liquid Laser Induced Fluorescence) measurements were used for determined the liquid column trajectory and breakup length of angles spray. As the result, this research has been shown that liquid column trajectories and liquid column breakup length were spatially dependent on air-stream velocity, fuel injection velocity, various injection angle, and normalized injector exit diameter. Furthermore, the empirical formula of liquid column trajectories and breakup length has been some different of drag coefficient results between forward injection and reverse angle injection in subsonic crossflow.

In the Appendix section, the optimum combustion control of real gas turbine combustor was introduced. On the basis of a MARK-Ⅵ system, the optimized tuning for operation of a DLN-2.6 combustor was studied for the maintenance of a GE 7FA+e gas turbine at a Seo-Incheon combined cycle power plant. Also, the optimum combustion control system was created by all of measuring the inlet and outlet combustion data of the GE 7FA+e gas turbine.

Keywords: Gas Turbine Combustor, Combustion Instability, Flame Vortex Structure, Central Recirculation Zone (CRZ), Inlet Mixing Section, Multi-Position Dynamic Pressure Sensing, Canted Injection, Liquid Column Trajectory, Breakup Length, Optimum Combustion Tuning

Student Number: 2005-20996

LIST

LIST OF FIGURES

LIST OF TABLES

NOMENCLATURE

Alphabet

1L	1st longitudinal instability mode
2L	2nd longitudinal instability mode
A	orifice area
c	speed of sound
C_v	constant-volume specific heat
C_d	discharge coefficient
d	orifice diameter
d_0	diameter of the centerbody
d_h	diameter of inlet duct
D	orifice chamber diameter
D_{inlet}	diameter of inlet mixing section
$D_{comb.}$	diameter of combustor
e	specific internal energy
f	combustion instability frequency
f_0	resonance frequency
I_0	laser beam intensity
K	constants
L	orifice passage length
L_{inlet}	axial distance of inlet mixing section
$L_{comb.}$	axial distance of combustor
L_{flame}	flame length
M	Mach number
$\dot{m}$	mass flow rate
P	static pressure
P_1	total pressure in the pressure vessel
P_2	ambient pressure
$P'(x,t)$	perturbation of dynamic pressure

q	liquid/air momentum flux ratio, $\rho_f u_f^2 \ / \ \rho_g u_g^2$
$q'(x,t)$	heat release oscillation
Q	volumetric flow rate
R	gas constant
Re	Reynolds number
R_o	orifice inner curvature radius
S	swirl number
S'	swirl number perturbation
St	Strouhal number, $f \cdot L_{flame} / v_{mix}$
t	time
T_{inlet}	inlet mixing section temperature
$T_{comb.}$	combustor temperature
u	axial velocity
u_2	axial velocity at swirler downstream section
v_a	air velocity in the airstream direction
v_f	liquid fuel velocity at the orifice exit
v_g	gas velocity in the airstream direction
v_{mix}	fuel - air mixture velocity
v_r	radial velocity
v_θ	tangential velocity
V'	vortex shedding oscillation
x	distance in the airstream(axial) direction
x_b	breakup distance in the airstream(axial) direction
x_f	location of flame zone
y	distance in the direction transverse(penetration) to the airstream
y_b	breakup distance in the direction transverse(penetration) to the airstream

Greek

a	flame angle

r	radial distance
ΔP	injection pressure drop
ρ_l	liquid density
ρ_f	fuel density
ρ_a	air density
ρ_g	ambient gas density
γ	specific heat ratio
ϕ	equivalence ratio
$\Phi(x,t)$	combustion instability damping source
θ	injection angle
θ_s	swirl vane angle
ω	angular frequency
μ	liquid viscosity
σ	surface tension
τ	period of oscillation

Subscripts

a	air
b	breakup
comb.	combustor section
d	discharge
f, flame	flame zone
g	gas
inlet	inlet mixing section
l	liquid
mix	fuel-air mixture
r	radial direction
s	swirl

CHAPTER 1
INTRODUCTION

1.1 Background

As a high-efficiency and low-pollution engine, a gas turbine is utilized for various different uses, ranging from the aviation industry to the electric power generation industry. Examples include domestic and industrial burners, steam and gas turbines, waste generators, and jet and ramjet engines. Continuous combustion processes exhibit a wide range of dynamics. Of these, conditions which promote coupling with the acoustic field and result in sustained, large amplitude oscillations remain as most challenging in the effort to develop ultra-low emission, lean premixed combustion to its full potential. Paradoxically, near stoichiometric burning in high-speed propulsion systems exhibits similar dynamics. In earlier days, for the purpose of promoting mechanical stability, such an engine was driven by a diffusion flame type combustor, but around the 1980s, when exhaust emissions like such as NOx were made an issue due to combustion in the existing stoichiometric ratio, the concept of a lean premixed flame [1, 2] and RQL (Rich burn Quick mix and Lean burn) type combustion [3, 4] quickly became important. As a result, the emission of NOx could be sharply decreased, but another problem arose in this context, which was that the flame became unstable in extreme reaction to the external disturbance. In a typical continuous combustion process, a highly flammable fuel-air mixture is ignited, and the hot gases generated due to the chemical transformation of the mixture are used to perform certain functions. In its simplest form, the combustion process can be considered as a reacting mixture flowing in a constant area duct with a flame anchored at a specific location in the duct. The latter ignites the reactants, releasing their chemical energy in the form of heat, thus raising their temperatures and reducing their density. Combustion chambers can be viewed as organ pipes in which acoustic pressure and velocity oscillations can be sustained. Flames, which are essentially surfaces

across which reactants are converted into products, not only possess their own inherent instabilities, but are also known to respond readily to impose fluctuations. The potential coupling between the unsteady components of pressure and heat release rate can lead to their resonant coupling, thus growth, is referred to as thermo-acoustic instability.

The combustion instability indicates that the local change of unsteady heat release waves and acoustic waves from the combustion chamber interact with each other, further generating a fluctuation of specific instability frequency. The fluctuation of unstable dynamic pressure generates a perturbation of fuel-air mixture flow, and then this fluctuation generates a perturbation of heat release waves, thus developing into the phenomenon of combustion instability. When the combustion instability characteristic takes place, it is able to satisfy the Rayleigh criterion theory [5], as formulated here:.

$$\int_0^{\tau}\int_0^{V} p'(x,t)\cdot q'(x,t)\,dVdt \;>\; \int_0^{\tau}\phi(x,t)\,dVdt \qquad (1.1)$$

The combustion instability mode is attributed to various other factors, such as heat release oscillation [6] by the flame vortex and acoustic pressure boundary formation with other space except the combustor, as well as the internal configuration of the combustor [7, 8, 9, 10]. For instance, the Seo-Incheon power plant of Korea Western Power Company, there is one of the latest engines made by the General Electric (GE) Company, called the 7FA+e DLN-2.6, and the fuel staging technique is used to stabilize the combustion as shown in Fig. 1.1. In the initial stage of combustion, a high level of NOx is generated in the section called Mode 3 (10~20 MW), that is, a yellow plume is generated by NO_2 in the chimney and lasts four hours at most., In the section of Mode 6B (20~45 MW), which leads to the maximum output, this has a feature that the engine combustion oscillation (the average pressure inside the combustion chamber is as follows: 15.1 bar, pressure fluctuation: 0.3 bar, about 2% oscillation of the average combustion chamber pressure) is caused by the conversion into the premixed mode. At this moment, through

the frequency of combustion instability, although the combustor temperature increases in proportion to the output increase in speed, there is no change in the instability frequency, and it is sustained as 120 ~ 140 Hz [11] Since the instability frequency does not increase as the temperature of the combustion chamber increases, we discovered that the instability mode, which is appears as an acoustic pressure field, is formed not by the combustor mode but other geometric characteristics [12, 13].

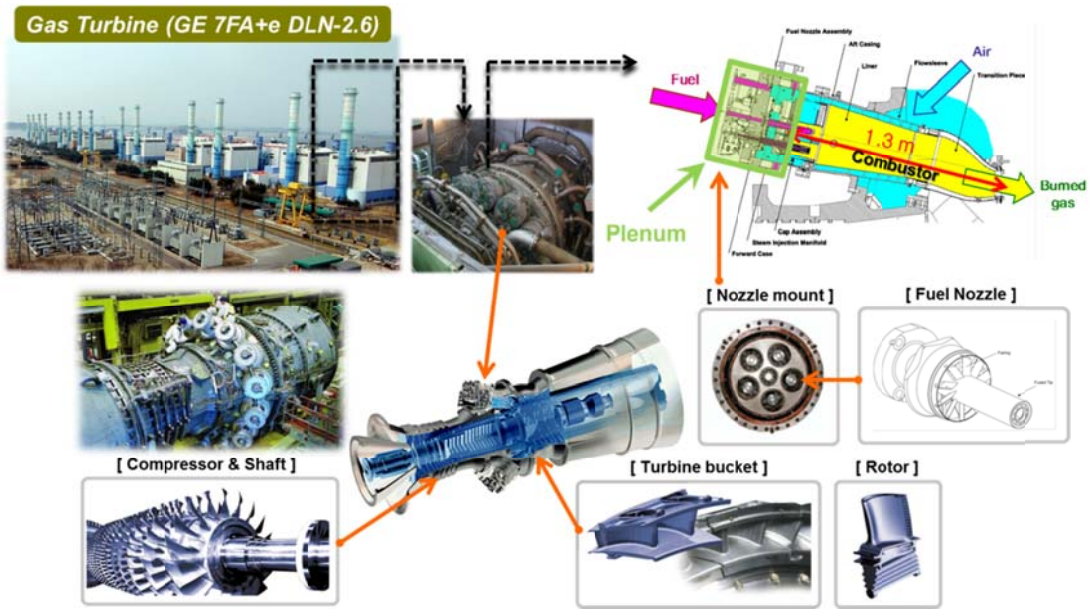

Fig. 1.1 GE 7FA+e DLN-2.6 (DLN : Dry Low NOx) ground state gas turbine engine used for power generation operated by Korea Western Power Co. Ltd. at Seo-Incheon power plant, Incheon, Republic of Korea.

In the past, aero gas turbine engine designers have sacrificed emissions to attain greater flight speeds and altitudes. For today's aero gas turbine engines, it is necessary to reduce these emissions, while at the same time, maintaining these same speeds and altitudes. In some European countries, airlines are being taxed for NOx emissions in their airspace. Concern for pollutant reduction is particularly strong for the next generation of

aircraft, represented by the High Speed Civil Transport, which is being designed to fly at stratospheric altitudes. In the stratosphere, NOx emissions could contribute to ozone depletion [14]. To achieve this reduction in NOx emissions, engine designers have been challenged to evaluate various combustor configurations. One promising configuration is the three-stage RQL combustor as shown in Fig. 1.2.

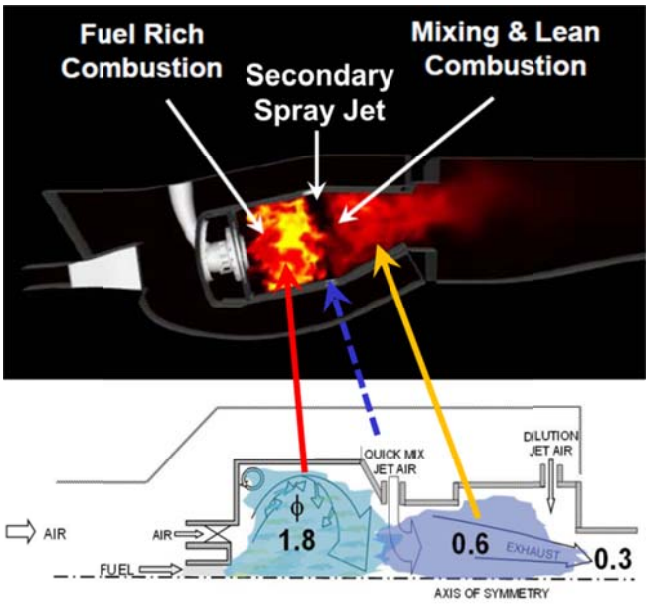

Fig. 1.2 Schematic of RQL (Rich burn - Quick mix - Lean burn) Combustor

(ϕ : *Equivalence Ratio*)

In the RQL (Rich burn - Quick mix - Lean burn) combustor, air is mixed with the fuel in two stages. In the primary zone of the combustor, a fraction of the total air is reacted with the fuel to form a fuel rich combustion mixture. By operating rich of stoichiometery, the flame temperature is reduced and an active pool of hydrocarbon is produced which can reduce NO formed. Downstream, the remaining air is added to the fuel rich product mixture via dilution jets to form a fuel lean mixture in the secondary

zone. Operating lean of stoichiometric keeps the combustion temperature low and also eliminates carbon monoxide (CO) and unburnt hydrocarbons (UHC). To date, the reduction of NOx from staged RQL type combustors operating at atmospheric, low temperature inlet conditions has been well documented. Staged combustion has been demonstrated successful at reducing thermal and fuel NO at atmospheric conditions with no air preheat [15, 16], and at atmospheric conditions with air preheat up to 600 K [17]. However, little information exists for the RQL's low NOx potential when operating at temperatures and pressures that correspond to actual gas turbine engines. A full evaluation of the RQL, for use in stationary and aero applications, requires a systematic study of the effects of current, as well as futuristic, operating conditions on the emissions of NOx and combustion efficiency.

1.2 Historical Overview of Combustion Instability

Historically, the first observation of combustion oscillation was the “singing flame” which was discovered by Higgins in 1777 [18]. This phenomenon caught the interest of several researchers [19, 20] and they described that high levels of sound can be produced by placing a flame, anchored on a small diameter fuel supply tube in a larger diameter tube. The flame was found to excite the fundamental mode or one of the harmonics of the larger tube. The “dancing flame” was discovered later by Le Conte [21] where a flame pulses in sync with the audible beats of music. “It was exceedingly interesting to observe how perfectly even the trills 1 of the musical instrument were reflected on the sheet of the flame. A deaf man might have seen the harmony!”, he quoted. Concomitantly, Rijke [22] showed that sound can be generated in a vertical tube open at both ends by placing a heated metal gauze inside the tube. The sound was heard only when the heating element was placed in the lower half of the tube, specifically at a distance of a quarter the tube length from the bottom. Rayleigh [23] was the first to hypothesize the onset of the instability, and define a criterion for positive coupling based on a phenomenological,

heuristic, description of the instability, his explanation was as follows: *"If heat be periodically communicated to, and abstracted from, a mass of air vibrating in a cylinder bounded by a piston, the effect produced will depend upon the phase of the vibration at which the transfer of heat takes place. If heat be given to the air at the moment of greatest condensation or to be taken from it at the moment of greatest rarefaction, the vibration is encouraged. On the other hand, if heat be given at the moment of greatest rarefaction, or abstracted at the moment of greatest condensation, the vibration is discouraged"*. This can also be compared to a thermodynamic cycle (e.g. the Carnot engine). In a continuous combustion. Fig. 1.3 shows an historical overview of combustion instabilities in devices for propulsion and power generation [24]. Combustion instability was observed in solid rockets in the 1930s, and was a major issue in the development of liquid rocket engines as well as solid rocket motors. A notable instability in liquid-fueled rockets was encountered during the development of the F-1 engine for the Saturn rockets. The F-1 experienced strong instability with oscillation amplitudes up to 100% of the mean pressure (more than 2000 psi) in the combustion chamber at the frequency range of 200 ~ 500 Hz [25, 26]. In developing solid-propellant rockets, combustion instability was observed in the Space Shuttle rocket boosters, Minuteman ICBM, and the decent motors of the Mars Pathfinder [26, 27]. Combustion instabilities in ramjets have been also problematic as they cause strong fluctuations in thrust and/or shock-system oscillations in the inlet diffuser [26, 28]. Similar problems have been experienced in afterburners, where transverse modes as well as axial mode instabilities have damaged engine components such as flame holders and liner sections. In land-based gas turbines, vibrations induced by oscillating pressure and entropy waves in the combustion chambers have given rise to fatigue in combustor liners and turbine blades, which can reduce system lifetimes significantly.

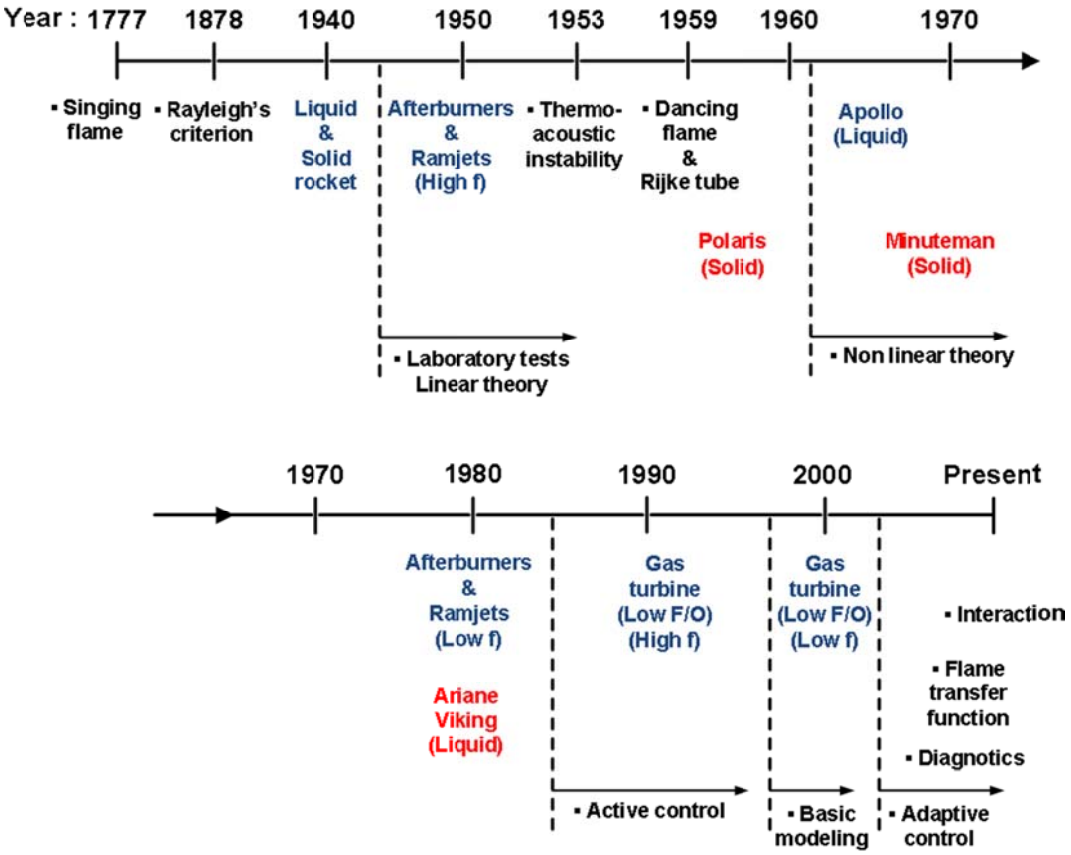

Fig. 1.3 Historical overview of combustion instabilities.

1.3 Mechanism of Combustion Instability

Combustion instabilities, in general, appear as large amplitude pressure oscillations with the natural frequency of the acoustic modes of combustion systems [26]. They are caused by complex, feedback type interactions between periodic flow and combustion processes that produce a periodic heat addition, exciting large amplitude acoustic oscillations in the combustor. An unsteady combustion process generates sound. If the combustion process occurs in a free field, the generated sound simply radiates away. However, if sound is generated in a confined region it can be reflected from the

boundaries, allowing the reflected waves to interact with the combustion process. Since the combustion process is sensitive to these flow field variations, a feedback loop is created and combustion instability can result [29].

Fig. 1.4 shows the feedback processes responsible and driving souses are involved in combustion instability [30]: a driving process and a coupling process. The driving process is the process that leads to the acoustic pressure oscillations due to the rate of heat release fluctuations, while the coupling process is the one that is responsible for the heat release fluctuation caused by the acoustic oscillations. When the two processes interact with a certain phase relationships, they can initiate and amplify combustion instability in a system.

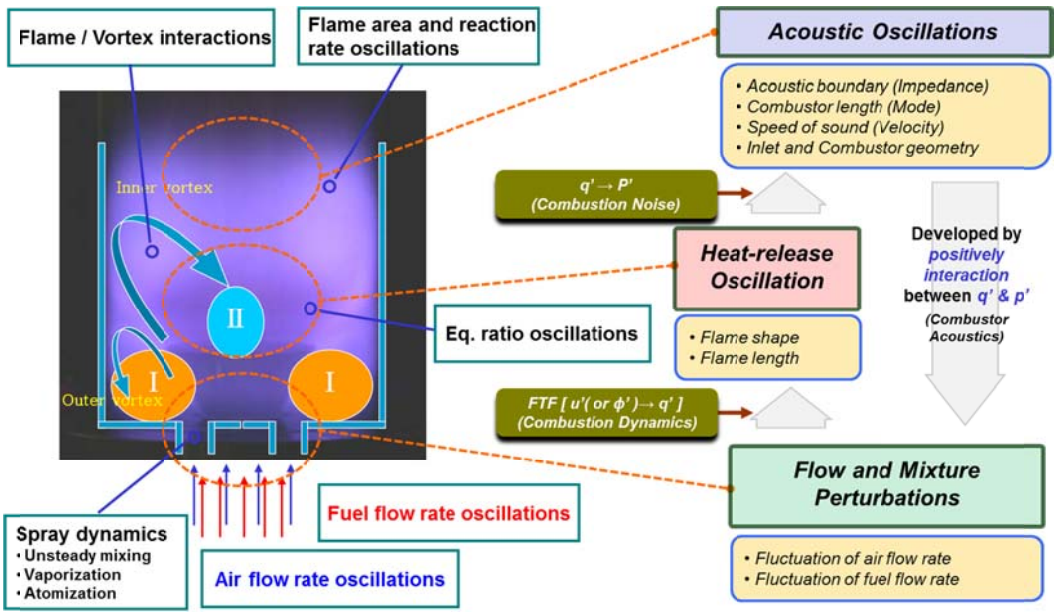

Fig. 1.4 Illustration of feedback loop and generic combustion instability mechanism.

1.4 Objectives and Outline

Optimum designing an advanced low NOx gas turbine combustor requires, essentially, the capability of predicting stability characteristics as a function of combustor operating conditions and geometry. This requires a substantial understanding of the physical processes which generate fluctuations of the rate of heat release and/or acoustic oscillations in lean and rich premixed combustors. Unfortunately, neither the driving nor coupling mechanisms of combustion instability are well enough understood, particularly under realistic combustor, inlet mixing section geometries and operating conditions.

For this purpose, experimental study is conducted to characterize the effects of flame-vortex interactions, fuel air mixture velocities and inlet mixing section geometry on unstable combustion in a swirl-stabilized, laboratory-scale gas turbine combustor. In chapter 2, the acoustic theory for each of the combustion instability mechanisms is presented to lay a theoretical foundation for the experiments. Chapter 3 then presents the experimental facility, including the model gas turbine combustor configuration and measurement techniques. The observed overall instability characteristics for swirl stabilized flame structure and recirculation zone are shown in Chapter 4. Based on the observations in Chapter 4, the combustion instability mechanisms due to flame-vortex interactions of various fuel-air mixture velocities and effect of mixing section geometry discussed in Chapters 5 and 6, respectively. Chapter 7 presents the secondary spray jet mechanism and characteristics of canted injection angles in secondary quick mixing zone for reducing the NOx level. The optimized tuning experience of a GE 7FA+e DLN-2.6 gas turbine combustor is shown in Appendix section. Lastly Chapter 8 presents the conclusions of this study.

CHAPTER 2

EXPERIMENTAL BACKGROUND

2.1 Acoustic Mode and Phase Analysis of Resonance Frequency

The combustion instability characteristics have very complicate mechanism such as flame-vortex and flame-acoustic interaction. This chapter is introduced to fundamental analytic theory for understand the combustion instability mechanism. Fig. 2.1 shows a model gas turbine with a blockage nozzle for turbine section where a flame sits in the main combustor. We can model either cases as a tube hosting a localized heat release zone (the flame), as seen in Fig. 2.2.

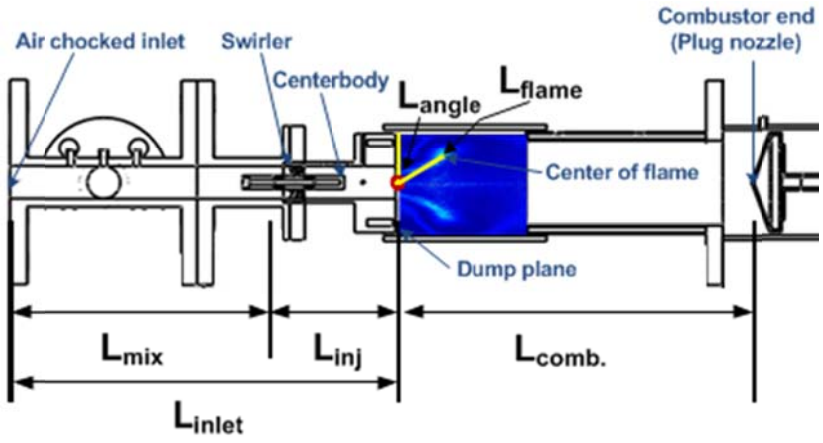

Fig. 2.1 Basic dimensions of model gas turbine combustor.

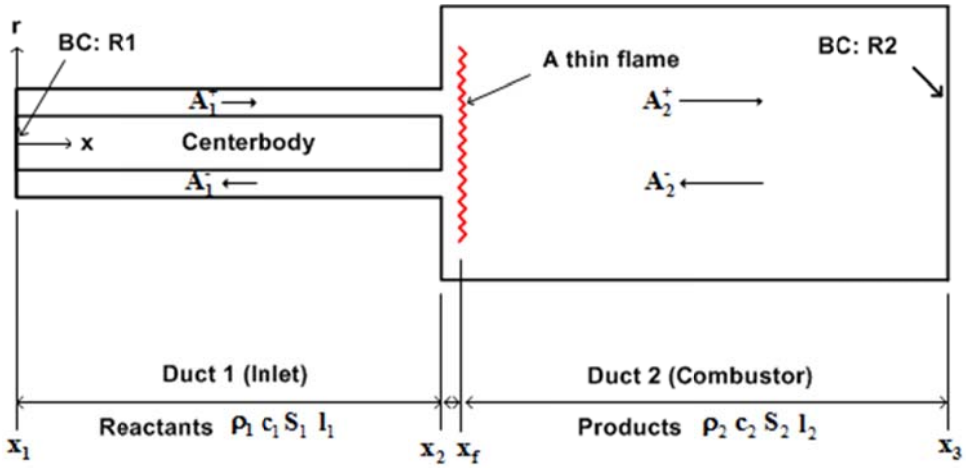

Fig. 2.2 Schematic of one dimensional reacting fluid flow with flame at $x = x_f$.

2.1.1 Acoustic wave equation

The basic assumptions used to derive the conservation equations for the flow in the combustor are: 1) One-dimensional flow, in the longitudinal direction of the combustor. (This is a valid assumption when the acoustic frequencies considered are low with respect of the cut-off frequency of the combustor, and hence waves considered are planar, and all modes are longitudinal), 2) Inviscid flow, i.e. the duct has negligible dissipation effect on the acoustic waves, 3) Negligible thermal conductivity to the surroundings, 4) Perfect gas and 5) Stationary flow.

In this Section, equations governing the acoustic pressure and velocity are obtained in the presence of unsteady heat addition within the field. These are manipulated to get the forced acoustic wave equation which is then reduced to the case when the mean heat release is negligible, i.e., approximately homogeneous field, and when the mean flow is also negligible.

Taking into consideration the three first assumptions above, the reactive-gas dynamics are described using the conservation equations as:

$$\text{Mass continuity}: \quad \frac{\partial \rho}{\partial t} + \frac{\partial (\rho u)}{\partial t} = 0 \tag{2.1}$$

$$\text{Momentum}: \quad \rho \frac{\partial u}{\partial t} + \rho u \frac{\partial u}{\partial x} + \frac{\partial p}{\partial x} = 0 \tag{2.2}$$

$$\text{Energy}: \quad \rho \frac{\partial e}{\partial t} + \rho u \frac{\partial e}{\partial x} = - p \frac{\partial u}{\partial x} + q \tag{2.3}$$

Where, t and x are time and space, respectively, ρ, u, p, and e are the density, velocity, pressure, and specific internal energy respectively, and q is the heat release rate per unit volume. We assume that the gases on both sides of the combustion zone behave as perfect gases, recall the perfect gas state equation Where, R is the gas constant, and T is the absolute temperature.

$$p = \rho R T \tag{2.4}$$

Combining Eq. (2.1), Eq. (2.3) (note, $\rho e = \rho C_v T = C_v \frac{p}{R} = \frac{p}{\gamma - 1}$, where C_v and γ are the constant-volume specific heat and the specific heat ratio, respectively) and Eq. (2.4), we get

$$\frac{\partial p}{\partial t} + u \frac{\partial p}{\partial x} + \gamma p \frac{\partial p}{\partial x} = (\gamma - 1) q \tag{2.5}$$

Since we are only interested in the small perturbation behavior at the onset of the instability, we use the perturbation method to linearize the system. We separate the system variables into their mean (function of space only) and small perturbation (function of space and time) components as follow, where $\overline{()}$ and $()'$ are the mean and the perturbation of a variable, respectively.

$$
\begin{aligned}
p(x,t) &= \overline{p}(x) + p'(x,t)\ ,\ u(x,t) = \overline{u}(x) + u'(x,t) \\
\rho(x,t) &= \overline{\rho}(x) + \rho'(x,t)\ ,\ and\ \ q(x,t) = \overline{q}(x) + q'(x,t)
\end{aligned}
\tag{2.6}
$$

Substituting the flow variable decompositions in Eq. (2.6) in Eqs. (2.2) and (2.5) and neglecting second order terms of the fluctuating components, we obtain the governing linear equations for the perturbations as:

$$
\overline{\rho}\frac{\partial u'}{\partial t} + \overline{\rho u}\frac{\partial u'}{\partial x} + \overline{\rho}u'\frac{d\overline{u}}{dx} + \rho'\overline{u}\frac{d\overline{u}}{dx} + \frac{\partial p'}{\partial x} = 0 \tag{2.7}
$$

$$
\frac{\partial p'}{\partial x} + \overline{u}\frac{\partial p'}{\partial x} + u'\frac{d\overline{p}}{dx} + \gamma\overline{p}\frac{\partial u'}{\partial x} + \gamma p'\frac{d\overline{u}}{dx} = (\gamma - 1)q' \tag{2.8}
$$

We also assume that the flame zone is spatially localized at x_f (see Fig. 2.2), i.e.,

$$
q'(x,t) = q'_f(t)\delta(x - x_f) \tag{2.9}
$$

Where, q'_f denotes the heat release rate per unit area and $\delta(\cdot)$ denotes the Dirac delta function. This implies that the mean variables are essentially constant over the length of the combustor except for a step change at x_f. For low Mach number flows, the effect of the step change in the pressure is negligible compared to the change in the mean velocity or mean density, and the spatial gradient of the mean pressure as well as the mean velocity can be considered small (see Ref. [1] for more details).

If the mean flow Mach number is negligibly small, Eqs. (2.7) and (2.8) can be obviously simplified as

$$
\left(\frac{\partial^2 p'}{\partial t^2} - \overline{c}^2\frac{\partial^2 p'}{\partial x^2}\right) = (\gamma - 1)\frac{\partial q'_f}{\partial t}\delta(x - x_f) \tag{2.10}
$$

$$\frac{\partial p'}{\partial t} + \gamma \bar{p} \frac{\partial u'}{\partial x} = (\gamma - 1) q'_f \delta(x - x_f) \tag{2.11}$$

Equations (2.10) and (2.11) capture the dominant characteristics of the thermoacoustic instability dynamics of the combustor. It should be noted also that the homogeneous form of Eq. (2.10) (i.e., when the RHS equals to zero) becomes the "classical acoustic wave equation". The general solution of the homogeneous wave equation can be represented as [2, 3, 4]:

$$p'(x, t) = \bar{p}\psi(x)\eta(t) \tag{2.12}$$

$$\psi(x) = \sin(kx + \phi_0) \tag{2.13}$$

$$\eta(t) = \sin(k\bar{c}x + \theta_0) \tag{2.14}$$

Where, $\psi(x)$ is called the basis function and describes the spatial component of the solution of the wave equation, and $\eta(t)$ represents the temporal component. k is the wave number, θ_0 is a given phase, and both are determined by the boundary conditions in the field. For example, in a tube open at both sides, the boundary conditions can be described as: $p'(0, t) = p'(L, t) = 0$. Solving Eq. (2.13) with these boundary conditions, we get

$$\phi_0 = 0, \pi, 2\pi... \tag{2.15}$$

$$k = \frac{n\pi}{L},\ n = 1, 2, 3, ... \tag{2.16}$$

We see that there exists an infinite set of discrete values of k, for which p' has non-trivial solutions (eigenvalues). Hence, $\psi(x)$ will represent the modes along the tube (n-modes). In Fig. 2.3, the first three modes for an open-open tube are shown, the points

where $\psi = 0$ are called nodes, and the crests are called anti-nodes [1, 4, 5].

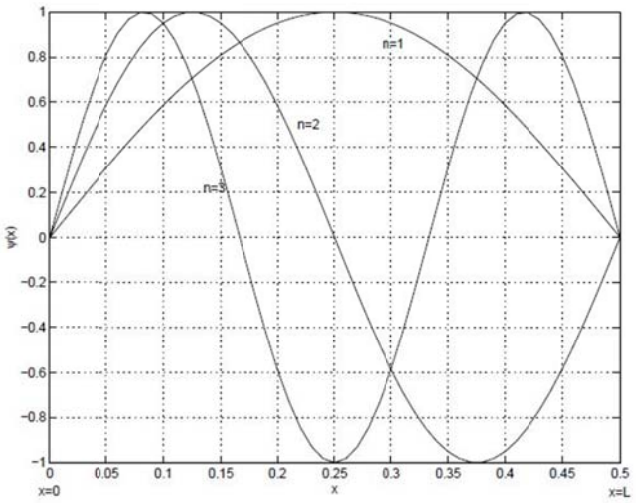

Fig. 2.3 Acoustic longitudinal modes for the open-open ended combustor geometry.

2.1.2 Theory of the Rayleigh criterion

In this section, we will carry out an energy balance of the combustor. We should note that the acoustic field (hosted by the combustor) is the primary energy storage mechanism in the combustor. Increasing or decreasing the storage (or internal) energy of this field can be achieved by exerting work or heating the field. Since, in our case, the flame is considered a localized heat source, only a small control volume in the acoustic field is heated, the small volume expands and in turn exerts work on the field.

The acoustic energy density, e', in a one-dimensional acoustic field can be derived from the unforced conservation equations as (see [2] for more details)

$$e' = \frac{\bar{\rho} u'^2}{2} + \frac{p'^2}{2\overline{\rho c^2}} \tag{2.17}$$

Where, the first term in the RHS is the kinetic acoustic energy and the second is the potential acoustic energy. It is clear that any system that would sustain waves (also, as in many vibration processes) should have these two components of energy, and the periodic conversion from one form to the other sustains the oscillatory behavior.

The temporary, over the period of oscillation, τ, and spatially, over the length of the combustor, L, we get

$$\Delta_\tau \int_0^L e' dx = \frac{(\gamma-1)}{\overline{\rho c}^2} \int_0^\tau \int_0^L p'(x,t) q'(x,t) dx dt - \Delta_L \int_0^L E' dt - \int_0^\tau \int_0^L \phi(x,t) dx dt \tag{2.18}$$

Where, Δ_τ and Δ_L are the changes over time and length, respectively. The LHS of Eq. (2.18) represents the change in the acoustic energy per cross-sectional area of the combustor. The first term in the RHS is the Rayleigh integral (similar to Eq. (1.1)), the second term represents the acoustic energy flux across the control surface of the field and is defined as $E' = \rho' u'$, and the last term quantifies the dissipation in the acoustic field. We can clearly see from the energy balance in Eq. (2.26) that when the Rayleigh criterion is satisfied, i.e. p' and q' become in phase, and the gain of the first term in the RHS is large enough to overcome both the dissipation and the energy flux terms (which are typically small), there will be an increase in the acoustic energy in the combustor, i.e. thermo-acoustic instability will be dominant [6].

The latter can happen when perturbations in the acoustic field affect the inlet conditions of one of the reactants (fuel or air), prior to mixing, and thus causes perturbations in the equivalence ratio which translate into perturbations in the unsteady heat release. This case could happen if the inlet conditions of one of the reactants to the combustor are not choked [7]. In both cases, if these perturbations are such that the phase between p' and q' is $\leq 90^o$, instability will occur.

2.1.3 Standing wave in combustor and inlet mixing section

For definition of the acoustic standing wave and phase analysis, we measured the multi-position dynamic pressure in combustor and inlet mixing section using the 11ea. dynamic pressure sensors. And the combustion instability characteristics in combustor and inlet mixing section are represented by below fundamental equations of acoustic standing wave. At the combustor section ($0 \le x \le L_{comb.}$) can be written as:

$$\text{First of half wave equation} = \frac{A_5}{\cos\left(\frac{\pi X_{D5}}{\lambda}\right)} * \cos\left(\frac{\pi x}{\lambda}\right) \qquad \lambda = L$$

$$\text{Second of half wave equation} = \frac{A_5}{\cos\left(\frac{\pi X_{D5}}{\lambda}\right)} * \cos\left(\frac{\pi x}{\lambda}\right) \qquad \lambda = \frac{L}{2}$$

$$\text{First of quater equation} = \frac{A_5}{\cos\left(\frac{\pi X_{D5}}{\lambda}\right)} * \cos\left(\frac{\pi x}{\lambda}\right) \qquad \lambda = 2L$$

$$\text{Second of quater equation} = \frac{A_5}{\cos\left(\frac{\pi X_{D5}}{\lambda}\right)} * \cos\left(\frac{\pi x}{\lambda}\right) \qquad \lambda = \frac{2L}{3} \tag{2.19}$$

At the inlet mixing section ($L_{inlet} \le x \le 0$) can be written as:

$$\text{First of half wave equation} = \frac{A_4}{\cos\left(\frac{\pi X_{D4}}{\lambda}\right)} * \cos\left(\frac{\pi x}{\lambda}\right) \qquad \lambda = L$$

$$\text{Second of half wave equation} = \frac{A_4}{\cos\left(\frac{\pi X_{D4}}{\lambda}\right)} * \cos\left(\frac{\pi x}{\lambda}\right) \qquad \lambda = \frac{L}{2}$$

$$\text{First of quater equation} = \frac{A_4}{\sin\left(\frac{\pi X_{D4}}{\lambda}\right)} * \sin\left(\frac{\pi x}{\lambda}\right) \qquad \lambda = 2L$$

$$\text{Second of quater equation} = \frac{A_4}{\sin\left(\frac{\pi X_{D4}}{\lambda}\right)} * \sin\left(\frac{\pi x}{\lambda}\right) \qquad \lambda = \frac{2L}{3}$$

(2.20)

2.2 Flow Dynamics of Swirl Injector

The swirling flows have been widely used in practical combustion systems such as industrial burners, furnaces, and gas turbine combustors because they enable high energy conversion in a small volume. Swirl flames exhibit good ignition and stabilization behavior over a wide operating range by promoting rapid mixing, improving flammability limits, shortening flame size, and reducing pollutant emissions [8]. The vast majority of gas turbine systems employ swirl injectors that provide a lot of advantages. Fuel injection and mixing efficiency is a very important factor for combustion emissions and gas turbine efficiency. Nowadays, most gas turbines use swirl injectors. Using this kind of injector affects flame stabilization and mixing quality. A swirl injector is composed of a central recirculation zone and an outer recirculation zone. This central recirculation zone re-circulates combusted hot gas to the nozzle part and it works as a heat source of the combustion and central recirculation zone, making a shear layer of the mixture and re-circulated flow, which will help the mixing efficiency [9].

As mentioned above, a recirculation zone is important for the stabilization of flames, and this is generated by swirl flow. The pressure gradient and distribution inside the combustor is the most important factor in forming a recirculation zone. As the flow passes through the swirl vane, tangential-direction velocity components are generated in the flow, further generating centrifugal force toward the outside of the combustor. A radial-direction pressure gradient is then formed in order to sustain equilibrium with the centrifugal force, which is called simple radial equilibrium flow. The pressure gradient

generated at this time can be calculated through a radial-direction momentum equation [10, 11]. First of all, an assumption can be established for the simple radial equilibrium flow as follows: Both the axial-direction and tangential velocity cannot exist in a steady state condition. Therefore, axial and radial velocities are related to radius functions, axial symmetry and radial-direction velocity. Under this assumption, the axial and tangential direction momentum equations become trivial solutions. The radial-direction momentum equation can be regarded as a governing equation that shows the pressure gradient of swirl flow.

$$\frac{\partial v_r}{\partial t} + (V \bullet \nabla) v_r - \frac{1}{r} v_\theta{}^2 = -\frac{1}{\rho}\frac{\partial p}{\partial r} + g_r + \nu(\nabla^2 v_r - \frac{v_r}{r^2} - \frac{2}{r^2}\frac{\partial v_\theta}{\partial \theta}) \quad (2.21)$$

Reduces to

$$\frac{\partial p}{\partial r} = \rho \frac{v_\theta{}^2}{r} \quad (2.22)$$

Figure 2.4 and Equation (2.22) show that the centrifugal force and the pressure gradient have equilibrium with each other. With this equation simply integrated, it was found that the closer it gets to the combustion chamber, that is, the smaller the radius becomes, the lower the stagnation pressure becomes. Since the tangential velocity component gets damped while moving closer toward the axial direction, the radial pressure gradient disappears in the back of the combustion chamber when it has a sufficient distance toward the axial direction, which indicates an achievement of pressure equilibrium. Therefore, around the combustion chamber wall, whose radius is large, a negative pressure gradient is formed, through which the pressure decreases gradually; meanwhile, in the central part of the combustion chamber, a positive pressure gradient is formed, through which the pressure gradually increases. Due to such a pressure distribution, outside flow comes rolling up the central part of the combustion chamber, enhancing the funnel-shaped recirculation zone existing in the central axis.

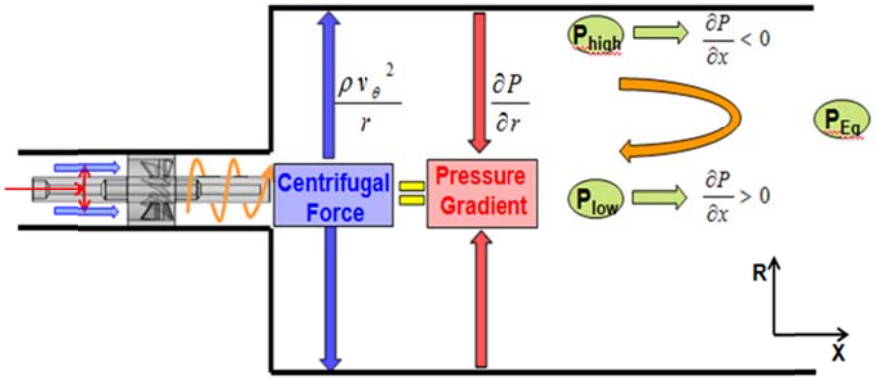

Fig. 2.4 Formation of recirculation zones for simple radial equilibrium flow condition.

2.3 Liquid Jet Column Trajectory

The theoretical expression of the liquid column trajectory shows the trajectory and the breakup point of the liquid column prior to the breakup, under the assumption that the horizontal acceleration is identical to the aerodynamic force acting on the front of the liquid column, as the relation of the momentum flux ratio (q) and the injected fuel jet velocity, the drag coefficient (C_D) and normalized axial (air-stream) distance (x/d), and showed the empirical formula by the injection angle (θ) as the liquid column trajectory equation. Also, using the breakup regime parameter of the time value from the secondary breakup of the spherical droplet, the horizontal and vertical breakup lengths were predicted and its reliability was confirmed by the empirical results in various cases [12, 13].

Under the 90° injection angle(Fig. 2.5(a)), trajectories of a liquid jet transversely injected into crossflows have been studied by numerous researchers. From previous research, it is known that the orifice diameter and liquid/air momentum flux ratio are the most important parameters for the trajectories. Schetz et al. [14] obtained the complete formula including the influence of q, the aspect ratio d_f/d_s of the injector and

injection angle θ as follows:

$$\frac{h}{d_j} = 1.32\ q^{0.5}\ C_d \left(\frac{d_{eq}}{d_f}\right)^{0.5} \left(\frac{d_f}{d_s}\right)^{0.46} \ln\left[1+6\frac{x}{d_j}\right] + \sin\left(\frac{2}{3}\theta\right) \qquad (2.23)$$

Assuming that liquid acceleration was balanced with aerodynamic drag forces and that the liquid column could be modeled as a cylindrical fluid element of the diameter of the nozzle exit. Wu et al. [15] calculated the correlation of the liquid column trajectory before the fracture point as follows:

$$\frac{y}{d} = 1.37\ \sqrt{q\left(\frac{x}{d}\right)} \qquad (2.24)$$

And the below 90° injection angle condition (Fig. 2.5(b)), By introducing an average drag coefficient, C_D, the axial momentum equation can be written as follows:

$$\frac{\pi}{4}\ \rho_f\ d^2\ \ell\ \frac{du_f}{dt} = \frac{1}{2}\ c_o\ \rho_g \left(u_g - u_f\right)\left[\left(u_g - u_f\right)^2 + \left(v_g - v_f\right)^2\right]^{\frac{1}{2}} ld \qquad (2.25)$$

To render the above equation more tractable, the following considerations were made. For the present investigation, $\left(v_g - v_f\right)^2$ was estimated to be considerably less than $\left(u_g - u_f\right)^2$ in most cases and was therefore neglected. In addition, the variation in u_f was, in most cases, very small as compared to u_g, so that the approximation $u_g - u_f \approx u_g - u_j$ could be made. Finally, ρ_g and u_g were presumed constant at their respective free stream values, and ρ_f and u_f were presumed constant at their

respective jet exit values, ρ_j and u_j.

$$u_f = \frac{2C_D}{d\pi}\frac{\rho_\infty}{\rho_j}\left(u_\infty - u_j\right)^2 \tag{2.26}$$

With $u_f = \frac{dx}{dt}$, a second integration with respect to time yields the following equation.

$$x = \frac{C_D}{d\pi}\frac{\rho_\infty}{\rho_j}\left(u_\infty - u_j\right)^2 t^2 + u_j t \tag{2.27}$$

Because the transverse velocity of the liquid column was presumed constant and equal to the transverse component of the jet exit velocity, $u_f = dy \big/ dt = v_j$, so $y = v_j t$ and the trajectory equation could be written as follows:

$$\frac{x}{d} = \frac{C_D}{\pi}\frac{\rho_\infty}{\rho_j}\frac{\left(u_\infty - u_j\right)^2}{v^2{}_j}\left(\frac{y}{d}\right)^2 + \frac{u_j}{v_j}\left(\frac{y}{d}\right) \tag{2.28}$$

With the momentum flux ratio $\overline{q}$ and the injection angle θ, the following equation was derived.

$$\frac{x}{dq} = \frac{1}{\pi}\frac{C_D}{\sin^2\theta}\left(1 - \frac{v_f \cos\theta}{v_a}\right)^2\left(\frac{y}{dq}\right)^2 + \frac{\cos\theta}{\sin\theta}\left(\frac{y}{dq}\right) \tag{2.29}$$

Therefore, the trajectory experimental formula of the liquid column region can be calculated depending on the injection angle that is less than 90° and on the reverse

injection. Here, x indicates the value of the axial distance of the axial (air-stream) direction, y indicates the value of the penetration distance of the penetration direction, d is the diameter of the orifice exit, θ is the injection angle, v_f is the fuel velocity and v_a is the value of the air velocity.

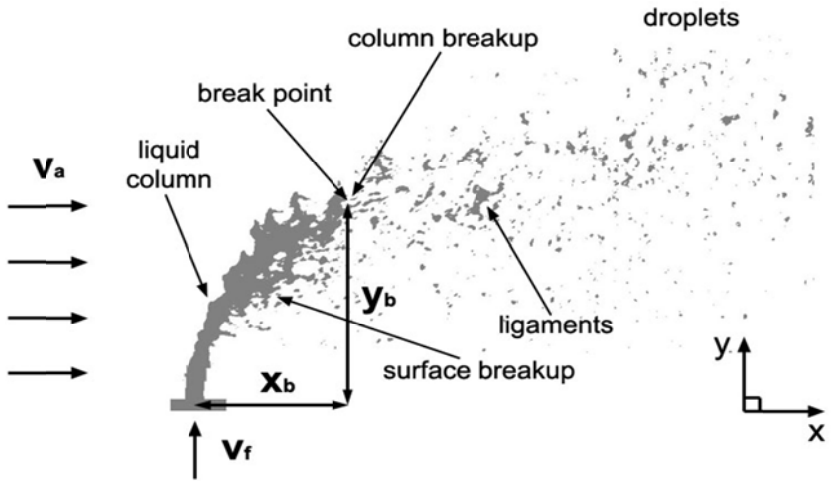

(a)

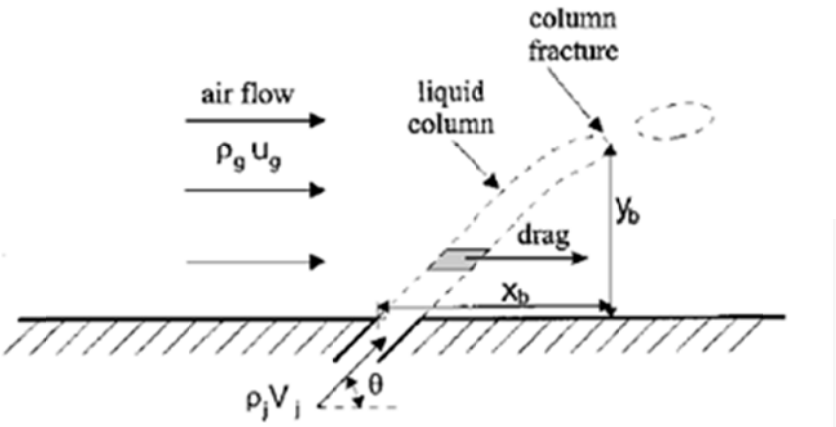

(b)

Fig. 2.5 Force diagram at the transverse liquid spray jet in crossflow; (a) 90° injection, (b) below the 90° injection.

CHAPTER 3

EXPERIMENTAL FACILITY AND TECHNIQUES

3.1 Model Gas Turbine Combustor

The combustor used for this study is a model gas turbine combustor simulating in the 1/3 scale downed of a GE 7FA+e DLN-2.6 gas turbine combustor, characterized with partially premixed and swirl stabilized flame, and the form is as shown in Fig. 3.1.

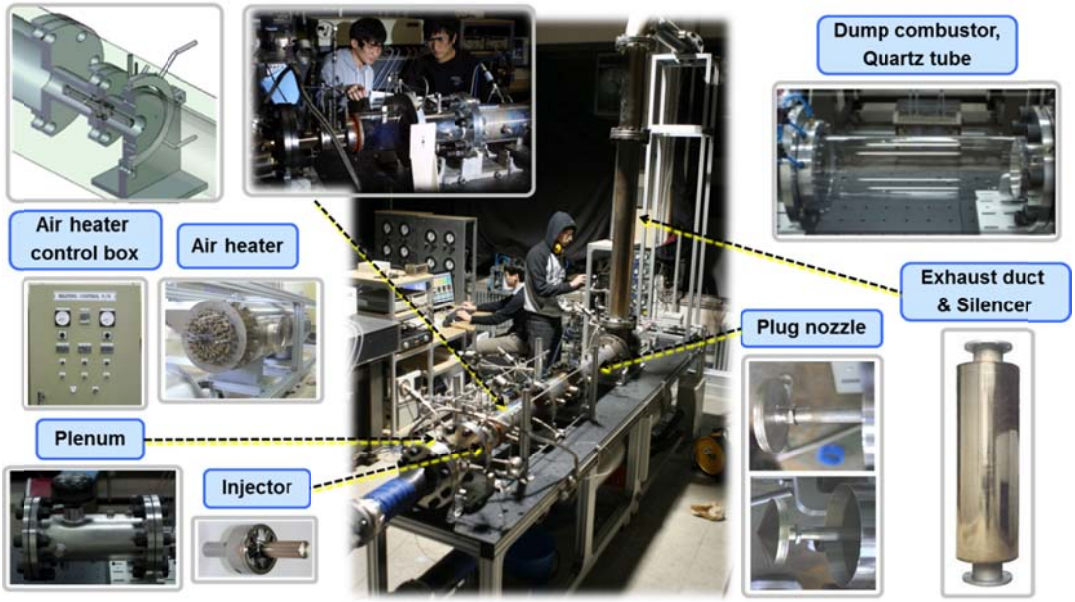

Fig. 3.1 Model dump shaped combustor simulating in the 1/3 scale downed of a GE 7FA+e DLN-2.6 gas turbine combustor and related component.

It is composed of air heating device, air supply lines, fuel nozzles, flame visualization quartz combustor and spike-typed plug nozzle of the exhaust duct for acoustic boundary. The air heating device consists of three 40 KW class electric heating element, functioning to heat the supplied air up to 873K. As shown in Fig 3.2, the

temperature of air supplied during the experiment is controlled within ±1%. And the air temperature is calibrated by K-type thermocouple at all of air velocity experimental conditions.

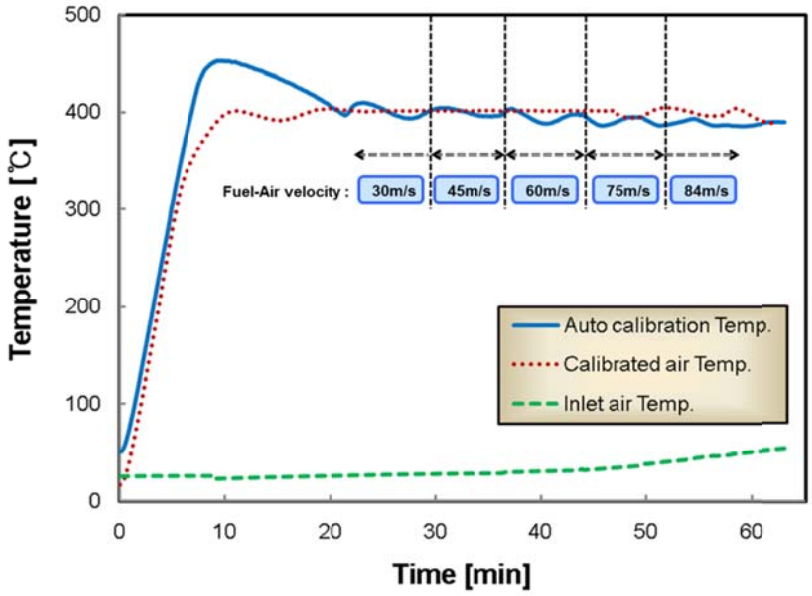

Fig. 3.2 Heated air calibration result of air heater control.

As shown in Fig 3.3, one of the main variables for this experimental study, the fuel-air mixing section was located between the combustor dump-side and the chocking orifice at the back of the air heating device, and there were three kinds in lengths, such as 470 mm, 550 mm and 870 mm, although they were all 40 mm inner diameter. The swirl injector used for this device is an axial-typed injector, and the angle of swirl vanes are 0°, 30° and 45°, and the number of vanes is 10. On the spot of 20 mm in front of the swirl vane, fuel is injected from 10ea nozzles with a 1.2 mm-sized hole, and through the 112 mm-sized mixing length in the back of the swirl vanes, fuel and air get partially premixed. The swirl effect can be expressed in the swirl number, which is the ratio of the tangential momentum and the axial momentum, and it can be approximately calculated through the

following equation [1].

$$S = \frac{2}{3}\left[\frac{1-(d_h/d)^3}{1-(d_h/d)^2}\right]\tan\Phi \approx \frac{2}{3}\tan\Phi \quad (d_h << d) \tag{3.1}$$

According to the above equation, the swirl number of the swirl injector used for this research was about 0.42(30°) and 0.72(45°). A circular stainless steel (@ Chapter 6, case 1, 2) and a quartz tube (@ Chapter 6, case 3 ~ 8) for the flame visualization were alternately used, and the diameter inside the combustor was 120 mm. The plug nozzle placed at the exhaust duct was supposed to function to change the resonant frequency of the combustor by making an acoustic boundary that blocks 91% of the combustor exhaust duct, which was designed to regulate the length of the combustor by 0.1 mm from 800 mm to 1680 mm through the stepper motor located in the exhaust part of model gas turbine combustor.

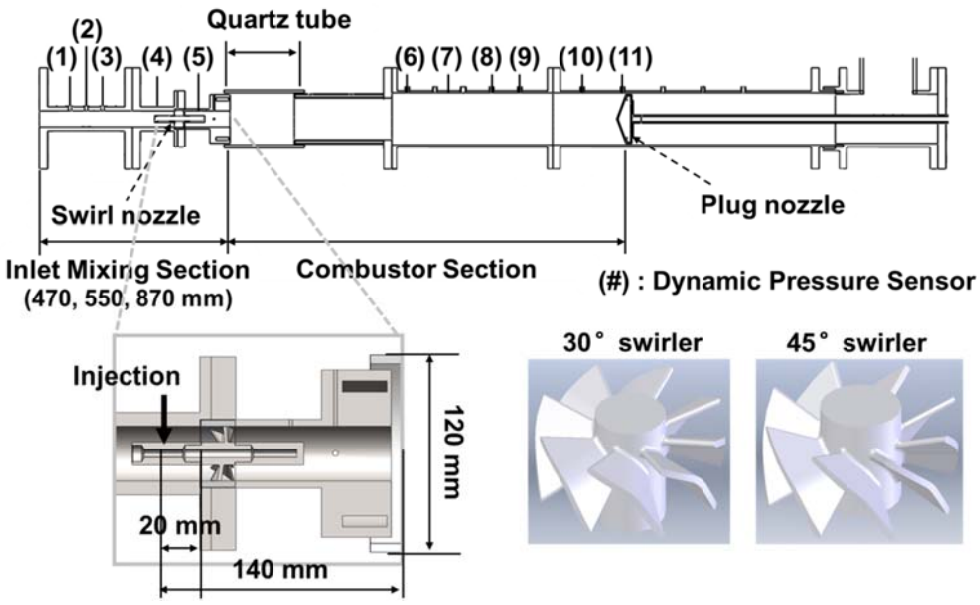

Fig. 3.3 Schematics of model gas turbine combustor and swirl injectors.

Figure 3.4 shows the calibration data and composition of air supply system. Working air was pressurized up to 8.5 bar by air compressor. The ACS100TA2 (Kyungwon compressor) was used for compressing air and it can blow out the air to 12.1 m^3/min. Many instruments, which are some chocked orifices, pressure differential gage and ball valves, were located in air supply line. Pressurized air was stabilized through the chocked orifice and then passed through the pressure differential gage. The air mass flow rate was controlled by ball valve using measured pressure differential gage. In addition, we measured air supply pressures and air temperatures, and these were used to control the air mass flow rate.

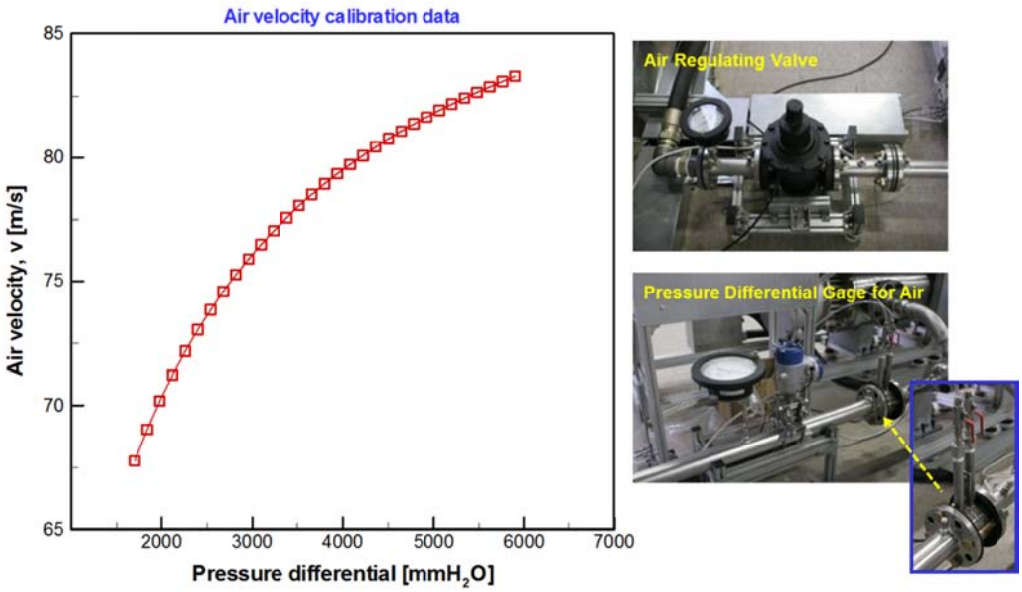

Fig. 3.4 The air calibration data and composition of air supply system.

Figure 3.5 shows the calibration data and composition of fuel supply system. In this experiments, Natural gas (89.4% CH_4, 8.6% C_2H_6, 1.39% C_3H_8, 0.25% i-C_4H_{10}, 0.32% n-C_4H_{10}, 0.04% N_2) was used as the fuel. And it was serviced by Seoul city gas Co., Ltd. (SCG). The fuel chocked orifice was used for precise control of equivalence ratio. In this

experimental study, fuel mass flow rate required about 0.9 ~ 3.5 g/s. So fuel orifice size (1 mm, 2.5 mm, 3 mm and 4 mm) were selected by each test condition for appropriate mass flow rate. And each orifice was calibrated by mass flow meter. The fuel mass flow supplied to the model dump combustor experimental device was measured with an M-1500SLPM-D Mass Flow Meter, made by Alicat Scientific Company. The fuel and air mass flow rate calculated through the flow meter and the differential pressure gauge was finally confirmed through Model 6332D, which is a Hot-wire velocimeter made by KANOMAX, and it was found that the errors of the values calculated and the mixture velocity measured at the combustor exit were within the range of ±3%.

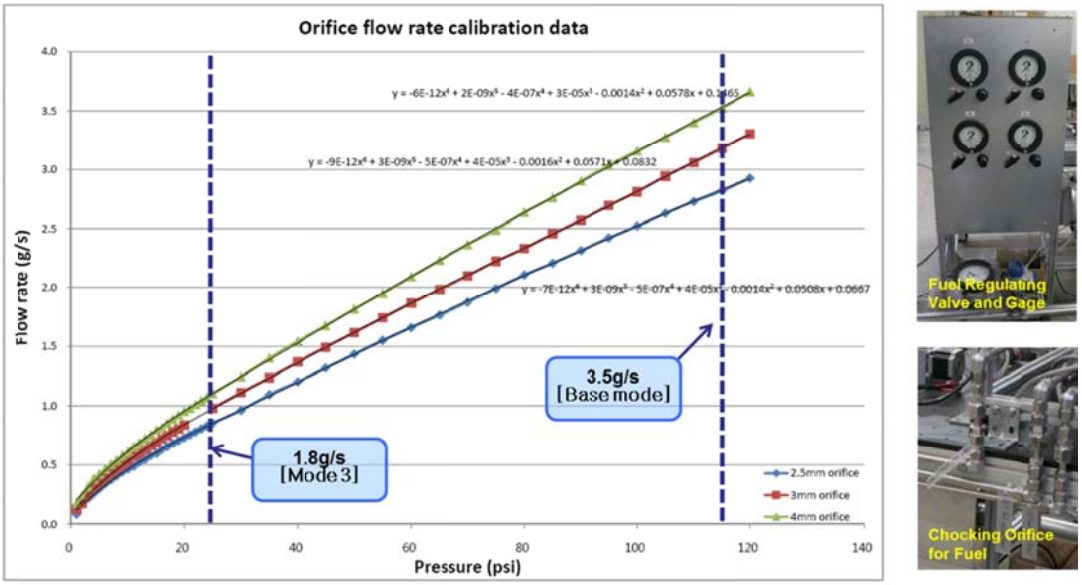

Fig. 3.5 The fuel calibration data and composition of fuel supply system.

Figure 3.6 shows the ignition system consisted of high voltage generator, tungsten wire and ceramic tube. About 18,000 volt was induced by high voltage generator. The tungsten wire was placed inside a ceramic tube for insulation. And the ceramic tube was inserted in a dump surface. Spark was induced by the gap between dump surface and

tungsten wire. The location of pyrotechnic initiator was selected to consider the vortex shedding zone. And the exhaust nozzle, dump surface and combustor were cooled down by water and the outer surface of combustor was cooled down by air.

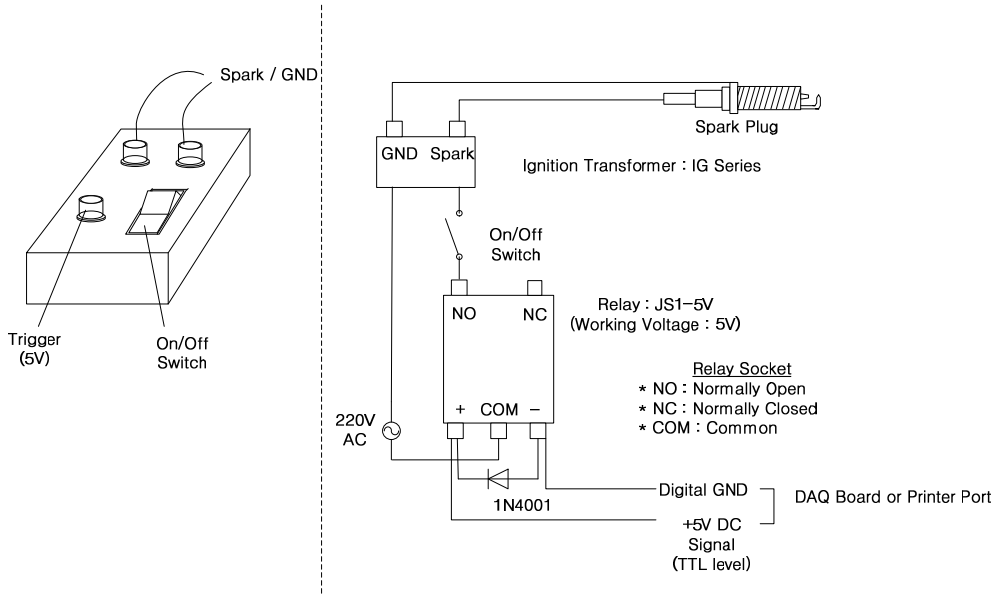

Fig. 3.6 The ignition system consisted of high voltage generator and spark plug.

3.2. Combustion Data Acquisition System

To measure the flow rate of fuel and air, combustion static pressure, exhaust emission and combustion dynamic characteristics of the model dump combustor, this experimental study used various kinds of sensors and a flow-meter to regulate the flow rate. First of all, to control the change of static pressure and the air flow rate before and after the combustion experiment, a total of six static pressure sensors made by Valcom Company were used. A K-type thermo couple was used to measure the temperatures of eight channels in total consisting of the air-supply (3 each), the combustor (4 each), and the exhaust emission sensor location (1 each), as well as the temperature around the

differential pressure gauge for the regulation of the fuel and air flow rate. To observe the oscillation of dynamic pressure occurring during the combustion experiment, we used five 102A05-type dynamic pressure sensors, manufactured by PCB Company, for the inlet mixing section and six for the combustor, as well as infinity probes, which suppress the reflected wave of dynamic pressure [2, 3]. In addition, the sampling rate was observed by receiving 10,000 data per second, and through Fast Fourier Transformation (FFT) techniques, it was possible to analyze them up to 5,000 Hz. The location of each dynamic pressure sensor is shown in Fig. 3.3. Moreover, OH* chemiluminescence was measured from the flame around the dump side. By using a high-speed ICCD camera made by Photron Company, we photographed flames at the speed of 1/6000 fps, and were able to obtain the pressure oscillation and heat release values from the time axis in the same experimental conditions by phase locking the dynamic pressure sensor. Fig. 3.7 indicated that phase locking system in this experimental study.

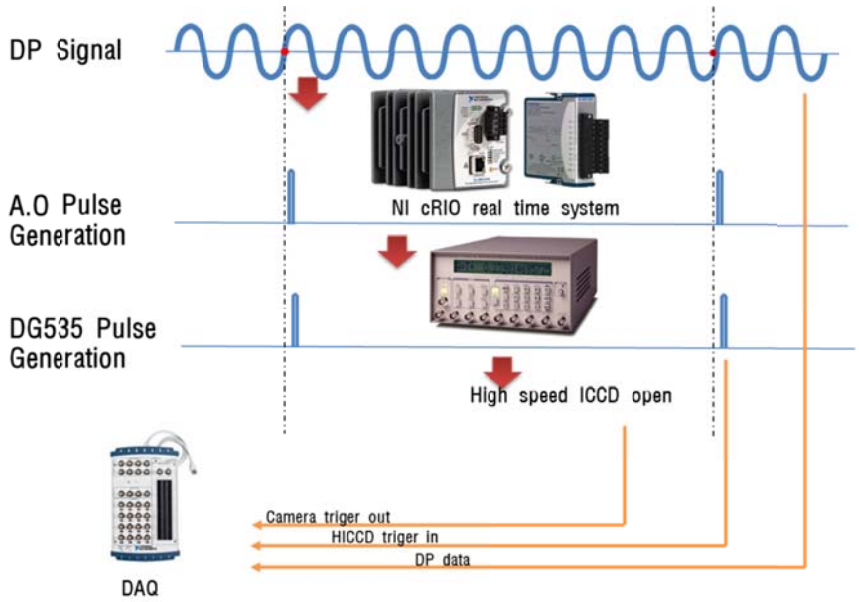

Fig. 3.7 LabView based phase locking system for heat release oscillation.

Data collection of the sensors was conducted with such devices as the C-RIO and DAQ made by National Instrument Company. The processing of the sensor data for the fuel and air mass flow rate control were performed with the use of a LabView-based program as shown in Fig. 3.8. And the heat release oscillation is basic data to be measured in order to understand causes of combustion instability. Thus, this study carried out a chemiluminescence signal measurement research and started photographing spots where – changes to + by observing dynamic pressure information through Nl cRIO. Besides, this study acquired signals that drive high-speed ICCD, signals of photos being taken and dynamic pressure signals by using DAQ and analyzed the flame visualization information and acoustic field oscillation information at the same time, especially about the combustion instability phenomenon, through the process of measuring the results of dynamic pressure and heat release waves in the same time domain.

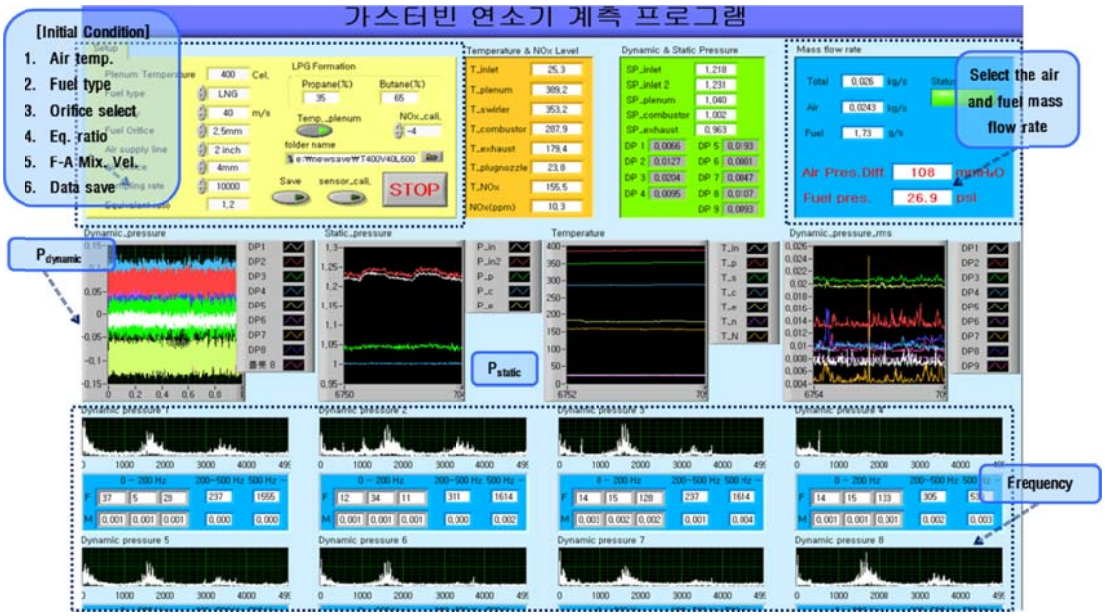

Fig. 3.8 LabView based combustion data collecting system and user interface program.

3.3 Multi-Position Dynamic Pressure Sensing System

To observe the oscillation of dynamic pressure and standing wave form occurring during the combustion experiment, this study used 5ea 102A05-type dynamic pressure sensors, manufactured by PCB Company, for the inlet mixing section, 6ea for the combustor, and the infinity probes that suppress the reflected wave of dynamic pressure [4]. In addition, the sampling rate was observed by receiving 10,000 data points per second. Through FFT, it was possible to analyze up to 5,000 Hz. The location of each dynamic pressure sensor is shown in Fig. 3.9. As aforementioned it, the data collection of the sensors was conducted with such devices as a C-RIO and DAQ made by National Instrument Company. The sensor data processing the fuel and air mass flow rate control were performed through a LabView-based program.

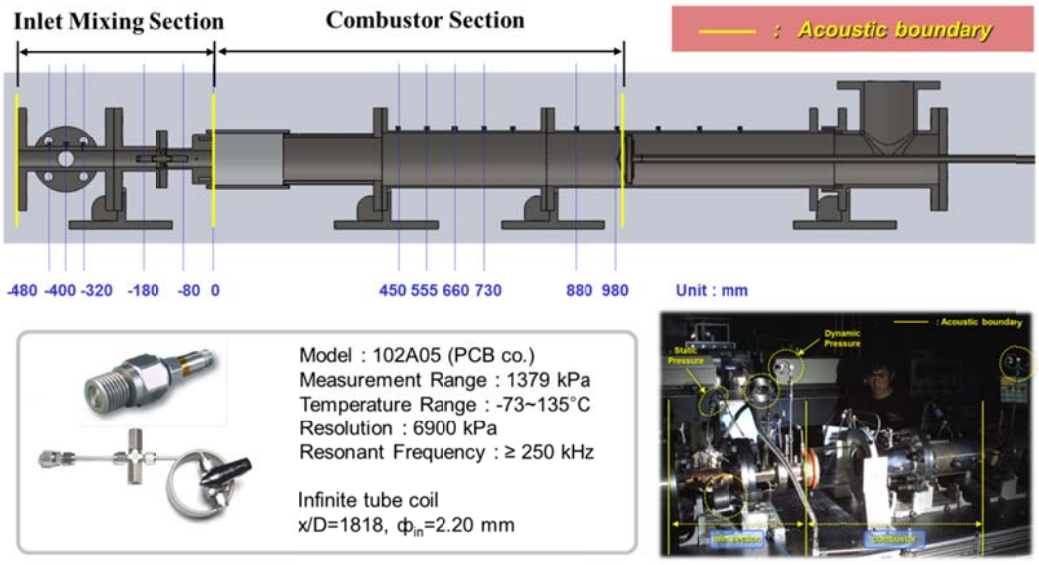

Fig. 3.9 Composition of dynamic pressure sensors and location in model gas turbine combustor.

3.4 Chemiluminescence and Flame Structure Analysis

Chemiluminescence from hydrocarbon flames arises from specific molecules that are lifted to an excited state by exothermic chemical reactions and then subsequently decay back to equilibrium energy levels by emitting a photon. Chemiluminescence emission occurs in specific wavelength bands that are characteristic of the emitting molecules. Because the molecules responsible for the chemiluminescence change for different combustion regimes and types, chemiluminescent emissions can provide information about the nature of the reactions and the fuel/airmixture [5].

Most naturally emitted ultraviolet and visible radiation of flames, called chemiluminescence, is caused by short lived electronically excited intermediate species such as OH*, CH* or C_2* formed during chemical reactions [6, 7]. An example is depicted in Fig. 3.10 (left panel) from a Bunsen burner, operated with a stoichiometric mixture of methane and air. If the radiation emitted by this flame is dispersed in a spectrometer into its wavelength components, spectra can be observed like those shown in Fig. 3.10 (right panel). On recognizes characteristic emission bands originating from the above mentioned species in their respective electronically excited (A) states of OH* (310 nm), CH* (388, 431 nm) und C_2* (473 nm), respectively. It is therefore of interest to investigate if the intensities or spectral shapes of these band systems can provide quantitative information on, e.g., local fuel/air ratios, heat release rate (HRR) or chemical processes of the combustion system investigated. If so, this would be of great importance for technical combustion systems, since detecting chemiluminescence radiation is a cheap and non-intrusive method for monitoring the combustion event in environments such as power plants, waste incinerators or combustion engines [8].

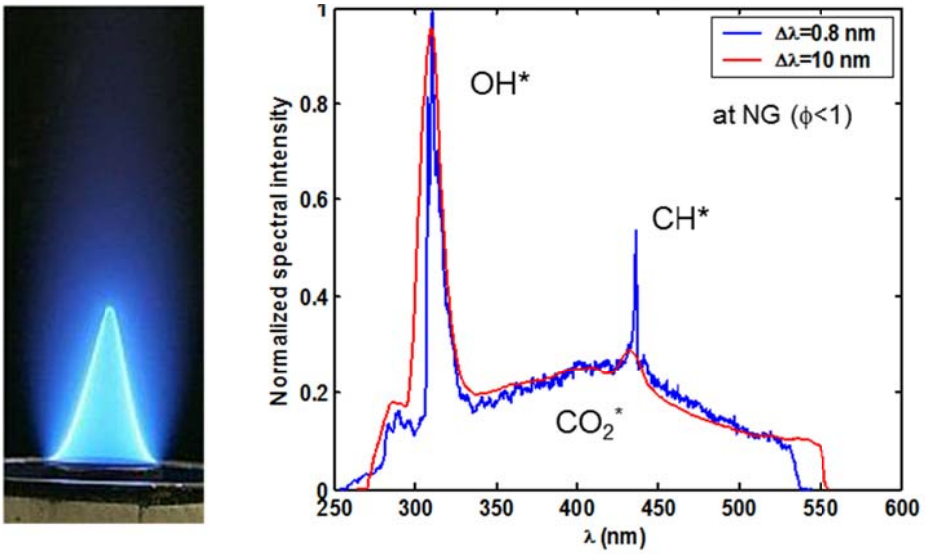

Fig. 3.10 Spectrum of the chemiluminescence radiation emitted from a premixed methane/air flame in Bunsen burner [8].

Abel convolution is one of optical diffraction tomography and integral transform, such as onion pilling method and back-projection algorithm. It is useful to transfer a 3-dimensional line-of-sight image to a 2-dimensional profile [9]. According to Pun et al. [10], light emission measurement of chemiluminescence cannot capture the fine flame structure, because the signal is integrated through the depth of the flame. Therefore, each image was processed with Abel convolution. With Abel inverted images, the time-averaged flame structure profile can be reconstructed, if the flame shape is axisymmetric.

This work is focused on the interpretation of OH and CH chemiluminescence data, because they have been widely employed as a flame marker [11] to study the combustion process by spectral combustion diagnostics [12, 13-18]. A high-speed ICCD Camera was used in this study for recording OH and CH chemiluminescence images of high-frequency instability phenomenon. For synchronization of heat release data from ICCD and dynamic data from PCB dynamic sensor, NI cRIO was used for triggering and NI DAQ was also used for recording data. NI cRIO operates at 40M Hz and has reliable

computation speed; therefore, it was used for detecting the rising edge of dynamic pressure data and triggering at the data changing point, which occurs when the data changes from positive to negative. To quantify the flame structure, the concept of maximum intensity location of the flame was used to calculate the flame center as shown in Fig. 3.11. The flame angle is computed from the intensity center and the center of the dump plane. In other words, the angle between the intensity center and the middle of the dump plane is regarded as the flame angle. Flame angle can demonstrate the axial and radial momentum ratio; a similar concept about flame center is used in the research of Kim et al [19, 20]. There, flame angle is a factor that can represent the flow structure of the flame. This calculation for the flame center is performed in all phases of the Abel-inverted image and shows the flame angle change at each phase.

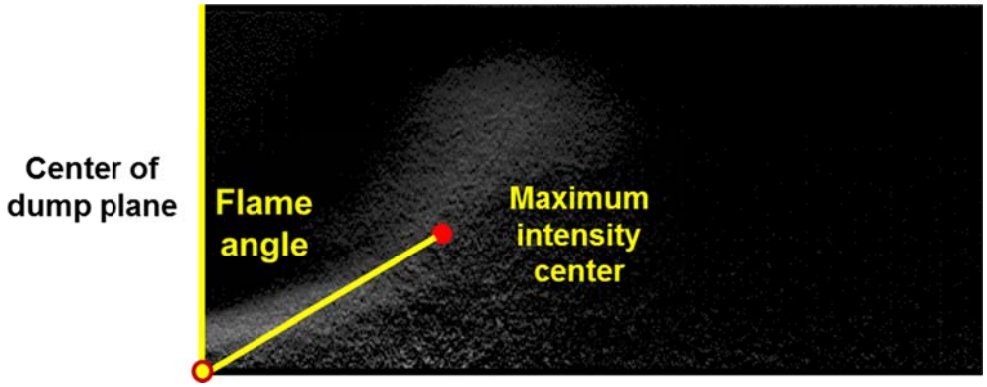

Fig. 3.11 Definition of flame angle and length of maximum intensity location.

3.5 PIV (Particle Image Velocimetry)

Particle Image Velocimetry (PIV) is a quantitative method for measuring 2-D velocity fields instantaneously, using consecutive images of particles illuminated by light sheets. The experimental setup of a PIV system typically consists of several subsystems [21]. Tracer particles have to be added to the flow, and these particles have to be illuminated in a plane of the flow at least twice within a short time interval. The light

scattered by the particles has to be recorded either on a single frame or on a sequence of frames. The displacement of the particle images between the light pulses has to be determined through evaluation of the PIV recordings. For evaluation, the digital PIV recording is divided in small subareas called “interrogation areas”. The local displacement vector for the images of the tracer particles of the first and second illumination is determined for each interrogation area by means of statistical method (auto- and cross- correlation). It is assumed that all particles within one interrogation area have moved homogeneously between the two illuminations. The projection of the vector of the local flow velocity into the plane of the light sheet (2-component velocity vector) is calculated taking into account the time delay between the two illuminations and the magnification at imaging. The process of interrogation is repeated for all interrogation areas of the PIV recording. Fig. 3.12 shows the typical procedures of PIV measurement.

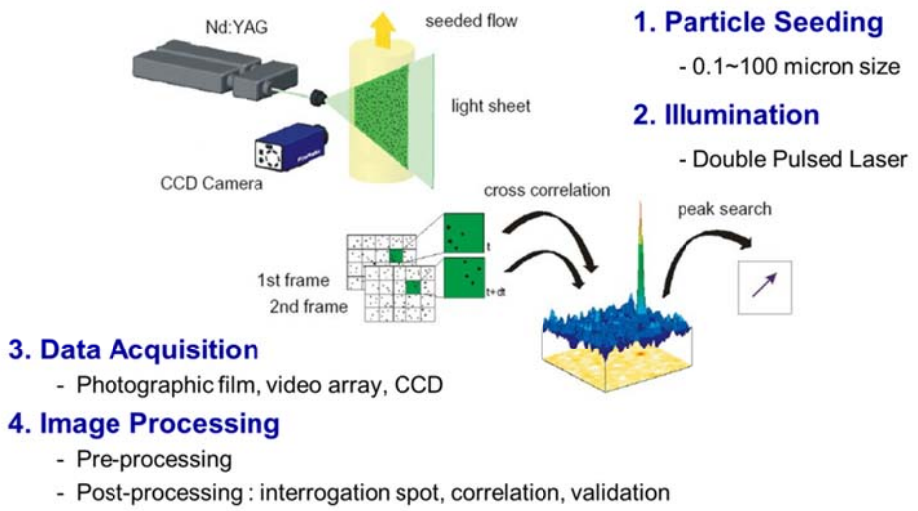

Fig. 3.12 Typical Procedures of PIV measurement.

The correlation function is expressed as follows:

$$h\left(s_x,\ s_y\right) = \int_0^\infty \int_0^\infty f\left(x,\ y\right) h\left(x + s_x,\ y + s_y\right) dxdy \tag{3.2}$$

A correlation method is classified into auto-correlation and cross-correlation according to the number of functions. Auto-correlation is for the case $f\left(x,\ y\right) = g\left(x,\ y\right)$ in Eq. (3.2) and the cross-correlation is the $f\left(x,\ y\right) \neq g\left(x,\ y\right)$ case. Auto-correlation is used when the first image and the second image are recorded in one frame (single frame / double exposure) and cross-correlation is used when the two images are recorded in separate frames (double frame / single exposure). Compared to auto-correlation method, cross-correlation method has some merits: 1) The problem of directional ambiguity is eliminated, 2) The algorithm is simple because there is only one peak as a result of correlation and 3) Dynamic range is relatively large.

3.6 PLLIF (Planar Liquid Laser Induced Fluorescence)

To measure the trajectory and breakup length of the liquid column spray jet, we used the PLLIF (Planar Liquid Laser Induced Fluorescence) technique. Another approach to the patternation of fuel sprays is the use of PLLIF (Planar Liquid Laser Induced Fluorescence). The PLLIF technique is based on the fact that the fluorescence signal intensity of a spray drop is proportional to the concentration of fluorescent molecules (i.e. the volume of the drop) under the condition that the laser light absorption is low enough for the molecules to be uniformly illuminated [22]. The grey level of the *i*-th and *j*-th pixel of the CCD array by the fluorescence signal can be expressed as follows [23]:

$$G\left(i,\ j\right) = CI_0 \sum_k n_k d_k^3 \tag{3.3}$$

Where, C is a constant and I_0, the incident laser beam intensity at the (i, j) pixel, is assumed to be constant within the pixel. Since the drop number density of the k_{th} size class $d_k(n_k)$ is the time-averaged value, the grey level in Eq. (3.3) indicates the total volume of drops which do not pass the unit volume but exist inside the volume during the camera exposure time, i.e. spatial volume (or mass) concentration of the liquid drops. Furthermore, the constant C in Eq. (3.3) is difficult to obtain, so that only the relative distribution of the spray mass concentration can be obtained directly from the PLLIF measurements.

A laser sheet is formed by some combination of cylindrical and spherical optic. A digital camera is used for imaging the energy of interest. Depending upon the information desired, either continuous or pulsed lasers can be employed. If a suitable light source is selected in conjunction with a suitable test fluid, fluorescence can be induced. Fluorescence is dependent upon the concentration of the fluorescing molecules. If a molecule which can be made to fluoresce is present within the test fluid in a homogeneous fashion, then the fluorescence can be related to the volume of material. Some materials may fluoresce naturally (e.g. ringed hydrocarbons), while others may not (e.g. octanes, alchohols, water). In this case, suitable dye can be added to the fluid (e.g. rhodamine, fluorescein). If a dye is added, it can be selected such that is absorption spectra conveniently overlaps with common laser wavelengths.

CHAPTER 4
SWIRL STABILIZED FLAME STRUCTURE AND RECIRCULATION ZONE

4.1 Background and Objectives

At the turn of 21st century, problems related with energy depletion and environmental pollution has become an important issue [1]. Under these circumstances, emission regulations have become more stringent. Many researchers have tried to develop a new type of combustor which burns fuel more efficiently and produces lower emissions [2, 3]. In the context of such efforts, a lean premixed combustor has been introduced and used for power generation all over the world. A lean premixed combustor produces less NOx than conventional gas turbines by burning the fuel at a low temperature. Conventional gas turbines that burning the fuel near stoichiometric condition have some advantages in terms of stability of combustion, but these produce locally high temperature regions which induce large amounts of NOx and soot production. On the other hand, lean premixed combustors can decrease combustion temperature significantly by burning the fuel near lean equivalence ratio conditions [4, 5, 6]. However, combustion instabilities occur under the lean burning conditions where they are designed to operate. To eliminate these instabilities and develop effective approaches for their control, the mechanisms responsible for their occurrence must be understood. The necessary condition for combustion instability was first determined by Lord Rayleigh [7] and can be summarized in the following mathematical expression called the Rayleigh Criterion.

It means that combustion is unstable when the net rate of energy added to the acoustic field exceeds the net rate of damping provided by inherent dissipative processes such as heat and acoustic energy loss. It also shows that combustion instability can occur when the phase between pressure oscillations and heat release oscillations is less than 90°. During the last decade, the underlying mechanisms of combustion instabilities in lean,

premixed gas turbine combustors have been investigated. These involved mechanisms of the combustion instability and the physics of acoustic interactions in premixed gas turbines [8, 9, 10], the flame transfer function measurements and the coupling of combustion instability mechanisms [11, 12, 13, 14], and the dynamics and stability of lean premixed swirl-stabilized combustion [15, 16, 17].

Other groups have investigated flow structures and flame behaviors in lean premixed gas turbine combustors via laser diagnostics. Observations included: flame behavior in a laboratory-scale premixed natural gas turbine combustor from Planar Laser Induced Fluorescence (PLIF) images of OH*, Laser Doppler Anemometry (LDA), and Coherent Anti-stokes Raman Spectroscopy measurements [18, 19], the investigation of flow field, structures, temperature and species distributions of swirl flames in a gas turbine model combustor [20, 21, 22]. Those two research parts have been performed somewhat separately, and studies on flow structures and flame behaviors are not well documented for confined laboratory gas turbine combustors in comparison with studies for unconfined combustors. This chapter has been performed to investigate the flow structure in cold flow and mechanism of the combustion instability in terms of flow structural characteristics. PIV measurements and dynamic pressure measurements were conducted simultaneously to examine the effects of structural characteristics on the combustion instability. The result strongly suggests that the formation of a recirculation zone and its structural characteristics contribute to the occurrence and development of combustion instability.

4.2 Experimental Method and Conditions

The combustor used for this study is a model gas turbine combustor simulating in 1/3 scale a GE 7FA+e DLN-2.6 gas turbine combustor [23], characterized with partially premix and swirl stabilized flame. The form is as shown in Fig. 3.3. It consists of five main parts: an air heater, a fuel-air mixing section, a swirl injector, an optically accessible

quartz combustor section, and a plug nozzle. Regulated inlet air enters the electric air heater and is heated to 673 K. The air heater consists of three heating elements. Each of the elements uses 40 KW power and can be controlled individually. The air heater can maintain the desired temperature throughout the experiments. The heated air enters the mixing section through a chocking plate which is installed at the entrance of the mixing section to prevent mass flow rate oscillations and to provide a well-defined acoustic boundary condition. The mixing section is 550 mm long and has an annular cross section whose diameter is 40 mm. An axial-entry type swirl injector with 30° swirl vane angle was mounted in the mixing section 53 mm upstream of the dump plane. The swirl effect can be expressed by the swirl number, which is the ratio of the tangential momentum and the axial momentum.

As for the working fuel in the model gas turbine combustor, this study used CNG (compressed natural gas) that has 89.4% methane. The fuel is issued from 10 holes located 20 mm upstream of the swirl vanes, and mixed with heated air by passing through the swirl vanes. The combustor consists of a stainless steel dump plane, an optically accessible quartz combustor section with an inner diameter 120 mm, and a length of 200 mm, and a stainless steel variable-length section, which is blocked by a water-cooled plug nozzle. The length of the combustor, which is defined as the distance from the dump plane to the plug, can be continuously varied between 825 mm to 1125 mm by moving the plug nozzle along the axial direction of the combustor. The nozzle not only changes the length of the combustor but also defines the acoustic boundary condition for measurements of self-excited instabilities. The blockage ratio of the plug nozzle is 91%, which is large enough to set a proper acoustic boundary condition. All of the experimental conditions from this study are listed in Table 4.1.

To measure the flow rate of fuel and air, combustion static pressure, exhaust emission and combustion dynamic characteristics of the model dump combustor, this experimental study used various kinds of sensors and a flow-meter to regulate the flow rate. First of all, to control the change of static pressure and air flow rate before and after the combustion experiment, a total of 6 static pressure sensors made by Valcom Company

were used. One was placed in the front and one in the back of the orifice, and two were in the front and back of the swirl injector, and two were in the combustor. A K-type thermo-couple was used to measure the temperature. In all, the temperatures of 8 channels were measured, including air-supply (3ea), combustor (4ea), exhaust emission sensor location (1ea) temperature, and the temperature around the differential pressure gauge for the regulation of fuel and air flow rate.

Table 4.1 Experimental conditions and parameters.

Parameters	**Values**
Fuel type	Natural gas [CH_4(89.4%) + C_2H_6(8.6%) + C_3H_8(1.39%)]
Inlet air temperature [K]	673
Fuel temperature [K]	318
Swirl vane angle	30°, 45° swirler (swirl number = 0.42, 0.72)
Fuel-Air mixture velocity [m/sec]	40, 50, 60, 70
Equivalence ratio (Φ)	Blowout limit ~ 1.2
Inlet mixing section length [mm]	550
Combustor length [mm]	850 ~ 1082
Blockage nozzle [mm]	128 (Blockage ratio : 91%)

In this chapter, flame structures were obtained using Particle Image Velocimety (PIV) and OH* chemiluminescence. PIV is an attractive and useful technique for capturing instantaneous flow fields [24]. PIV is the simultaneous measurement of fluid or particulate velocity vectors at many (e.g. thousands) points, using optical imaging techniques. The measurements are usually made in planar “slices” of the flow field. It is a qualitative visualization method that can instantaneously capture 2-dimensional velocity fields, along with additional information such as turbulent intensity, strain rate, and vorticity. Several processes are required to get useful information, such as adding tracing

particles to the flow, laser illumination with periodic time delay, recording of Mie scattering images, and post-processing of recorded images. Fig. 4.1 shows the configuration of a PIV measurement system in a model gas turbine combustor.

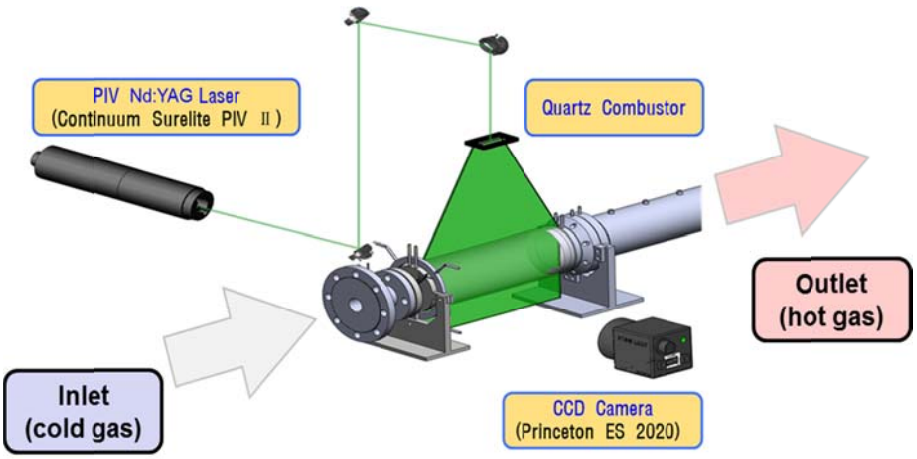

Fig. 4.1 Configuration of a PIV measurement system in a model gas turbine combustor.

A double pulse PIV laser (ND:YAG laser, 532 nm, Max. 3W per one head, 5 ns of laser pulse, 1 mm of laser sheet width, 8μs of double-pulse interval and 10 Hz of PIV repetition rate) was used to illuminate seeding particles, and Mie scattering images were captured by a CCD camera with a pixel resolution of 1600 × 1200 (Princeton ES2020). The size of the test section is 120 mm × 200 mm. Zirconium Oxide was used as a seeding particle, and its' mean diameter was about 1μm. The biggest challenge in applying the PIV technique to velocity measurements in strongly swirling flows is the strong out-of-plane motion decreasing the number of valid particle-pair images within the laser sheet [25]. Therefore, the laser sheet profile, the time interval between laser pulsed, and the seeding density in the flow have to be controlled to obtain valid velocity vectors. The addition of seeding particles to the flow and their contamination of the quartz combustor present an additional challenge in applying the PIV technique. This is extremely serious for the application of PIV and is a main reason for the relatively few publications describing PIV

measurements in gas turbine combustors. However, 2-dimensional images of the instantaneous flow field provide new insights into the dynamics of turbulent swirl-stabilized flames, which are very important for the understanding of combustion instabilities. Moreover, to measure the heat release oscillation of flame under stable and unstable combustion conditions, OH chemiluminescence was measured from the flame around the dump side. By using the high speed ICCD camera made by Photron Company, this study photographed flames at a speed of 6000 fps. This study was able to obtain the pressure oscillation and heat release values from the time axis in the same experimental conditions by linking with the dynamic pressure sensor, while locking the phase.

4.3 Results of Recirculation Zones

Previous researchers have used the size of the recirculation zone to examine the intensity of the recirculation zone which is based on how well recirculation zones move hot gases to the middle of the combustor and down into the ignition zone. Therefore, the intensity of the recirculation zone can be examined in terms of the size and the mass flow rate of hot burnt gases that the recirculation zone provides to the middle of the combustor. The examination of the zero axial velocity and the zero radial velocity helps define recirculation regions. The sizes of the recirculation zones are directly related to the height and width of the zero velocity contours.[26] Based on the size of the recirculation zone and the mass flow rate of hot burnt gases in the recirculation zone, the effect of each operating condition on the formation of recirculation zone was experimented.

4.3.1 Effect of various combustion parameters in cold flow

For the study of recirculation zones in cold flow, numerous experiments were conducted under the various operating conditions: fuel-air mixture velocities, equivalence ratios, and swirl numbers. Fig. 4.2 shows the averaged PIV images at different fuel-air mixture velocity conditions. The recirculation size can be defined by the contours of the zero axial and radial velocity. It is observed that the size of the recirculation zone

increases as the fuel-air mixture velocity increases form 40 m/s (Fig. 4.2 (a)) to 60 m/s (Fig. 4.2 (b)). The position of the vortex core was rarely changed and the magnitude of negative velocity vectors has increased as increase of the fuel-air mixture velocity. The formation of recirculation zones is the pressure gradient in the combustor so the trend with respect to the change of mixture velocities can be explained about the pressure gradient. The magnitude of the tangential velocity component is proportional to that of the axial velocity component determined by the fuel-air mixture velocity. According to Eq. (2.30), the magnitude of the pressure gradient is proportional to that of the square of the tangential velocity component, so the pressure gradient becomes larger as the mixture velocity increases. The pressure gradient disappears gradually along the axial direction because the tangential velocity component decays with axial distance. However, the more time and distance are necessary for the decay of the tangential velocity component under higher mixture velocity conditions, that is, the pressure gradient that is essential to drive the formation of the recirculation zone exist in the further downstream region under higher mixture velocity conditions.

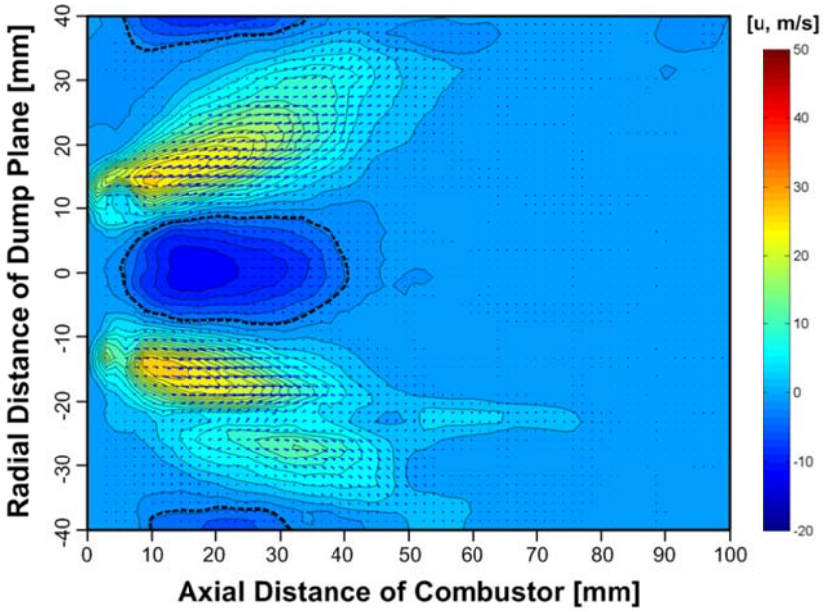

(a)

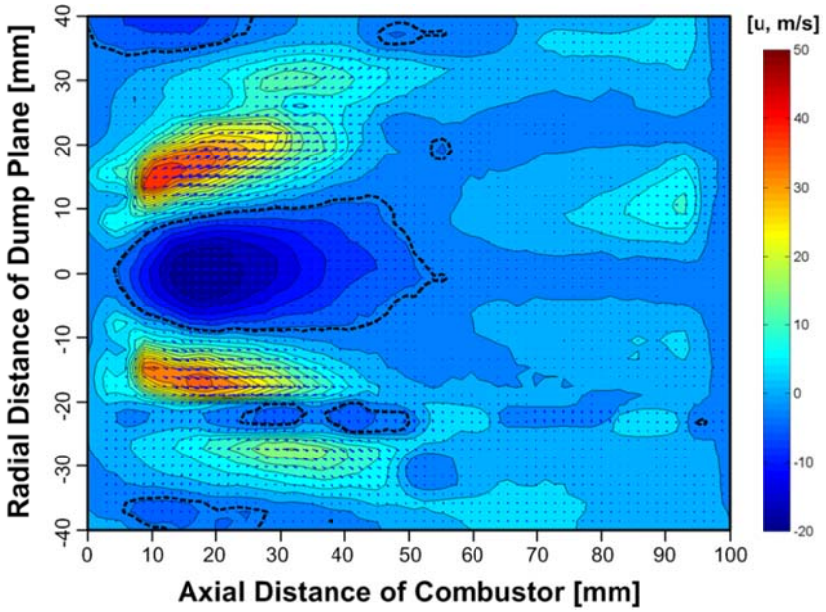

(b)

Fig. 4.2 Averaged PIV images and mean flow structures in a non-reacting flow at $L_{comb.}$ = 1050 mm, Φ = 0.8 and 30° swirl; (a) v_{mix} = 40 m/s, (b) v_{mix} = 60 m/s.

As shown in Fig. 4.3, the equivalence ratio doesn't have any effects on the formation of recirculation zones in a non-reacting flow. Actually, the equivalence ratio is one of the most important parameters that understand and driving issue the combustion dynamics. However, that does not have any influence on the flow structure without the combustion.

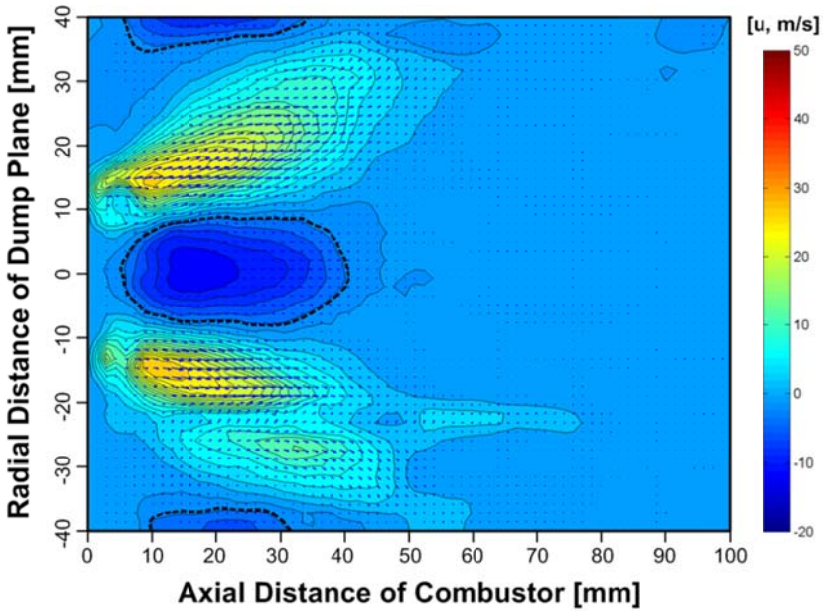

(a)

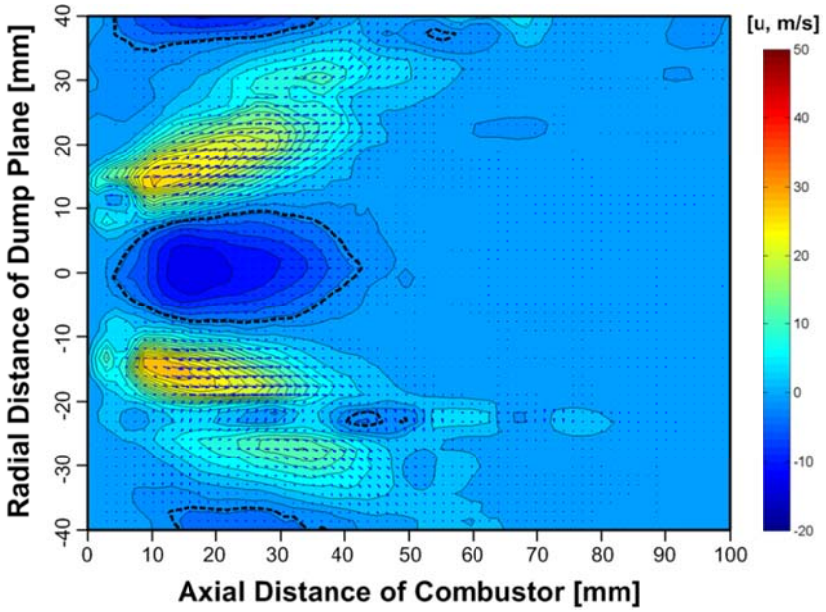

(b)

Fig. 4.3 Averaged PIV images and mean flow structures in a non-reacting flow at $L_{comb.}$ = 1050 mm, v_{mix} = 40 m/s and 30° swirl; (a) Φ = 0.8, (b) Φ = 0.65.

Figure. 4.4 shows the effect of the swirl number on the flow structure result. The swirl number was changed from 0.42 (30°) and 0.72 (45°) by using different swirl vane angles. An increase in the magnitude of the swirl number directly means the increase of tangential velocity components in the flow. According to the governing equation of the swirl flow Eq. (2.30), the pressure gradient becomes stronger as the tangential velocity increases. Consequently, the pressure gradient that drives the formation of recirculation zones can exist over a wider region of the combustor, so the size of the recirculation zone increase. The increase of the swirl number has the same effect with the increase of the mixture velocity on the size of recirculation zones.

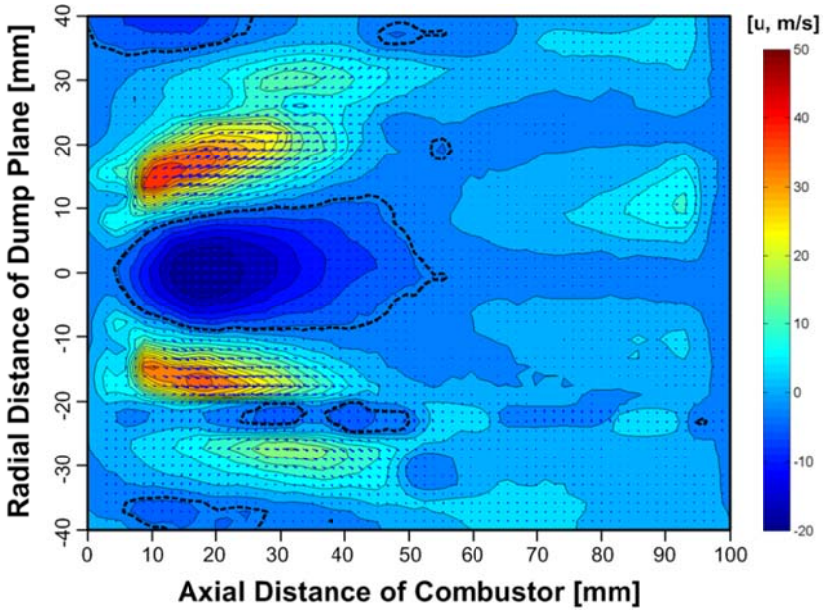

(a)

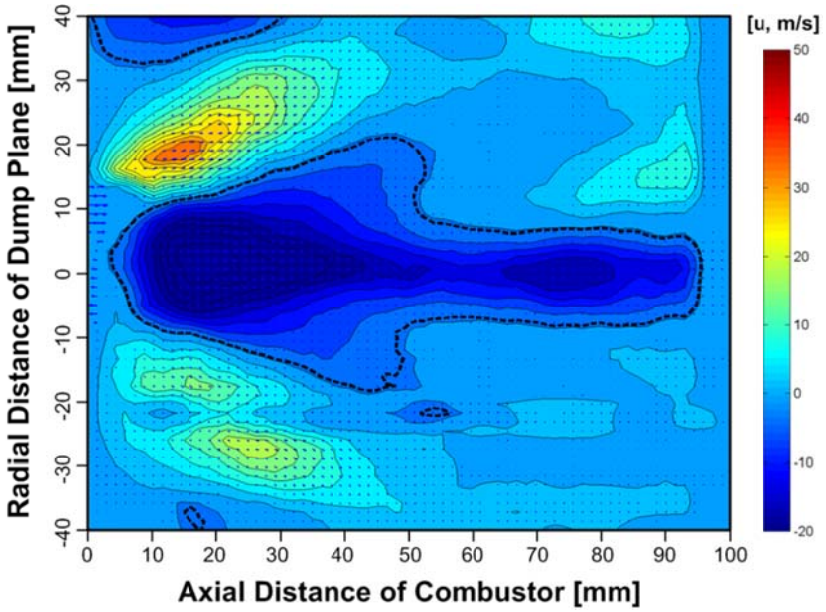

(b)

Fig. 4.4 Averaged PIV images and flow structures in a non-reacting flow at $L_{comb.}$ = 1050 mm, v_{mix} = 60 m/s and Φ = 0.8; (a) 30° swirl, (b) 45° swirl.

4.3.2 Effect of combustion and instability characteristics

Figures 4.5 (a) and (b) show values obtained through PIV measurement in a combustion field. After measuring 600 pairs of instant fields, this study calculated their average, which shows that a recirculation zone is formed in actual combustion conditions. To compare recirculation zone size, many researchers used the height or width of a recirculation zone, with the size of such a recirculation zone defined with borderlines connecting points whose axial-direction velocity and radial-direction velocity are 0 [18]. Fig. 4.5 (a) shows the characteristics of a recirculation zone formed under stable combustion conditions, while Fig. 4.5 (b) shows a recirculation zone formed in unstable combustion conditions. In this section, when combustion instability took place, it was observed that the size of a recirculation zone became remarkably enlarged. This finding indicates that the occurrence of combustion instability has an effect on the formation of a recirculation zone. Fig. 4.6 shows a calculating process used to simply compare the size of volume flux in a recirculation zone. Through this process, this study compared quantitative volume flux in a recirculation zone every moment in the random-phase PIV images in both flame stable and unstable conditions.

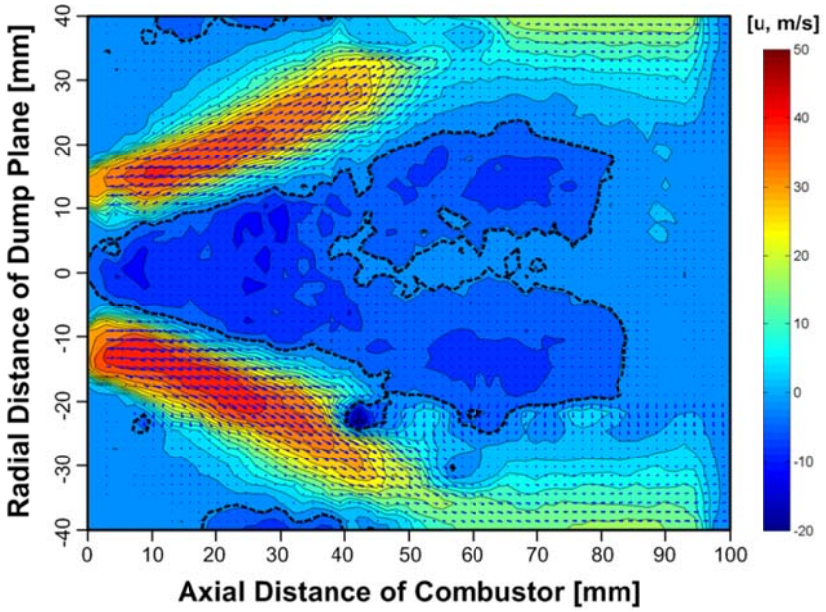

(a)

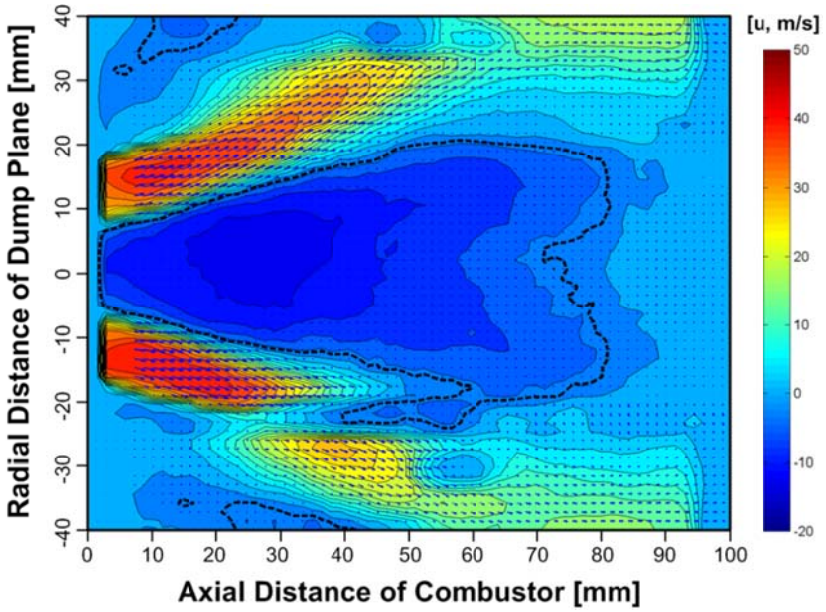

(b)

Fig. 4.5 Averaged PIV images in combustion condition at $L_{comb.}$ = 1050 mm, v_{mix} = 40 m/s and 30° swirl; (a) stable, Φ = 0.65, (b) unstable, Φ = 0.8.

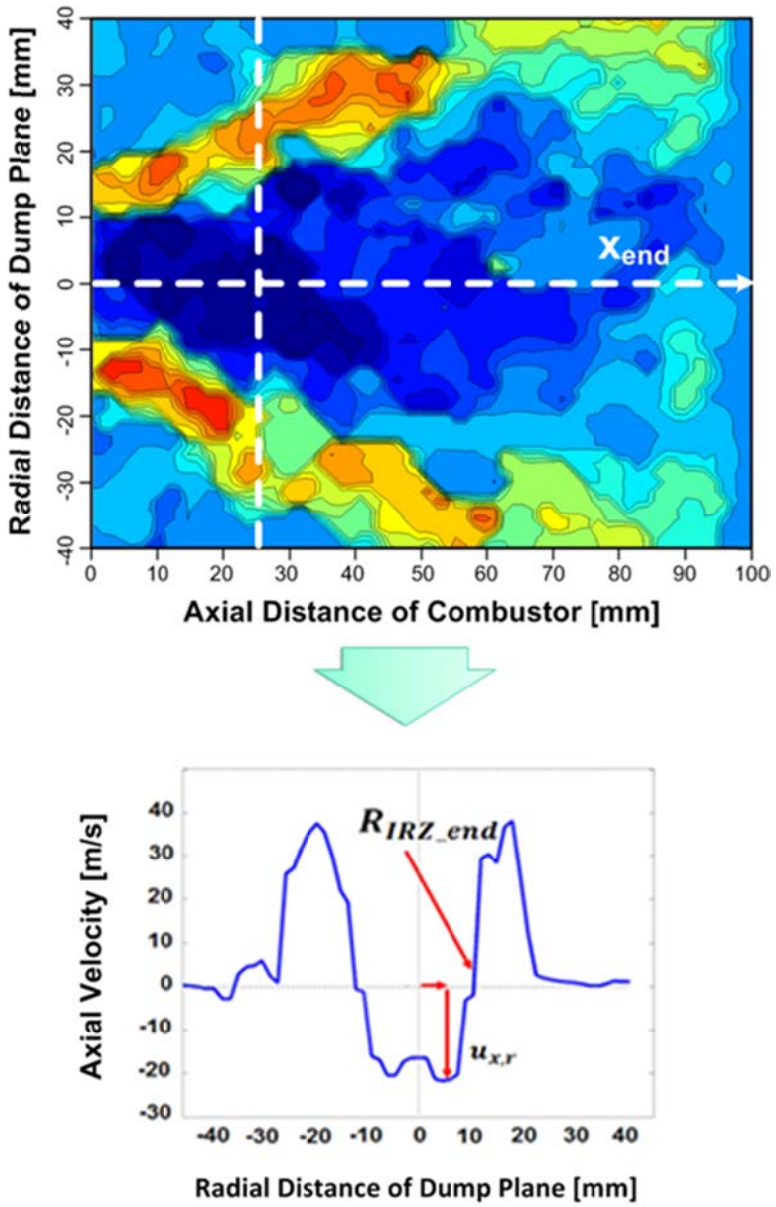

Fig. 4.6 Calculation for volume flow rate of swirling flame zone at 30 mm detached measurement point from the dump plane in stable and unstable conditions.

To find out the relation between the formation of a recirculation zone and combustion instability, this study adopted the PIV measurement technique. As combustion instability is a kind of a dynamic phenomenon, its characteristics are hard to investigate through mean-field images only. In this section, therefore, this study investigated the characteristics of a recirculation zone by using instantaneous images under the condition of combustion instability. Fig. 4.7 (a) shows the 4 cycles of random phase unstable flame images obtained through PIV under combustion instability. The phase of each image is not clear, owing to the phase locking method, but its cycle shows that the recirculation zone vibrates with a main instability frequency. In contrast, Fig. 4.7 (b) shows cycles composed of instantaneous images in stable combustion conditions, through which it was observed that the size of a recirculation zone hardly changed but was sustained almost throughout.

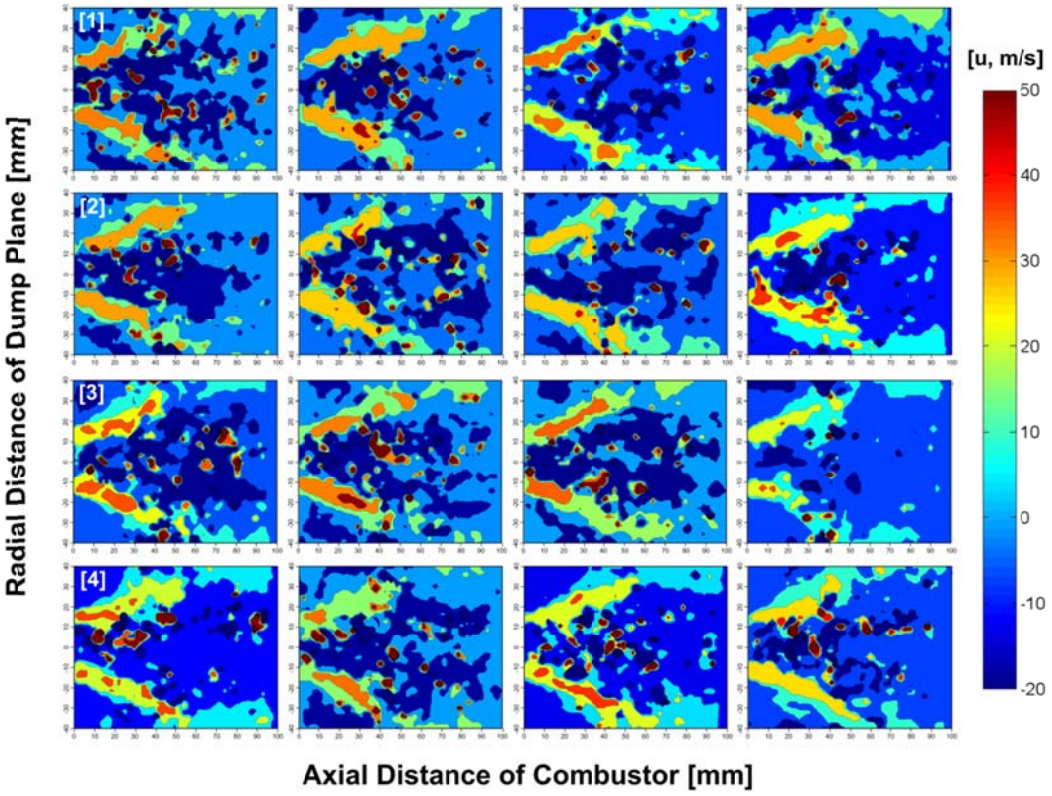

(a)

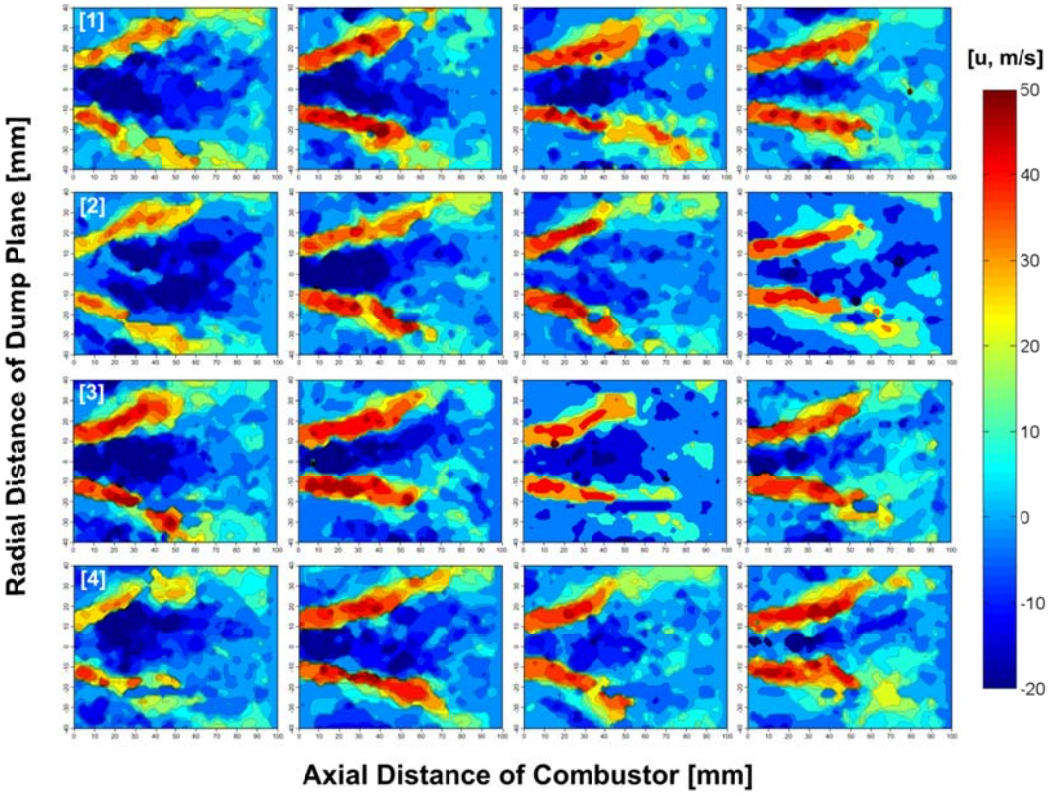

(b)

Fig. 4.7 Instantaneous PIV images in combustion condition at $L_{comb.}$ = 1050 mm, v_{mix} = 40 m/s and 30° swirl; (a) stable, Φ = 0.6, (b) unstable, Φ = 0.8.

Also, this experimental investigation is confirmed by Fig. 4.8 (a) and (b). That figures indicate that the axial velocity profile result of the each instantaneous PIV images at 20 mm detached measurement point from the dump plane in stable and unstable conditions. As mentioned earlier, the recirculation zone contributes to the stability of combustion by moving high-temperature combustion gas to the central part of a combustion chamber and near the fuel-air injected nozzle where ignition takes place. So, the most important assumed item is the volume flux of re-circulated combustion gas and which has almost the same value of flame zone air density. The volume flux can be calculated through the area of a recirculation zone and the size of negative-direction

velocity components. Therefore, the size of a constantly-changing recirculation zone means that the volume flux of recycled high-temperature gas changes as well, which is essential for the stabilization of combustion. Such change of volume flux causes the fluctuation of reaction rate and heat release rate oscillation, ultimately leading to combustion instability.

Unlike a case where stable combustion takes place as usual, it was observed that the size of a recirculation zone constantly changes in a condition of unstable combustion condition. Moreover, when this study examined the sizes of recirculation zones in the last picture in Figs. 4.7 (a) and (b), it was found that the formation was so weak that it contributed nothing to the stabilization of combustion, further causing flame quenching. Also, the fluctuation of a recirculation zone seems to have an effect on the occurrence of combustion instability. For the validation of this experimental study, we found the volume flow rate of a recirculation zone in combustion condition.

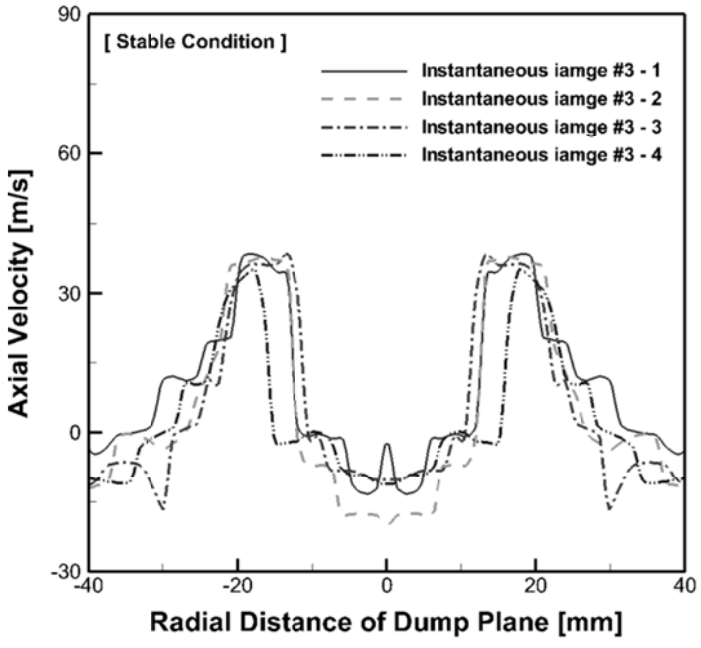

(a)

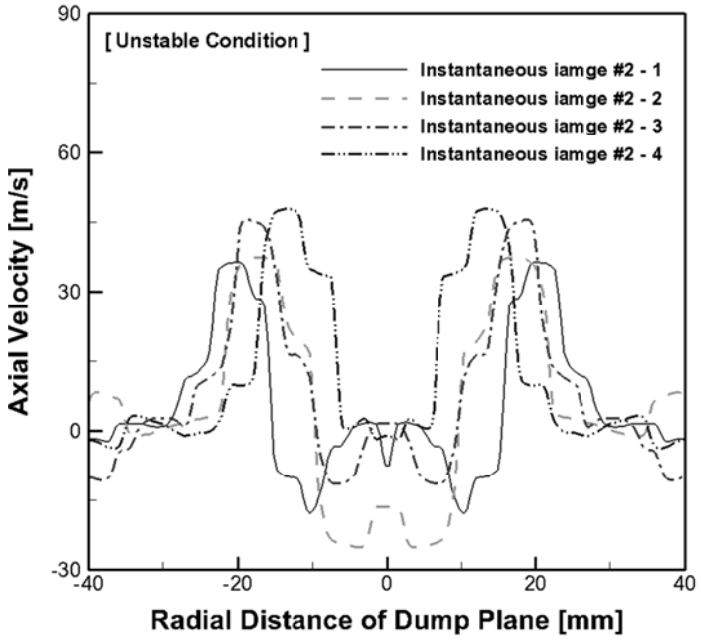

(b)

Fig. 4.8 Velocity profile result of instantaneous PIV images at $L_{comb.}$ = 1050 mm, v_{mix} = 40 m/s and 30° swirl vane angle; (a) stable, Φ = 0.6, (b) unstable, Φ = 0.8.

Figures 4.9 (a) and (b) indicate the result of volume flow rate changing in each random phase conditions through stable and unstable flame conditions. As shown this figure, there have larger volume flow rate region in the recirculation zone and its fluctuation at unstable combustion region than the stable combustion conditions.

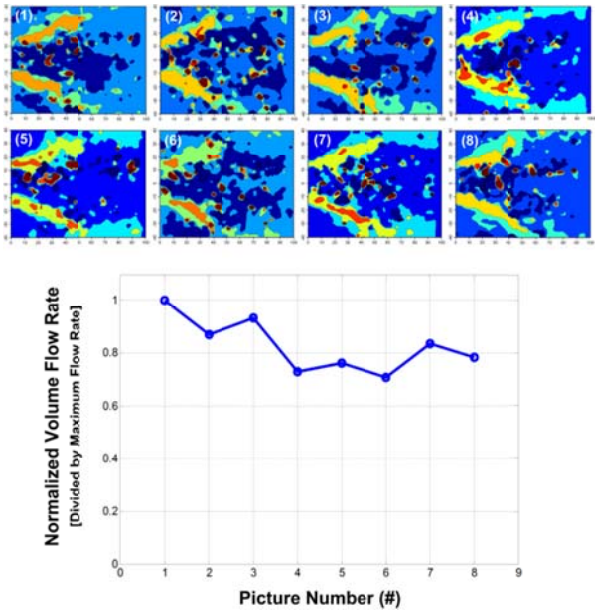

(a)

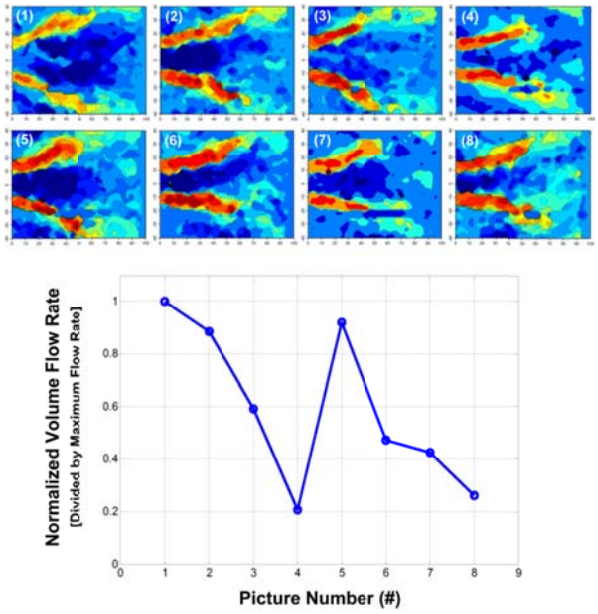

(b)

Fig. 4.9 Result of volume flow rate in each random phase conditions at $L_{comb.}$ = 1050 mm, v_{mix} = 40 m/s and 30° swirl; (a) stable, Φ = 0.6, (b) unstable, Φ = 0.8.

4.4 Analysis of combustion instability frequency

To investigate whether a recirculation zone vibrates cyclically and what that frequency of the vibration means When it occurs, this study measured the OH* chemiluminescence with a high-speed ICCD camera. At each moment, the camera frame speed was set at 2048 Hz. Figs. 4.10(a) and (b) are the results arranged in each phase, which shows that flame vibrates cyclically in conditions of combustion instability (Fig. 4.10(b)). In stable combustion conditions as shown in Fig. 4.10(a), it was observed that there was almost no change in the intensity of chemiluminescence signals, which shows that the form and size of flame were constant.

This study converted the values of intensity of chemiluminescence images obtained in instability conditions to analyze the frequency. Through the sum of them, this study examined the change of intensity by time and performed FFT. As a result, it was found that it vibrated with its natural frequency, 315Hz of combustor longitudinal mode. As a result of FFT with dynamic pressure information obtained during the process of this experiment, the frequency was found to be 313Hz. Furthermore, when theoretical instability modes were calculated with the length of a combustion chamber (1.05 m), and temperature (868 K, the average obtained from 3 points on the combustion chamber) in the closed-closed boundary condition, this study found the natural frequency of combustor at 322 Hz. Since the average temperature of the entire combustion chamber was actually lower than the temperature measured, this study found that the fluctuation of flame, the fluctuation frequency of instability phenomenon, and the theoretically-calculated unstable mode all have very similar values. This result supports the assumption that there is a direct relation between combustion instability and the fluctuation of a recirculation zone.

A theoretical analysis to calculate this phenomenon is shown in Eq. (4.1) and Eq. (4.2). It is assumed that the movement course of energy in a gas turbine combustor is axial direction and the average temperature is constant with 1-D standing waves theory.

$$\text{Quarter wave mode} : f_0 = \frac{(2n-1)c}{4L} \tag{4.1}$$

$$\text{Half wave mode} : f_0 = \frac{nc}{2L} \tag{4.2}$$

$$\left[\textit{where}, n = 1,2,3..., c = \sqrt{\gamma RT} \right]$$

Combustion instability has an essential relation with the fluctuation of a recirculation zone, and it can be explained through procedures shown in Fig. 4.11. When combustion instability takes place, high pressure fluctuation occurs inside the combustion chamber. As mentioned above, the most important factor in forming a recirculation zone is the very formation of a pressure gradient inside the combustion chamber. However, when combustion instability takes place, a pressure gradient is not smoothly formed due to the pressure fluctuation inside the combustion chamber, which is needed for the formation of a recirculation zone. Consequently, the recirculation zone proceeds to vibrate under the influence of instability-caused pressure fluctuation. The vibration of a recirculation zone further causes mass flow rate fluctuation of high-temperature recycled gas needed for stable combustion. It is at this moment that, mass flow late fluctuation in recirculation zone leads to the fluctuation of heat release as one of the factors sustaining and developing combustion instability.

In summary, the fluctuation in a recirculation zone functions as one of several factors causing and developing combustion instability. It can be regarded as an essential accompanying phenomenon when combustion instability takes place.

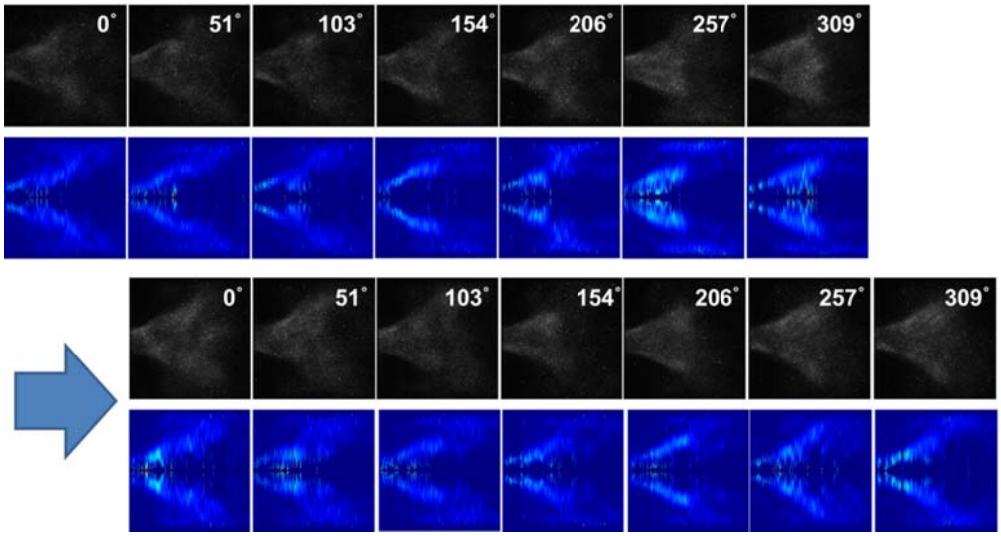

(a)

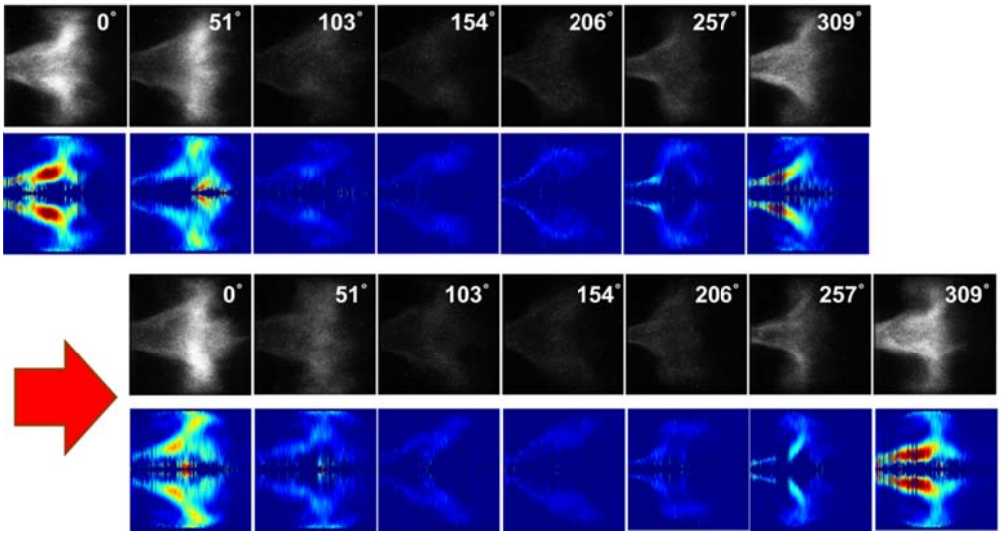

(b)

Fig. 4.10 OH chemiluminescence and abel-inverted images at $L_{comb.}$ = 1050 mm, v_{mix} = 40 m/s and 30° swirl; (a) stable, Φ = 0.6, (b) unstable, Φ = 0.8.

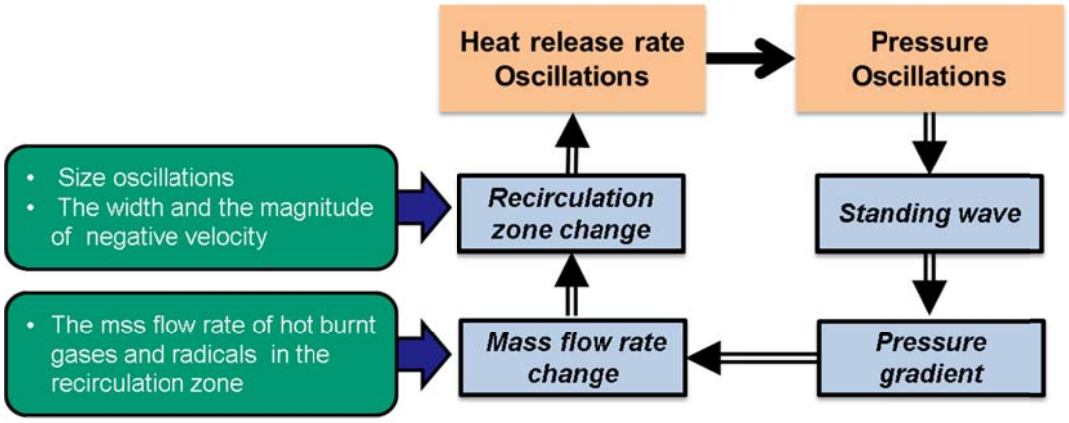

Fig. 4.11 Relation between the recirculation zone oscillation and combustion instability.

CHAPTER 5
EFFECT OF FUEL-AIR MIXTURE VELOCITY

5.1 Background and Objectives

Combustion instabilities occur when different combustion processes combine in such a way that inherent disturbances in the system are self-excited via interactions with the combustion process. These are caused by complex, feedback-type interactions between periodic flow and combustion processes that produce a periodic heat addition, exciting large-amplitude acoustic oscillations in the combustor [1].

In addition, a recent study by Meier et al. [2, 3, 4] has shown the relation between ignition delay time and combustion instability occurrence by CFD and experimental studies using the PIV and PLIF measurements in a model gas turbine combustor. Candel et al. [5, 6] investigated the flame response by measuring the unsteady heat release induced by an imposed velocity perturbation and flame dynamic, which is documented by the calculating the phase averages. As concerns the flame vortex interaction research field, Kim et al. [7] investigated the effects of acoustic forcing on flame length and NOx emission in turbulent hydrogen non-premixed jet flames with coaxial air, which was acoustically forced at the resonance frequency of the combustor. Also, in order to examine mixing and dynamic behaviors during flame-vortex interaction, the local properties on the flame surface were characterized quantitatively. The behavior of the precessing vortex core (PVC) is also significantly altered by combustion heat release and by the system parameters (e.g. swirl number, axial velocity and geometry). Previous studies [8, 9] suggest that the type of combustion (i.e., premixed or non-premixed) can affect the PVC frequency and its intensity.

However, there is no other research about the interaction of vortex structure and combustion instability phenomenon. The flame recirculation zone (flow patterns in combustion region) is very important, as it can modulate the air flow rate at instability condition and may be the source of instability by modulation local equivalence ratio. In

this chapter, we conducted experiments under various fuel-air mixture velocity and operating conditions with a model gas turbine combustor to examine the relation of combustion instability and flame structure using the OH chemiluminescence and multi-channel dynamic pressure sensing system.

5.2 Experimental Method and Conditions

Figure 5.1 shows a schematic of a partially premixed, variable length, model gas turbine combustor (same as facility of Fig. 3.3). It consists of an air heater, an inlet mixing section, which is called the plenum, a swirl injector, an optically accessible quartz combustor section, a steel combustor section, and an exhaust duct. An air heater provides heated air (673K) to a combustor through an air inlet section. There is a choking orifice at the entrance of the air inlet section to provide a well-defined acoustic boundary condition and to protect the fluctuation of inlet air. In the inlet mixing section, the mixing process between the fuel and heated air is done by a swirl injector, which provides a spatially and temporally homogeneous reactant mixture to the combustor. The length of the steel combustor can be varied continuously from 850 mm to 1100 mm by moving a water-cooled plug nozzle along the axial direction of the combustor. The temperature of plug nozzle varies from 350 to 490K, which is based on inlet velocity conditions. PCB 102A05 piezoelectric transducers are used to measure unsteady pressure perturbations in the inlet mixing section and combustor section. Five pressure transducers are installed in the mixing section, and six pressure transducers are installed in the combustor, respectively. Five static pressure sensors made by Valcom inc. are used to measure the combustion static pressure and control the mass flow rate of inlet air and five K-type thermocouples are also used.

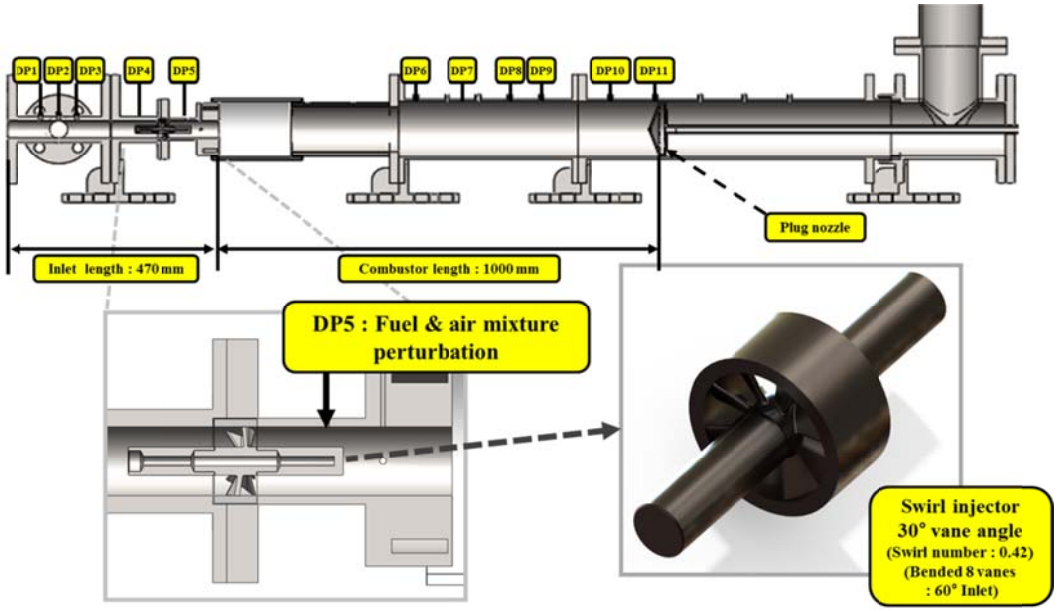

Fig. 5.1 Schematics of model gas turbine combustor for variable fuel-air mixture velocity.

Figure 5.2 shows the stability map of our dump combustor. Changes occur in the combustion instability phenomenon trend, based on inlet mixture velocity, and vary from 30 to 70 m/s. In the low and high fuel-air mixture velocity regions, high-levels of instability occur and the middle of the velocity conditions has a low-level unstable effect. Therefore, inlet mixture velocity was selected as the main variable and other variables, such as combustor length, equivalence ratio, and plenum length were fixed of 470 mm during this study and then flame visualization and dynamic pressure analysis was performed at these conditions as shown in Table 5.1. Since almost same phenomenon occurs at both slightly lean and rich conditions, and rich condition was much easier to maintaining instability conditions, slightly rich condition which means equivalence ratio 1.2 was selected in this study. Through this process, various mixture velocities for the cause of combustion instability and its maintenance process were performed to understand the relevant processes in this study. The velocity variable can be treated as a condition of the burner output and then low velocity conditions when low fuel flow rates

condition. In this experiment, somewhat high instability occurs at low inlet velocity conditions. The mechanism of these results was the subject of the investigation of this study.

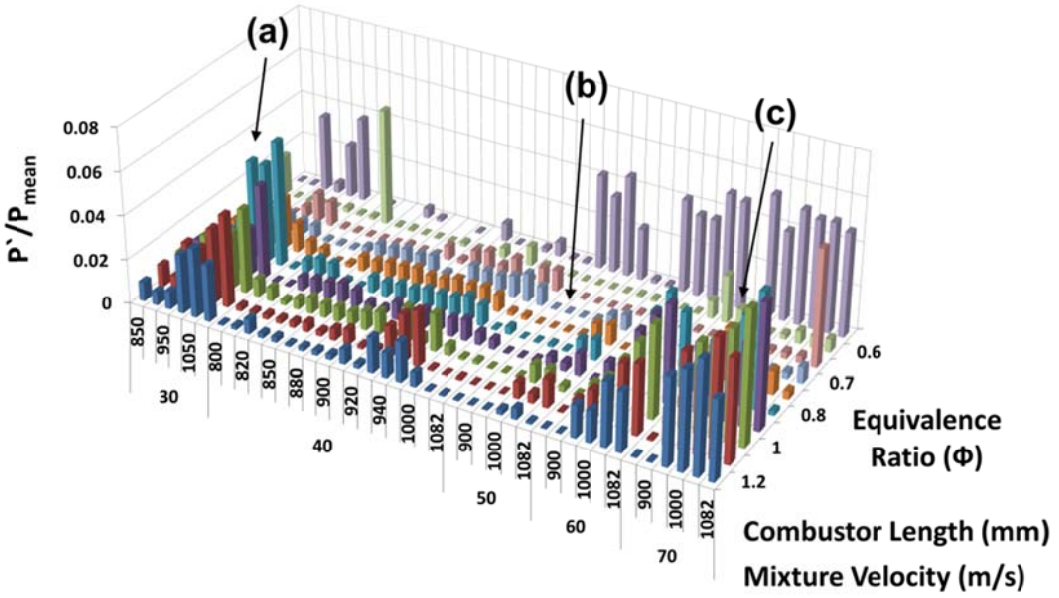

Fig. 5.2 Stability map for all experimental conditions; (a) unstable, v_{mix} = 30 m/s, 370 ~ 390 Hz, (b) stable, v_{mix} = 50 m/s and (c) unstable, v_{mix} = 70 m/s, 340 ~ 360 Hz.

Table 5.1 Experimental conditions.

Parameters	Values
Fuel type	Natural gas [CH_4(89.4%) + C_2H_6(8.6%) + C_3H_8(1.39%)]
Combustor Length [mm]	1000
Inlet Temperature [K]	637
Equivalence Ratio (Φ)	1.2
Swirl Injector	30° swirler (swirl number = 0.42)
Mixture Velocity [m/s]	30, 35, 40, 45, 50, 55, 60, 65, 70

5.3 Flame and Abel-inverted Images

To investigate of flame structure and high-frequency phenomena, high-speed ICCD camera was used in this study. The recorded frame rate was 6000 frame/sec and image size was 512 by 512 pixels. The dynamic pressure sensor and high speed ICCD triggering signal were recorded to measure heat release rate oscillation and dynamic pressure at the same time. These data were also used for phase-locking of the chemiluminescence imaging. The phase-locking process is performed based on 6th dynamic pressure, which was located at the detached section of the existing flame zone. The peak amplitude of 6th dynamic pressure was selected as 0 degree and the OH chemiluminescence image is collected by 12 phases, which means that 30-degree gaps per phase and Abel-inversion was carried out for each averaged picture. Abel-inversion is the process by which 2D images can be reconstructed from an accumulated 3D image [10, 11]. So, that is indicated the analysis of flame structures.

Figure 5.3 shows the three mixture velocity conditions for investigation of flame structure in stable and unstable condition. At 30 and 70 m/s fuel-air mixture velocity conditions, combustion instability took place and the stable condition is 50 m/s. First, a low velocity condition as some flame intensity changes according to phase changes,

however, there have few axial length variations and flame structural changes at the edge of the flame, which indicated vortex-flame interaction zone. Second, the stable conditions (50 m/s) produce no changes in flame length and intensity at each phase of the averaged image. Lastly, high mixture velocity conditions, which means that condition of 70 m/s, shows a drastic change of flame structures, which means length variation, heat release intensity oscillation, and outer recirculation size is changeable, which helps flame stabilization.

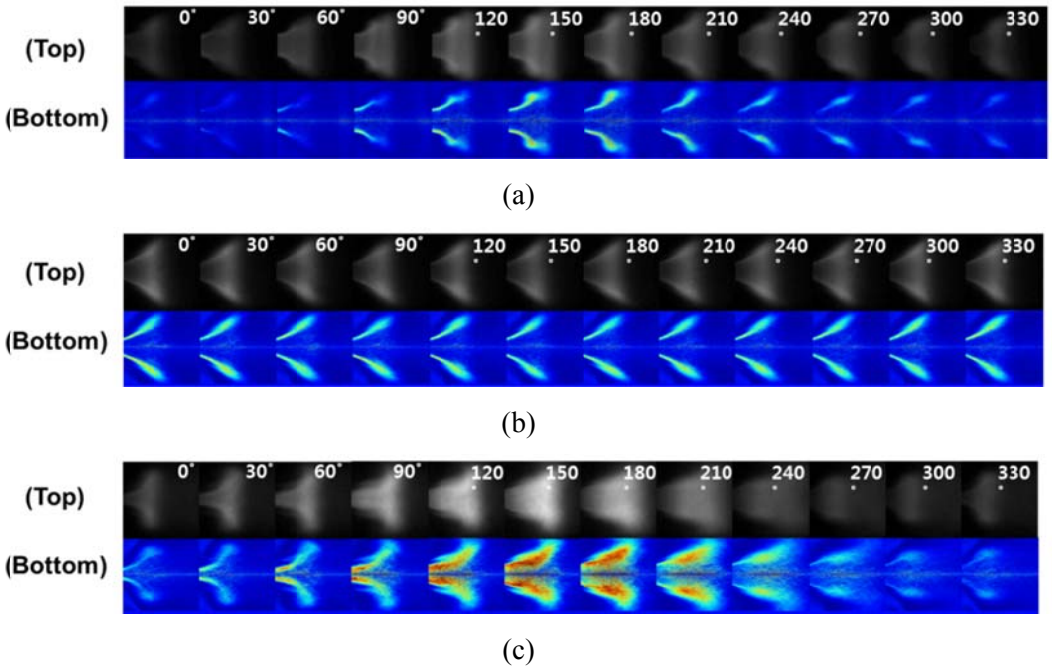

Fig. 5.3 OH chemiluminescence (top) and Abel-inverted images (bottom) at $L_{comb.}$ = 1000 mm, Φ = 1.2 conditions; (a) unstable, v_{mix} = 30 m/s, 370 ~ 390 Hz, (b) stable, v_{mix} = 50 m/s and (c) unstable, v_{mix} = 70 m/s, 340 ~ 360 Hz.

5.4 Main Instability Frequency and Strouhal Number

Figure 5.4 shows the experimental results of combustor temperature and instability frequency relation. There have separated into the three parts of low fuel-air mixture velocity instability region, stable region, and high fuel-air mixture velocity instability regions. The instability frequency and mean temperature of the combustion chamber have a linear correlation because the mean temperature of combustor affects the speed of sound about main combustion fluid and the instability frequency varies the increasing or decreasing temperature conditions. This analytic theory is well matched with the high fuel-air mixture velocity instability conditions from around 55 to 70 m/s. In contrast, at condition of low velocity instability condition about 30 and 35 m/s, combustion zone has much lower temperature zone via a high mixture velocity instability case and have a higher instability frequency. This phenomenon is not a general tendency of acoustic theory. This chapter main investigation is the relation between inlet fuel-air mixture velocity and combustion instability. Also, distinguish the difference between low and high levels of instability. To investigate such a relation, the flame structures during condition of instability will be discussed.

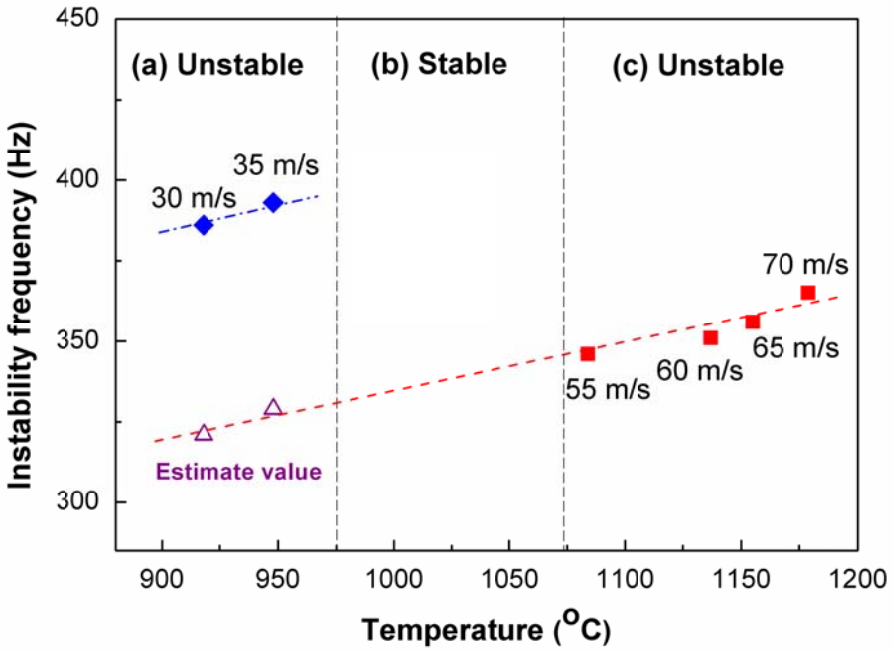

Fig. 5.4 Combustion instability frequency shifting results at various fuel-air mixture velocity conditions; (a) unstable, v_{mix} = 30 m/s, 370 ~ 390 Hz, (b) stable, v_{mix} = 50 m/s and (c) unstable, v_{mix} = 70 m/s, 340 ~ 360 Hz.

So, to examine the flame structure and instability characteristics, we calculated the Strouhal number for each combustion instabilities condition. A Strouhal number is the most famous of dimensionless number describing oscillating flow mechanisms. Instability frequency and inlet mixture velocity were used and characteristic length was replaced as flame length, which was measured by using the flame center with the averaged image. Table 5.2 shows the low mixture velocity (30, 35 m/s) conditions of unstable flame region has a higher Strouhal number than the high mixture velocity instability cases. Further, there is no acoustic boundary build up caused by influence heating flux value on the lower mixture velocity condition. So, very low instability amplitude exists, and the instability mode does not matched with others one.

Table 5.2 Strouhal number calculation for conditions of each fuel-air mixture velocity.

State	Flame shape	Length (mm)	Velocity (m/s)	Frequency (Hz)	Strouhal number
Unstable (@ low velocity)	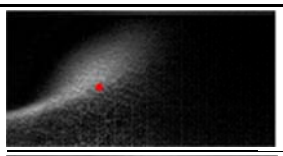	50.72	30	370	0.626
	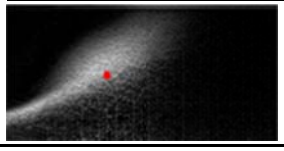	54.64	35	393	0.614
Stable	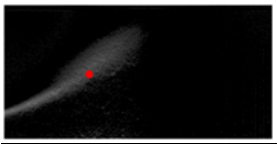	48.52	40	-	-
	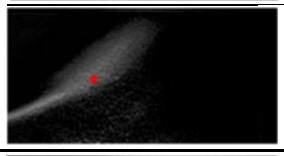	47.42	50	-	-
Unstable (@ high velocity)	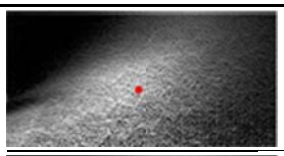	66.13	65	356	0.362
	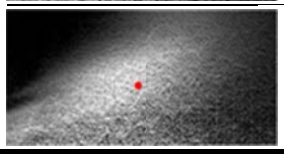	66.53	70	365	0.347

C. Kulsheimer et al.[12] and M. Escudier[13] are suggest that when the Strouhal number is high, the critical pressure for making a vortex shedding structure is less when the Strouhal number is lower condition. Applying that result in this chapter for the low mixture velocity instability case, which shows a high Strouhal number, can more easily generate the vortex structure and, therefore the interaction of this vortex structure with an acoustic wave will be the cause of unstable combustion. When the OH chemiluminescence image has not been averaged, the low velocity condition shows

sharper vortex structures, and these images can help confirm the hypothesis about the origin of frequency shifting at low-speed instability.

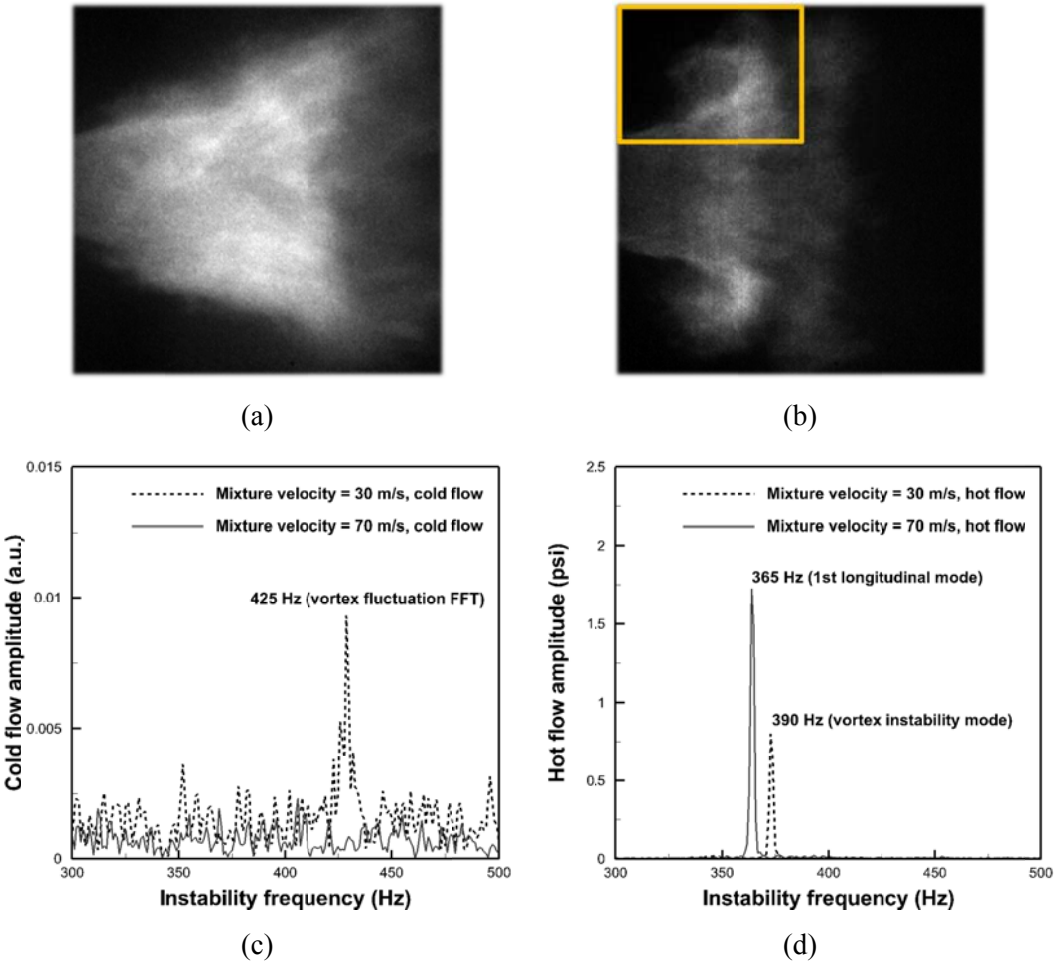

Fig. 5.5 High speed camera instantaneous image and heat release wave FFT analysis in vortex instability region; (a) v_{mix} = 70 m/s, (b) v_{mix} = 30 m/s, (c) FFT analysis of instability intensity fluctuation in cold flow and (d) FFT analysis of instability intensity fluctuation in combustion condition.

Figure 5.5 shows the FFT results, which means the local vortex frequencies in cold and hot flow condition. At cold condition, frequency was detected even though there was no acoustic forcing. This vortex instability frequency which was measured at vortex structure is same as the heat release rate instability frequency of the total flame oscillation (Fig. 5.5 (b), (d)).

5.5 Combustion Instability Mode and Phase Analysis

To analyze the frequency shifting characteristics, we performed a mode and phase analysis using the multi position dynamic sensing system in the flame at conditions of low and high fuel-air mixture velocity instability. First, the dynamic mode analysis was conducted with dynamic pressure sensors (#5) to confirm the instability mode at 30, 70 m/s mixture velocity conditions. We assumed that both the combustor and the inlet mixing section have closed-closed acoustic boundary conditions which one-dimensional acoustic wave condition and constant temperature condition in each combustor and inlet mixing sections. Fig. 5.6(a) and 5.7(a) show the result of dynamic pressure mode analysis. Dots indicate experimental data obtained by dynamic pressure sensor and the mean pressure amplitudes at each position. Black dotted lines indicate the acoustic boundary of the inlet section and combustor. Solid lines indicate ideal standing waves of ideal acoustic boundary. The result of mode and phase analysis represents the longitudinal mode of the inlet mixing section and combustion chamber. Experimental data follow the ideal standing wave and are quite well matched which means that the mode of instability is the first half wave longitudinal mode of the combustor for all of fuel-air mixture velocity conditions. This means that no change in instability mode occurs during inlet velocity variation. In other words, frequency jumping is not the result of a change in instability mode. Second, we investigated the heat release and dynamic pressure sensor data which are located near the combustion section to use phase locking each other. At conditions of high mixture velocity instability as shown Fig. 5.6(b), there is an in-phase of heat release

and dynamic pressure sensor #5. There are combustion instabilities caused by the coupling between pressure oscillations and heat release oscillations and the necessary condition for sustaining the combustion unstable is explained by Rayleigh's Criterion. But, at a low velocity instability condition as shown Fig. 5.7(b), heat release and pressure wave phase are delayed at around 130 degrees, in other words, the out-of-phase phenomenon occurs. This means that at conditions of low velocity instability there is another reason for the occurrence of combustion instability, except for the coupling of heat release and pressure perturbation waves. Conclusively, we found the frequency-shifting phenomenon during a variety of inlet mixture velocity conditions. Based on mode analysis and heat release, as well as dynamic pressure data, there is no reason for the 30 m/s mixture velocity case leading to the arising of combustion instability except the Rayleigh Criteria. From the Strouhal number result and direct images of the conditions of instability, it seems that fluid dynamic instability and vortex structure interactions are the main causes of frequency shifting during low fuel-air mixture velocity instability.

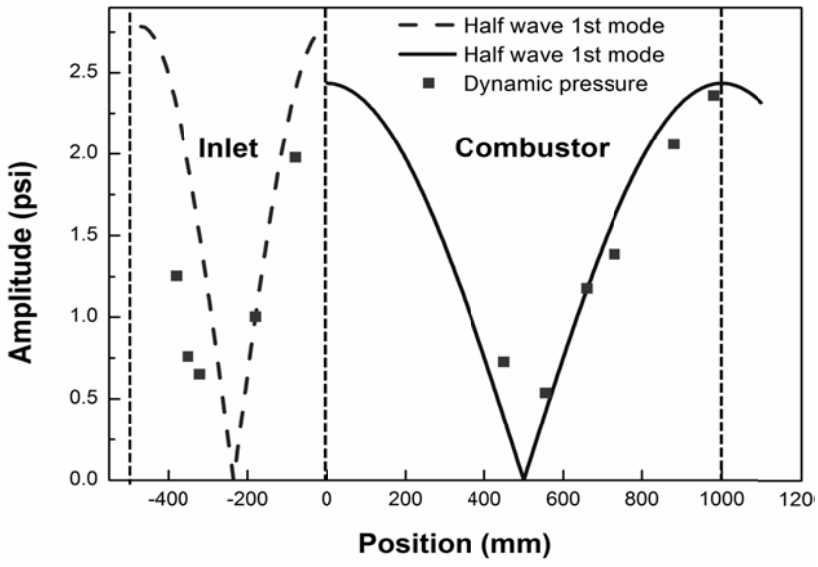

(a)

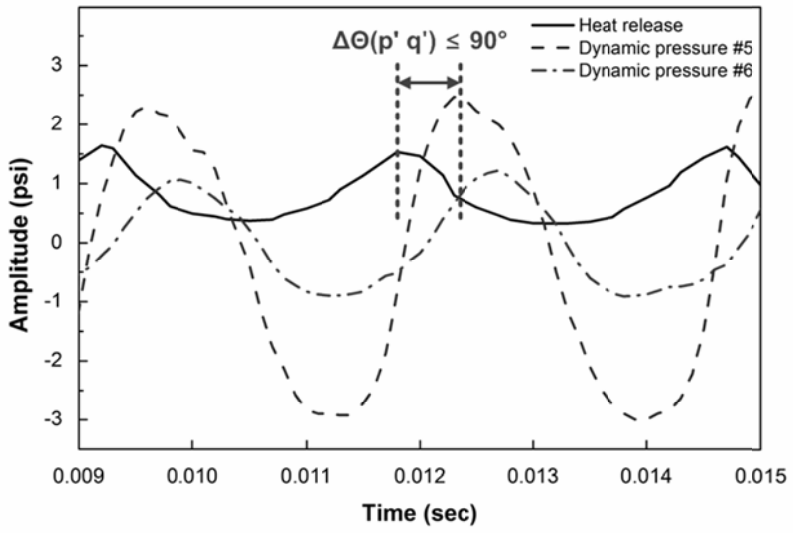

(b)

Fig. 5.6 Dynamic pressure results at fuel-air mixture velocity of 70 m/s conditions; (a) acoustic standing mode, (b) phase difference.

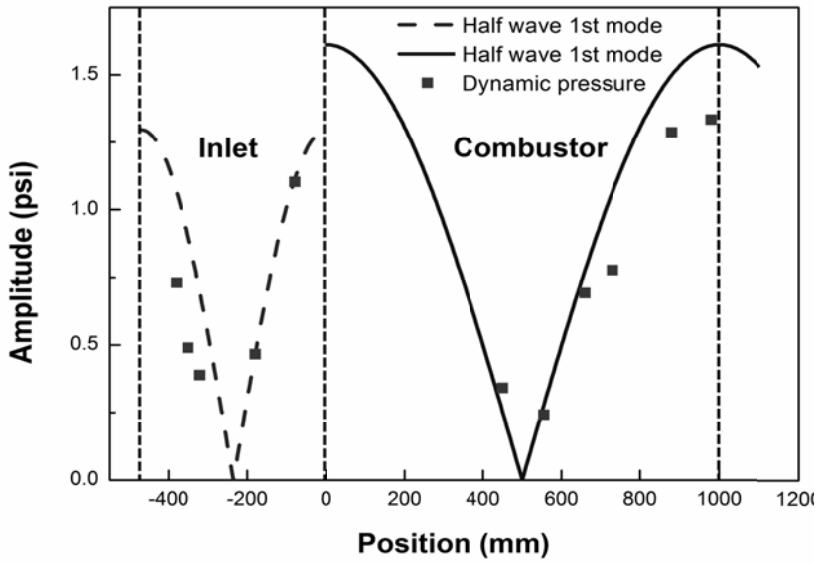

(a)

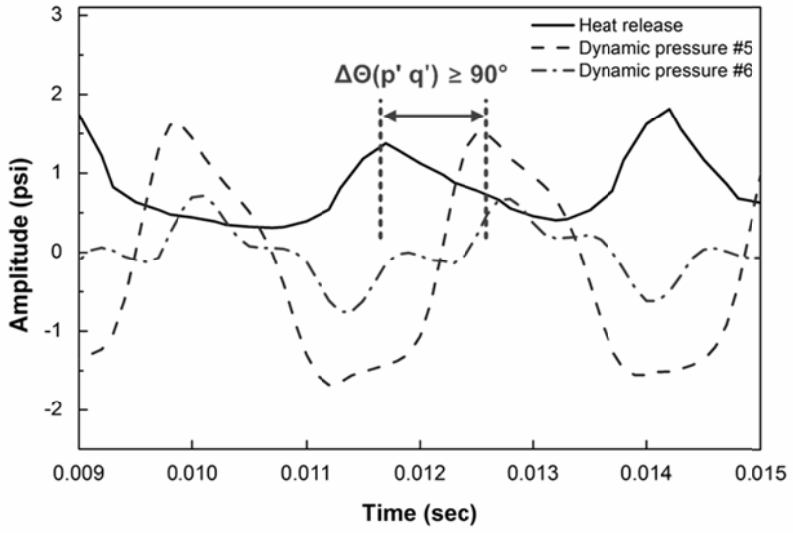

(b)

Fig. 5.7 Dynamic pressure results at fuel-air mixture velocity of 30 m/s conditions; (a) acoustic standing mode, (b) phase difference.

5.6 Dynamic Pressure Gradient Variation

An analysis was conducted on the basis of a phase-averaged, Abel inversion transform image as identified above, and the structural change in flame according to the unstable phenomenon was largely analyzed into two types – changes in flame angle and flame length. A study was carried out on the pressure gradient that is formed inside of the combustion chamber and change in the flame structure based on dynamic pressure fluctuations inside the combustion chamber. For the pressure gradient, the information concerning the dynamic pressure on no.5 sensor at the front of the combustion chamber (fuel-air nozzle exit) and on no.6 sensor closest to the combustion chamber from the exhaust exit was used.

It was confirmed through measuring that the unstable flame under high fuel-air mixture velocity conditions showed a higher value in the constant pressure at the front end of the combustion chamber than the exhaust duct. Looking into the phase 120° ~ 270° zone showing an increase in the dynamic pressure at the front end, as shown in Fig. 5.8(a), the pressure at the front of the combustion chamber increase as much as dynamic pressure, with the exhaust duct also showing an increase, but the growth rate is expected to be relatively small. That is, the mass flow rate is expected to increase by the pressure gradient relatively getting greater and this phenomenon can be confirmed through a substantial change in length and brightness of the flame. On the contrary, checking the area where the pressure at the front of the combustion chamber decreases more than the exhaust duct pressure brings an expectation that the dynamic pressure at the front of the combustion chamber is relatively reduced more than the dynamic pressure at the back, which would lead to a relative decline in pressure gradient formed inside the combustion chamber. That is, the overall flow is expected to be less and this phenomenon can be confirmed through the phase-averaged OH chemiluminescence images. The unstable flame under fuel-air mixture velocity conditions, shown in Fig. 5.8(b), is confirmed to have a different behavior from the flame under high fuel-air mixture velocity conditions. When the constant pressure was first measured, the pressure difference between front and

rear of the combustion chamber was almost constant. Therefore, it is expected that the flame will be retarded in an area where the dynamic pressure at the front of the combustion chamber relatively gets smaller than the rear, that is, in an area where the pressure gradient relatively gets lowered. Unlike the fact that the brightness of flame under high fuel-air mixture velocity conditions is reduced, it is possible to check that the brightness of flame becomes brighter than the flame of low mass flow rate on average. Besides, it was possible that the vortex structure developed at the flame edge and the vortex structure developed this way was pushed backward while gradually losing the flame brightness by the rise in mass flow rate in an area where the pressure at the front of the combustion chamber increases. In other words, an explanation can be presented as to changes in flame length through the pressure gradient formed of combustor inside. Especially the flame under low fuel-air mixture velocity conditions was confirmed to reveal characteristics different from the flame under high fuel-air mixture velocity conditions such as forming the vortex structure at the flame edge.

We conducted an analysis on the basis of variation in flame angle, illustrating a graph through the flame angle for each phase and the OH chemiluminescence intensity. Fig. 5.9 could check out change in flame angle and heat emissions, and that the behavior of the 5th dynamic pressure sensor closest to the combustion chamber displays a small phase difference and issues a sequential vibration. That is, it can be confirmed that this does meet the Rayleigh's criterion that causes combustion thermo-acoustic instability. On top of this, it is possible to confirm that the fluctuations caused by heat release rate oscillation through the phase difference in each data are propagated to the upper class and that such a fluctuation in pressure waves causes a change in flame angle. The paper of Candel et al. [14, 15] once reportedly says the pressure fluctuations change the swirl number of a swirler to bring change to the flame structure. This means that the flame structures are influenced by mixture perturbation and this oscillation changes the flame angles.

$$\frac{S-\overline{S}}{S}=\frac{S'}{\overline{S}}=\alpha\left[\exp i\left(\frac{\omega}{\overline{u}_2}x\right)-\exp i\left(\frac{\omega}{\overline{c}}x\right)\right]\exp i\left(-i\omega t\right) \tag{5.1}$$

Equation (5.1) shows that velocity fluctuation results in swirl number perturbation and dynamic pressure oscillation. Therefore during at instability conditions when pressure oscillation occurs, it results in swirl number perturbation and this phenomenon has an effect on flame stability and fluctuation of heat release. As identified in Fig. 5.10, a difference is created if the identical analysis is performed in instability under low fuel-air mixture velocity conditions. The order of generating heat release rate oscillation wave and pressure fluctuations and change in flame angle is consistent, but its phase difference can be confirmed to be over 90° or close to 90°.

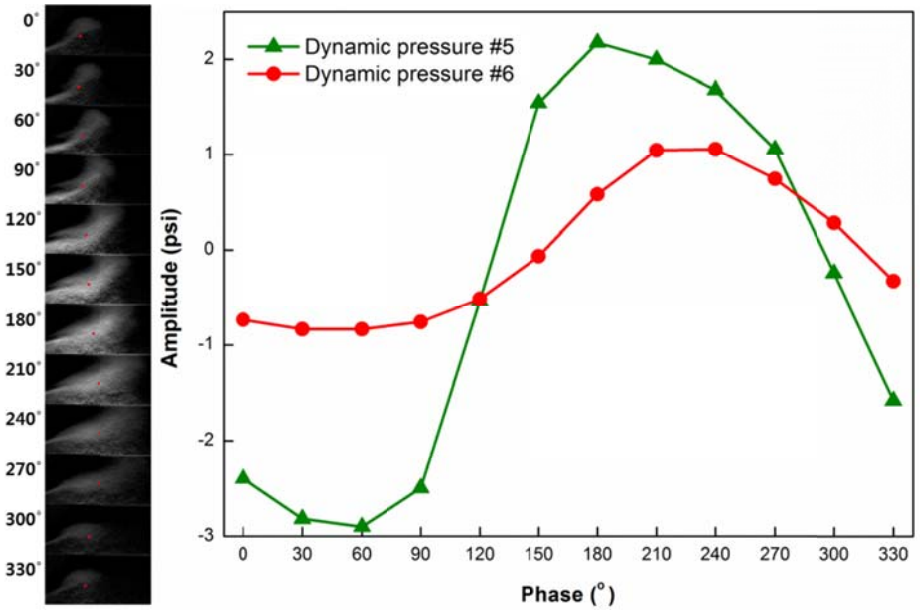

(a)

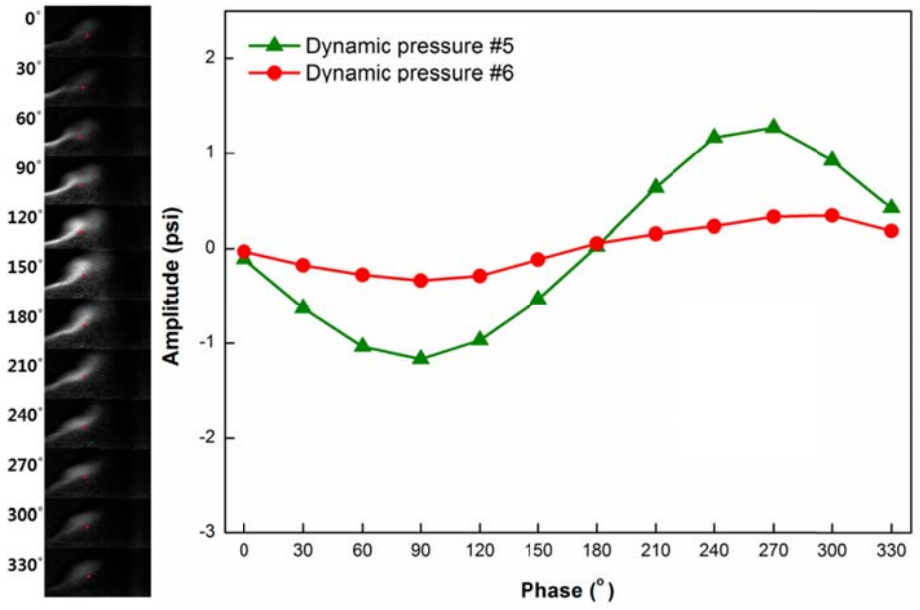

(b)

Fig. 5.8 Dynamic pressure gradient variation and flame structure results at various fuel-air mixture velocity conditions; (a) v_{mix} = 70 m/s, (b) v_{mix} = 30 m/s.

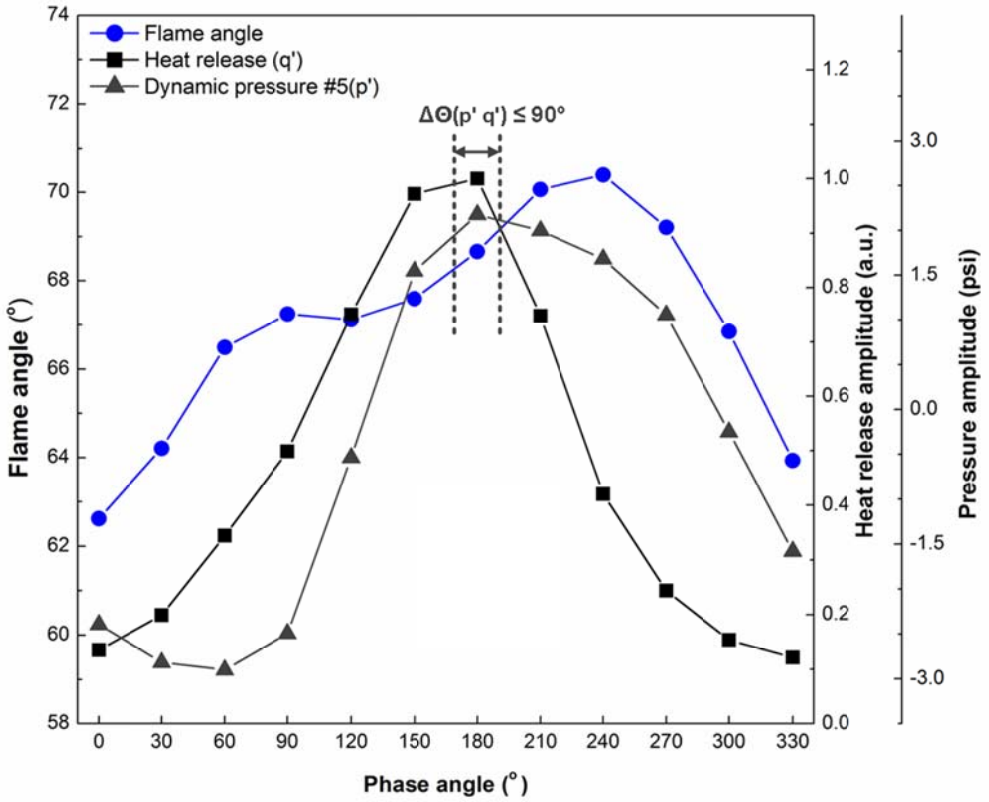

Fig. 5.9 Heat release, dynamic pressure, and flame angle change results at 70 m/s fuel-air mixture velocity conditions.

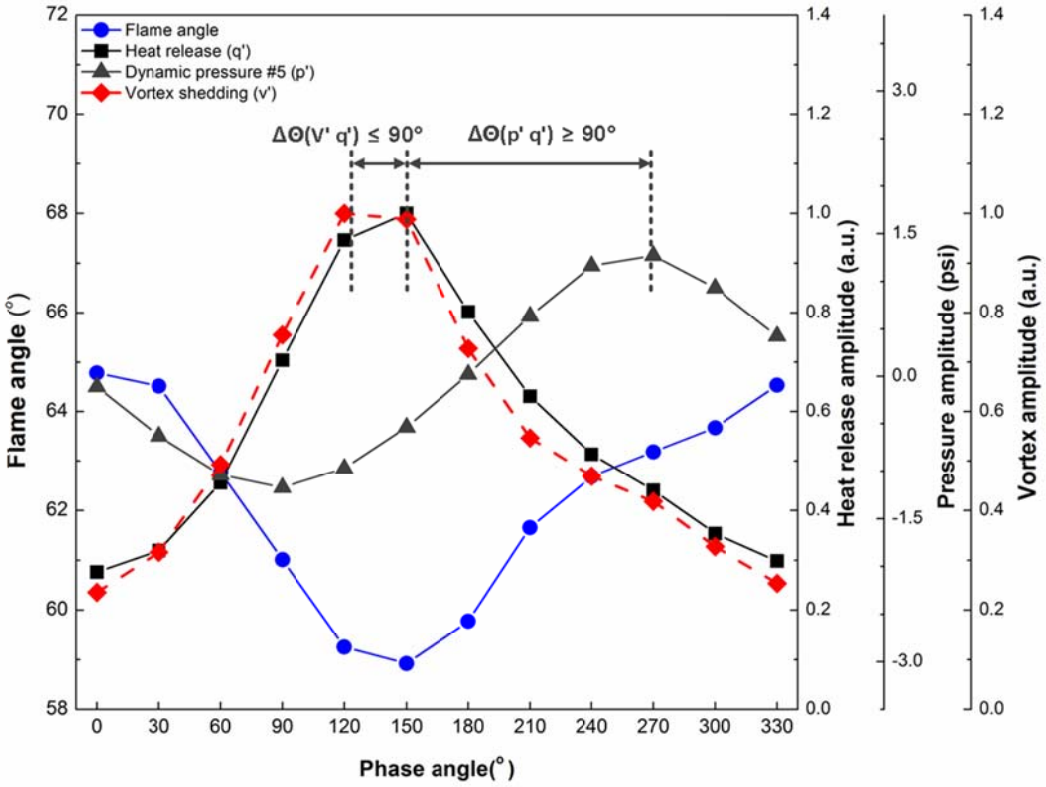

Fig. 5.10 Heat release, dynamic pressure, and flame angle change results at 30 m/s fuel-air mixture velocity conditions.

CHAPTER 6
EFFECT OF FUEL-AIR MIXING SECTION

6.1 Background and Objectives

This chapter is focused on studies of combustion instability characteristics relate with the model combustor length and inlet mixing section geometry. Previous studies were conducted to observe the phenomenon of combustion instability and flame structure [1, 2] in the combustor having a simple fuel nozzle with the swirl effect and to investigate a method of analyzing the cause and mode of combustion instability [3, 4]. Based on the results of the previous studies, however, this chapter observed the phenomenon of combustion instability by changing the combustor length and its fuel-air mixture velocity to discover the characteristics of the combustion instability mode and their kinds in a combustor simulating an actual gas turbine for power generation. At this point, this study of fuel-air mixing section geometry confirmed the conditions of heat release oscillation by changing the fuel-air mixture velocity and equivalence ratio and verified the exact causes of combustion instability by analyzing the instability modes and phases appearing during the combustion instability by multi-channel dynamic pressure sensing measurement [5] in both the combustor and the inlet mixing section.

6.2 Experimental Method and Conditions

The combustor used for this study is a 1/3 scale model gas turbine combustor simulating the GE 7FA+e DLN-2.6 gas turbine combustor, which is characterized with premix and a swirl-stabilized flame as shown in Fig. 6.1. The model is composed of an air-heating device, air supply lines, fuel nozzles, a flame visualization quartz combustor and a spike-typed plug nozzle for the exhaust duct as an acoustic boundary. As one of the main variables for this experimental study (as shown in Table 6.1.), the fuel-air mixing section was located between the combustor dump-side and the choking orifice at the back

of the air-heating device, which came in three lengths, 470 mm, 550 mm, and 870 mm, although all inlet mixing section had an inner diameter of 40 mm as shown in Fig. 6.2. Table 6.2 shows the experimental conditions of this chapter. A swirl injector used for this device is an axial-typed injector, which has 10 swirl vanes set at the angles of 0° and 30°. Fuel is injected at 20 mm detached spot from the swirl vane, 10 nozzles, each of which has a 1.2 mm-sized hole, and is pre-mixed with air through the 140 mm-sized mixing length. The swirl number of the swirl injector used for this research was about 0.42. A circular stainless steel (@ case 1, 2) and a quartz tube (@ case 3 ~ 8) for the flame visualization were alternately used, and the diameter inside the combustor was 120 mm. The plug nozzle placed at the exhaust duct was supposed to function to change the resonant frequency of the combustor by making an acoustic boundary that blocks 91% of the combustor exhaust duct, which was designed to regulate the length of the combustor by 0.1 mm from 800 mm to 1680 mm through the stepper motor located in the exhaust part of model gas turbine combustor.

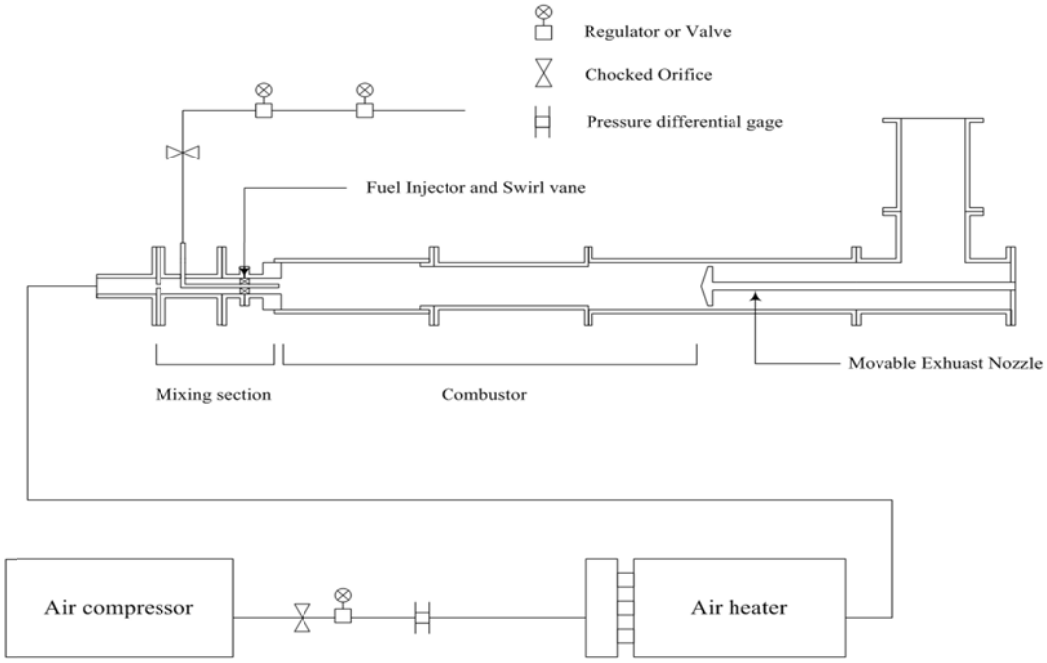

Fig. 6.1 Schematics of a model dump shaped gas turbine combustor simulating in the 1/3 scale downed of a GE 7FA+e DLN-2.6 gas turbine combustor.

Table 6.1 Experimental cases for various combustion instability conditions.

Test case	Injector type	Combustion instability mode	Inlet length [mm] (Plenum)	Combustor length [mm]	Mixture velocity [m/sec]	Equivalence ratio (Φ)
Case 1	No swirl	1L	470	1000	70	0.9
Case 2	No swirl	2L	470	950	70	1.1
Case 3	30° swirl	1L	470	1000	70	1.1
Case 4	30° swirl	2L	470	950	40	1.2
Case 5	30° swirl	1L	550	1050	70	1.0
Case 6	30° swirl	2L	550	950	40	1.1
Case 7	30° swirl	1L	870	1650	60	1.1
Case 8	30° swirl	2L	870	1650	70	0.8

Table 6.2 Experimental conditions.

Parameters	Values
Fuel type	Natural gas [CH_4(89.4%) + C_2H_6(8.6%) + C_3H_8(1.39%)]
Inlet air temperature [K]	673
Fuel temperature [K]	318
Swirl vane angle	No swirl, 30° swirl (swirl number = 0.42)
Mixture velocity [m/sec]	30, 40, 50, 60, 70
Equivalence ratio (Φ)	Blowout limit ~ 1.2
Inlet mixing section length [mm]	470, 550, 870
Combustor length [mm]	800 ~ 1680
Blockage nozzle [mm]	128 (Blockage ratio : 91%)

To observe the oscillation of dynamic pressure occurring during the combustion experiment, we used five 102A05-type dynamic pressure sensors, manufactured by PCB Company, for the inlet mixing section and six for the combustor, as well as infinity probes, which suppress the reflected wave of dynamic pressure [6, 7]. In addition, the sampling rate was observed by receiving 10,000 data per second, and through Fast Fourier Transformation (FFT) techniques, it was possible to analyze them up to 5,000 Hz. Moreover, OH* chemiluminescence was measured from the flame around the dump side. By using a high-speed ICCD camera made by Photron Company, we photographed flames at the speed of 1/6000 fps, and were able to obtain the pressure oscillation and heat release values from the time axis in the same experimental conditions by phase locking the dynamic pressure sensor.

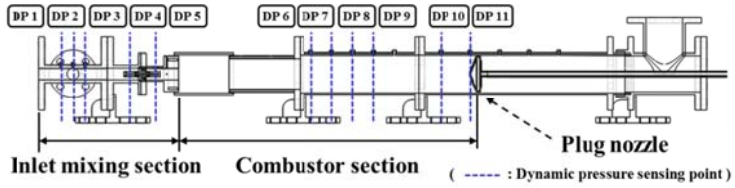

(a)

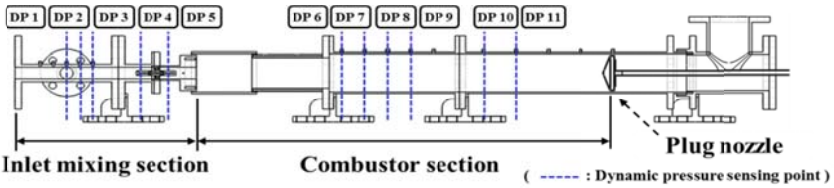

(b)

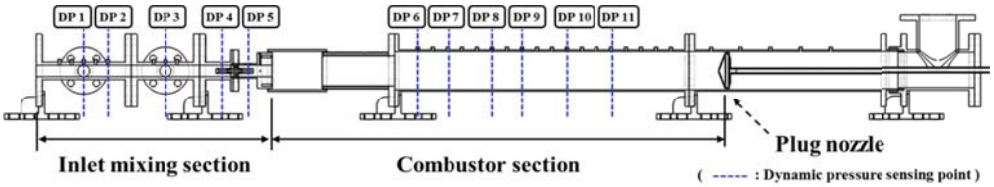

(c)

Fig. 6.2 Location of dynamic pressure sensors in fuel-air mixing section and combustor; (a) L_{inlet} = 470 mm, (b) L_{inlet} = 550 mm and (c) L_{inlet} = 870 mm conditions.

To understand the combustion instability origin mode, we measured the heat release oscillation as shown in Fig. 6.3. Furthermore, this study acquired signals that drive the high-speed ICCD camera, signals of photos being taken and dynamic pressure signals by using DAQ and analyzed the flame visualization information and acoustic field oscillation information at the same time. This was especially the case for combustion instability phenomenon, which was accomplished the process of measuring the results of dynamic pressure and heat release waves in the same time domain.

(a)

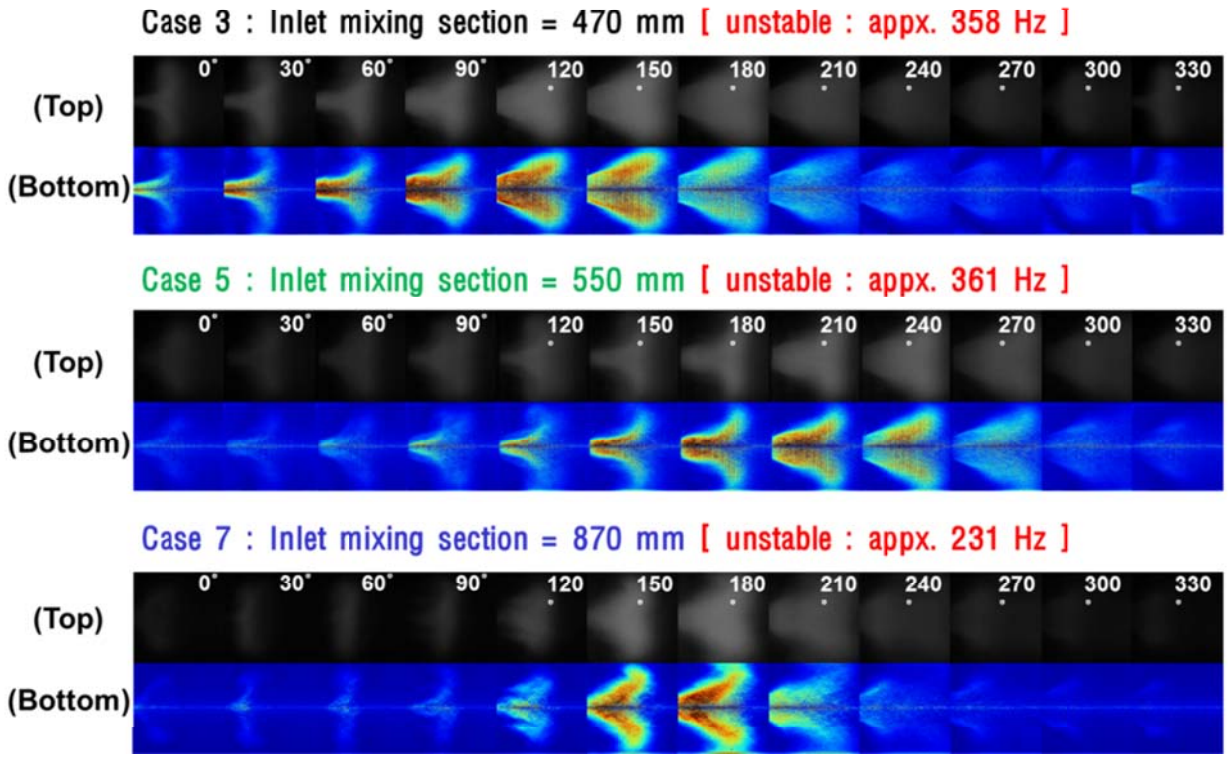
Case 3 : Inlet mixing section = 470 mm [unstable : appx. 358 Hz]
(Top)
(Bottom)
0° 30° 60° 90° 120 150 180 210 240 270 300 330
Case 5 : Inlet mixing section = 550 mm [unstable : appx. 361 Hz]
(Top)
(Bottom)
0° 30° 60° 90° 120 150 180 210 240 270 300 330
Case 7 : Inlet mixing section = 870 mm [unstable : appx. 231 Hz]
(Top)
(Bottom)
0° 30° 60° 90° 120 150 180 210 240 270 300 330

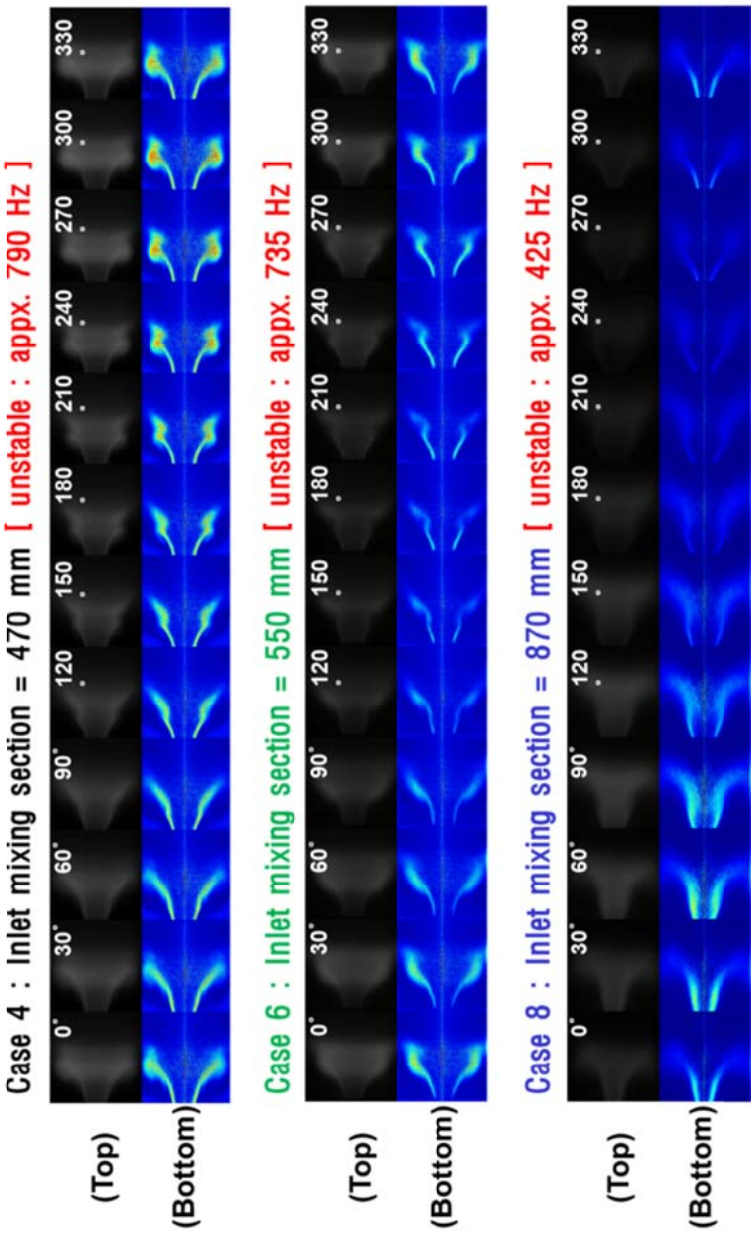

(b)

Fig. 6.3 OH chemiluminescence (top) and abel-inverted (bottom) images at 30° swirl effect; (a) 1st longitudinal instability mode, (b) 2nd longitudinal instability mode.

6.3 Stability Map

By conducting a combustion experiment in different experimental conditions with a model gas turbine combustor, this study conducted an experiment to confirm the flame stability map. Fig. 6.4 is a graph showing the dynamic pressure values observed in all the experimental conditions when the angle of swirl was 0° and the length of the fuel-air mixing section was 470 mm. At this point, the 4th dynamic sensor detached from the dump plane was used as the standard dynamic pressure point. As shown in the graph, as the mixture velocity increased, the combustion tended to be unstable, and especially the combustion generally appeared unstable when the fuel-air mixture velocity was 70 m/s. In conditions where the fuel-air mixture was higher in the velocity region, the modes of combustion instability were divided into two kinds, depending on the combustor length and the equivalence ratio. Also, in the sections where the fuel-air mixture was lower in the velocity region, an insufficient supply of heat energy led to unclear acoustic boundaries, as well as failing to cause the phenomenon of thermo-acoustic instability. Also, it was found that instability did not occur under all of the conditions of the combustor length but in specific conditions of the combustor length, between 950 to 1050 mm. In other words, in the condition of combustor resonant frequencies calculated on the assumption that the combustor is a closed boundary condition, combustion instability took place by coupling with heat release oscillation, through which the combustion length was verified as an important variable causing combustion instability [8, 9, 10].

Figure 6.5 is a graph showing the dynamic pressure values observed in all the experimental conditions when the fuel-air mixing section length was 470 mm with conditions of the 30° swirl effect. At this point, 6th dynamic sensor detached from the dump plane was used as the standard point. In the graph with a 470 mm inlet mixing section with a length condition of 30 m/s in the mixture velocity, another kind of combustion instability phenomenon occurred. This is caused by the flame vortex, which in turn result from a low mixture velocity according to the geometric condition of a provided dump combustor. This, in turn is, not a phenomenon of thermo-acoustic

instability caused by the heat release oscillation of the combustor and flame [11, 12]. In an experimental condition in which fuel and air mixed relatively well, when the mixture velocity was 40 m/s and the length of the fuel-air mixing section was 470 mm, the acoustic boundary of the inlet mixing section was established as a closed-open boundary [13, 14] since the fuel-air mixture should be delivered to the combustor, and it was found that combustion instability was well matched with the mode when resonant frequencies of the 2nd mode of the closed-closed boundary occurred in the combustor. Thus, this study found that the length of the fuel-air mixing section in the driving part of the combustor is an important variable causing combustion instability, which will be verified by analysis of the mode and phase from the results values on the next section and the multi-channel dynamic pressure sensing system.

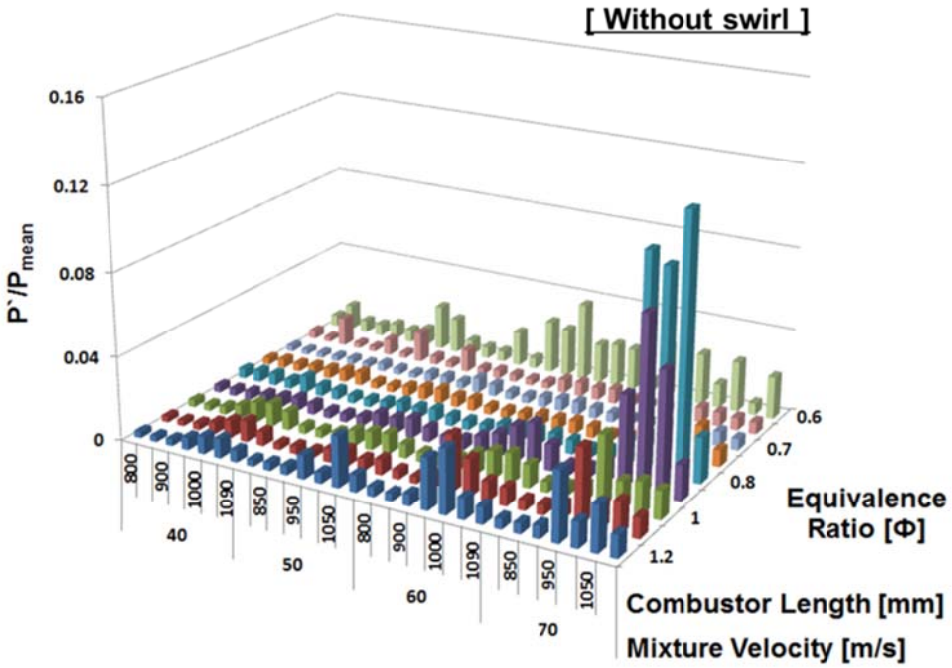

Fig. 6.4 Stability map for all of the experimental conditions at no swirl effect and L_{inlet} = 470 mm (case 1, case 2) conditions.

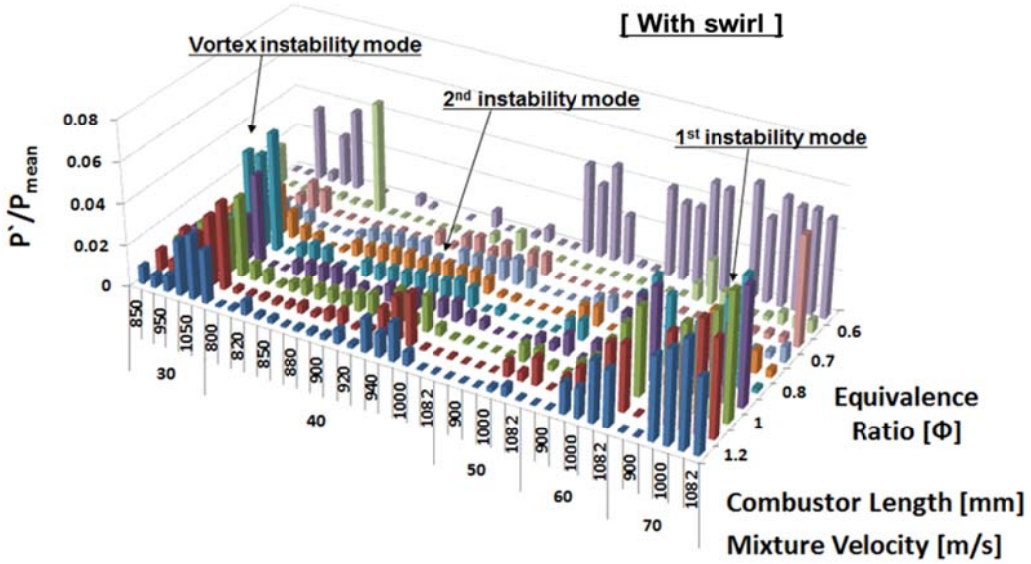

Fig. 6.5 Stability map for all of the experimental conditions at 30° swirl effect and L_{inlet} = 470 mm (case 3, case 4) conditions.

And, it was found that instability did not occur under all of the conditions of the combustor length but in specific conditions of the combustor length, between 950 to 1050 mm, as shown in Fig. 6.6 for example of no swirl, inlet mixing section is 470 mm conditions.

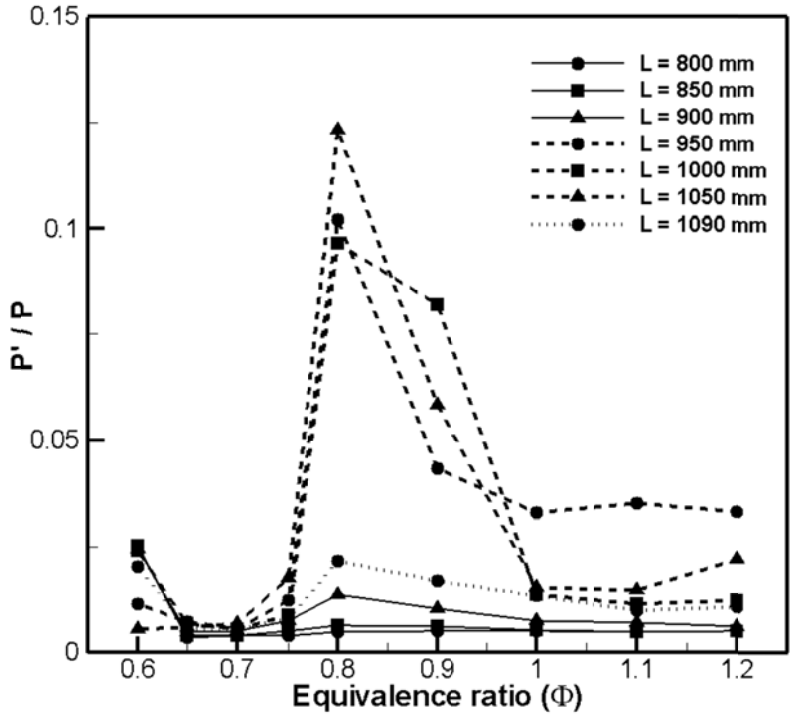

Fig. 6.6 Combustion instability results for various combustor length conditions at no swirl effect and L_{inlet} = 470 mm (case 1, case 2) conditions.

Figures 6.7 and 6.8 is a graph showing the dynamic pressure values observed in all the experimental conditions when the angle of swirl was 30° and the length of the fuel-air mixing section was 550 and 870 mm. Thus, this study found that the length of the fuel-air mixing section in the driving part of the combustor is important variable causing combustion instability, which will be verified by analyzing mode and phase analysis from the result values on next section and multi position dynamic pressure sensing system. To find out if the specific combustion instability characteristics of 2^{nd} longitudinal mode (2L), appeared in another experimental condition, it was tested in different lengths of the mixing section, such as 550 mm and 870 mm. When the length of the mixing section was 550 mm as shown in Fig. 6.7, the flame stability map, combustion instability characteristics were found to occur in all the mixture velocity conditions as well. As a result, it was clear that in the mixture velocity condition related to the mixing section length where fuel and air get mixed well with about 0.42 swirl number, combustion instability characteristics existed as well. As result from previous section, however, it was confirmed that the combustion instability phenomenon doesn't appear in all the combustion chamber length conditions, but instability characteristics became stronger as the combustion chamber became longer in length. When the mixing section length was 870 mm as shown Fig. 6.8, this experimental study attempted to find out if the instability frequency of 2L mode occurs in other frequency band domains, not in such similar conditions as 470 and 550 mm in the length of the mixing section. Therefore, by changing the mixing section length, this experiment provided a flame stability map by confirming all the experimental variable conditions. As shown in the picture, as the higher mixture velocity condition into the combustion chamber, heat flux energy increases as well, leading to confirming that combustion instability characteristics also increase. Besides, it was also found that combustion instability characteristics occurred in a specific length of the combustion chamber through the coupling of heat release and acoustic oscillation energy.

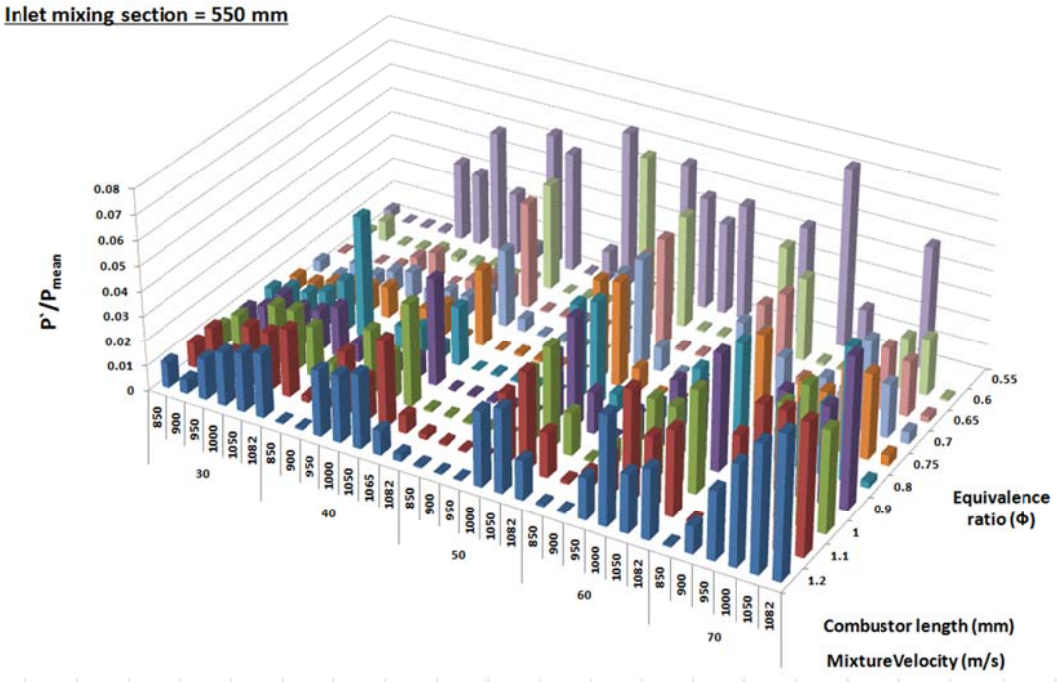

Fig. 6.7 Stability map for all of the experimental conditions at 30° swirl effect and L_{inlet} = 550 mm (case 5, case 6) conditions.

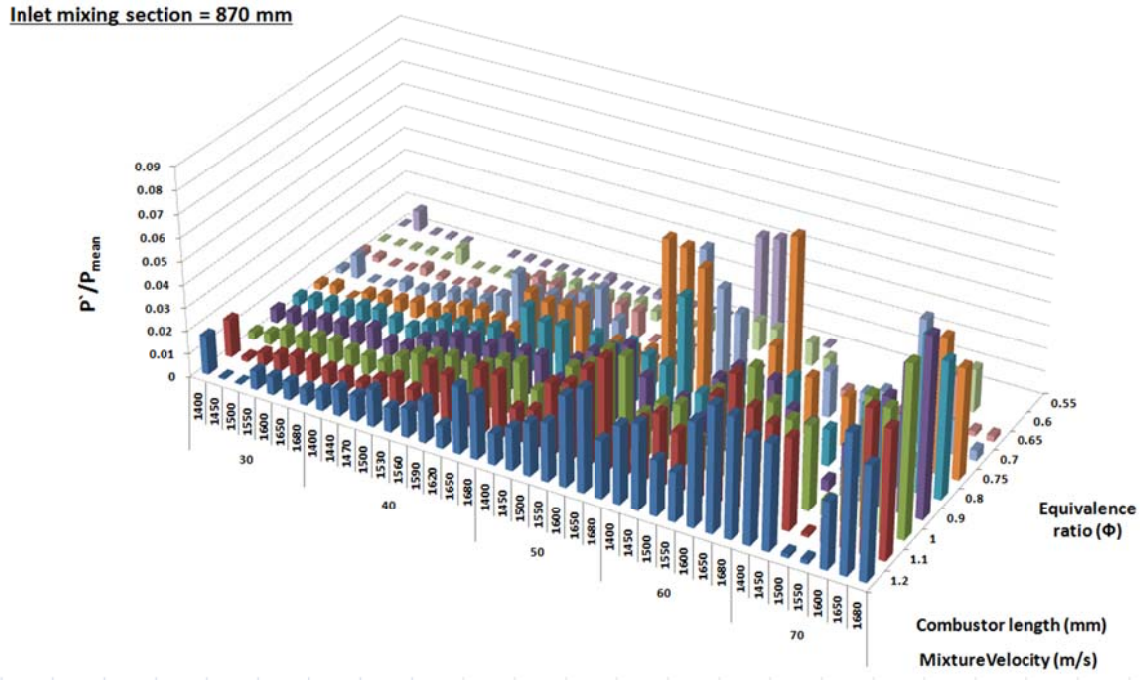

Fig. 6.8 Stability map for all of the experimental conditions at 30° swirl effect and L_{inlet} = 870 mm (case 7, case 8) conditions.

6.4 Main Instability Frequency Analysis

Figure 6.9 shows details about the intensity of each frequency obtained through the FFT analysis of dynamic pressure data in comparison with the all of experimental conditions about no swirl effect of 470 mm inlet mixing section. According to the experiment conducted by Lee et al. [15, 16], when the FFT intensity analysis was conducted on the dynamic pressure data measured in various experimental conditions, it was observed that the maximum intensity appeared in 1 or 2 specific frequency bands in case that combustion instability phenomenon took place. In this study, the combustion instability phenomenon was observed to occur in such frequency bands as 367 ~ 404 Hz and 820 ~ 850 Hz. At this point, when the combustion chamber length was 800 ~ 1090 mm, the combustion chamber temperature appeared in the range of about 1200 ~ 1500K.

To analyze the combustion instability frequency, on the assume that acoustic waves occurring inside the combustion chamber was a 1-dimentional acoustic wave and the temperature was constant value in the combustion chamber, the resonant frequency of the combustion chamber was predicted. The predicted frequency of longitudinal mode (n=1) of the combustion chamber had a range of about 330 ~ 490 Hz, but in this study, it was found that the combustion instability characteristic mostly appeared in an experimental condition where the longitudinal mode was in the frequency band of 367 ~ 404 Hz. This experiment also found that when the resonant frequency of the combustion chamber, calculated by the length and temperature of a combustion chamber, accorded with a specific frequency, a strong combustion instability phenomenon appeared. Also, there have different of secondary instability mode around 829 Hz. This instability frequency indicated that second half wave mode of combustor and quarter wave mode of inlet mixing section acoustic boundary which is related to closed-closed acoustic boundary condition of combustor and closed-opened boundary condition of plenum. And this experimental study has been almost same combustion instability characteristics in another inlet mixing section length conditions.

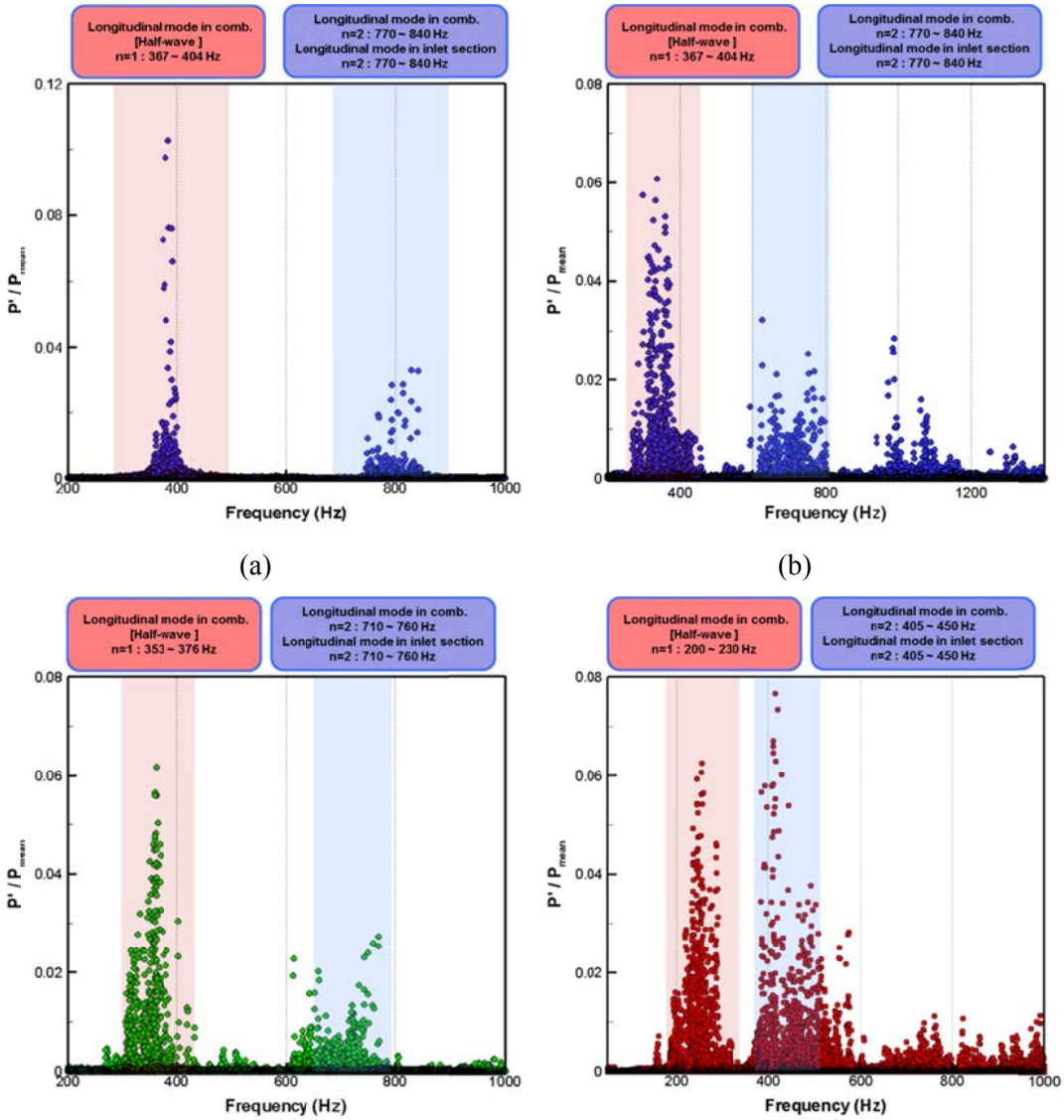

Fig. 6.9 Combustion instability frequency distribution for all of the experimental conditions; (a) no swirl effect and L_{inlet} = 470 mm (case 1, case 2), (b) 30° swirl effect and L_{inlet} = 470 mm (case 3, case 4), (c) 30° swirl effect and L_{inlet} = 550 mm (case 5, case 6) and (d) 30° swirl effect and L_{inlet} = 870 mm (case 7, case 8) conditions.

When the inlet mixing section length changed to 470, 550, and 870 mm, the FFT spectrum of the main frequencies of combustion instability was affected by the change of the equivalence ratio, which is shown in Fig. 6.10. When the circumstances of the inlet mixing section length were 470 mm with a combustor length condition of 1000 mm without a swirl effect and the fuel-air mixture velocity was 70 m/s, the equivalence ratio was 0.9 and 1.2 respectively, and the combustion instability appeared strongest when the equivalence rate was 0.9. At this point, the combustion instability frequency was 375 Hz. That is, a phenomenon was found in which the frequency of combustion instability changed by the combustor length, and when it was outside of the specific instability frequencies, the combustion instability phenomenon disappeared. When the equivalence ratio was 1.2 and the length of a combustor was 950 mm, the combustion instability phenomenon appeared at the strongest. Also, when the combustor length tuned where a specific frequency of, 829 Hz, and the acoustic mode of a combustion chamber accorded with each other, a strong combustion instability phenomenon appeared. Furthermore, when the inlet mixing section length was 550 mm and the equivalence ratio was 1.0, the combustion instability mode occurred relative to the 1st longitudinal mode (1L) of the combustion chamber while the length of the combustion chamber was changing to 1050 mm. In the case when the equivalence ratio of 1.1 became larger, an instability mode occurred related to the inlet mixing section length. Likewise, even when the inlet mixing section length was 870 mm, the instability mode changed as the equivalence ratio changed. In consequence, we discovered, the phenomenon in which the average temperature changes as the inlet mixing section mixture velocity and the equivalence ratio change, further changing the instability frequency, and the combustion instability mode suddenly changes by the matching of the lengths of the combustion chamber and the inlet mixing section.

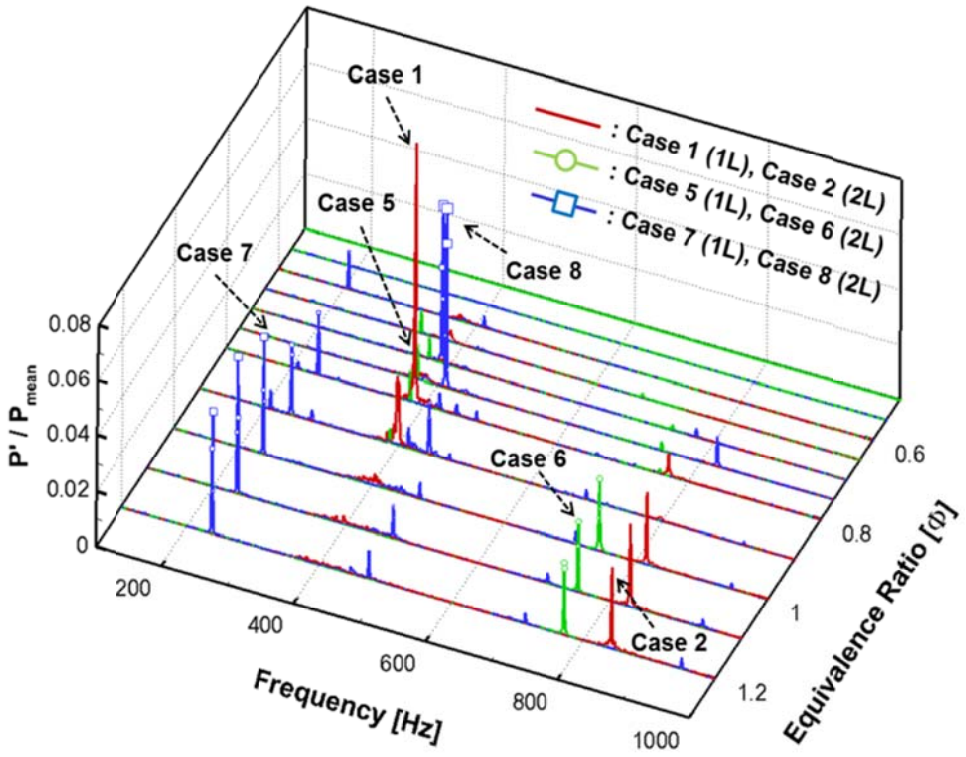

Fig. 6.10 Instability frequency FFT spectrum results for various inlet mixing section conditions.

Figures 6.11(a) and (b) are graphs showing how instability frequencies of half wave mode and quarter wave mode, which occur in the combustion chamber of a model gas turbine combustor related to the various equivalence ratio and its inlet mixing section, occurred as main modes. As shown in the picture below, the instability of an injector without swirl effect has higher instability frequencies and larger sizes than that with swirl effect. Unlike the diffusion flame without swirl effect, the premixed flame with swirl effect causes the combustor average temperature to decrease relatively, which corresponds with a theoretical ground that holds that instability frequencies of the combustion chamber are formed at low temperatures. Moreover, it was also found that as the combustor length and its inlet mixing section increase, the instability frequency

decreases, and the result of the 1L mode shows the combustion instability characteristics in conditions related to the inlet mixing section length of an injector group having swirl effect. Also, it was found that as the equivalence ratio increases, the heating energy of the combustion chamber increases as well, leading to thermal choking. Then, the acoustic boundary of the combustion chamber became clearer, which made it possible to see the size of the increase in combustion instability.

As shown in Fig. 6.11(b), where the inlet mixing section length was in a short condition (470, 550 mm), that is, in the section where the 2L mode changed to high frequencies, since the temperature and length of the combustion chamber accorded with those of the fuel-air mixing section, the combustion instability of the 2L mode was suitable for the inlet mixing section and combustor lengths in the section over 1.0 of the equivalence ratio, and as the energy dispersion into surrounding areas became larger than the case of the 1L mode, the size of the instability was found to be smaller by about on half. On the contrary, in the section where the frequency of the 2L mode was in the low instability frequency region with 870 mm in the length of the fuel-air mixing section, the 2L mode occurred when the equivalence ratio was low. It was also found that in a condition where the equivalence ratio was high, the 1L mode occurred. This was because in a flame condition where the combustion chamber temperature became suitable to accord with the frequency, the relevant combustion instability phenomenon occurred as well. A theoretical analysis likely to calculate this phenomenon is as shown in Eq. (4.1) and (4.2). And it is assumed that the movement course of energy in a gas turbine combustor is in the axial direction and the average temperature is constant with 1-D standing waves theory.

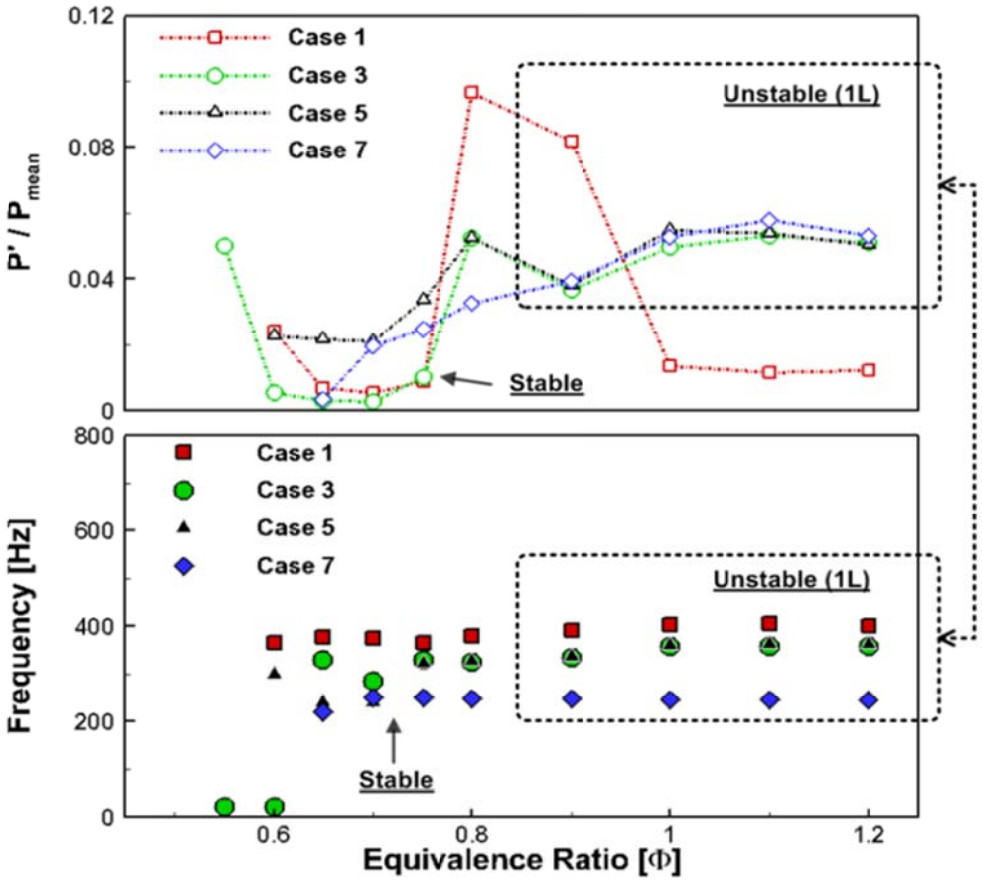
0.12
0.08
0.04
0
P' / P mean
Case 1
Case 3
Case 5
Case 7
Unstable (1L)
Stable
800
600
400
200
0
Frequency [Hz]
Case 1
Case 3
Case 5
Case 7
Unstable (1L)
Stable
0.6
0.8
1
1.2
Equivalence Ratio [Φ]

(a)

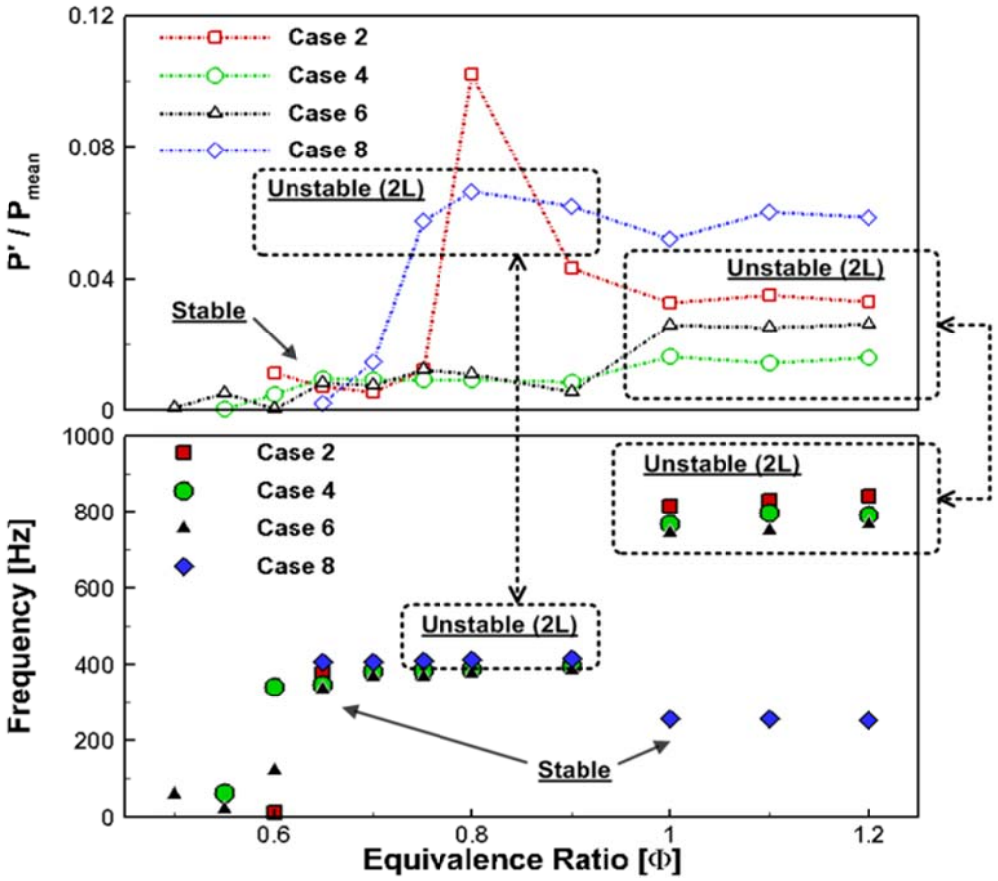

(b)

Fig. 6.11 Combustion instability characteristics for the equivalence ratio conditions; (a) 1st longitudinal instability mode, (b) 2nd longitudinal instability mode.

Figure 6.12 shows the combustion instability characteristics depending on the change of the combustor length. As explained earlier, the reason why the 1L and 2L modes have main combustion instability is not because of the conditions related to the combustor length condition but because of the conditions related to specific combustion chamber lengths. Especially, in an instability case where the 2L mode occurred, it was found that instability modes appear when the acoustic boundary of the inlet mixing section accords with the frequency corresponding to the second quarter wave mode. All of the experimental results from this study are listed in Table 6.3.

Table 6.3 Experimental results for various combustion instability conditions.

Test case	**Plenum temperature [K]**	**Combustor temperature [K]**	**Main instability frequency [Hz]**	**Main instability magnitude (p'/p_{mean})**	**Estimate value of plenum [Hz] (Quarter wave mode)**	**Estimate value of combustor [Hz] (Half wave mode)**
Case 1	397	1150	378	0.1242	276	375
Case 2	398	1268	829	0.0351	829	827
Case 3	395	1126	358	0.0531	264	353
Case 4	396	1068	790	0.0189	791	785
Case 5	401	1116	361	0.0548	237	360
Case 6	403	995	735	0.0253	712	750
Case 7	385	1050	231	0.0578	144	225
Case 8	388	950	425	0.0673	432	442

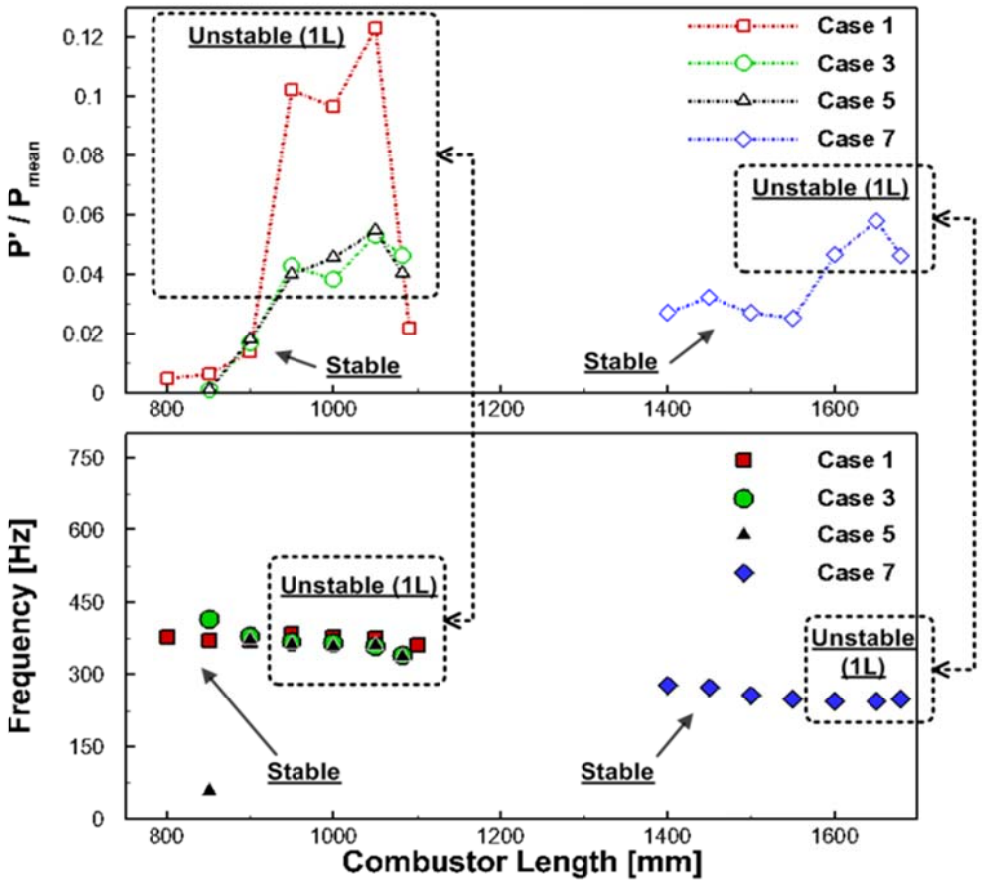
Unstable (1L)
Case 1
Case 3
Case 5
Case 7
Unstable (1L)
Stable
Stable
P' / P mean
0.12
0.1
0.08
0.06
0.04
0.02
0
800
1000
1200
1400
1600
Case 1
Case 3
Case 5
Case 7
Unstable (1L)
Unstable (1L)
Stable
Stable
Frequency [Hz]
750
600
450
300
150
0
800
1000
1200
1400
1600
Combustor Length [mm]

(a)

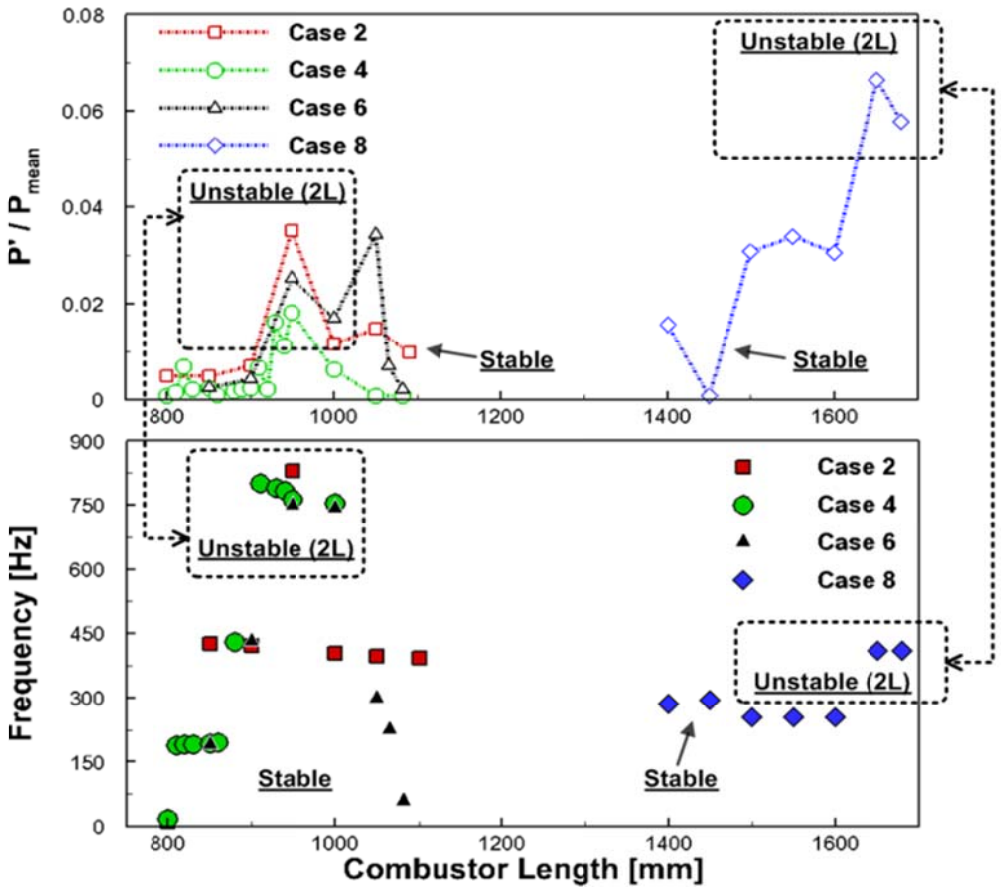

(b)

Fig. 6.12 Combustion instability characteristics for various combustor length conditions; (a) 1st longitudinal instability mode, (b) 2nd longitudinal instability mode.

6.5 Combustion Instability Mode and Phase Analysis

For the combustion instability phenomenon to take place in a model gas turbine combustor, acoustic waves and heat release waves, which are likely to appear due to the form of the combustion chamber, are required to interact with each other. Basically, therefore, combustion instability frequencies are generated by the acoustic wave from the combustion chamber or the fuel-air mixing section connected to it. Fig. 6.13(a), 6.14(a), 6.15(a) and 6.16(a) show the results of the combustion instability of the 1L mode having frequencies between 240 and 350 to 400 Hz occurring in specific combustion chamber lengths, fuel-air mixture velocities, and equivalence ratio conditions and also show the pressure oscillation magnitude and phase differences observed from 11 dynamic sensors installed in the fuel-air mixing section and the combustor section. The lines in the graphs show the estimated values of dynamic pressure in each location of the combustion chamber, and the round red dots show the values of dynamic pressure measured in each location. As shown in the graphs, most of the dynamic pressure values obtained from each location are almost the same value as the estimated ones, but there was a slightly different value in the dynamic pressure data from the end of the combustor because of the lower temperature around the blockage nozzle located at the back of the combustion chamber. In the case that the length of the inlet mixing section with no swirl effect was 470 mm, as the sensor located in the air supply device got closer to the combustion chamber, the phase difference got smaller, further having almost the same phase and oscillation in the combustor. This is well described with square-shaped black dots indicating phase differences from the standard dynamic sensing point. Likewise, from such different length conditions as 470, 550, and 870 mm along with a 30° swirl effect, the same experimental results can be obtained. Furthermore, based on the middle location of the combustion chamber where the pressure node is located, it was found that there was a phase difference of about 180° in the values of dynamic sensors in the front and in the back of the combustion chamber. This can be explained by reference to the response characteristics of a flame, as described in a recently conducted research titled “Flame

Transfer Function" [17, 18]. Specific frequency bands where combustion instability appears strong are determined by the combustor length, the location of a fuel injector, and the type of fuel-air mixing. When a combustion instability, the pressure oscillation from the combustion chamber appears stronger than that from the air supply line, through which the flame response function of a combustor used for the related experiment can be obtained, thus predicting that the band of 240 Hz and between 350 and 400 Hz can be the maximum frequency band by which the flame is affected by acoustic waves around the 1L mode, depending on the length conditions of the inlet mixing section.

Figures 6.13(b), 6.14(b), and 6.15(b) show the amplitudes and phase differences of the pressures measured when the combustion instability phenomenon takes place mainly in a higher equivalence ratio between 1.0 and 1.2. At this point, the acoustic wave of the combustor was assumed to be in the half-wave mode, and for the inlet mixing section, it was assumed to be in the quarter-wave mode. The lines in the graph show the expected values of the longitudinal mode (n = 2) of the combustion chamber, while the dashed lines show the expected values of the longitudinal mode (n = 2) of the fuel-air mixing section. Each dot shows the pressure amplitude measured from the dynamic sensors in each position. In addition, the fifth dynamic sensor is the one located after the swirler and was found to be greatly affected by the pressure field of the combustor section. Like the previous results, most of the dynamic pressure values tend to be almost the same as the expected values, and in a condition in which the combustion instability phenomenon appears, which corresponds to the longitudinal mode (n = 2), the same results can be observed. Square-shaped black dots show the phase difference between dynamic pressure sensors, and in a spot between 1/3 and 2/3 of the combustion chamber, the pressure node appears, and it was found that the phase difference of dynamic pressure sensors in the front and in the back of the spot was about 180°, through which it was possible to confirm the combustion instability of the 2L mode connected with the combustion chamber and the fuel-air mixing section that are assumed above. Unlike the 1st longitudinal mode (n = 1), which is describe in the previous results above, the pressure value measured from a pressure sensor located in the inlet mixing section was a little higher than that measured

from the combustion chamber. Therefore, when such a combustion instability phenomenon takes place, the pressure oscillation occurring in the inlet mixing section has large values around 10%, compared to the average static pressure, through which the combustion instability phenomenon of the 2L mode has an effect on the acoustic pressure field occurring in the inlet mixing section and even on the oscillation of the supplied fuel-air mixture. In this experiment, when the combustion instability phenomenon takes place in each frequency band, the fluctuation of the equivalence ratio due to the oscillation of the supplied fuel-air mixture can be regarded as combustion instability caused by a relatively strong pressure oscillation from the inlet mixing section, rather than being amplified through interaction with acoustic waves. When such a phenomenon of combustion instability appears, not only the resonant frequency of a combustion chamber but the resonant frequency appearing in the inlet mixing section are calculated as values similar to the frequency of combustion instability.

In a condition where there is no swirl effect as shown in Fig. 6.13(b), the frequency of combustion instability obtained from this experiment was found to be 829Hz, and the resonant frequency of the fuel-air mixing section, which was calculated by 1-D acoustic wave theory, was found to be 829 Hz and the resonant frequency of the combustion chamber was 827 Hz. This appeared equal in the various other inlet mixing section experimental conditions, and, depending on the mean temperature conditions of the combustion chamber and its inlet mixing section, the instability frequency became a little lower. However, given the results of this research on the modes and phase differences of dynamic pressure, this study verified the validity. It is the same in the condition as shown in Fig. 6.16(b), where the equivalence ratio was formed to the contrary, and it was found that when the combustion instability phenomenon of the 2L mode with relatively high frequencies actually took place, the form of the fuel-air mixing section is greatly affected.

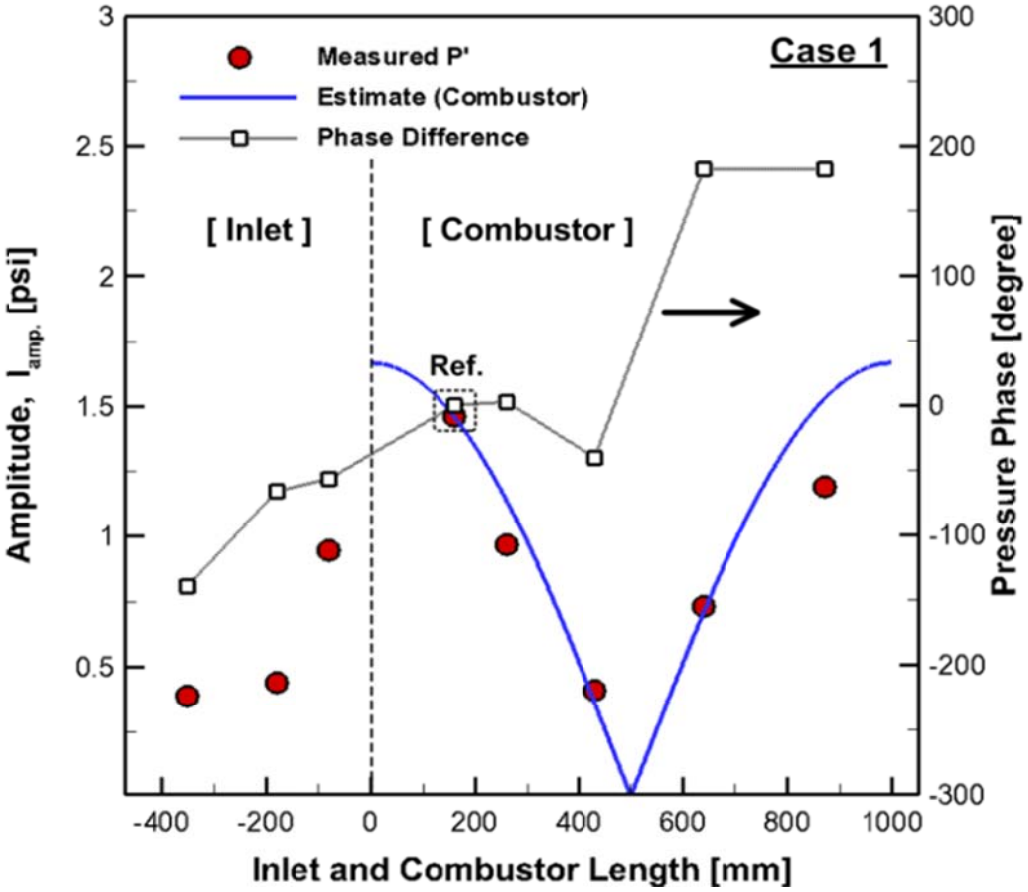
Measured P'
Estimate (Combustor)
Phase Difference
Case 1
[Inlet]
[Combustor]
Ref.
Amplitude, $I_{amp.}$ [psi]
Pressure Phase [degree]
Inlet and Combustor Length [mm]
3
2.5
2
1.5
1
0.5
300
200
100
0
-100
-200
-300
-400
-200
0
200
400
600
800
1000

(a)

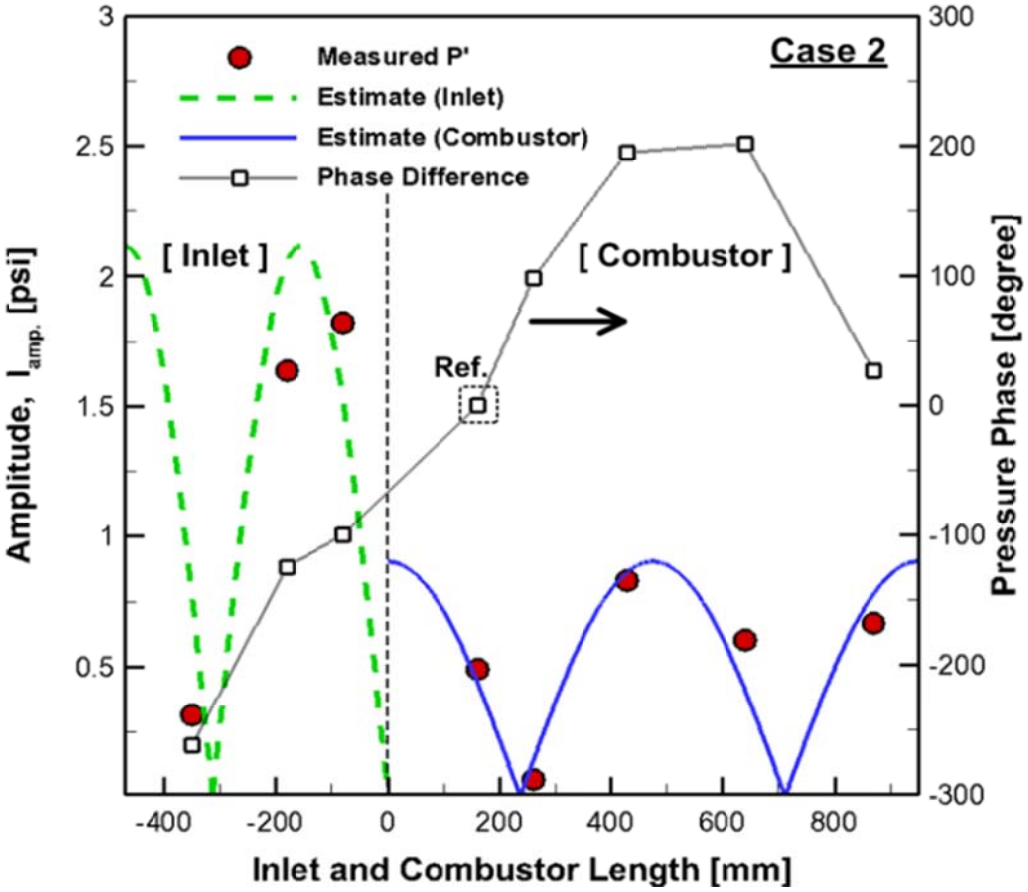

(b)

Fig. 6.13 Dynamic pressure amplitude and phase difference between each sensor at no swirl condition and L_{inlet} = 470 mm; (a) 1st longitudinal instability mode, $L_{comb.}$ = 1000 mm, Φ = 0.9, v_{mix} = 70 m/s, case 1, (b) 2nd longitudinal instability mode, $L_{comb.}$ = 950 mm, Φ = 1.1, v_{mix} = 70 m/s, case 2.

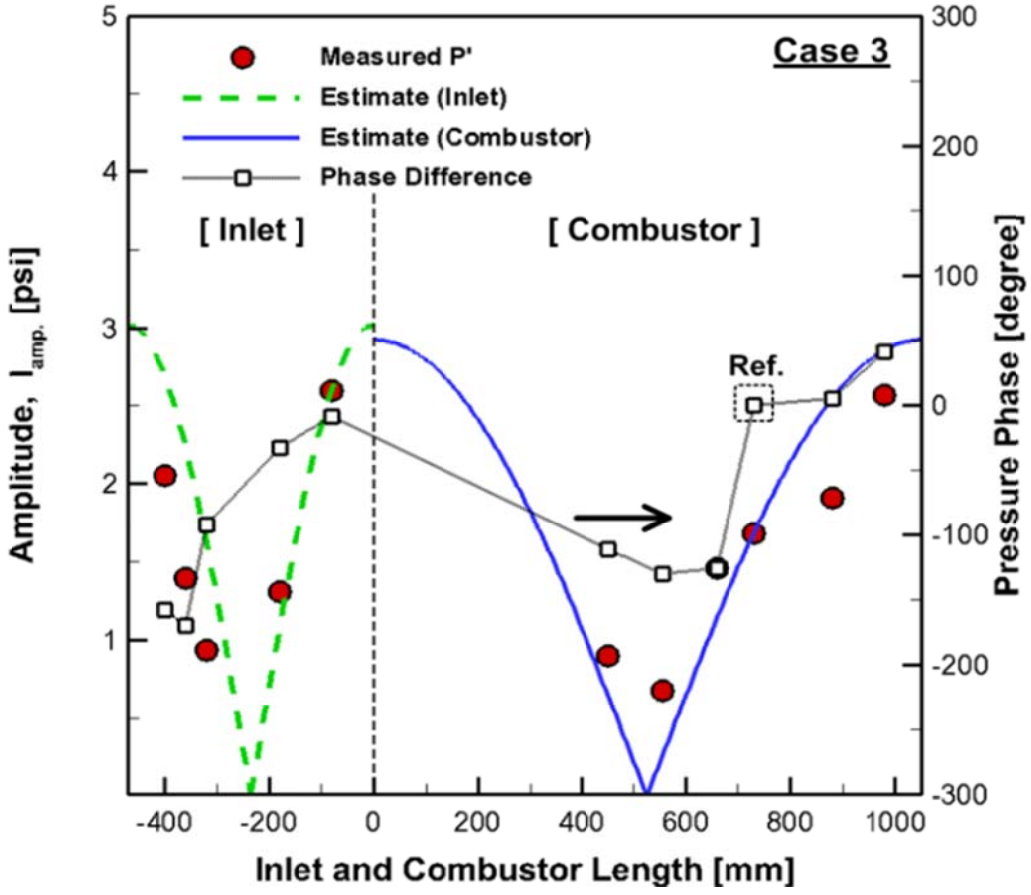
Case 3
Measured P'
Estimate (Inlet)
Estimate (Combustor)
Phase Difference
[Inlet]
[Combustor]
Ref.
Amplitude, $I_{amp.}$ [psi]
Pressure Phase [degree]
Inlet and Combustor Length [mm]
5
4
3
2
1
300
200
100
0
-100
-200
-300
-400
-200
0
200
400
600
800
1000

(a)

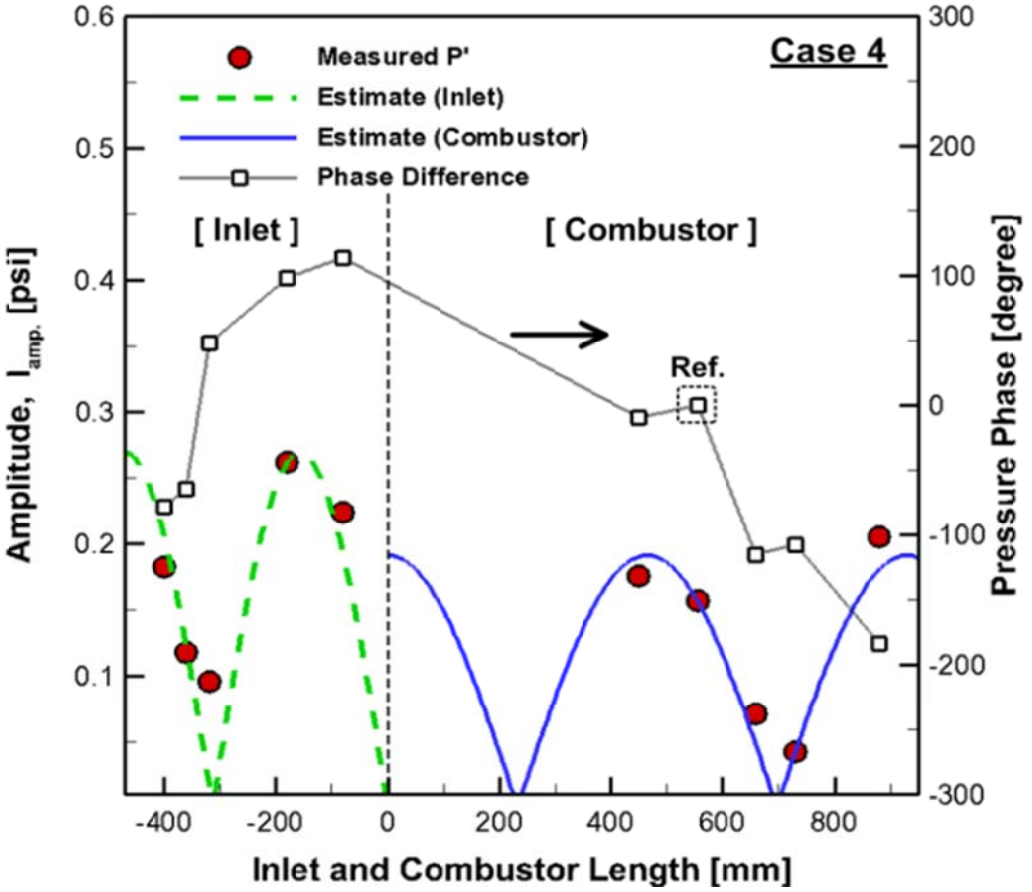

(b)

Fig. 6.14 Dynamic pressure amplitude and phase difference between each sensor at 30° swirl condition and L_{inlet} = 470 mm; (a) 1st longitudinal instability mode, $L_{comb.}$ = 1050 mm, Φ = 1.1, v_{mix} = 70 m/s, case 3, (b) 2nd longitudinal instability mode, $L_{comb.}$ = 930 mm, Φ = 1.2, v_{mix} = 40 m/s, case 4.

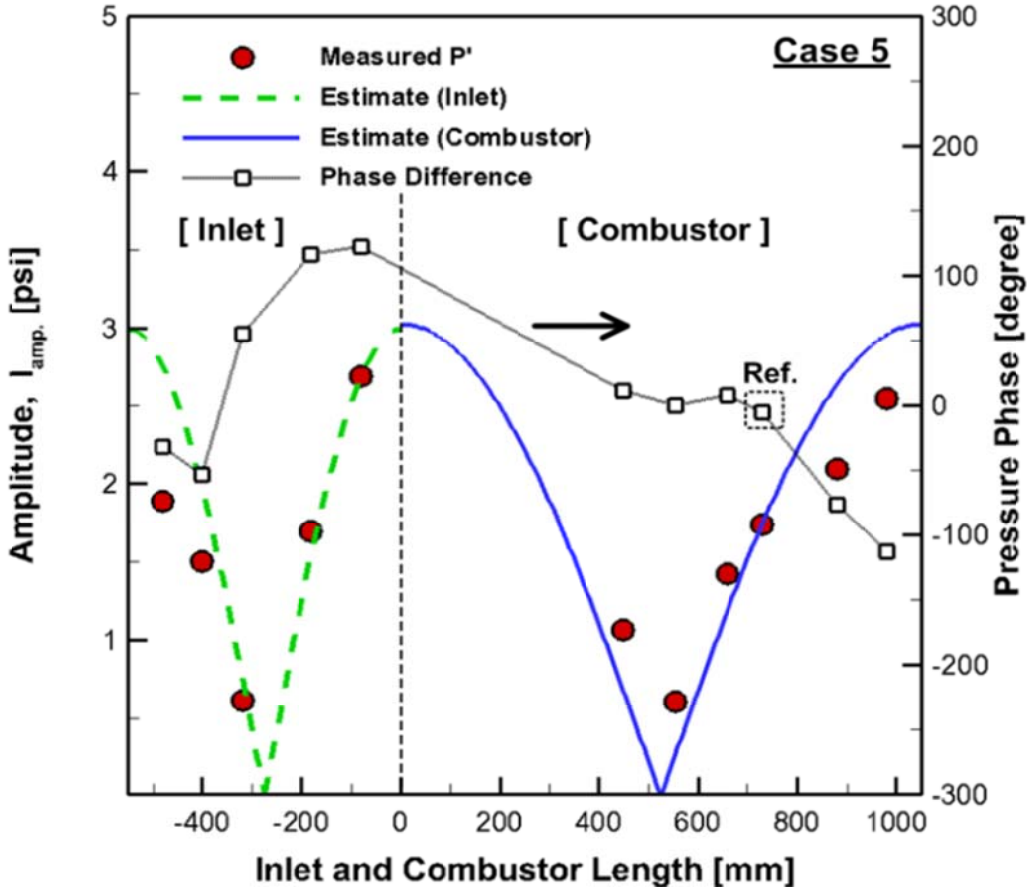
Case 5
Measured P'
Estimate (Inlet)
Estimate (Combustor)
Phase Difference
[Inlet]
[Combustor]
Ref.
Amplitude, $I_{amp.}$ [psi]
Pressure Phase [degree]
Inlet and Combustor Length [mm]
5
4
3
2
1
300
200
100
0
-100
-200
-300
-400
-200
0
200
400
600
800
1000

(a)

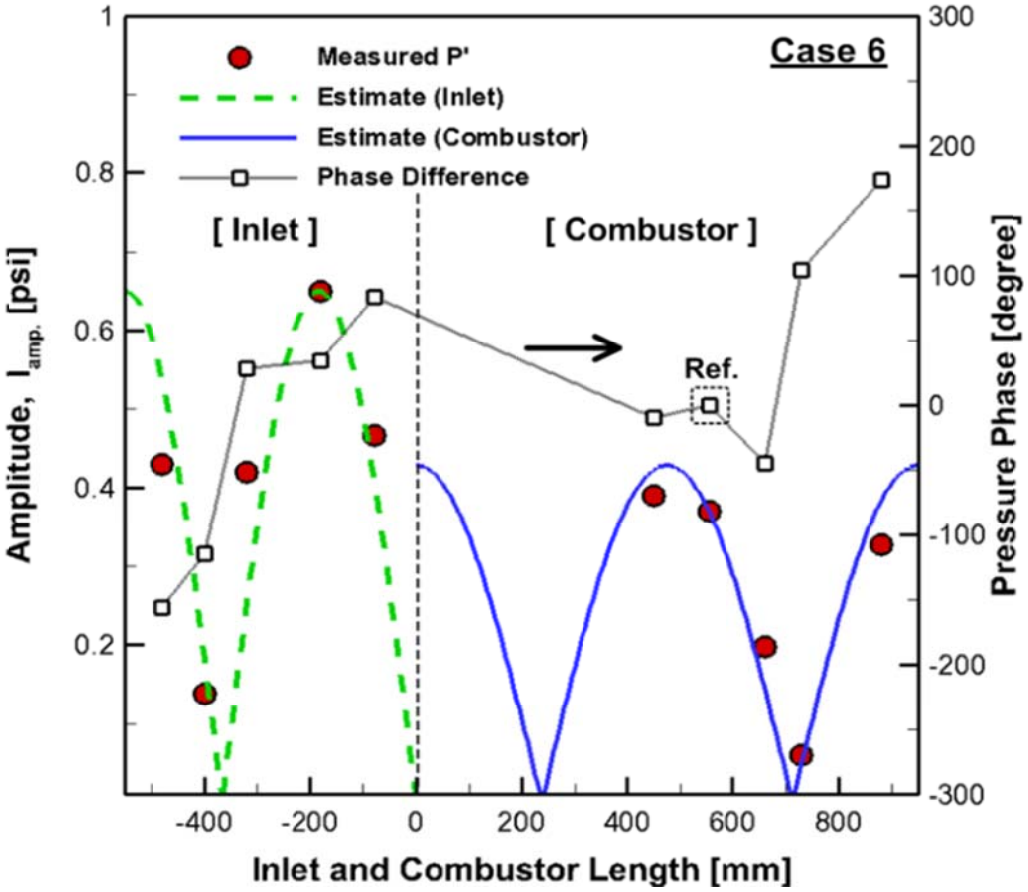

(b)

Fig. 6.15 Dynamic pressure amplitude and phase difference between each sensor at 30° swirl condition and L_{inlet} = 550 mm; (a) 1st longitudinal instability mode, $L_{comb.}$ = 1050 mm, Φ = 1.0, v_{mix} = 70 m/s, case 5, (b) 2nd longitudinal instability mode, $L_{comb.}$ = 950 mm, Φ = 1.1, v_{mix} = 40 m/s, case 6.

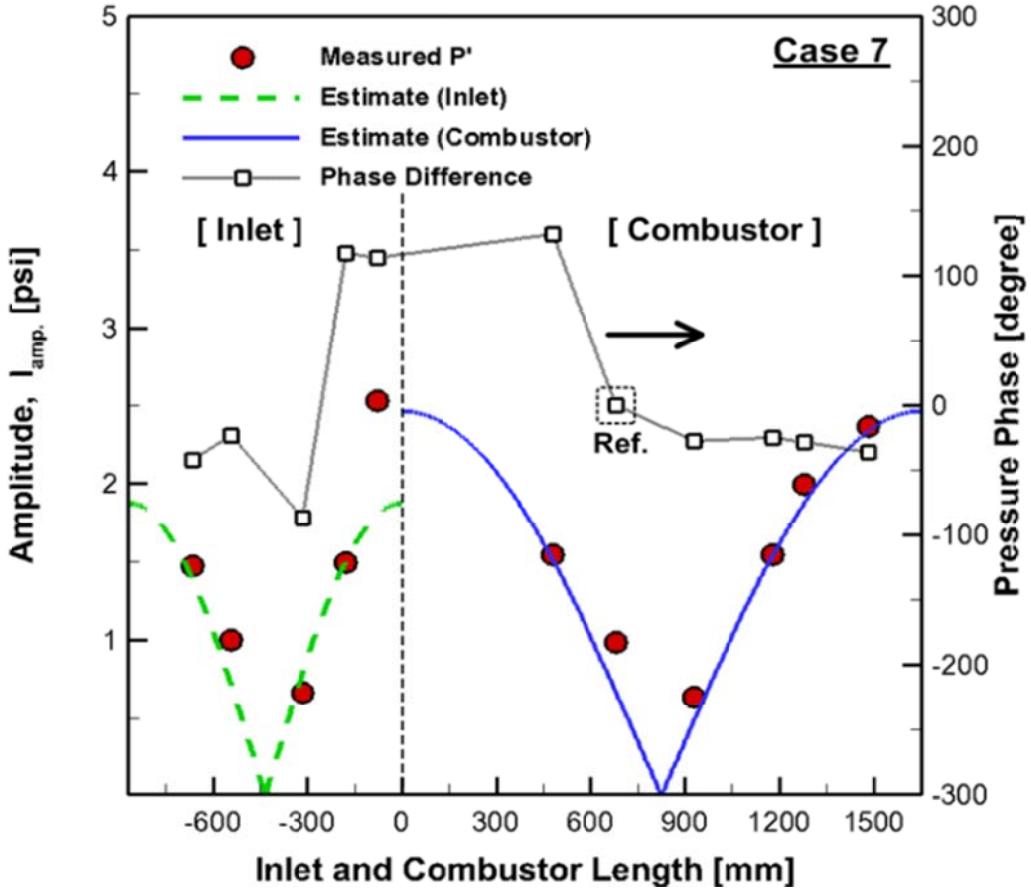
Case 7
Measured P'
Estimate (Inlet)
Estimate (Combustor)
Phase Difference
[Inlet]
[Combustor]
Ref.
Amplitude, $I_{amp.}$ [psi]
Pressure Phase [degree]
Inlet and Combustor Length [mm]
5
4
3
2
1
300
200
100
0
-100
-200
-300
-600
-300
0
300
600
900
1200
1500

(a)

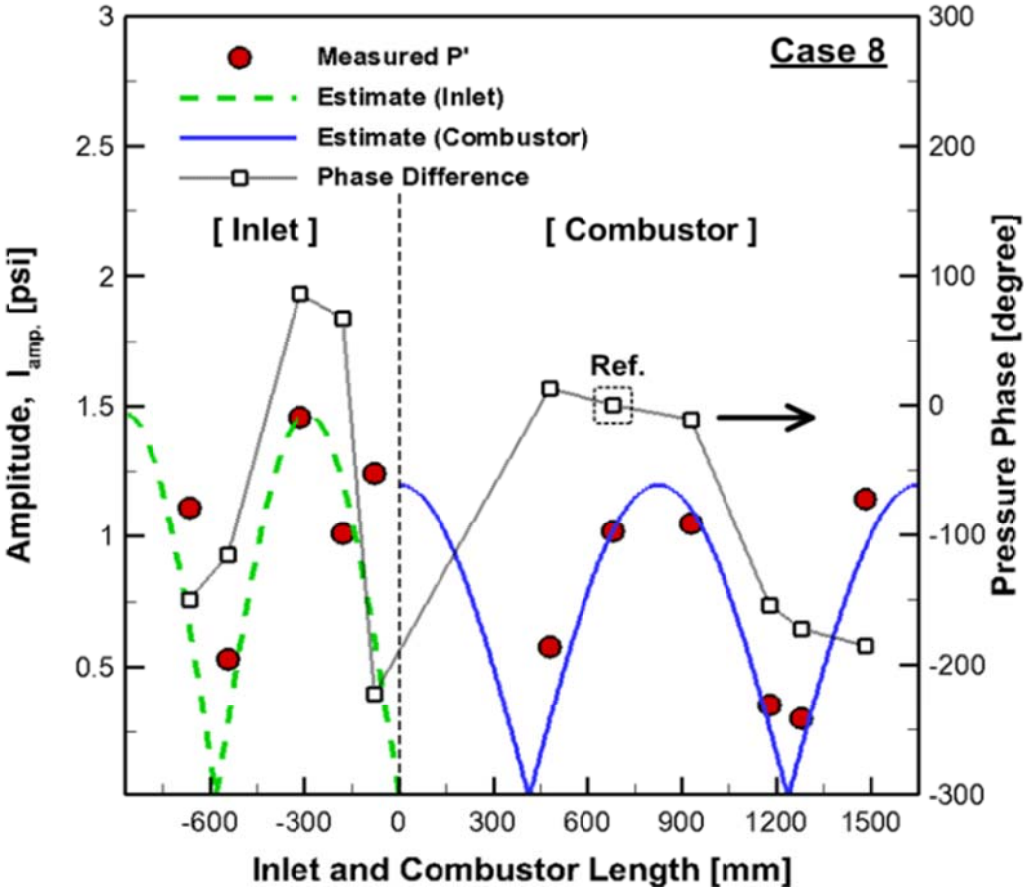

(b)

Fig. 6.16 Dynamic pressure amplitude and phase difference between each sensor at 30° swirl condition and L_{inlet} = 870 mm; (a) 1st longitudinal instability mode, $L_{comb.}$ = 1650 mm, Φ = 1.1, v_{mix} = 60 m/s, case 7, (b) 2nd longitudinal instability mode, $L_{comb.}$ = 1650 mm, Φ = 0.8, v_{mix} = 70 m/s, case 8.

CHAPTER 7
SPRAY CHARACTERISTICS OF CANTED INJECTION ANGLES

7.1 Background and Objectives

The liquid spray jet, which injects perpendicularly into the crossflow, is used as the fuel, air and steam injection device for propulsion units. These units then take the air as the oxidizer, such as the secondary injection for RQL burner, liquid ramjet engine, running on the power obtained through the combustion of the mixture of the air and the fuel, or the after-burner of the gas turbine engine. In addition to these propulsion and power devices, it is also used in the flow control for the aircraft engine performance enhancement and stability, the film-cooling of the turbine blades, and, recently, the second fuel injectors to actively control the combustion instability of the liquid ramjet engine or the gas turbine engine. As shown in Fig. 7.1 the injection structures of the vertical spray jet are generally defined according to three types: the liquid column region which is maintained in proportion to the size of the injector exit immediately after the initial injection; the liquid clumps (ligaments) region where the droplets are bigger than the droplets of the wake flow due to the start of the division generated by the injection velocity of the fluid and the drag of the air-flow field and later on, the spray plume region (droplet region) where the atomization into tiny droplets occurs as it proceeds to the wake flow.

Also, the trajectories of the test spray jets are classified into two types: the trajectory of the liquid column region which is the liquid column of the test fuel immediately after the initial injection and that of the spray plume region formed by the small droplets after the breakup point. Each of the spray jet trajectories infers the exiting distance of the flames as being mixed with the cold air or hot one, decides the shape of the combustion chamber depending on the design of the injector, and can decide mixing time of the fuel

and the air and the evaporation of the droplets prior to the ignition of the fuel. It also decides the location of the second injection for the control of combustion instability, and infers a factor for the flame transfer function of the active control by the presumption of the delay time. Therefore, the combustor designed through the research on the inaccurate fuel injection trajectory can cause performance degradation and flame instability and have a great impact on the performance of the combustor. Research on the injections that perpendicularly spray into the crossing air-flow has already been experimentally conducted along with theoretical research through the proper modeling by a number of researchers.

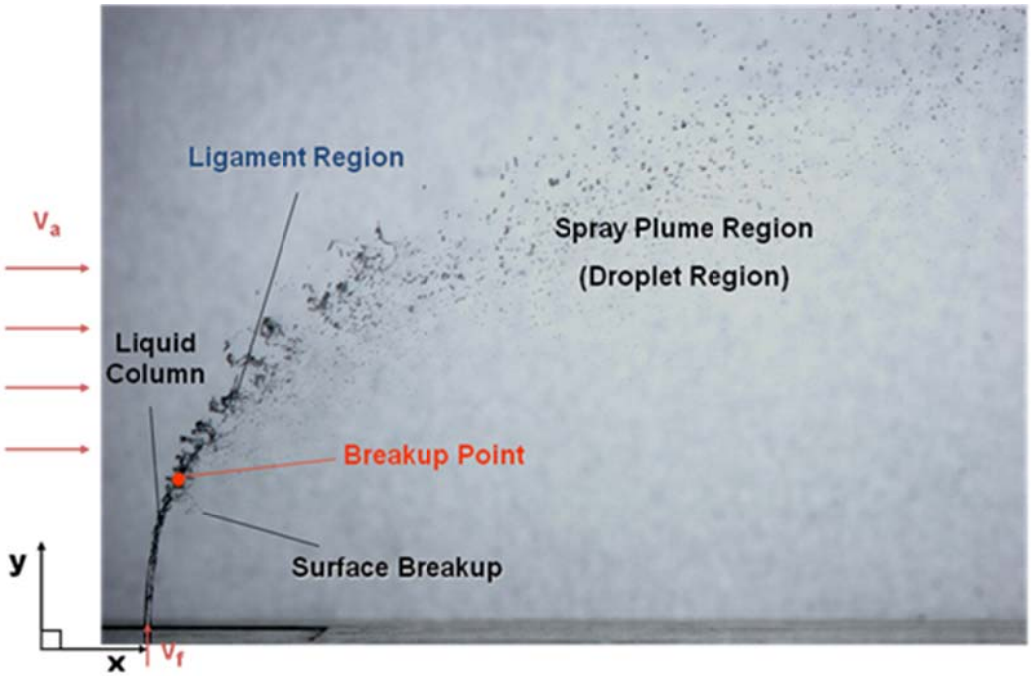

Fig. 7.1 Typical breakup process image of spray jets in subsonic crossflow.

For the experimental methodologies, research has been conducted on the spray structure, the penetration length and the breakup of the liquid column using Schlieren, Mie scattering, direct photography and PDA (Phase Doppler Anemometry), etc. The

representative research on the trajectory of the vertical injection, whose fuel injection angle with the crossflow of the air is 90°, is as follows; Schetz and Padhye et al. [1] suggested that the maximum penetration height is the distance required to turn the momentum flux of the liquid jet injection into the air flow direction. They stated that the penetration height is approximately ~6.25 times the nozzle diameter and that it relates to the liquid/gas momentum flux ratio. Wu et al. [2] derived the spray trajectory and the breakup point of the liquid column region from the free-body diagram of the force equilibrium [3, 4]. Nguyen and Karagozian et al. [5] predicted the trajectories under the combustion condition and the non-reaction condition by converting the interaction between the crossflow and the fuel injection liquid column into a numerical modeling method. Tamaki et al. [6] performed a study on the spray injection and breakup characteristics of the cavitation phenomena decided by the internal shape of the orifice. Song et al. [7] found that cavitation or hydraulic flip effect has an influence on trajectory and Sauter Mean Diameter (SMD) of spray plume region. An introduction of effective jet diameter and effective jet velocity with various spray conditions was proposed.

For the research on the spray whose injection angle is less than 90°, Fuller et al. [8] suggested the liquid column trajectory relation at the injection jet using the same method as Wu et al. Also, the research on the liquid column location defines the breakup regime parameter in proportion to the aerodynamic breakup, which breaks due to rapid air-flow depending on each injection condition and spray angle, and the non-aerodynamic breakup, which in turn breaks due to the inertia and the turbulent forces that the jet itself has without getting influenced much by the air, and deprives the relation to the breakup point through the experiments. Also, Costa et al. [9] confirmed that the liquid column region trajectory relation of the injection is influenced more by the injection velocity than the crossing air velocity, and analyzed the phenomena using the SMD by the fuel injection angle, through the research on the injection angle of less than 90°.

Therefore, this research suggests the relation between the liquid column trajectory and the distance to the breakup point at various forward injections through high resolution direct photography technique [10, 11, 12] and PLLIF (Planar Liquid Laser Induced

Fluorescence), which is an applied measurement technique, conducts the comparison analysis with the prior research findings and additionally aims to confirm the relation to the reverse injection.

7.2 Experimental Methods

7.2.1 Design of angle injectors

The exit diameter of the injector (d) was fixed at 0.5 mm, and the internal structure of the injector was formed by the orifice and the chamber. The diameter of the chamber (D) is 12 mm and here, the type of internal flow is decided depending on the ratio of the orifice length (L) and diameter (L/d), and it is known that hydraulic flip occurs generally when $L/d \leq 8$ [6] and in other cases, instead cavitation phenomena occur. Also, the flow with or without cavitation is decided by the curvature of the inner chamber and orifice. Since this research did not consider the phenomenon of the internal flow of the injector by the cavitation or hydraulic flip, the curvature was set as $R/d = 1$, which indicates that the inlet radius (R) and the orifice diameter are the same. It is known that when $R \geq 0.14d$, normally the vena-contracta does not form and coordinately the cavitation does not occur either [6]. Fig. 7.2 is a picture of the injector shape used for this research. For the study of injection characteristics according to injection angle, we were manufactured the orifices of the various injection angles such as 30°, 45°, 60°, 75°, 90°, 105°, 120°, 135° and 150°.

Table 7.1 Experimental conditions.

Parameters	**Values**	
Air velocity [m/s]	60	
Air temperature [K]	300	
Fuel temperature [K]	318	
Fuel (Mixture ratio)	Water + Ethanol Water : Ethanol = 4 : 1 (Ethanol 20%)	
Orifice diameter [mm]	0.5	
Orifice shape	Inner round edged (L/d=20)	
Pressure Differential [ΔP, bar]	1, 2, 3, 4, 5	
x/d (Normalized Transverse Distance)	40, 60, 80, 100, 120	
Injection angle (Normalized Transverse Distance)	30°, 45°, 60°, 75°, 90° (Forward injection)	105°, 120°, 135°, 150° (Reverse injection)

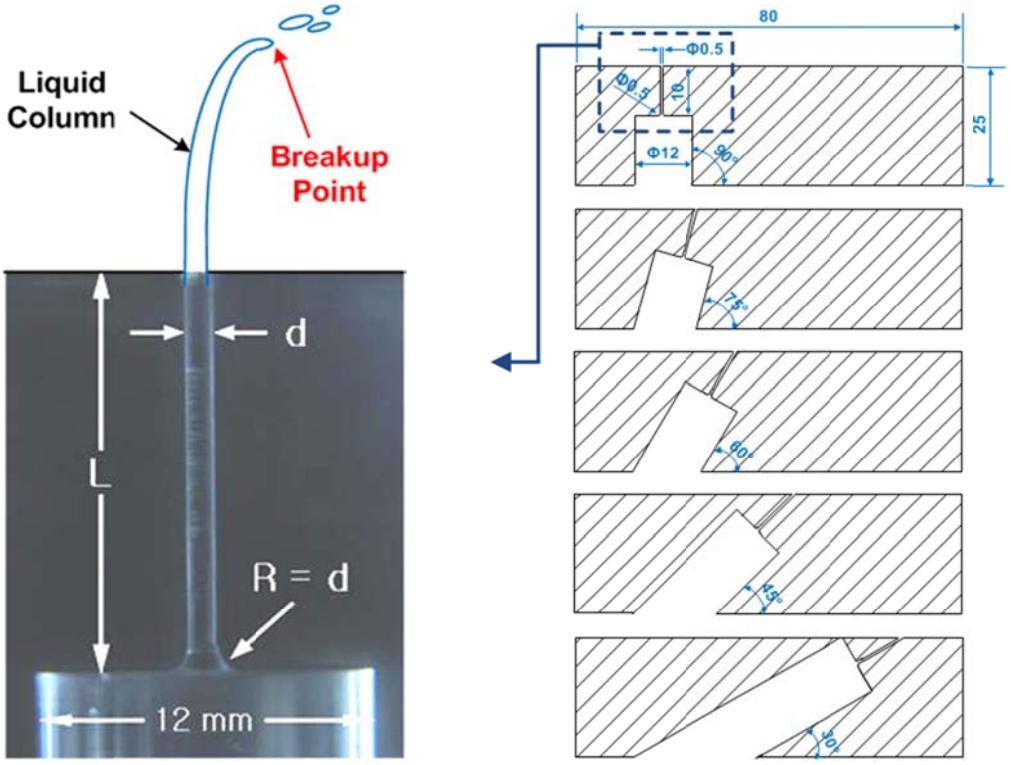

(a) (b)

Fig. 7.2 Angled injector shape; (a) round-edge orifice (L/D = 20), (b) angled orifices.

7.2.2 Experimental apparatus and conditions

The liquid column trajectory of the injection and the breakup length, for the forward injection whose injection angles are 30°, 45°, 60°, 75° and 90°, and on the reverse injection whose injection angles are 105°, 120°, 135° and 150°, was measured. First, for the direct photography technique, the photos for the liquid column trajectory were taken with a Canon EF 100mm f/2.8 Macro USM lens which supports high resolution photography. And the liquid breakup distances were taken with a Canon MP-E 65mm f/2.8 1-5x Macro Photo lens. The photos were taken by synchronizing the digital camera (Canon EOS 20D) and the stroboscope, the light source; the expansion ratio per pixel is

about 2~10㎛. About 2000~3000 photographs for each experimental case of the trajectory and the breakup point of the liquid column region were taken to maintain the experimental error range within 5% [13]. Also, the injection structure was observed using the PLLIF technique, which is capable of measuring the intensity values of the fluorescence signal and the scattering signal for the comparison analysis with the present experimental results of the trajectories and the breakup length obtained by direct photography technique.

Figure 7.3 shows the experimental devices for PLLIF and the direct photography techniques. The mixture of water and ethyl alcohol (of volumetric ratio 4:1) was used as working fuel, and the fluorescent ($C_{20}H_{12}O_5$, Aldrich F245-6) of 30 mg was dissolved into the simulant working fuel of 1 liter. Because of the fluorescent absorbs light in the wavelength range from 400 to 530 nm, and the experiment fuel was heated to 318 K to obtain the non-cavitation flow. For the specific gravity of the experiment working fuel, the fuel similar to that of the previous research result was used, and the working fluid similar to the fuel specific gravity at the real combustor was used. The size of the visible area is 50 mm x 50 mm x 330 mm, air with a velocity of 60 m/s was blown in by the 20 hp blower, and the stabilized air in the settling chamber was supplied to the test section after passing through the honeycomb for the uniform air-flow.

For the LEXEL's, an argon-ion laser was used, and for the major beam, Dantec's fiber-optics were used to convert into the planer beam. The fluorescence signal and the scattering signal obtained by PLLIF were installed into the digital camera Canon EOS D30 with the 28-105mm standard lens, and the 2X Vivitar enlargement lens was installed so that the image could be enlarged and taken. The high-pass filter that detects the 550 nm wavelengths and the band-pass filter that detects the 514±5 nm wavelengths were installed into both cameras to obtain the fluorescence signal and the scattering signal. It was possible to obtain the experimental values by scanning the picture gained by the PLLIF scattering signal through the image processing and by considering the point where the lights are rapidly scattered as the breakup point.

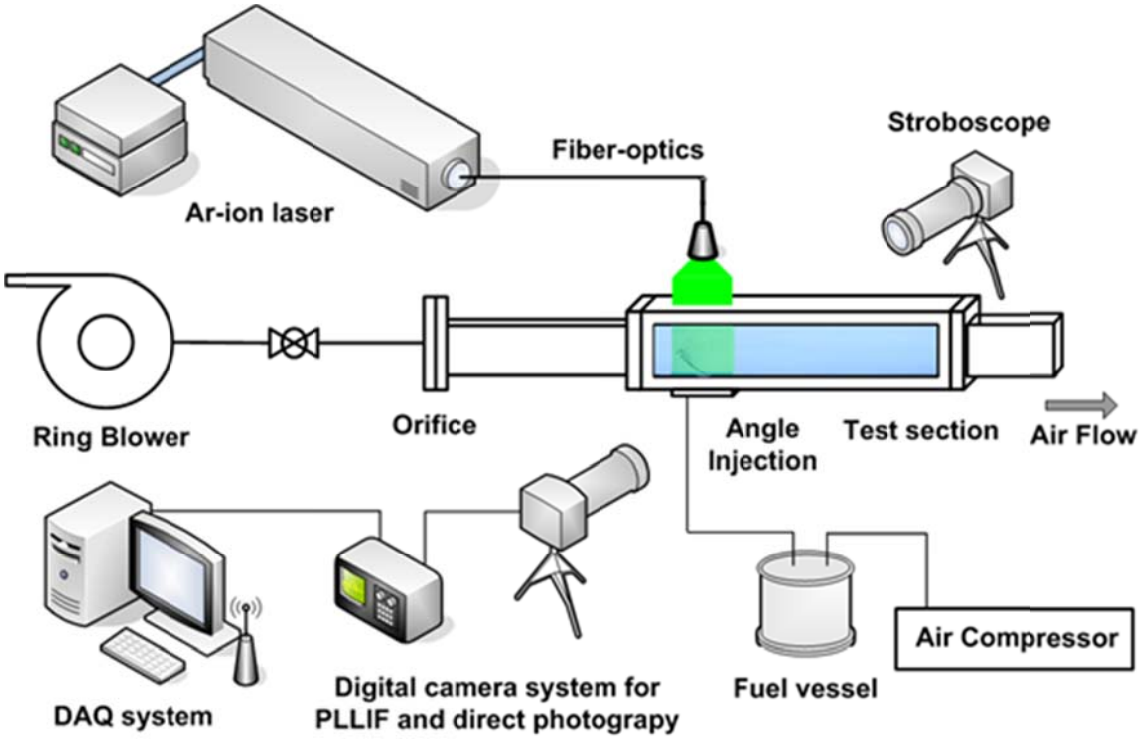

Fig. 7.3 Experimental setup for direct photography and PLLIF measurement.

7.3 Canted Injection Characteristics

The air velocity of the experiment was fixed at 60 m/s, and the injection characteristics of the liquid column region and the droplet region of the injection jet were studied by changing the injection pressure differential of the fuel (water + ethanol) to 1~5 bar; in other words, by varying the values of fuel/air momentum flux ratio, q($\rho_f u_f^2 \ / \ \rho_g u_g^2$) as 21~105, to identify the characteristics of the fuel velocity. This is the value of the momentum flux ratio in the prior research that can be compared with this study. Fig. 7.4 is a direct photography and Fig. 7.5 shows the PLLIF images of the vertical injection with the angles of 30°, 60°, 90°, 120°, 135° and 150° from the datum of the nozzle exit at the normal flow injector group without any cavitation or hydraulic flip

effects, under the normal injection conditions that the fuel injection pressure differential is 3 bar and that the momentum flux ratio is 65.

In the forward injection whose angle is less than 90° and in the reverse injection, as the fuel velocity q increases, the jet velocity increases accordingly so that it can be confirmed that the penetration distance of the crossflow into the air-flow field also increases. As shown in the following Fig. 7.4, in the area with the injection angle of less than 90°, as the injection angle decreases, the liquid column gets straighter and the penetration distance becomes decrease than the injections with other angles. Therefore, since the shear stress on the liquid column surface decreases, the atomization performance degrades compared to the cases with other angles injection. And since the velocity of the injection jet with the 30° injection angle processes is almost the same as the value of the velocity of the blowing air compared with the other injection angle conditions. The breaking forces due to the effects of the wavelengths caused by the free vibrations and the power of inertia, the own turbulence effect of the liquid column becomes bigger than the breakups caused by the air. Fuller at el. [8] mentioned that the factors that decide the penetration distance of the vertical injection jet are the injection angle and fuel/air momentum flux ratio (q) and also mentioned that in the low fuel/air momentum flux ratio (q) region, the liquid column has big waves. Furthermore, they state that due to this phenomenon, the surface of the liquid column gets distorted and breaks up due to the kink phenomenon. Chigier and Reitz et al. [14] mentioned that this is the fiber-type breakup.

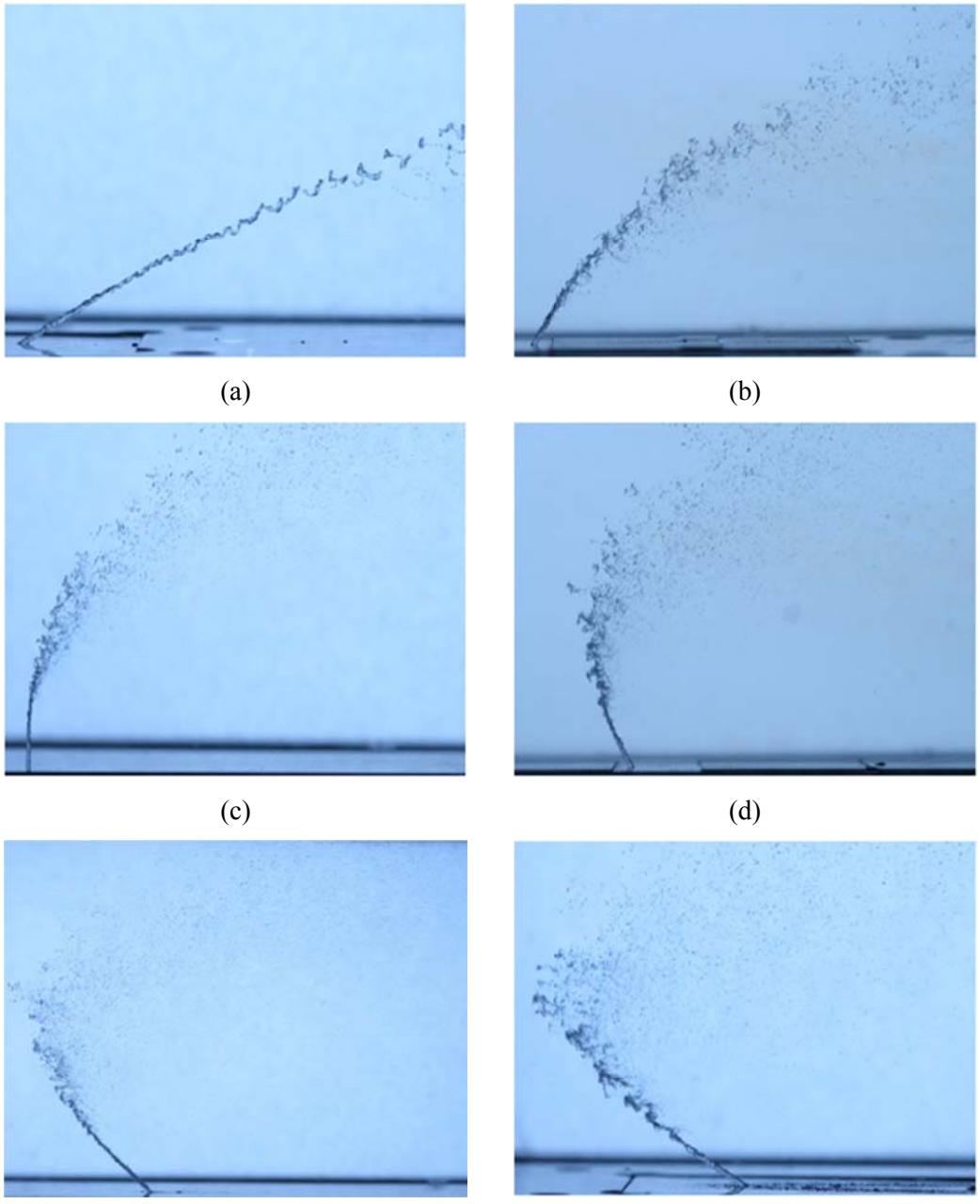

Fig. 7.4 Spray patterns at variously angled injections (ΔP = 3 bar, q = 65); (a) 30°, (b) 60°, (c) 90°, (d) 120°, (e) 135° and (f) 150°.

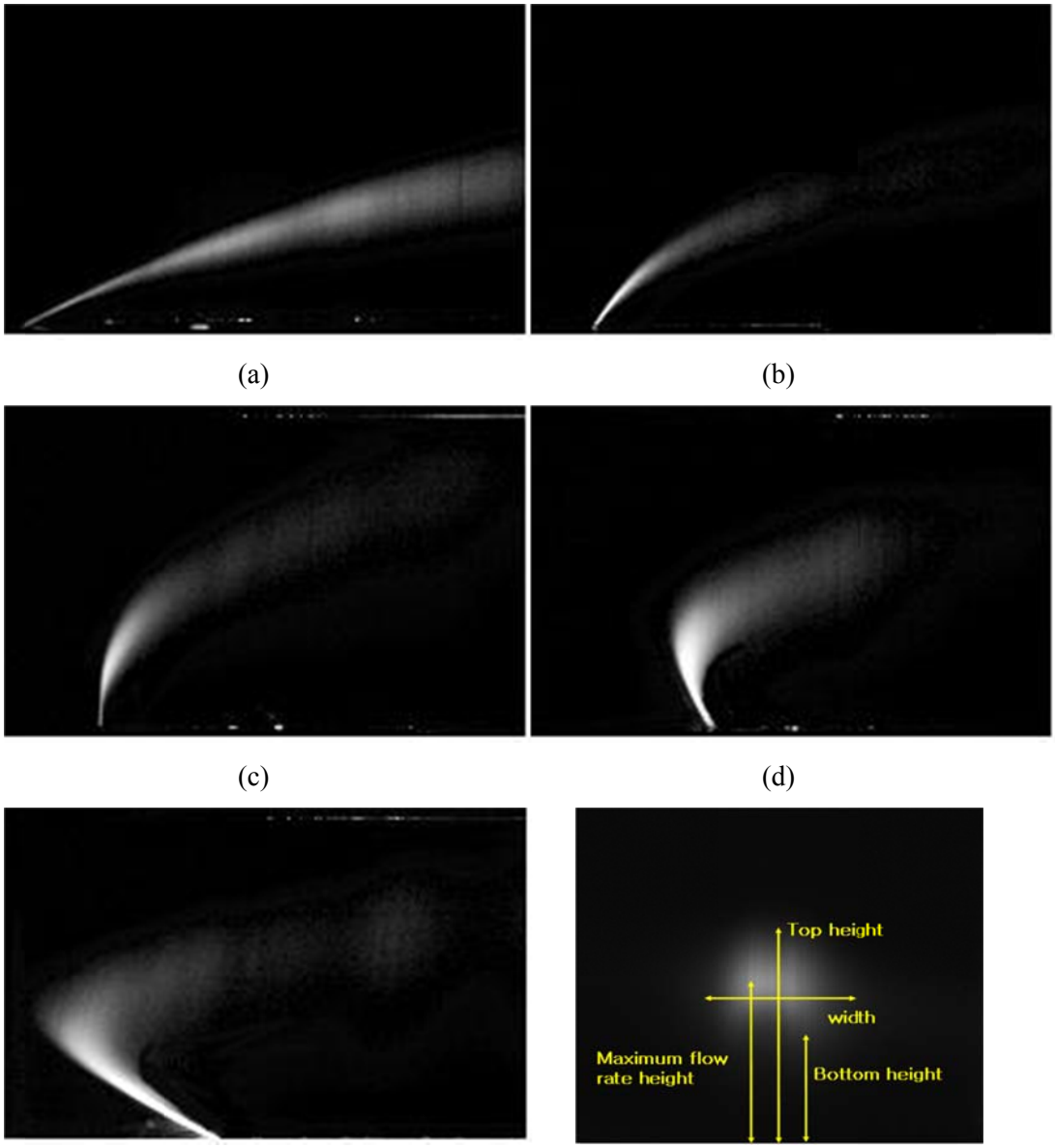

Fig. 7.5 LIF images by PLLIF measurement (ΔP = 3 bar, q = 65); (a) 30°, (b) 60°, (c) 90°, (d) 120°, (e) 150° injections and (f) spray plume structure.

7.4 Liquid Column Trajectory in Forward and Reverse Injections

Therefore, the trajectory experimental formula of the liquid column region can be calculated depending on the injection angle that is less than 90° and on the reverse injection. Here, x indicates the value of the axial distance of the axial (air-stream) direction, y indicates the value of the penetration distance of the penetration direction, d is the diameter of the orifice exit, θ is the injection angle, v_f is the fuel velocity and v_a is the value of the air velocity.

The liquid column trajectory is decided by the drag coefficient, and Fuller et al. [8] defined the drag coefficient value of the sections where the experimental values of this study fit smoothly into the comparison with the theoretical value obtained by the equation derived of the experimental results with less than 90° and the force equilibrium. By the empirical formulas about liquid column trajectory of Fuller et al. [8], the error range was set within about 30% across the entire experiment, and the drag coefficient (C_D) was obtained 4.4. Fig. 7.6 (a) shows the drag coefficient values through the comparison between the experimental and the theoretical value of the liquid column trajectory whose injection angle is less than 90° in this experiment, and this coefficient result was compared to the previous research result. In this research, the drag coefficient value, gained within a 3% error range across the entire experiment of 30°, 45°, 60°, 75° and 90° injection conditions was obtained as 1.3. Wu et al. [2] computed the drag coefficient value 1.7 based on the liquid column trajectory, obtained by taking the variables of the fuel type, injector exit diameter, air velocity, etc.

The result of this experiment shows a good match with the experiment of Wu et al. [2] more than the drag coefficient value that Fuller et al. [8] suggested. This can be explained as the q condition of this experiment and the fuel type used in the experiment involving the mixed fuel of water and ethanol are similar to Wu's experiment, resulting in a similar coefficient value. Also, it was detected that the drag coefficient value showed its difference caused by the errors of each experimental environment, the injector manufacturer, the orifice passage length, and the thickness difference of the liquid column.

In this experiment, the Reynolds number (Re) value for the liquid column region is as follows: 5000≤Re≤15000 [15]. This matches to a certain degree with the approximate drag coefficient value for the smooth circular cylinder, which remains as 1~1.5. Fig. 7.6 (b) is the graph that decides the drag coefficient of the trajectory equation for the liquid column region. The drag coefficient was decided as 0.2 through the comparison between the experimental value, which was obtained for the reverse injection and for the theoretical value of the Eq. (7.1).

$$\frac{x}{dq} = \frac{1}{\pi}\frac{C_D}{\sin^2\theta}\left(1-\frac{v_f\cos\theta}{v_a}\right)^2\left(\frac{y}{dq}\right)^2 + \frac{\cos\theta}{\sin\theta}\left(\frac{y}{dq}\right) \tag{7.1}$$

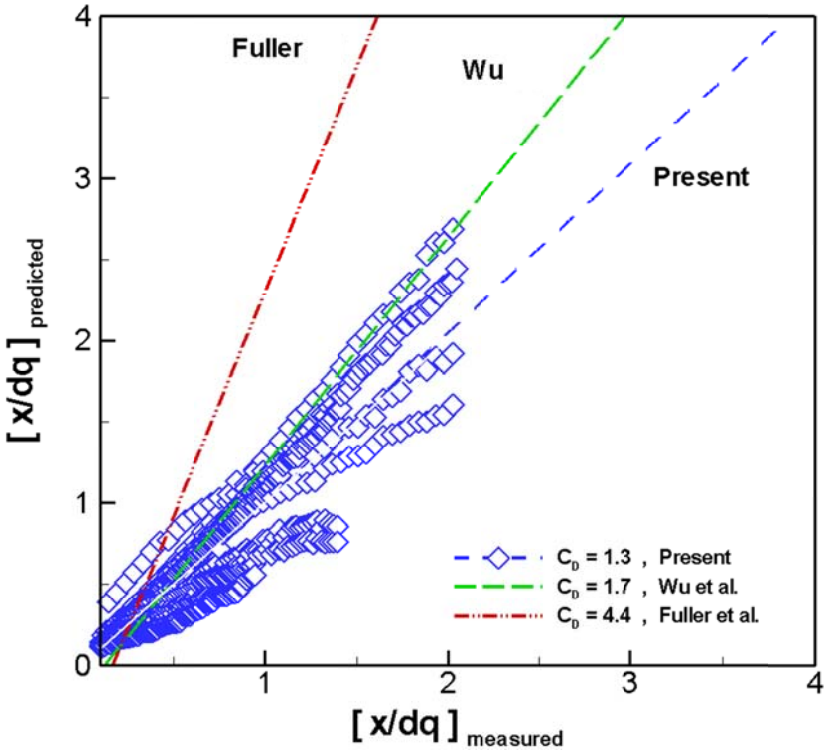

(a)

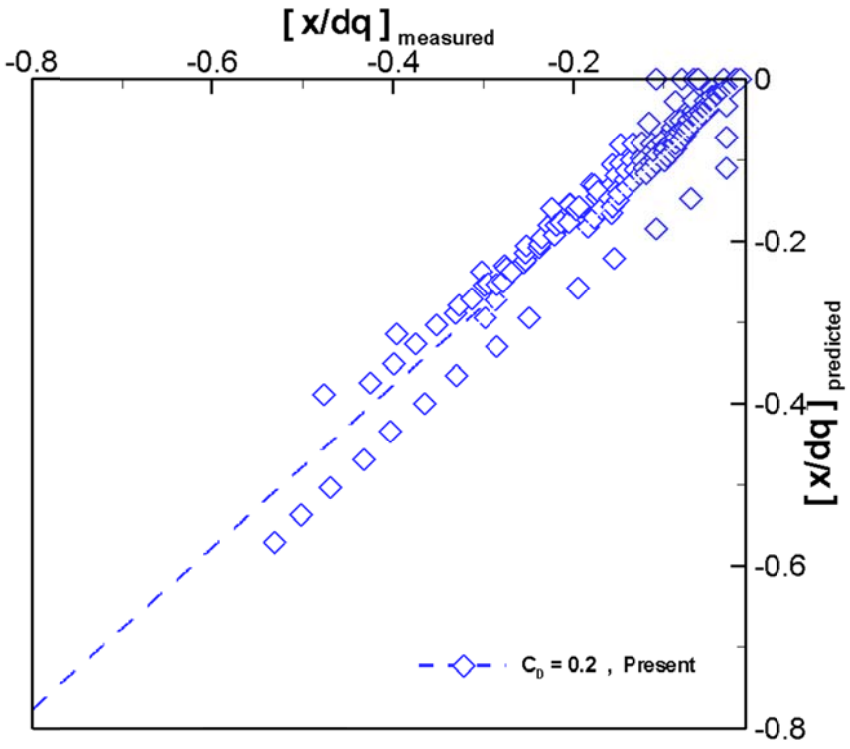

(b)

Fig. 7.6 Drag coefficient for all of experimental cases (C_D); (a) forward injection (Θ = 30°, 60°, 90°), (b) reverse injection (Θ = 120°, 150°).

7.5 The Verification of Liquid Column Trajectory

The trajectories of the liquid column region obtained by the experiment were compared with the previous research to verify the trajectory, and then an analysis was conducted as to whether it validated all injection angle cases. Fig. 7.7 is a graph of the comparison of the experimental values compiled by direct photography at 30°, 60°, 90° of the injection angle, and the figure also shows the results of the PLLIF technique presented by Wu et al. [2] and Fuller et al. [8]. It is clear that in the cases of 30° and 60° in the following Fig. 7.7, the drag coefficient result is different from that of Fuller et al. [8], and

it could be suggested that this was due to the differences in the proportion of the working fluid according to the Eq. (7.1), the experimental conditions and the drag coefficient which were used in the previous experiment. Fig. 7.7(c) is the graph that compares the measured experimental values in the injector group with the 90° injection angle and the previous research results.

Likewise, the present study shows the different drag coefficient (C_D) results from the studies by Wu et al. [2] and Fuller et al. [8]. This research derived the trajectory of the liquid column by the each injection angle, maintaining the error range of the experimental value and the theoretical value, through the experiment result with various injection angles condition provided than the previous research result, within 3%. Also, the drag coefficient for the 90° injection result has a similar value with Wu's drag coefficient, and its reliability was confirmed since the experimental conditions that were formerly mentioned were similar. It was verified that the case with the forward injection angle showed differences due to the experimental condition and due to the experimental fluid in the prior experimental result. Fig. 7.8 shows a graph that compares the empirical formula of the liquid column trajectory obtained from the reverse injection experiment of the 120° and 150° injectors with the data categorized according to each angle. In the case of the experimental equation of the reverse injection, it can be verified that the reverse injection result matches the experimental value when the drag coefficient is 0.2. Moreover, it was confirmed that the drag coefficient of reverse injection matched in all regions with the results of additional experiments involving angles of 105°, 135° and others.

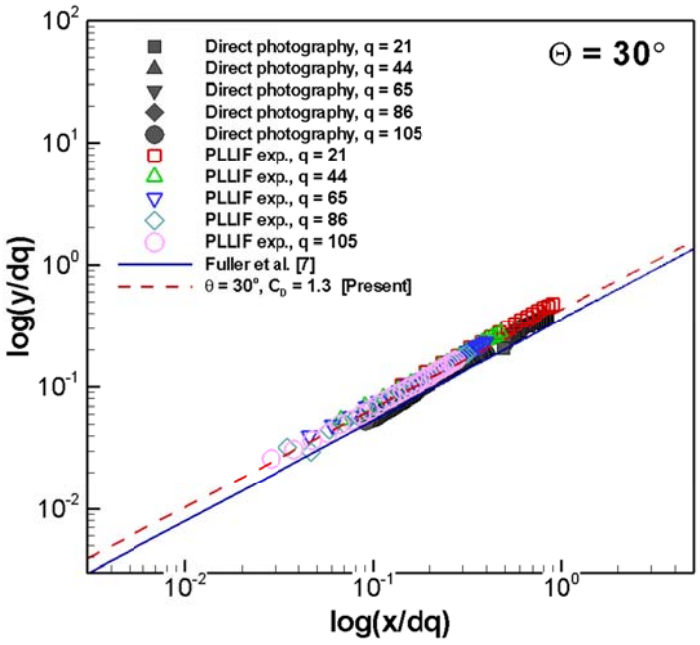
Direct photography, q = 21
Direct photography, q = 44
Direct photography, q = 65
Direct photography, q = 86
Direct photography, q = 105
PLLIF exp., q = 21
PLLIF exp., q = 44
PLLIF exp., q = 65
PLLIF exp., q = 86
PLLIF exp., q = 105
Fuller et al. [7]
θ = 30°, C0 = 1.3 [Present]
Θ = 30°
log(y/dq)
log(x/dq)

(a)

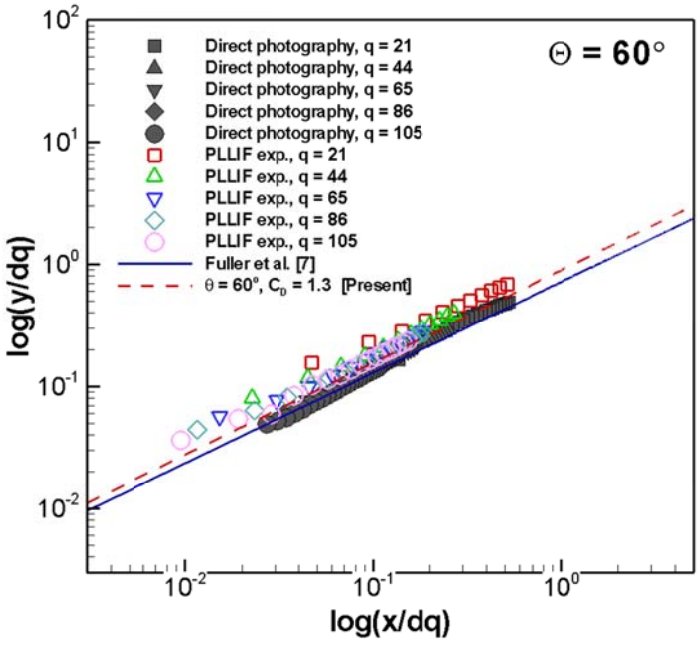
Direct photography, q = 21
Direct photography, q = 44
Direct photography, q = 65
Direct photography, q = 86
Direct photography, q = 105
PLLIF exp., q = 21
PLLIF exp., q = 44
PLLIF exp., q = 65
PLLIF exp., q = 86
PLLIF exp., q = 105
Fuller et al. [7]
θ = 60°, C0 = 1.3 [Present]
Θ = 60°
log(y/dq)
log(x/dq)

(b)

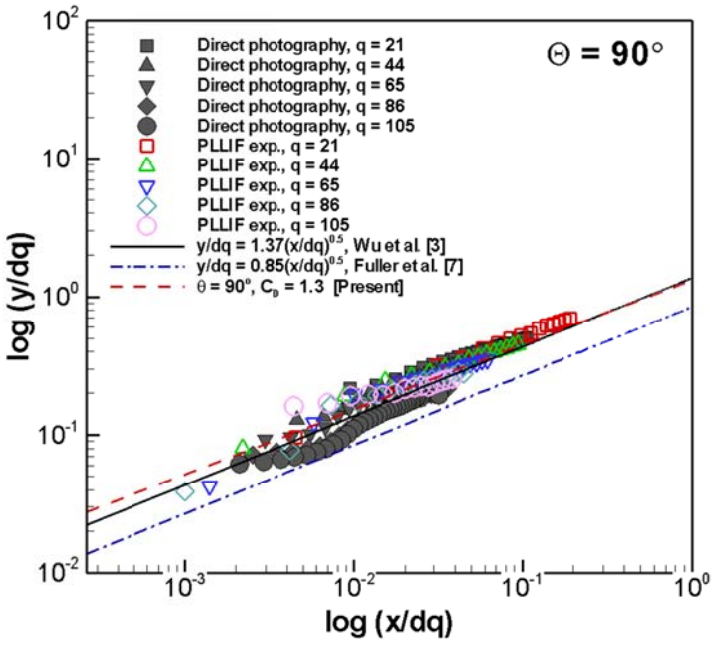

(c)

Fig. 7.7 Comparison with previous and present correlated liquid column trajectory results at forward injection ($\Theta \leq 90°$); (a) 30°, (b) 60° and (c) 90° injection.

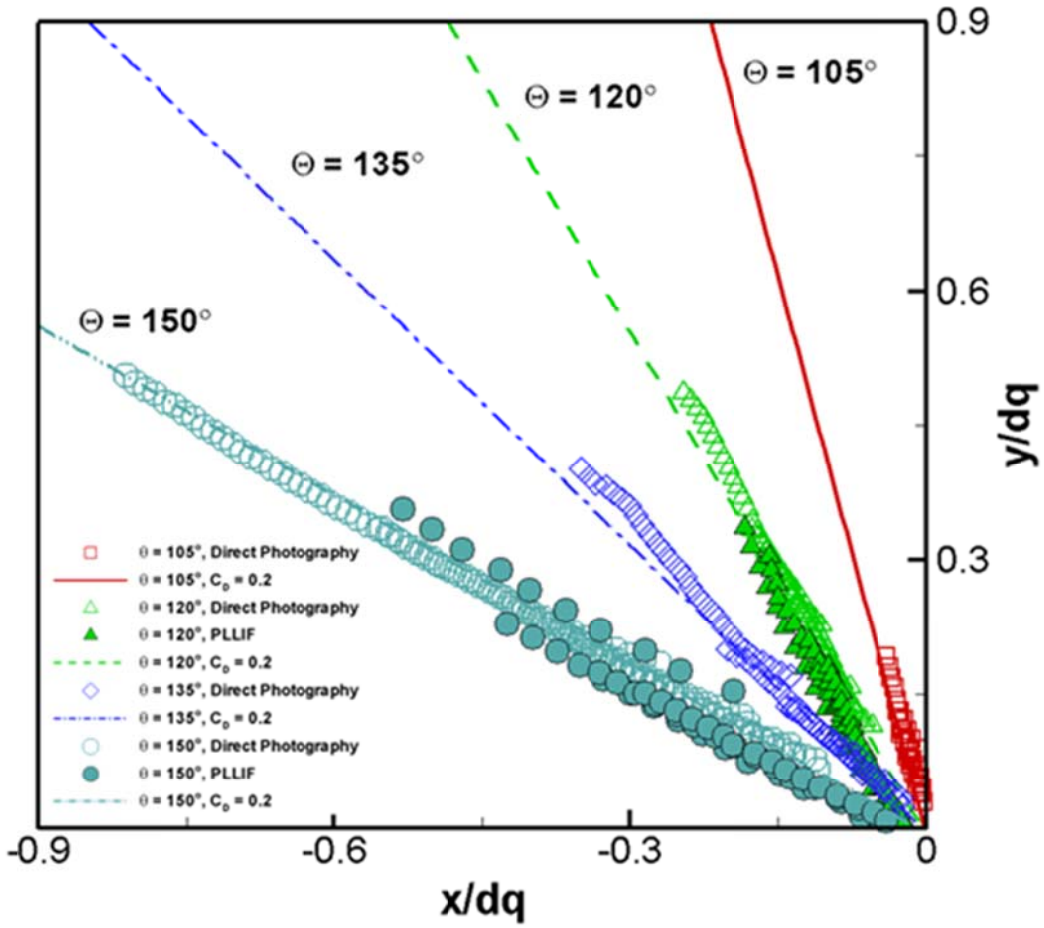

Fig. 7.8 Correlated liquid column trajectory in reverse injection (Θ > 90°) injection.

7.6 Spray Breakup Characteristics

Figure 7.9 shows a graph that expresses the distance to the breakup point, which is the border of the liquid column region and the droplet region of the spray experiments with the various injection angles. In the case of the reverse injection, spray in the reverse direction from the datum of the injector exit. Therefore, the measured distance to the breakup point was taken and compared with the results of the other injection angles in

this experiment. Wu et al. [2] found out the relation of axial distance with respect to the wake flow to the breakup point (*x*-direction) and the penetration distance (*y*-direction) through the experiment.

In the case of the 90° injection, it could be verified that most of the results of this research match with Wu's equation because the drag coefficient value was similar in the trajectory result. Fig. 7.9(a) shows a graph of the axial direction breakup of the air-flow. The cases of 60°, 75°, 105°, 120° injection, which are similar to the 90° injection, show that the breakup points in the forward direction are similar. However, in the case of the reverse injection where it injects in the opposite of the proceeding direction, since the injection occurs in the opposite direction of the rapid airflow intake, it was identified that the distance to the breakup point becomes shorter due to aerodynamic forces.

In the cases of the 30° and 150°, the axial breakup distance has the bigger value than in the cases of the rest of the injection angles where it similarly injects into the vertical plane of the flow field. This is considered since it indicates the tendency of it to breakup due to the power of the liquid jet rather than breaking up due to the air. The distance to the breakup point in the proceeding direction has somewhat larger value than the other injector group. In the case of the 150° reverse injection, the value is than 30° since it penetrates in the opposite direction of the air-flow direction. However, in case of 150°, in spite of the fact that it is a reverse injection, the axial distance to the breakup point shows similar results with the 30° injection. This is because as the q value increases, also for the reversed injection, the penetration distance remains constant to a certain degree. Furthermore, when it passes the maintained penetrated distance, rapid atomization is observed. Fuller et al. [8] suggested that in case of the injection with lesser angles, the penetration distance influences the injection velocity more than the breakup due to the air velocity, and the larger injection angles condition has shorten the axial direction distance to the breakup point in the experimental result performed to the range of 90°. It was shown that in the 90° case, the result showed a similar tendency with the breakup equation suggested by Wu et al. [2], and for the lesser angles, the contents were well matched with the findings by Fuller et al. [8] Finally, the distance to the breakup point

shortens as it injects closer to the vertical plane of the air-flow direction regardless of the normal injection or of the reverse injection.

Figure 7.9 (b) shows the result related to the distance to the breakup point of the penetration direction. Since the injectors with the angle of less than 90° in the result of the graph have the relatively smaller penetration distance, their distances to the breakup point of the penetration direction become shorter than those of the injectors with other given angles. It was also verified that if the injection pressure differential increases, the penetration distance increases generally and so the breakup point lengthens.

In the case of 30° injection, the flow velocity of the air and the velocity of the jet are almost identical. Also, in the case of 30° injection, compared to the other angled injections, the large scale atomization performance cannot occur. Therefore, it was identified that the distance to the breakup point of the penetration direction remains almost constant. In the case of 150° reverse injection, the distance to the breakup point of the proceeding direction is similar to the case of 30°, but as the trajectory wraps upwards by the characteristic of the reverse injection, the distance to the breakup point of the penetration direction gains a relatively bigger value.

Also, in the cases of 60° and 120°, the distance to the breakup point of the penetration direction remains similar regardless of whether it is the reverse injection or the normal injection. And it was verified that in the region where the injection pressure is low, there is no difference in the breakup lengths, but in the region where the injection pressure differential is high, there are different breakup length scale effects. It could also be identified that the distance to the breakup point of the penetration direction shortens in cases of 75°, 90° and 105° injection whose direction is close to the vertical plane of the air flow direction regardless of the normal injection or the reverse injection.

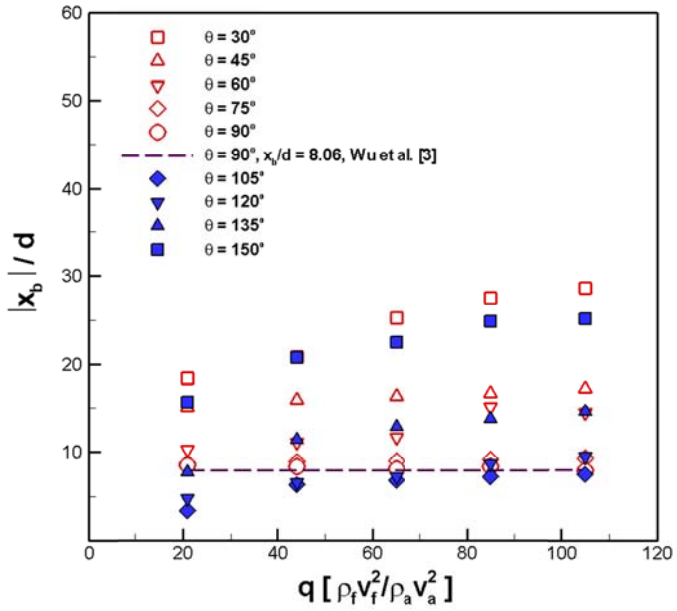

(a)

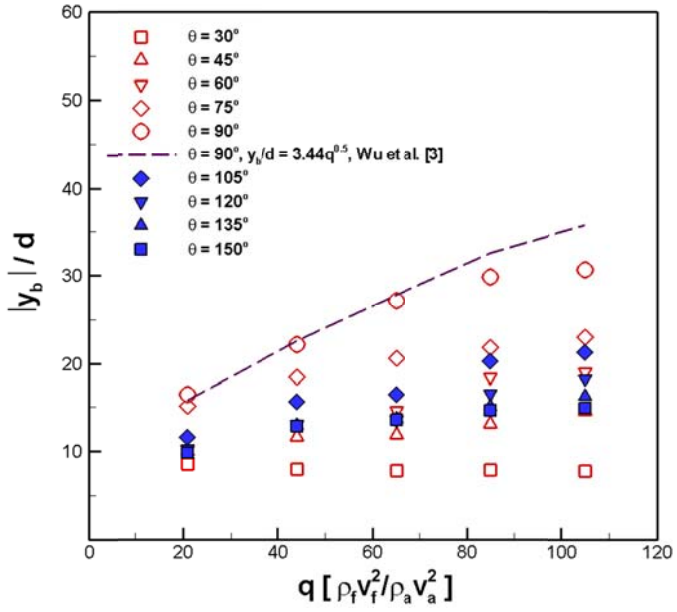

(b)

Fig. 7.9 Breakup length characteristics; (a) axial distance (*x*-direction), (b) penetration distance (*y*-direction).

Figure 7.10 is the result of the ratio of the proceeding direction of the fluid and the distance to the breakup point of the penetration direction. Except the 30° injection which has the breakup characteristic due to the velocity of the liquid jet rather than the effect of the aerodynamic drag, each of the experimental results maintained almost constant values. Thus, this study could suggest an empirical formula for the airstream direction of the sprays in all injection angles and the distance to the breakup point of the penetration direction as in the following

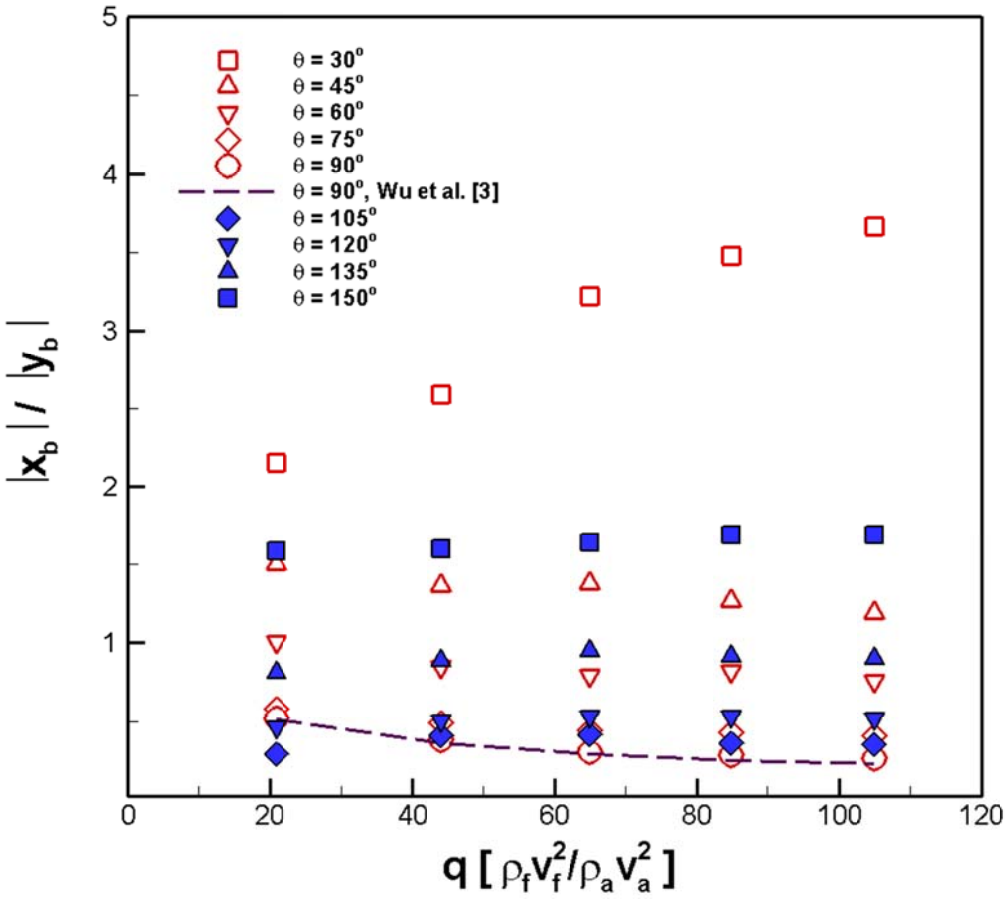

Fig. 7.10 Ratio of liquid column breakup length with normalized axial and penetration distances.

Figure 7.11 shows the empirical formula for the distance to the breakup point derive as Eqs. (7.2), (7.3), (7.4) and (7.5). It was demonstrated that the relation of the proceeding direction of the air flow and the breakup distance of the penetration direction varies depending on the forward injection or the reverse injection.

Forward injection cases :

$$\left.\frac{|x_b|}{d}\right|_{\theta \le 90^o} = \frac{6.34\, q^{0.07}}{\sin^2 \theta} \tag{7.2}$$

$$\left.\frac{|y_b|}{d}\right|_{\theta \le 90^o} = 6.33\, q^{0.314} \sin^2 \theta \tag{7.3}$$

Reverse injection cases :

$$\left.\frac{|x_b|}{d}\right|_{\theta > 90^o} = \frac{1.14\, q^{0.39}}{\sin^2 \theta} \tag{7.4}$$

$$\left.\frac{|y_b|}{d}\right|_{\theta > 90^o} = 4.64\, q^{0.317} \sin^{0.5} \theta \tag{7.5}$$

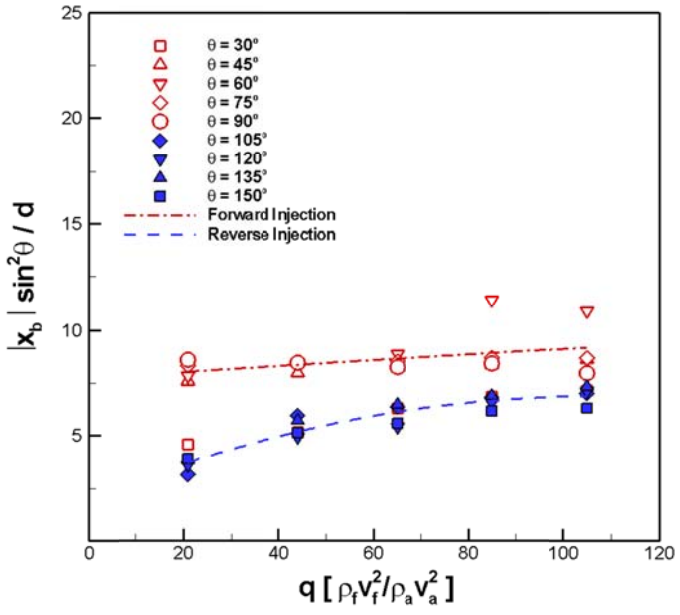

(a)

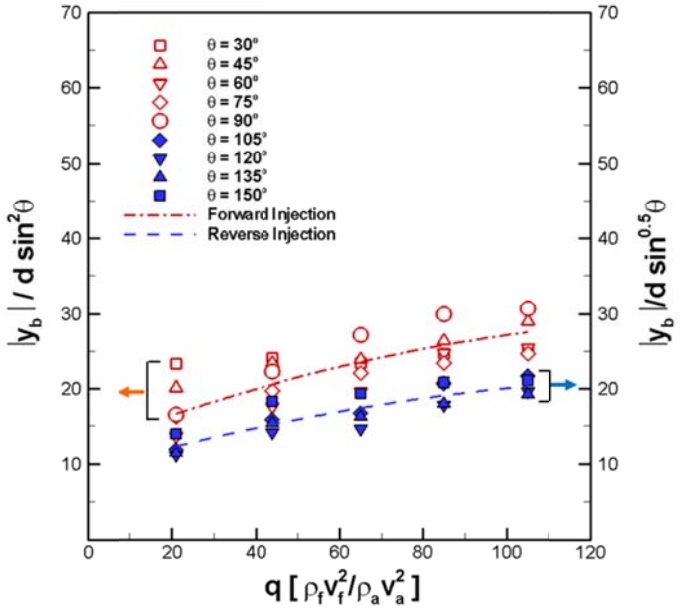

(b)

Fig. 7.11 Empirical formula of liquid column breakup length; (a) axial distance (*x*-direction), (b) penetration distance (*y*-direction).

CHAPTER 8
CONCLUSION

Experimental investigations were performed on the flame structure and combustion instability characteristics of model gas turbine combustor for low NOx combustion. Also, secondary spray jet mechanism and the optimum combustion tuning method were conducted on model and stationary gas turbine combustor for validation of this experimental study. This study carried out a research on the combustion dynamic characteristics of partially premixed flame by changing the combustor length, the equivalence ratio, and the fuel-air mixture velocity of nozzle exit and depending on the length of the fuel-air mixing section length. The fuel-air mixture velocity and equivalence ratio were confirmed to be main variables for the phenomenon of combustion instability as they changed the response characteristics of flame and the average temperature conditions in the combustion chamber, and in such a condition as a diffusion flame without swirl effect, there was a higher dynamic perturbation value during combustion instability than in the condition of more premixed type flame, causing a 30° swirl effect. In addition, it was found that larger combustion instability took place in the section where the fuel-air mixture velocity was high.

This study also investigated the relation between the combustion instability phenomenon and the formation of a recirculation zone through the PIV measurement technique. Although there has been considerable research on the mechanism of flame stabilization, the results mostly cover the closed-open boundary of combustors. This study, however, observed the structural characteristics of swirl-stabilized flame in a limited combustor through the PIV technique, and associated the results with thermo-acoustic instability characteristics. This study observed that when combustion instability occurred, flame vibrated cyclically, accompanied with the fluctuation of a recirculation zone. The fluctuation frequency of the recirculation zone was the same as the frequency of combustion instability, through which the fluctuation of the recirculation zone was

generated under combustion instability. It also was found that such a fluctuation in the recirculation zone causes fluctuations in the rate of mass flow and heat release within the recirculation zone, further functioning to generate and reinforce combustion instability.

Experimental results of the relation between inlet velocity and combustion instabilities in model gas turbine combustor. In our experimental conditions, two dominant mechanisms affect the rising combustion instability. Structural change is mainly related with mixture fluctuation and this is proven by the changing of flame angles. As a result, the combustion instability mechanism was specified in two ways: one is swirl number perturbation and the other is flame length fluctuation based on pressure gradient variation. Swirl number perturbation was experimentally proven by OH chemiluminescence results and the change in flow rate was well matched with the pressure gradients of the combustor. These two dominant mechanisms work to amplify heat release fluctuation and this feedback loop maintains combustion instability. It was also found that frequency shifting occurs in conditions of low fuel-air mixture velocity condition. Therefore, we performed mode and dynamic pressure analysis, and consequently we estimate that at condition of low velocity, there is another reason for the occurrence of combustion instability. This is because of phase delay of heat release and dynamic pressure in low fuel-air mixture velocity conditions. Therefore, we calculated Strouhal number and found a difference in those conditions. We concluded that fluid dynamical vortex frequency has major effects on the combustion of low velocity conditions, making it unstable.

From the results of inlet mixing section characteristics, this experiment observed two different modes of strong combustion instability frequencies, and it was found that both the frequency bands had a relation with the acoustic mode (Longitudinal mode, n = 1, 2) caused by the combustor length through amplitudes and phases measured by dynamic sensors located in the combustion chamber. Since a specific instability band frequency in which that combustion instability actually appears existed and since either the 1L or 2L modes were bands of acoustic mode likely to appear in case of combustion instability, it was found that the mean temperature (or equivalence ratio) and length of a combustion

chamber, which determine the acoustic frequency inside the combustion chamber, had an important influence on the phenomenon of combustion instability. The combustion instability phenomenon of the 1L mode observed in this experiment had a relation with the longitudinal mode of the combustor, and such a phenomenon of combustion instability is caused by the flame response characteristics while being coupled with heat release oscillation. This is also described in the previous researches on the existing gas turbine combustion instability. In the case of the combustion instability phenomenon where an instability mode is transited into a higher instability frequency, this experiment confirmed that it was a mode generated by the combination of the longitudinal mode of the combustor and the longitudinal mode of the inlet mixing section. When both the inlet mixing section and the combustion chamber had similar acoustic frequency domains, which correspond to n = 2 of the acoustical longitudinal mode, the combustion instability phenomenon was caused by the related frequency. It was also found that this phenomenon was more affected by the pressure oscillation from the fuel-air mixing section than from the combustion chamber.

The findings as follows were achieved through experimental research on the spray injection characteristics depending on the injection angle (forward, reverse) within the jets in a subsonic crossflow field of RQL combustor for reducing the NOx emissions. Through the experimental studies on canted injection, it was identified that the trajectory and the distance to the breakup point of the liquid column region are the function of the fuel/air momentum flux ratio (q), injection angle (θ), axial distance, penetration distance and the drag coefficient (C_D). The empirical formula of the trajectory and breakup length in the liquid column region by the injection angle was derived, and there generated the differences at constant value, the drag coefficient between the experimental equation of the liquid column trajectory on the forward injection which has a matching direction with the normal air-flow direction and that of the reverse injection.

These experimental results make it possible to infer that when an actual gas turbine is optimum designed. The combustion values such as v_{mix}, Φ, fuel and air mass flow rate are very important factor for study of combustion instability mechanism. Also, the swirl

vane angle, combustor and inlet mixing section geometries of a gas turbine should be optimally designed in addition to the optimal design of a combustion chamber by the flame oscillation. On the contrary, when combustion instability takes place, the combustor and inlet mixing section geometries are possible to create optimum control of combustion instability modes through the tuning of plenum or transient piece devices. Fig. 8.1 shows the relation between combustion instability mechanism and each chapter result of this study.

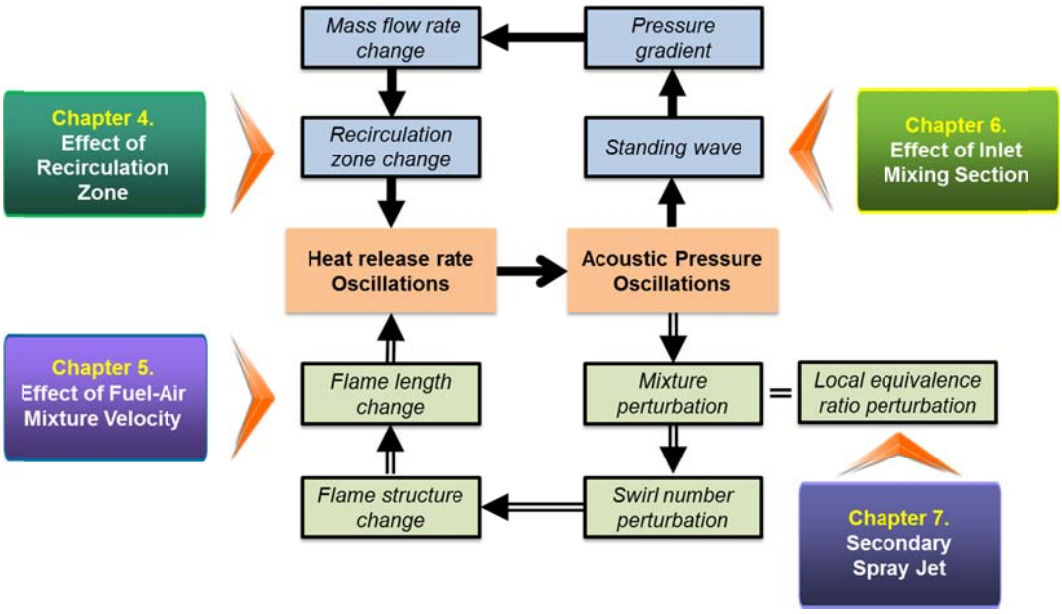

Fig. 8.1 Mechanism of combustion instability results from this study.

APPENDIX A

GE 7FA+e DLN-2.6 GAS TURBINE COMBUSTOR

A.1 Introduction of DLN-2.6 Combustor

The new utility gas turbine (GT) that often require compliance with NOx emissions as low as 2.5 ppm (5 mg/Nm^3) based on a combination of 9-ppm (18 mg/Nm^3) DLN technology coupled with 75% reduction Selective Catalytic Reduction (SCR) [1, 2, 3]. To suppress NOx levels to 9 ppm DLN combustors of many modern GTs must operate in lean premix mode near the lean blowout (LBO) limit, where the quantity of fuel in the air/fuel mix at the burner is barely sufficient to sustain combustion at low flame temperatures. The safe and reliable operation of modern combustors near the LBO requires a number of vital elements: (1) an in-depth understanding of the mechanisms that promote combustion stability at these extremely low fuel equivalence ratios, (2) precise manufacturing of key components with narrow design tolerances, (3) a reliable monitoring system to detect onset of instabilities in individual combustors and (4) protective passive or active control hardware and systems that can implement corrective actions such as changes in fuel splits or, in case of emergencies, Protective Load Shedding (PLS) or turbine trip. Obviously, PLS and turbine trips are not desirable events. Thus, operators often need to remain proactive in preventing onset of excessive pressure oscillations and combustion-induced vibrations and flame instabilities. The phenomenon of combustion instability has afflicted a wide range of ultra-low-NOx machines for a variety of reasons, including GE 7F, ABB 13E2 and GT24 and GT26, Siemens/Westinghouse 501F, and Siemens V64.3 and V84.3. Today, combustion instability is viewed as the major challenge facing the gas turbine industry.

The GE 7FA+e is a high-performance gas turbine for a power generation that has been developed by General Electric and has the generating capacity (P_{out}) of 180 MW. This gas turbine engine is composed of an Inlet Guide Vane (IGV) to control air flow rate, a 15-stage compressor, a 14 can-type combustor, and a 3-stage turbine. For a combined-

cycle thermal power generation, the GE 7FA+e gas turbine engine operates in connection with a starting motor, heat exchanger (heat-recovery steam generator or HRSG), and steam turbine. A Seo-Incheon power plant is located in the west side of Incheon city, South Korea. This electric power plant is a subsidiary company of WP (Korea Western Power Company) and operates 8ea GE 7FA+e gas turbines for a combine-cycle power generation. To reduce maintenance costs, the company is attempting to reduce NOx emission levels (involving a yellow plume; NO_2 flue gas) during the start-up mode and combustion vibration during the loading mode for the GE 7FA+e DLN-2.6 gas turbine combustor.

A.2 Operating Combustion Conditions of a DLN-2.6 Combustor

The GE 7FA+e gas turbine is controlled by a microprocessor-based MARK-Ⅵ as an operating system. For power generation, the gas turbine mode changes during a mode transfer operation from the starting mode (Mode 1) to the base mode (Mode 6AQ) at the speed of up to 3600 rpm of a turbine shaft rotation. However, the combustor has a critical operating section with high NOx levels and a high degree of combustion oscillation. At the beginning of operation at P_{out} = 20 ~ 45 MW (Mode 3), the NOx level increases, while at P_{out} = 40 ~ 45 MW (Mode 6B), the combustion vibration increased with the increase of output power. Both problems are minimized by optimizing the mode transfer. The main idea of GT tuning is to control the amount of fuel and air mass flow rate entering the combustors. Fuel to the DLN-2.6 combustor is staged to operate the machine over the entire load range. Burners are brought on in stages, starting at Full Speed No Load (FSNL) with the center burner only and turning on additional burners as load is increased. The staging is accomplished by using four fuel systems. Each fuel system consists of a different number of nozzles coupled together via a common manifold. These systems are used alone or in combination with one another to maintain fuel / air ratio within a desirable range in the reaction zone. The mode names reflect the number of

burners that are being fueled in that mode. The suffix Q in mode 6Q reflects the fact that quaternary fuel may be in use. Mode 6Q spans the load range for 9/9 ppm NOx / CO operation. The machine lights on the PM2 and PM1 circuits. Following ignition, the PM1 nozzles are turned off and the PM2 nozzles support combustion while the unit ramps to 95 percent speed. At 95 percent speed, the unit transfers from mode 2 to mode 1 for continued acceleration to full speed no load (FSNL) and leading to synchronization. At approximately 10 percent load, the PM2 manifold is turned back on (3 nozzles = mode 3) and continues until 25 percent load. At this transfer point, the PM2 manifold is switched off, with the PM3 manifold turned on for operation in mode 4 to 50 percent load. All nozzles are turned on to enter mode 6 or 6Q with quaternary. Originally, the system also used modes 5 or 5Q with the five outer nozzles in operation. However, this mode was eliminated to simplify the staging and controls strategies [4]. Fig. A.1 shows the strategy of fuel staging and the process of mode transfer from Mode 3 to Mode 6AQ in a GE 7FA+e gas turbine. Fig. A.2 shows the DLN2.6 fuel nozzle end cover downstream face with partial fairings. The nozzle has a plane orifice-type hole in a swirl vane and on the top of the nozzle. The choke orifice hole acts as an injector and acoustic barrier that prevents both the flow-oscillation effect on fuel injection and distribution in delivery lines and external disturbances from a reaction zone. The compressed air was supplied to a nozzle mount, and become partially premixed with fuel after delivery along the swirl vanes before combustion.

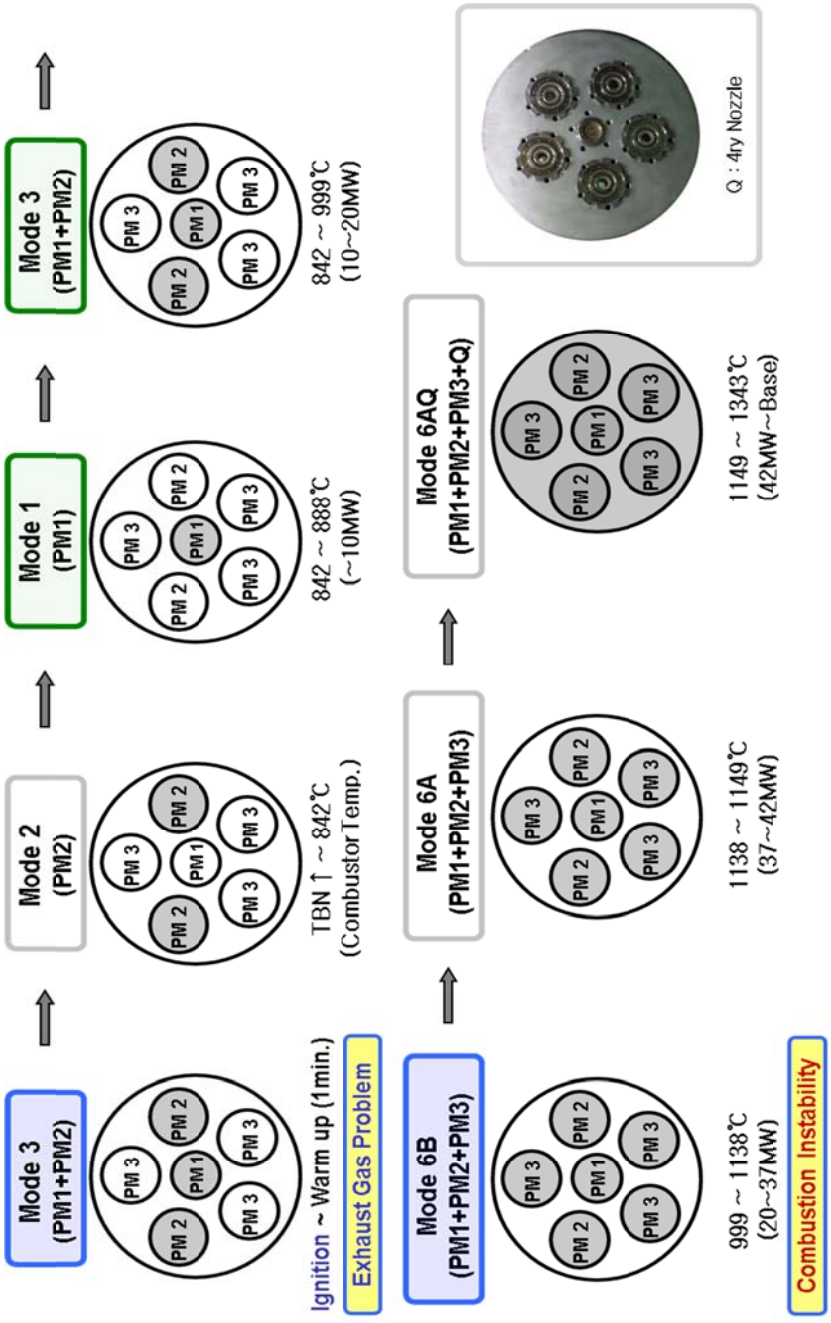

Fig. A.1 Fuel staging methods in GE 7FA+e DLN-2.6 combustor.

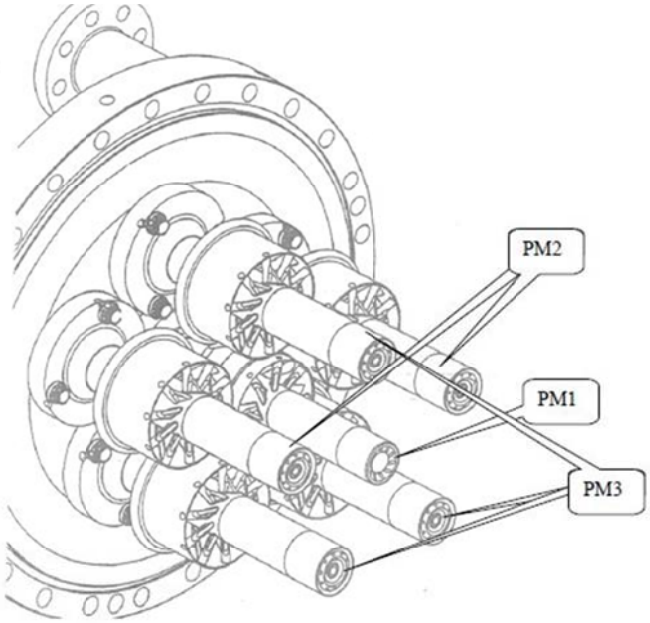

Mode 3:	PM1+PM2	Ignition to 18% speed
Mode 2:	PM2	18% to 95% speed
Mode 1:	PM1	95% speed to 10% load
Mode 3:	PM1+PM2	10% load to 25% load
Mode 4:	PM1+PM3	25% load to 50% load
(Originally, Mode 5:	PM2+PM3	transfer mode on start)
Mode 6 or 6Q:	PM1+PM2+PM3+(quaternary)	50% to 100% load

Fig. A.2 GE 7FA+e DLN 2.6 fuel nozzle end cover downstream face with partial fairings.

A.3 Measurement of Combustion Values

The main control elements of the GE DLN-2.6 gas turbine is the air mass flow rate affected by the opening of FSRSEL (Fuel Stroke Reference Selection) and IGV (Inlet Guide Vane) getting into each fuel nozzle at the time of changing the mode [5]. Therefore, MARK VI enables checking air and fuel mass flow rate by the desired output net power. All gas turbine plants in Korea Western Power Co. Ltd. at Seo-Incheon power plants were used to measure the property of a combustion value, dynamic pressure and exhaust

emission (NOx) levels while changing their outputs by 5～10 MW unit within the range of 20～60 MW. The total amount of fuel in the mode transfer varies linearly for outputs and the fuel quantity in each nozzle is known to be changed mainly by PM1 in Mode3, PM3 in Mode 6B, PM2 and 3 in Mode 6AQ. It is thought that such fuel quantities as PM1 in Mode3, PM3 in Mode 6B, and PM2/3 in Mode 6AQ will work as main elements to fit the optimum dynamic pressure and exhaust emission levels when tuning the burner.

A.4 Combustion Instability and NOx Emission Characteristics

EINOx (Emission Index of NOx) depends on the fuel-mass flow rate and the residence time for exposure to hot flow of more than 1800K, as exposure time is proportional to the flame volume and length [6]. To understand the optimum tuning of gas turbine, the exhaust emissions and frequency spectrum of dynamic pressure measured along with fluctuations in value of control constants per output. First, we identified characteristic growth of the quantity of thermal NOx formed by higher temperatures at the combustion chamber in Mode 3 than in other Modes. The dynamic pressure had a higher level in Mode 6B (30～45 MW) than in other Modes, and the characteristic frequency was close to 140Hz, outputs being kept at a 35～45MW range, with the magnitude of dynamic pressure reaching approximately 0.6 psi. This feature comes up as the fuel quantity in PM3 fuel nozzle shows a rapid change, and given that almost no change in characteristic frequency according to turbine exit temperature is made, dynamic pressure is regarded to have the reflection of the cold flow prior to combustion and the characteristics of the chamber geometry near the nozzle, instead of the impact of the combustion field. This constant frequency is evidence that the flow is not affected by combustion. In addition, the fuel mass flow rate for nozzle PM3 is significantly changed in Mode 6B (P_{out} = 40 ~ 45 MW). Therefore, the pressure fluctuation may be caused by cold flow, and occur in the plenum chamber between the compressor outlet and the combustor inlet. The peak frequency of 140 Hz is therefore thought to be revealed as a

resonance frequency for the plenum chamber of nozzle PM3.

The equation for bulk or Helmholtz mode is as follows;

$$f_H = \frac{c}{2\pi} \cdot \sqrt{\frac{A}{L_n \cdot V_p}} \qquad \left(where,\ c = \sqrt{\gamma RT}\right) \tag{A.1}$$

Where, A is the nozzle neck area, L_n is the nozzle neck length, and V_p is the plenum chamber volume [7]. Hubbard and Dowling [8] used a numerical calculation to study the acoustic resonances effect on an industrial gas turbine combustion system. These researchers reported that the resonance in a plenum chamber or in the delivery lines affects the local mixture of fuel and air around nozzles. The oscillation of the local mixture fraction influences the turbulent burning velocity and becomes one cause of combustion instability [9]. The plenum resonance frequency can be reduced by a Helmholtz resonator attached to a plenum chamber; this is a significant factor to keep in mind when designing a combustion system.

APPENDIX B
DEVELOPMENT OF DYNAMIC PRESSURE TOOLKIT

The main purpose of a stationary gas turbine is to generate power, and diagnostics will only be implemented when they are absolutely necessary for reliable power production. That is why optical access is only available as a safeguard to check for the presence of the flame, and not for detailed study. However, monitoring of the combustion process and related phenomena in large gas turbines though still limited is increasingly being recognized as a necessary part for safely operating ultra-low-NOx power turbines.

Because of cost and other maintenance needs, combustion dynamic sensors are typically mounted on modern GE, Alstom, and S/W gas turbines only when required for intermittent measurement and burner tuning. GE performs tuning in the commission stage and after a major overhaul. For these intermittent tuning requirements, a permanent monitoring system may not be required. However, GE also offers remote monitoring, diagnostic and tuning of modern DLN 2.6 combustors with the permanent installation of a monitoring system. In most large Siemens and Alstom gas turbines, on-line dynamic pressure transducers are employed to generate an alarm if acoustic amplitudes exceed a preset limit, thus preventing damage to structural components. For purpose of completeness, this subsection presents technically available options to monitor combustion instabilities, although the industry relies almost exclusively on piezo-electric pressure transducers, which can pick up pressure pulsations over a wide range of frequencies pertinent to GT combustors. Sensors available to monitor flame stability under extreme lean combustion conditions can be divided into three main groups. Pressure sensors that monitor the frequency and amplitude of pressure pulsations caused by unstable combustion in enclosed chambers. These are Piezo-resistive transducers, piezo-electrical transducers and accelerometers [10].

Figure B.1 shows the dynamic pressure sensor module for GE stationary gas turbine

combustor. To measure combustion vibration, we developed a dynamic pressure measurement device which was composed of a sampling probe, pressure transducer (102A05, PCB Piezotronics Co., Depew, NY, USA), a signal conditioner (482A22, PCB Piezotronics Co.), and a data acquisition (DAQ) board (USB-6218, NI Co., Austin, TX, USA).

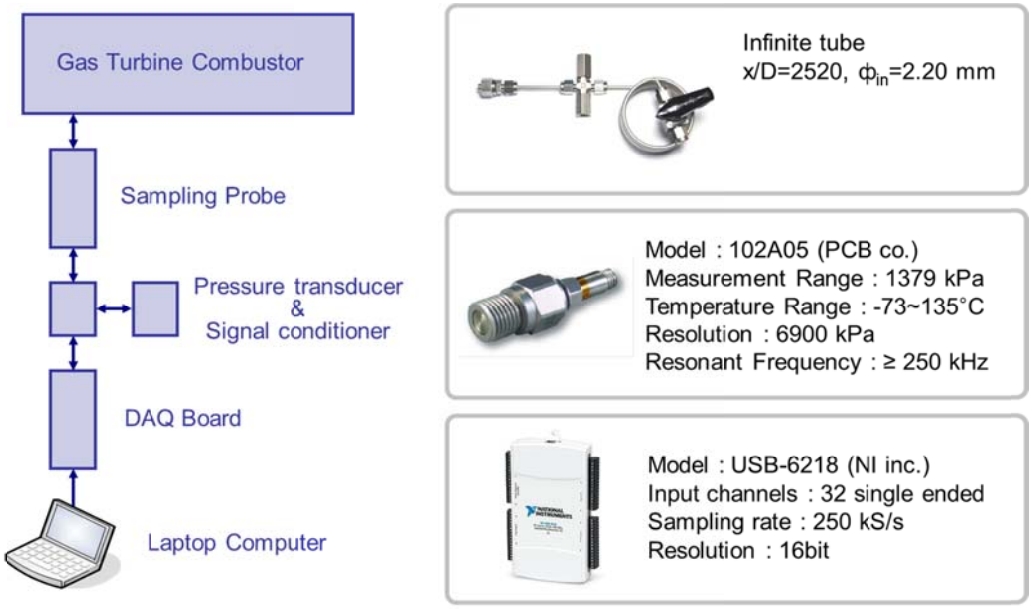

Fig. B.1 Dynamic pressure sensor module for GE stationary gas turbine combustor.

Fig. B.2 shows the experimental setup for the measurement of dynamic pressure at GE stationary gas turbine. The measurement system could detect dynamic pressure in a range of 10~10000 Hz by connecting with a gas turbine combustor. The sampling tube was designed as an infinite cylindrical tube to minimize the dynamic pressure loss at a certain frequency; this tube acts as a Helmholtz resonator [11]. The ratio of length (l) to inner diameter (d) for a long-tube type of probe was greater than l/d = 2500 ~ 3000, providing the advantage of reduction of wave reflection and interruption. To make the size compact, the probe end was rolled as a pig tail. In addition, the transducer was

mounted on the side of the infinite tube and located as close as possible near a combustor wall to maximize the signal intensity. According to Rea et al. [12], because of the acoustic cavity effect, the location of l/d = 20 from a combustor wall is suitable for the dynamic pressure measurement.

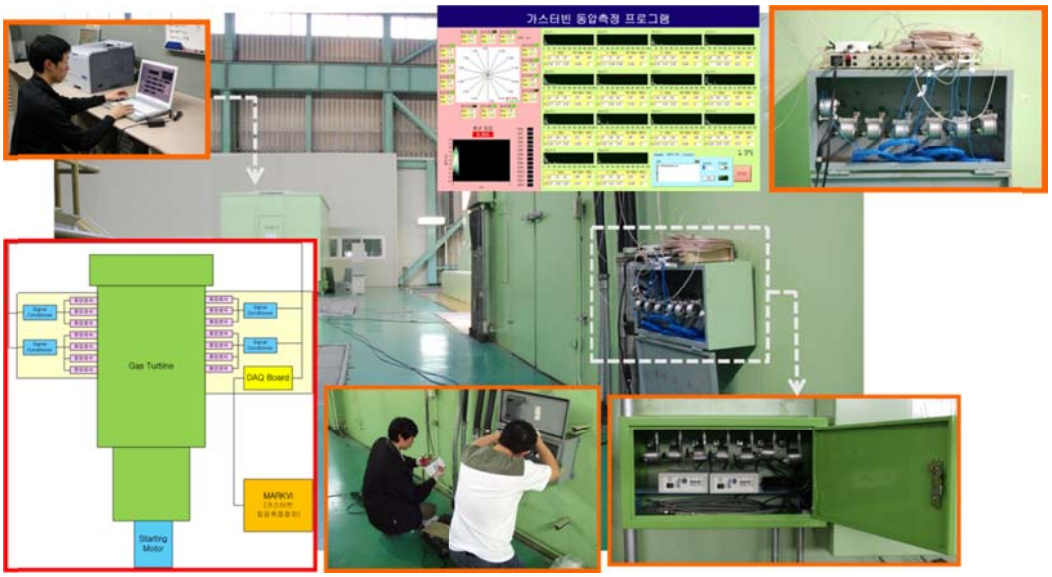

Fig. B.2 Experimental setup for the measurement of dynamic pressure at GE stationary gas turbine.

Appendix C
OPTIMUM COMBUSTION TUNING

It is helpful for a more fundamental understanding of combustion conditions to check out the equivalence ratio in each nozzle (PM 1, PM 2, PM 3, Quaternary) along with the trends in the dynamic pressure distribution per output and exhaust emissions in DLN-2.6. If the Φ is 1, complete combustion takes place as it gets close to the theoretical air-fuel ratio. And if below 1, lean combustion takes place as the fuel gets a smaller portion in the fuel-air mixture, and conversely, rich combustion occurs as the fuel gets a higher portion. Table C.1 represents the variation in the control constant of a fuel nozzle changed in each mode as the combustion temperature shows an increase. This way, the fluctuations in flow rate of a fuel nozzle in each mode were able to be identified and a flame structure could be predicted. Table C.1 could identify that in Mode 3 the Φ was relatively high near the PM1 fuel nozzle, enough to impose impacts on the characteristics of exhaust emissions. In Mode 6B the equivalence ratio near the PM3 fuel nozzle noticeably dropped to induce heat release fluctuations by lean burn and caused combustion instability to occur in the combustion chamber. In general, the reactant attains complete combusting at a stoichiometric conditions (Φ = 1). However, from the point of view NOx emissions, the thermal NOx production is maximized due to the combustion temperature approaching adiabatic temperature [13]. In Φ < 1, the flame utilizing lean premixed fuel has the advantage of low NOx production, and the disadvantage of conferring a potential risk for combustion instability. At Φ > 1, the rich premixed-flame is available for flame stabilization, while it is disadvantageous to NOx reduction. So, The fuel rate of PM1 nozzle decrease as the NOx emissions level was decrease around 25 ppm in GE combustor. Hence, in Mode3 with a problem of exhaust emissions when tuning the burner, the fuel nozzle constant dropped by 25～30 ppm, and in Mode 6B the pressure amplitude was reduced by about 52% compared to the existing one as the PM 2 constant value shows an increase, which leads to experiencing the optimal combustion control.

Table C.1 Tuning the equivalence ratio of each fuel nozzle.

Combustion mode	Nozzle / Power	PM1	PM2	PM3	Quat.	Total
Mode 3	Negative (5)	**0.487**	0.359	0	0	0.196
	20 MW	**0.509**	0.345	0	0	0.195
	Positive (5)	**0.538**	0.329	0	0	0.195
	Negative (5)	**0.621**	0.370	0	0	0.222
	30 MW	**0.643**	0.352	0	0	0.220
	Positive (5)	**0.700**	0.337	0	0	0.223
Mode 6B	Negative (5)	0.378	0.399	**0.102**	0	0.247
	40 MW	0.380	0.386	**0.119**	0	0.252
	Positive (5)	0.379	0.383	**0.123**	0	0.252
	Negative (5)	0.373	0.416	**0.120**	0	0.261
	45 MW	0.372	0.389	**0.148**	0	0.266
	Positive (5)	0.375	0.360	**0.155**	0	0.260
Mode 6AQ	Negative (5)	0.373	**0.115**	0.346	0.016	0.273
	50 MW	0.375	**0.119**	0.347	0.013	0.276
	Positive (5)	0.376	**0.124**	0.347	0.016	0.277
	Negative (5)	0.385	**0.176**	0.338	0.019	0.292
	60 MW	0.386	**0.174**	0.340	0.017	0.292
	Positive (5)	0.383	**0.170**	0.338	0.013	0.290

Prepared was the optimal combustion control program able to analyze real-time data by each mode from the gas turbine engine showing a rise in output up to the base mode through the real-time receipt of the data on the combustion property of MARK VI in GE 7FA+e DLN-2.6, and through the researchers added who got the values of dynamic pressure variation in measurement module for dynamic/static pressure. (See Fig. C.1) [14] The empirical equation for combustion control constants was obtained through the connection with the constant value of fuel nozzles for optimal combustion control using the combustion property values acquired from the tuning experiment (about 50 times) with several gas turbine burners. This program presents the user friendly combustion environments where the combustor can operate under optimal conditions, by conducting a swift analysis into the equivalence ratio, exhaust emissions, dynamic pressure and control constants in the troubled mode. This program also enables providing types of fuel nozzles to control in each mode and optimal constant values. Furthermore, it can also present how the gas turbine combustor is operating in each situation by monitoring the combustion conditions across the mode area.

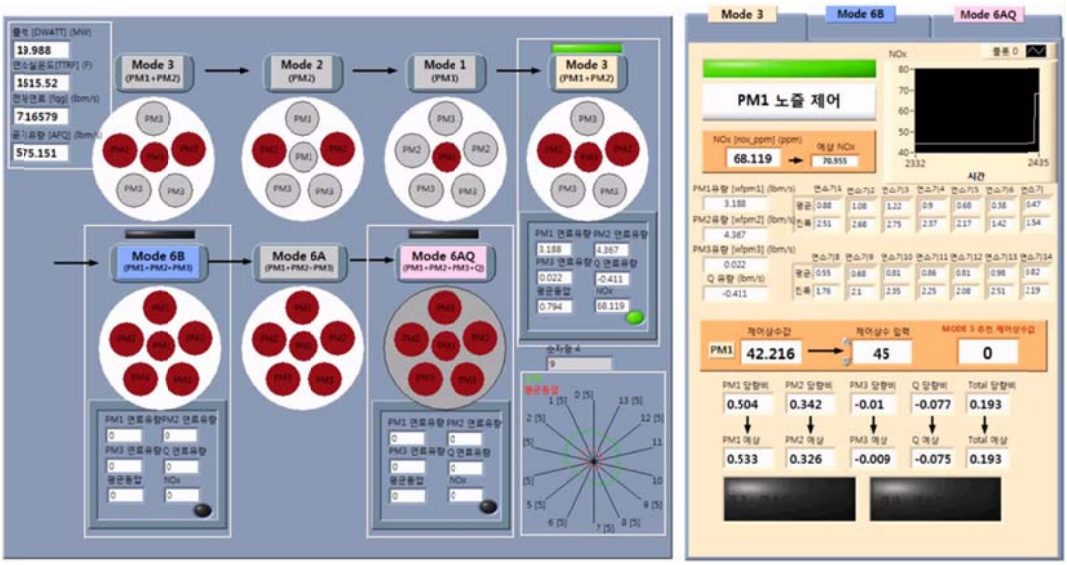

Fig. C.1 Optimum combustion control program in GE gas turbine combustor.

BIBLIOGRAPHY

Chapter 1 Introduction

[1] M.P. Boyce, Gas Turbine Engine, Handbook-3rd ed., Gulf Professional Publishing, New York, 2001, pp. 47.

[2] T.C. Lieuwen, Investigation of Combustion Instability Mechanisms in Premixed Gas Turbines, PhD. thesis, Georgia Institute of Technology, USA, pp. 1-52. 1999.

[3] A.H. Lefebvre, Gas Turbine Combustion-2nd ed., Taylor and Francies, USA, 1999, pp. 364.

[4] C.O. Peterson, W.A. Sowa, G.S. Samuelsen, Performance of a Model Rich Burn-Quick Mix-Lean Burn Combustor at Elevated Temperature and Pressure, NASA Report CR-2002-211992, University of California, USA, pp. 1-19, 2002.

[5] J.W.S. Rayleigh, The Theory of Sound, Nabu Press, New York, Vol. 2, 1945, pp. 226.

[6] N. Syred, J.M. Beer, Combustion in Swirling Flows. A Review, Combust. Flame, 22(2) (1974) 143-201.

[7] T. Poinsot, C.L. Chatellier, S. Candel, E. Esposito, Experimental Determination of the Reflection Coefficient of a Premixed Flame in a Duct, J. Sound Vib., 107 (1986) 265–278.

[8] C. Paschereit, E. Gutmark, W. Weisenstein, Excitation of Thermo-acoustic Instabilities by the Interaction of Acoustics and Unstable Swirling Flow, AIAA J. 38 (2000) 1025–1034.

[9] N. Tran, S. Ducruix, T. Schuller, Damping Combustion Instabilities with Perforates at the Premixer Inlet of a Swirled Burner, Proc. Combust. Inst., 32 (2009) 2917–2924.

[10] M.R. Bothien, J.P. Moeck, A. Lacarelle, C.O. Paschereit, Time Domain Modelling and Stability Analysis of Complex Thermo-acoustic Systems, J. Power and Energy, 221(5) (2007) 657-668

[11] J. Oh, M.-K. Kim, Y. Yoon, The Tuning Methodology of a GE 7FA + e DLN-2.6 Gas

Turbine Combustor, Appl. Therm. Eng., 36 (2012) 14-20.

[12] T. Schuller, D. Durox, S. Candel, Self-induced Combustion Oscillations of Laminar Premixed Flames Stabilized on Annular Burners, Combust. Flame, 135 (2003) 525–537.

[13] N. Noiray, D. Durox, T. Schuller, S. Candel, Self-induced Instabilities of Premixed Flames in a Multiple Injection Configuration, Combust. Flame, 145 (2006) 435–446.

[14] H. Johnston, Reduction of Stratospheric Ozone by Nitrogen Oxide Catalysts from Supersonic Aircraft Exhaust, Science, 173 (1971) 517-521.

[15] K. Yamagishi, M. Nozawa, T. Yoshie, T. Tokumoto, Y. Kakegawa, A Study of NOx Emissions Characteristics in Two-Stage Combustion, 15th Symposium on Combustion, The Combustion Institute, 15(1) (1975) 1157-1166.

[16] J.M. Beer, M.T. Jacques, W.F. Farmayan, A.K. Gupta, S. Hanson, Reduction of NOx and Solid Emissions By Staged Combustion of Coal Liquids Fuels, 19th Symposium on Combustion, The Combustion Institute, (1982) 1301-1309.

[17] M. Sadakata, Y. Fujioka, D. Kunii, Effects of Air Preheating on Emissions of NO, HCN, and NH_3 from Two-Stage Combustion, 18th Symposium on Combustion, The Combustion Institute, (1981) 65-72.

[18] J. Tyndall, Sound, Appleton & Company, New York, 1915

[19] G.J. Bloxsidge, A.P. Dowling, N. Hooper, P.J. Langhorne, Active Control of an Acoustically Driven Combustion Instability, Journal of Theoretical and Applied Mechanics, 6 (1987) 161-175.

[20] A.A. Putnam, Combustion Driven Oscillations in Industry, American Elsevier Publishing Company, USA, 1971.

[21] A.P. Dowling, Nonlinear Self-excited Oscillations of a Ducted Flame, J. Fluid Mech., 346 (1997) 271−290.

[22] G.J. Bloxsidge, A.P. Dowling, N. Hooper, P.J. Langhorne, Active Control of Reheat Buzz, AIAA J., 26 (7) (1989) 783-790

[23] J.W.S. Rayleigh, The Explanation of Certain Acoustical Phenomena, Nature, 18(455) (1878) 319-321.

[24] F.E.C. Culick, Combustion Instabilities in Liquid Rocket Engines : Fundamentals and Control, ONERA, 2002.

[25] J.C. Oefelein, V. Yang, Comprehensive Review of Liquid-Propellant Combustion Instabilities in F-1 Engines, Journal of Propulsion and Power, 9 (1993) 657-677.

[26] B.T. Zinn, T.C. Lieuwen, Combustion Instabilities : Basic Concepts - Combustion Instabilities in Gas Turbine Engines : Operational Experience, Fundamental Mechanisms, and Modeling, Progress in Aeronautics and Aeronautics Series, AIAA 210 (2005) Chapter1.

[27] F.S. Blomshield, Historical Perspective of Combustion Instability in Motors: Case Studies, AIAA J., (2001) 2001-3875

[28] F.E.C. Culick, Combustion Instabilities in Liquid-Fueled Propulsion Systems - An Overview, AGARD 72B Specialists' Meeting of the Propulsion and Energetics Panel AGARD CP 450, 1977.

[29] K.R. McManus, T. Poinsot, S.M. Candel, A Review of Active Control of Combustion Instabilities, Progress in Energy and Combustion Science, 19(1) (1993) 1-30.

[30] S. Ducruix, T. Schuller, D. Durox, S. Candel, Combustion Dynamics and Instabilities : Elementary Coupling and Driving Mechanisms, Journal of Propulsion and Power, 19(5) (2003) 722-734.

Chapter 2 Experimental Background

[1] A.M. Annaswamy, M. Fleifil, J.P. Hathout, A.F. Ghoniem, Impact of Linear Coupling on the Design of Active Controllers for Thermoacoustic Instability, Combustion Science and Technology, 128 (1997) 131-180.

[2] A.P. Dowling, J.E. Efowcs, Sound and Sources of Sound, Ellis Horwood Limited, West Sussex, England, 1983.

[3] A.D. Pierce, Acoustics : An introduction to Its Physical Principles and Applications, McGraw-Hill, USA, 1981.

[4] L. Debnath, Nonlinear Partial Differential Equations for Scientists and Engineers,

Birkhauser, USA, 1997.

[5] B.T. Zinn, Pulsating Combustion : Advanced Combustion Methods, Academic Press Inc. LTD., England, 1986.

[6] M. Fleifil, A.M. Annaswamy, Z. Ghoniem, A.F. Ghoniem, Response of a Laminar Premixed Flame to Flow Oscillations : A Kinematic Model and Thermoacoustic Instability Result, Combustion and Flame, 106 (1996) 487-510.

[7] A.A. Peracchio, W. Proscia, Nonlinear Heat Release/Acoustic Model for Thermoacoustic Instability in Lean Premixed Combustors, In ASME Gas Turbine and Aerospace Congress, Sweden, 1998.

[8] P.M. Anacleto, E.C. Fernandes, S.I. Shtork, Swril Flow Structure and Flame Characteristics in a Model Lean Premixed Combustor, Combust. Sci. and Tech., 175(8) (2003) 1369-1388.

[9] Y. Huang, V. Yang, Dynamics and Stability of Lean-Premixed Swirl-Stabilized Combustion, Progress in Energy and Combustion science 35(4) (2009) 293-364.

[10] E.M. Greitzer, C.S. Tan, M.B. Graf, Internal Flow : Concepts and Applications, Cambridge University Press, England, 2004.

[11] R.L. Murray, Laser Doppler Anemometry measurements in a Turbulent, Premixed, Natural Gas/Air combustor, Brigham Young University, USA, 1998.

[12] P.-K. Wu, K.A. Kirkendall, R.P. Fuller, A.S. Najad, Spray Structures of Liquid Jets Atomized in Subsonic Crossflows, J. Propul. Power 14(2) (1998) 173-182.

[13] R.P. Fuller, P.-K. Wu, K.A. Kirkendall, A.S. Najad, Effects of Injection Angle on Atomization of Liquid Jets in Transverse Airflow, AIAA Journal 38(1) (2000) 64-72.

[14] J.A. Schetz, E.A. Kush, P.B. Joshi, Wave Phenomena in Liquid Jet Breakup in a Supersonic Crossflow, AIAA Journal, 18(7) (1980) 774-778.

[15] P.-K. Wu, K.A. Kirkendall, R.P. Fuller, A.S. Najad, Breakup Processes of Liquid Jets in Subsonic Crossflows, J. Propul. Power 13(1) (1997) 64-73.

Chapter 3 Experimental Facility and Techniques

[1] N. Syred, J.M. Beer, Combustion in Swirling Flows : A Review, Combust. Flame, 22(2) (1974) 143-201.

[2] R.S.S. James, On-line Cmbustion Mnitoring on Dry Low NOx Industrial Gas Turbines., Measurement Science & Technology, 14(7) (2003) 1123-1130.

[3] H. Zinn, M. Habermann, Developments and Experiences with Pulsation Measurements for Heavy-Duty Gas Turbines, ASME Paper, 1 (2007) 639-648.

[4] Min-Ki Kim, Jisu Yoon, Youngbin Yoon, Method of analyzing combustion state, Patent, NO.12-101799. Republic of Korea, 2012.

[5] A.G. Gaydon, The Spectroscopy of Flames, Springer, Halsted Press, USA, 1974.

[6] P.H. Paul, H.N. Najm, Planar Laser-Induced Fluorescence Imaging of Flame Heat Release, Proc. Combust. Inst., 27 (1998) 43-50.

[7] B.D. Stojkovic, T.D. Fansler, M.C. Drake, V. Sick, High-Speed Imaging of OH* and Soot Temperature and Concentration in a Stratified-Charge Direct-Injection Gasoline Engine, Proc. Combust. Inst. 30 (2005) 2657-2665.

[8] A.G. Gaydon, The Spectroscopy of Flames 2nd ed., Campman and Hall, UK, 1974, pp. 1-13.

[9] A.G. Gaydon, H. G. Wolfhard, Flames : Their Structure, Radiation, and Temperature, Chapman and Hall, London, 1978.

[10] W. Pun, S.L. Palm, F.E.C. Culick, Combustion Dynamics of an Acoustically Forced Flame, Combust. Sci. Tech. 175 (2003) 499-521.

[11] K.H. Yu, A.C. Trouve, J.W. Daily, Low Frequency Pressure Oscillations in a Model Ramjet Combustor, J. Fluid Mech. 232 (1999) 47−72.

[12] J.P. Hathout, A.M. Annaswamy, M. Fleifil, A.F. Ghoniem, Model-Based Active Control Design for Thermoacoustic Instability, Combustion Science and Technology, 132 (1998) 99-138.

[13] H.N. Najm, P.H. Paul, C.J. Mueller, P.S. Wyckoff, On the Adequacy of Certain Experimental Observables as Measurements of Flame Burning Rate, Combust. Flame,

113 (3) (1998) 312-332.

[14] N. Docquier, F. Lacas, S. Candel, Closed-loop Equivalence Ratio Control of Premixed Combustors using Spectrally Resolved Chemiluminescence Measurements, Proc., Combust. Inst., 29 (1) (2002) 139-145.

[15] V.N. Nori, J.M. Seitzman, CH∗ Chemiluminescence Modeling for Combustion Diagnostics, Proc., Combust. Inst., 32(1) (2009) 895-903.

[16] P.G. Aleiferis, Y. Hardalupas, A.M.K.P. Taylor, K. Ishii, Y. Urata, Flame Chemiluminescence Studies of Cyclic Combustion Variations and Air-to-Fuel Ratio of the Reacting Mixture in a Lean-Burn Stratified-Charge Spark-Ignition Engine, Combust. Flame, 136(1-2) (2004) 72-90.

[17] T.M. Muruganandam, B.-H. Kim, M.R. Morrell, V. Nori, M. Patel, B.W. Romig, J.M. Seitzman, Optical Equivalence Ratio Sensors for Gas Turbine Combustors, Proc., Combust. Inst. 30(1) (2005) 1601-1609.

[18] C.S. Panoutsos, Y. Hardalupas, A.M.K.P. Taylor, Numerical Evaluation of Equivalence Ratio Measurement using OH* and CH* Chemiluminescence in Premixed and Non-Premixed Methane-Air Flames, Combust. Flame, 156(2) (2009) 273-291.

[19] K.T. Kim, J.G. Lee, H.J. Lee, B.D. Quay, D.A.Santavicca, Response of Partially Premixed Flame to Acoustic Velocity and Equivalence Ratio Perturbations, Combust. Flame 157(9) (2010) 1731-1744.

[20] D. Kim, J.G. Lee, B.D. Quay, D.A. Santavicca, Effect of Flame Structure on the Flame Transfer Fuction in a Premixed Gas Turbine Combustor, J. Eng. Gas Turb Power, 132 (2010) 021502-1-021502-7.

[21] M. Raffel, C.E. Willert, J. Kompenhans, Particle Image Velocimetry, Springer, USA, 1998.

[22] P. Le Gal, N. Farrugia, D.A. Greenhalgh, Laser Sheet Dropsizing of Dense Sprays, Opt. Laser Technology, 31 (1999) 75-83.

[23] D.G. Talley, T.S. Thamban, V.G. McDonell, G.S. Samuelsen, Laser Sheet Visualization of Spray Structure Recent Advances in Spray Combustion : Spray

Combustion Measurements and Model Simulation, Progress in Astronautics and Aeronautics, 2 (1995) 113-141.

[24] K. Jung, H. Koh, Y. Yoon, Assessment of PLLIF Measurement for Spray Mass Distribution of Like-Doublet Injector, Measurement Science and Technology, 14(8) (2003) 1387-1395.

Chapter 4 Swirl Stabilized Flame Structure and Recirculation Zone

[1] Y.S.H. Najjar, Efficient use of Energy by Utilizing Gas Turbine Combined Systems, Appl. Therm. Eng., 21 (2001) 407-438.

[2] G. Kelsall, C. Troger, Prediction and Control of Combustion Instabilities in Industrial Gas Turbines, Appl. Therm. Eng., 24 (2004) 1571-1582.

[3] N.H. Afgan, M.G. Carvalho, P.A. Pilavachi, A. Tourlidakis, G.G. Olkhonski, N. Martins, An Expert System Concept for Diagnosis and Monitoring of Gas Turbine Combustion Chambers, Appl. Therm. Eng., 26 (2006) 766-771.

[4] T.J. Poinsot, A.C. Trouve, D.P. Veynante, S.M. Candel, E.J. Esposito, Vortex-Driven Acoustically Coupled Combustion Instabilities, J. Fluid Mech., 177 (1987) 265−292.

[5] T. Lieuwen, K. McManus, That Elusive Hum, Mechanical Engineering, 2002.

[6] A.H. Lefebvre, Gas Turbine Combustion-2nd ed, Taylor & Francies, Philadelphia, 1999, pp.364

[7] P. Palies, D. Durox, T. Schuler, S. Candel, Acoustic–Convective Mode Conversion in an Aerofoil Cascade, J. Fluid Mech. 672 (2011) 545−569.

[8] A. Huber, W. Polifke, Dynamics of Practical Premixed Flames, part II : Identification and Interpretation of CFD Data, Int. J. Spray Combust. Dynamics, 1 (2009) 229−249.

[9] T. Lieuwen, B.T. Zinn, The Role of Equivalence Ratio Oscillations in Driving Combustion Instabilities in Low NOx Gas Trubines, Proc. Combust. Inst., 27 (1998) 1809-1816.

[10] K.K. Venkataraman, D.A. Satavicca, Mechanism of Combustion Instability in a Lean Premixed Dump Combustor, J. Propul. Pow., 15(6), (1999) 909-918.

[11] K.T. Kim, S. Hochgreb, The Nonlinear Heat Release Response of Stratified Lean-Premixed Flames to Acoustic Velocity Oscillations, Combust. Flame, 158 (2011) 2482−2499.

[12] N.A. Worth, J.R. Dawson, Cinematographic OH-PLIF Measurements of Two Interacting Turbulent Premixed Flames with and Without Acoustic Forcing, Combust. Flame, 159 (2012) 1109−1126.

[13] T. Lieuwen, Y. Neumeier, Nonlinear Pressure Heat Release Transfer Function Measurement in a Premixed Combustor, Proc. Combust. Inst., 29 (2002) 99-105.

[14] B.D. Bellows, M.K. Bobba, A. Forte, J.M. Seitzman, B.D. Bellows, T.Lieuwen, Flame Transfer Function Saturation Mechanisms in a Swirl-Stabilized Combustor, Proc. Combust. Inst., 31 (2007) 3181-3188.

[15] C. Paschereit, E. Gutmark, W. Weisenstein, Excitation of Thermo-acoustic Instabilities by the Interaction of Acoustics and Unstable Swirling Flow, AIAA J., 38 (2000) 1025–1034.

[16] T. Schuller, D. Durox, S. Candel, Self-induced Combustion Oscillations of Laminar Premixed Flames Stabilized on Annular Burners, Combust. Flame., 135 (2003) 525–537.

[17] A. Birbaud, S. Ducruix, D. Durox, S. Candel, The Nonlinear Response of Inverted “V” Flames to Equivalence Ratio Nonuniformities, Combust. Flame, 154 (2008) 356−367.

[18] A.X. Sengissen, J.F. Van Kampen, R.A. Huls, G.G.M. Stoffels, J.B.W. Kok, T.J. Poinsot, LES and Experimental Studies of Cold and Reacting Flow in a Swirled Partially Premixed Burner with and Without Fuel Modulation, Combust. Flame, 150(1) (2007) 40−53.

[19] U. Stopper, M. Aigner, M. Stohr, I.S. Kim, Flow Field and Combustion Characterization of Premixed Gas Turbine Flames by Planar Laser Techniques, J. Eng. Gas Turb. Power., 131(2) (2009) 021504-1-021504-8.

[20] P.M. Anacleto, E.C. Fernandes, S.I. Shtork, Swirl Flow Structure and Flame Characteristics in a Model Lean Premixed Combustor, Combust. Sci. and Tech., 175(8)

(2003) 1369-1388.

[21] P. Weigan, W. Meier, Investigations of Swirl Flames in a Gas Turbine Model Combustor Internal Flow Field, Structures, Temperature, and Species Distributions, Combust. Flame., 144 (2006) 225-236.

[22] P. Petersson, J. Olofsson, C. Brackman, H. Seyfried, J. Zetterberg, M. Richter, M. Aldén, M.A. Linne, R.K. Cheng, A. Nauert, D. Geyer, A. Dreizler, Simultaeous PIV/OH-PLIF, Rayleigh Thermometry/OH-PLIF and Stereo PIV Measurements in a Low-Swirl Flame, Applied Optics., 46(19) (2007) 3928-3936.

[23] J. Cho, T. Lieuwen, Laminar Premixed Flame Response to Equivalence Ratio Oscillations, Combust. Flame, 140 (2005) 116−129..

[24] D.G. Lilley, Swil Flows in Combustion: A Review, AIAA J., 15(8) (1977) 1063-1078.

[25] M. Raffel, C.E. Willert, J. Kompenhaus, Partcle Image Velocimetry: A particle Guide. Springer-Verlag Berlin Heidelberg, Germany, 1998, pp.3-8.

[26] P.O. Hedman, T.H. Fletcher, G.W. Timothy, Observation of Flame Behavior in a Laboratory-scale Premixed Natural Gas/Air Gas Turbine Combustor from Planar Laser Induced Fluorescence Measurements of OH, Laser Doppler Anemometer Velocity Measurements, and Coherent Anti-stokes Roman Spectrometer Temperature Measurements, J. Eng. Gas Turbines Power., 127 (2005) 724-739.

Chapter 5 Effect of Fuel-Air Mixture Velocity

[1] R. Balachandran, B. Ayoola, C. Kaminski, A. Dowling, E. Mastorakos, Experimental Investigation of the Nonlinear Response of Turbulent Premixed Flames to Imposed Inlet velocity Oscillations, Combust. Flame, 143 (2005) 37−55.

[2] M. Stohr, I. Boxx, C. Carter, W. Meier, Dynamics of Lean Blowout of a Swirl-Stabilized Flame in a Gas Turbine Model Combustor, Proc. Combust. Inst., 33 (2011) 2953-2960.

[3] A.M. Steinberg, I. Boxx, M. Stohr, C. Carter, W. Meier, Flow-Flame interactions causing Acoustically Coupled Heat Release Fluctuations in a Thermo-Acoustically

Unstable Gas Turbine Model Combustor, Combust. Flame, 157 (2010) 2250-2266

[4] M. Stohr, R. Sadanandan, W. Meier, Experimental Study of Unsteady Flame Structures of an Oscillating Swirl Flame in a Gas Turbine Model Combustor, Proc. Combus. Inst., 32 (2009) 2925-2932

[5] P. palies, D. Durox, T. Schuller, S. Candel, The Combined Dynamics of Swirler and Turbulent Premixed Swirling Flames, Combust. Flame, 157(9) (2010) 1698-1717.

[6] P. palies, D. Durox, T. Schuller, P. Morenton, S. Candel, Dynamics of premixed Confined Swirling Flames, C.R.Mecanique, 337 (2009) 395-405

[7] M. Kim, Y. Choi, J. Oh, Y. Yoon, Flame-Vortex Interaction and Mixing Behaviors of Turbulent Non-Premixed Jet Flames under Acoustic Forcing, Combust. Flame, 156(12) (2009) 2252-2263.

[8] D.G. Lilley, Swil Flows in Combustion: A Review, AIAA J., 15(8) (1977) 1063-1078.

[9] N. Syred, J.M. Beer, Combustion in Swirling Flows. A Review, Combust. Flame, 22(2) (1974) 143-201.

[10] N. Bouvet, C. Chauveau, I. Gökalp, S.Y. Lee, R.J. Santoro, Characterization of Syngas Laminar Flames using the Bunsen Burner Configuration, Int. J. Hydrogen Energy, (36) (2011) 992-1005.

[11] C.J. Dasch, One Dimensional Tomography : a Comparison of Abel, Onion-Peeling, and Filtered Back Projection Methods, Applied Optics, 31(8) (1992) 1146-1151.

[12] C. Külsheimer, H. Büchner, Combustion Dynamics of Turbulent Swirling Flames, Combust. Flame, 131(2) (2002) 70-84.

[13] M. Escudier, Prog. Vortex Breakdown: Observation and explanations, Prog. Aerosp. Sci. 25 (1988) 189-229.

[14] V.K. Khanna, A Study of the Dynamics of Laminar and Turbulent Fully and Partially Premixed Flames, Ph.D. Dissertation, Dept. of Mechanical Engineering, The Virginia Polytechnic Institute and State University, Blacksburg, VA, USA, 2001.

[15] J.P. Hathout, M. Fleifil, A.M. Annaswamy, A.F. Ghoniem, Heat Release Actuation for Control of Mixture-Inhomogeniety-Driven Combustion Instability, Proceedings of the Combustion Institute, 28 (2000) 721-730.

Chapter 6 Effect of Fuel-Air Mixing Section

[1] T. Lieuwen, B.T. Zinn, The Role of Equivalence Ratio Oscillations in Driving Combustion Instabilities in Low NOx Gas Trubines, Proc. Combust. Inst. 27 (1998) 1809-1816.

[2] T. Gabrielson, Acoustic Data Measurements and Analysis, Lecture Notes, Graduate Program in Acoustics, The Pennsylvania State University, University Park, PA, 2009.

[3] W. Meier, X.R. Duan, P. Weigand, Reaction Zone Structures and Mixing Characteristics of Partially Premixed Swirling CH_4/air Flames in a Gas Turbine Model Combustor, Proc. Combust. Inst., 30(1) (2005) 835–842.

[4] M. Stohr, I. Boxx, C. Carter, W. Meier, Dynamics of Lean Blowout of a Swirl-Stabilized Flame in a Gas Turbine Model Combustor, Proc. Combust. Inst., 33 (2011) 2953-2960.

[5] M.K. Kim, J. Lee, S. Park, J.G. Lee, Y. Yoon, An Experimental Study of Instability Mode Analysis in a Model Gas Turbine Combustor, J. KOSCO, 15(1) (2010) 12-21.

[6] R.S.S. James, On-line Cmbustion Mnitoring on Dry Low NOx Industrial Gas Turbines., Measurement Science & Technology, 14(7) (2003) 1123-1130.

[7] H. Zinn, M. Habermann, Developments and Experiences with Pulsation Measurements for Heavy-Duty Gas Turbines, Proceedings of ASME Turbo Expo, (2007) GT2007-27475.

[8] K.K.Venkataraman, D.A. Satavicca, Mechanism of Combustion Instability in a Lean Premixed Dump Combustor, J. Propul. Pow., 15(6) (1999) 909-918.

[9] M.P. Auer, C. Hirsch, T. Sattelmayer, Influence of Air and Fuel Mass Flow Fluctuations in a Premix Swirl Burner on Flame Dynamics, Proceedings of ASME Turbo Expo, (2006) GT2006-90127

[10] G. Kelsall, C. Troger, Prediction and Control of Combustion Instabilities in Industrial Gas Turbines, Appl. Therm. Eng., 24 (2004) 1571-1582.

[11] Y. Huang, V. Yang, Dynamics and Stability of Lean-premixed Swirl-stabilized Combustion, Prog. Energy Combust. Sci., 35(4) (2009) 293-364.

[12] A. Toffolo, M. Masi, A. Lazzaretto, Low Computational Cost CFD Analysis of Thermoacoustic Oscillations, Appl.Therm.Eng., 30 (2010) 544-552.

[13] T. Schuller, D. Durox, P. Palies, S. Candel, Acoustic Decoupling of Longitudinal Modes in Generic Combustion Systems, Combust. Flame, 159(5) (2012) 1921-1931.

[14] S. Candel, Combustion dynamics and control: Progress and challenges, Proc. Combust. Inst., 29(1) (2002) 1-28.

[15] J.G. Lee, D.A. Santavicca, Experimental Diagnostics for the Study of Combustion Instabilities in Lean Premixed Combustors, Journal of Propulsion and Power, 19(5) (2003) 735-750.

[16] J.G. Lee, K.T. Kim, D.A. Santavicca, Measurement of Equivalence Ratio Fluctuation and Its Effect on Heat Release during Unstable Combustion, Proceedings of the Combustion Institute, 28(2000) 415-421.

[17] K.T. Kim, J.G. Lee, B.D. Quay, D.A. Santavicca, Spatially Distributed Flame Transfer Functions for Predicting Combustion Dynamics in Lean Premixed Gas Turbine Combustors, Combust. Flame 157 (2010) 1718−1730.

[18] K.T. Kim, J.G. Lee, B.D. Quay, D.A. Santavicca, Reconstruction of Heat Release Response of Partially Premixed Flames, Combust. Sci. Tech. 183 (2011) 122−137.

Chapter 7 Spray Characteristics of Canted Injection Angles

[1] J.A. Schetz, A. Padhye, Penetration and Breakup of Liquids in Subsonic Airstreams, AIAA Journal, 15 (1977) 1385-1390.

[2] P.-K. Wu, K.A. Kirkendall, R.P. Fuller, A.S. Nejad, Breakup Processes of Liquid Jets in Subsonic Crossflows, J. Propul. Power, 13(1) (1997) 64-73.

[3] T.F. Fric, A. Roshko, Vortical Structure in the Wake of a Transverse Jet, J. Fluid Mech., 279 (1994) 1-47.

[4] T. Oda., H. Hiroyasu, Breakup Model of Liquid Jet Across a High-Speed Air Stream, Proceeding of the 9th Annual Conference on Liquid Atomization and Spray Systems, San Francisco, CA, USA, 1996, pp. 99-103.

[5] T.T. Nguyen, A.R. Karagozian, Liquid Fuel Jet in Subsonic Crossflow, J. Propul. Power, 8(1) (1992) 21-29.

[6] N. Tamaki, M. Shimizu, K. Nishida, H. Hiroyasu, Effects of Cavitation and Internal Flow on Atomization of a Liquid Jet, Atomization and Sprays, 8 (1998) 179-197.

[7] J. Song, K. Ahn, M.-K. Kim, Y. Yoon, Effects of Orifice Internal Flow on Liquid Jets in Subsonic Crossflows, J. Propul. Power, 27(3) (2011) 608-619.

[8] R.P. Fuller, P.-K. Wu, K.A. Kirkendall, A.S. Nejad, Effects of Injection Angle on Atomization of Liquid Jets in Transverse Airflow, AIAA Journal, 38(1) (2000) 64-72.

[9] M. Costa, M.J. Melo, M.M. Sousa, Y. Levy, Spray Characteristics of Angled Liquid Injection into Subsonic Crossflow, AIAA Journal, 44(3) (2006) 646-653.

[10] T. Inamura, N. Nagai, Spray Characteristics of Liquid Jet Traversing Subsonic Airstream, J. Propul. Power, 13(2) (1997) 250-256.

[11] T. Inamura, Trajectory of a Liquid Jet Traversing Subsonic Airstreams, J. Propul. Power, 16(1) (2000) 155-157.

[12] N.S. Jacob, J.G. Lee, D.A.Santavicca, Penetration of Liquid Jets in a Crossflow, Atomization and Sprays, 16(8) (2006) 887-906.

[13] A.H. Lefebvre, Atomziation and Sprays, Hemisphere, New York, USA, 1989.

[14] N. Chigier, R.D. Reitz, Regimes of Jet Breakup and Breakup Mechanisms, Recent Advances in Spray Combustion : Spray Atomization and Drop Burning Phenomena, edited by K. Kuo AIAA , 1996.

[15] J. Vennard, Elementary Fluid Mechanics 3rd ed., Wiley, New York, USA, 2008, pp. 216-219.

Appendix A, B, C

[1] F.A. Williams, Combustion Theory 2nd ed., Benjamin Cummings Publishing Company (Pearson), San Francisco, USA, 1985.

[2] L.B. Gary, W.R. Kenneth, Combustion Engineering, 1st edition, McGraw-Hill, New York, 1998.

[3] A.S. Morgans, S.R. Stow, Model-based control of combustion instabilities in annular combustors, Combust. Flame, 150 (2007) 380-399.

[4] L.B. Davis, S.H. Black, Dry Low NOx Combustion Systems for GE Heavy-Duty Gas Turbines, GE Power Systems, GER-3568G, 2010.

[5] J. Oh, M.K.Kim, Y. Yoon, The tuning methodology of a GE 7FA + e DLN-2.6 gas turbine combustor, 36 (2012) 14-20.

[6] J. Oh, J. Hwang, Y. Yoon, EINOx Scaling in a Non-Premixed Turbulent Hydrogen Jet with Swirled Coaxial air, Int. J. Hydrogen Energy, 35 (16) (2010) 8715-8722.

[7] E. Kinsler, A.R. Frey, Fundamentals of Acoustics 2nd ed., John Wiley and Sons, Hoboken, NJ, USA, 1990.

[8] S. Hubbard, A.P. Dowling, Acoustic Resonances of an Industrial Gas Turbine Combustion system, J. Eng. for Gas Turbines Power 123 (2001) 766-773.

[9] S. Candel, Combustion Dynamics and Control; progress and challenges, Proc. Combust. Inst., 29 (2002) 1-28.

[10] N. Docquier, S. Candel, Combustion Conrtrol and Sensors - A Review, Progress in Energy and Combustion Science, (28) (2002) 107-150.

[11] D.R. Englund, W.B. Richards, The Infinite Line Pressure Probe, Thirty-ninth International Instrumentation Symposium, Denver, Colorado, USA, 1984.

[12] S. Rea, S. James, C. Goy, M.J.F. Colechin, On-Line Combustion Monitoring on Dry Low NOx Industrial Gas turbines, Meas. Sci. Technol., 14 (2003) 1123-1130.

[13] S.R. Turns, An Introduction to Combustion, 2nd ed., McGraw Hill, New York, USA, 2000.

[14] J. Sewell, P. Sobieski, C. Beers, Application of Continuous Combustion Dynamics Monitoring on Large Industrial Gas turbines, Proceedings of the ASME Turbo Expo (2004) GT2004-54310.

초 록

본 연구는 친환경 저 NOx 가스터빈 연소기의 최적설계 인자 도출에 대한 연구이며 항공용 및 발전용 가스터빈에서 사용되는 예혼합 연소기에서의 연소 동특성에 대한 실험적 결과를 제시한다. 가스터빈 연소기의 설계 인자인 연료-공기 혼합기 속도, 당량비, 연료노즐 전의 연료-공기 혼합부의 공간 (plenum) 및 연소실의 길이 등의 변화에 따른 화염안정화 지도를 작성하였고, PIV (Particle Image Velocimetry), OH 자발광, He-Ne 레이저 광산란 기법 등을 동압과 위상동기화 하여 안정 및 불안정한 화염의 구조를 분석하였으며, 자체 개발한 다체널 동압측정 시스템을 이용하여 전체 연소기에서 구간별 동압을 실시간으로 측정하여 연소실에서 발생하는 불안정 특성의 원인을 파악하였다. 열방출의 섭동과 11개의 동압센서에서 측정되는 동압의 모드와 위상차 분석을 통하여 연소불안정의 원인을 정확히 파악할 수 있었고, 연료-공기 혼합기의 내제적 불안정에 의해 발생되는 화염의 와동구조 불안정과 연료-공기의 혼합부의 길이가 연소불안정에 크게 영향을 미치는 것을 확인하였다. 이를 통해서 친환경 가스터빈 연소기 제작을 위한 설계 인자를 명확히 확인하였다. 또한 RQL 연소기에서 사용되는 2차 산화제의 빠른 혼합을 유도하는 분무의 분사각도별 액주의 궤적과 분열거리를 측정하여 실험으로 인한 경험식을 도출하였다.

부분 예혼합 연소기와 30도 각도의 스월러를 가진 천연가스 연료분사기에서 발생한 화염구조와 재순환 영역의 형성이 연소불안정에 미치는 영향에 대하여 실험적으로 연구한 부분에서는 PIV 계측기법으로 연소장에서의 화염의 안정화 그리고 불안정한 영역에서 유동장을 확인해 보았다. 스월러에 의한 재순환 영역은 화염의 안정화 및 난류의 강도뿐만 아니라 재순환 영역의 크기에 따른 화염 재점화에도 영향을 주었고, 연소불안정으로 인한 연소기 내부의 압력구배에 의하여 중앙 재순환 영역에서 유입되는 연소가스의 질량유량의 변동

이 화염의 각도와 모양을 변경시키고 이것이 열방출 섭동을 발생시켜 연소불안정 발생의 주요 원인이 되고 있음을 확인하였다.

연료-공기 혼합기 속도에 의한 연소불안정과 화염구조와의 상관관계에 대한 연구에서는 당량비 1.2 조건에서 연료-공기 혼합기 속도를 30 ~ 70 m/s까지 다양한 실험조건에서 수행하였다. 이를 통하여 연소불안정 현상이 낮은 혼합기 속도조건과 높은 혼합기 속도조건에서 발생하는 것을 확인할 수 있었고, 낮은 혼합기 속도조건의 불안정에서는 화염의 끝단의 와동구조가 연소불안정 현상에 영향을 끼친다는 것을 확인할 수 있었다.

모형 가스터빈의 연소실과 연료-공기 혼합부의 공진모드의 관계가 연소불안정에 어떤 영향을 미치고 있는지에 대하여 실험적으로 확인한 연구에서는 다체널 동압측정을 통하여 각각 위치에서 동압의 모드와 각 센서들간의 phase를 분석하여 연소불안정의 원인을 규명하였다. 연소실의 길이 (800 ~ 1800 mm)와 혼합부의 길이 (470, 550, 870 mm)를 음향학적 경계로 일치시켜 연소불안정 특성을 확인해 보았을 때 두가지 서로 다른 연소불안정 모드를 확인할 수 있었는데 저주파 연소불안정 특성은 화염의 열방출 섭동과 연소실의 공진모드에 기인하며, 고주파 영역대의 연소불안정 현상은 혼합부의 길이를 변경하였을 때 발생하는 또 다른 불안정 현상임을 실험적으로 확인할 수 있었다.

친환경 연소기 설계에 있어서 이차분무 연구의 일환으로 분사각도에 따른 산화제 분무특성에 대한 실험적 연구를 수행하였다. 여기서 액주영역의 궤적과 분열지점까지의 거리는 연료분사 속도, 공기의 속도에 의한 연료/공기 모멘텀 플럭스와 분사각도, 항력계수의 함수임을 확인하였다. 분사각도에 의한 액주영역의 궤적 및 분열길이에 대한 실험식을 도출하였으며, 일반적인 공기유동 방향과 일치하는 정방향 분사와 반대방향으로 분사되는 대향분사 액주궤적 실험식과는 항력계수의 차이가 발생하는 것을 확인하였다.

마지막으로 첨부자료에서는 앞에서 소개된 연소불안정 현상에 영향을 미치는 인자들을 고려하여 실제 서인천 복합화력 발전소에서 운용중인 발전용 GE 7FA+e DLN-2.6 연소기에 적용하여 연소최적 튜닝에 대한 결과와 실시간으로 최적제어가 가능하며, 튜닝 대상의 연료노즐과 상수를 제시하고 연소상태를 모니터링 할 수 있는 프로그램을 개발한 내용을 소개하였다.

중심어: 가스터빈 연소기, 연소불안정, 와류화염구조, 중앙재순환영역, 연료-공기 혼합부, 다체널 동압측정 시스템, 분사각도, 액주분무궤적, 분열길이, 최적연소튜닝

학 번: 2005-20996

공학박사학위논문

Experimental Study on Flame Structure and Combustion Dynamic Characteristics in a Low NOx Model Gas Turbine Combustor

저 NOx 모형 가스터빈 연소기에서 화염구조 및 연소동특성에 대한 실험적 연구

2016년 2월

서울대학교 대학원
기계항공공학부
김민기

ABSTRACT

Experimental Study on Flame Structure and Combustion Dynamic Characteristics in a Low NOx Model Gas Turbine Combustor

Min-Ki Kim

School of Mechanical and Aerospace Engineering

The Graduate School

Seoul National University

There has been increased demand in recent years for low NOx gas turbines to meet stringent emissions goals by operating in a lean, premixed combustion and an advanced combustion system for aero gas turbine engine such as the Rich-Burn, Quick-Mix, Lean-Burn (RQL) combustor. Unfortunately, detrimental combustion instabilities are often excited within the combustor when it operates under lean and rich equvalence ratio conditions, degrading performance and reducing combustor life. To eliminate the onset of these combustion instabilities and develop effective approaches for their control, the mechanisms responsible for their combustion oscillation chartacteristics and jet spray mechanism of secondary quick mix zone must be understood. The main objective of this study was conducted to identify the secondary spray jet mechanism for the turbulent quick mixing zone and combustion instability characteristics in a swirl-stabilized and partially premixed model gas turbine combustor, with the attention focused on the effect of the various fuel-air mixing section geometries, fuel-air mixture velocities and effect of the formation of recirculation zones and vortex interaction on the combustion instability characteristics. Lastly, for the confirmed the this experimental study and analyzed mechanisms, we investigated an optimized operating strategy and developed a

combustion tuning methodology for the GE 7FA+e DLN-2.6 (DLN : Dry Low NOx) ground state gas turbine engine used for power generation operated by Korea Western Power Co. Ltd. at Seo-Incheon power plant, Incheon, Republic of Korea.

The flame recirculation zone is very important, as it can modulate the fuel flow rate and may be the source of instability, plus its flame structure has a major impact on heat release rate oscillation and flame stabilization. This study addresses structural characteristics of natural gas flames in a lean premixed swirl-stabilized combustor with attention focused on the effect of the formation of recirculation zones and vortex interaction on the combustion instability. To improve our understanding of the role of the recirculation zone and vortex combustion instability, the flame structure was investigated for various mixture velocities, equivalence ratios and swirl numbers. The optically accessible combustor allowed for the laser diagnostics of Particle Image Velocimetry (PIV) measurement, while OH chemiluminescence was used to characterize the flow structure under both cold flow conditions and hot flow combustion conditions. and heat release oscillation rate with the use of a high-speed ICCD camera under both stable and unstable flame conditions. Multi-channel dynamic pressures were also measured at the same time to investigate characteristics of the combustion phenomenon. We also observed fundamental longitudinal type of combustion instability characteristics related to the instability of thermo-acoustics. The result suggests that the formation of the recirculation zone is strongly related to the occurrence of combustion instabilities.

The effect of fuel-air mixture velocity on combustion instability characteristics have been investigated by measuring the flame structure, dynamic pressure mode and phase. The swirling CH_4 - air flame was investigated with an overall equivalence ratio of 1.2 to lean blowout limit and dump plane velocity of 30 ~ 70 m/s. Phase locking analysis was performed to identify structural changes at each phase of the reference dynamic pressure sensor under conditions of instability. At an unstable condition, flame root size varies a lot compared to stable condition which is because of air and fuel mixture flow rate changes due to combustor pressure modulation. After this structural change, local extinction and re-ignition occur and it can generate a feedback loop for combustion instability. This analysis suggests that pressure fluctuation of combustion causes

deformation of flame structure and variation of flame has a strong effect on combustion instability. In this section, we observed two types of combustion instability characteristics related to the instability of both the thermo-acoustics and flame vortex interaction mode.

To investigate the instability characteristics of combustor geometry. The combustor and inlet mixing section length was varied in order to have different acoustic resonance characteristics from 800 to 1680 mm of the combustor and 470, 550 and 870 mm of the inlet mixing section. In this study, we observed two dominant instability frequencies. Lower instability frequencies were obtained around 240 ~ 380 Hz, which were associated with a fundamental longitudinal mode of combustor length. Higher frequencies were observed around 410 ~ 830 Hz. These were related to the secondary longitudinal mode in the combustion chamber and the secondary quarter wave mode in the inlet mixing section. These second mode instability frequency characteristics are coupled with the conditions of the combustor and inlet mixing section acoustic geometry. Also, these higher combustion instability characteristics include dynamic pressure oscillation of the inlet mixing section part, which was larger than the combustor section. As a result, combustion instability was strongly affected by the acoustically coupling characteristics of the combustor and inlet mixing section geometry, which is called the plenum.

The effects of variable angled injection characteristics for quick mixing zone such as liquid column trajectory and breakup length has been experimentally studied in liquid jets injected into subsonic crossflow. With water as fuel injection velocity and injection angle were varied to provide of jet operation conditions. The pulsed shadowgraph photography with highly resolution and PLLIF (Planar Liquid Laser Induced Fluorescence) measurements were used for determined the liquid column trajectory and breakup length of angles spray. As the result, this research has been shown that liquid column trajectories and liquid column breakup length were spatially dependent on air-stream velocity, fuel injection velocity, various injection angle, and normalized injector exit diameter. Furthermore, the empirical formula of liquid column trajectories and breakup length has been some different of drag coefficient results between forward injection and reverse angle injection in subsonic crossflow.

In the Appendix section, the optimum combustion control of real gas turbine combustor was introduced. On the basis of a MARK-Ⅵ system, the optimized tuning for operation of a DLN-2.6 combustor was studied for the maintenance of a GE 7FA+e gas turbine at a Seo-Incheon combined cycle power plant. Also, the optimum combustion control system was created by all of measuring the inlet and outlet combustion data of the GE 7FA+e gas turbine.

Keywords: Gas Turbine Combustor, Combustion Instability, Flame Vortex Structure, Central Recirculation Zone (CRZ), Inlet Mixing Section, Multi-Position Dynamic Pressure Sensing, Canted Injection, Liquid Column Trajectory, Breakup Length, Optimum Combustion Tuning

Student Number: 2005-20996

LIST

LIST OF FIGURES

LIST OF TABLES

NOMENCLATURE

Alphabet

1L	1st longitudinal instability mode
2L	2nd longitudinal instability mode
A	orifice area
c	speed of sound
C_v	constant-volume specific heat
C_d	discharge coefficient
d	orifice diameter
d_0	diameter of the centerbody
d_h	diameter of inlet duct
D	orifice chamber diameter
D_{inlet}	diameter of inlet mixing section
$D_{comb.}$	diameter of combustor
e	specific internal energy
f	combustion instability frequency
f_0	resonance frequency
I_0	laser beam intensity
K	constants
L	orifice passage length
L_{inlet}	axial distance of inlet mixing section
$L_{comb.}$	axial distance of combustor
L_{flame}	flame length
M	Mach number
$\dot{m}$	mass flow rate
P	static pressure
P_1	total pressure in the pressure vessel
P_2	ambient pressure
$P'(x,t)$	perturbation of dynamic pressure

q	liquid/air momentum flux ratio, $\rho_f u_f^2 \ / \ \rho_g u_g^2$
$q'(x,t)$	heat release oscillation
Q	volumetric flow rate
R	gas constant
Re	Reynolds number
R_o	orifice inner curvature radius
S	swirl number
S'	swirl number perturbation
St	Strouhal number, $f \cdot L_{flame} / v_{mix}$
t	time
T_{inlet}	inlet mixing section temperature
$T_{comb.}$	combustor temperature
u	axial velocity
u_2	axial velocity at swirler downstream section
v_a	air velocity in the airstream direction
v_f	liquid fuel velocity at the orifice exit
v_g	gas velocity in the airstream direction
v_{mix}	fuel - air mixture velocity
v_r	radial velocity
v_θ	tangential velocity
V'	vortex shedding oscillation
x	distance in the airstream(axial) direction
x_b	breakup distance in the airstream(axial) direction
x_f	location of flame zone
y	distance in the direction transverse(penetration) to the airstream
y_b	breakup distance in the direction transverse(penetration) to the airstream

Greek

a	flame angle

r	radial distance
ΔP	injection pressure drop
ρ_l	liquid density
ρ_f	fuel density
ρ_a	air density
ρ_g	ambient gas density
γ	specific heat ratio
ϕ	equivalence ratio
$\Phi(x,t)$	combustion instability damping source
θ	injection angle
θ_s	swirl vane angle
ω	angular frequency
μ	liquid viscosity
σ	surface tension
τ	period of oscillation

Subscripts

a	air
b	breakup
comb.	combustor section
d	discharge
f, flame	flame zone
g	gas
inlet	inlet mixing section
l	liquid
mix	fuel-air mixture
r	radial direction
s	swirl

CHAPTER 1
INTRODUCTION

1.1 Background

As a high-efficiency and low-pollution engine, a gas turbine is utilized for various different uses, ranging from the aviation industry to the electric power generation industry. Examples include domestic and industrial burners, steam and gas turbines, waste generators, and jet and ramjet engines. Continuous combustion processes exhibit a wide range of dynamics. Of these, conditions which promote coupling with the acoustic field and result in sustained, large amplitude oscillations remain as most challenging in the effort to develop ultra-low emission, lean premixed combustion to its full potential. Paradoxically, near stoichiometric burning in high-speed propulsion systems exhibits similar dynamics. In earlier days, for the purpose of promoting mechanical stability, such an engine was driven by a diffusion flame type combustor, but around the 1980s, when exhaust emissions like such as NOx were made an issue due to combustion in the existing stoichiometric ratio, the concept of a lean premixed flame [1, 2] and RQL (Rich burn Quick mix and Lean burn) type combustion [3, 4] quickly became important. As a result, the emission of NOx could be sharply decreased, but another problem arose in this context, which was that the flame became unstable in extreme reaction to the external disturbance. In a typical continuous combustion process, a highly flammable fuel-air mixture is ignited, and the hot gases generated due to the chemical transformation of the mixture are used to perform certain functions. In its simplest form, the combustion process can be considered as a reacting mixture flowing in a constant area duct with a flame anchored at a specific location in the duct. The latter ignites the reactants, releasing their chemical energy in the form of heat, thus raising their temperatures and reducing their density. Combustion chambers can be viewed as organ pipes in which acoustic pressure and velocity oscillations can be sustained. Flames, which are essentially surfaces

across which reactants are converted into products, not only possess their own inherent instabilities, but are also known to respond readily to impose fluctuations. The potential coupling between the unsteady components of pressure and heat release rate can lead to their resonant coupling, thus growth, is referred to as thermo-acoustic instability.

The combustion instability indicates that the local change of unsteady heat release waves and acoustic waves from the combustion chamber interact with each other, further generating a fluctuation of specific instability frequency. The fluctuation of unstable dynamic pressure generates a perturbation of fuel-air mixture flow, and then this fluctuation generates a perturbation of heat release waves, thus developing into the phenomenon of combustion instability. When the combustion instability characteristic takes place, it is able to satisfy the Rayleigh criterion theory [5], as formulated here:.

$$\int_0^{\tau}\int_0^{V} p'(x,t)\cdot q'(x,t)\,dVdt \;>\; \int_0^{\tau}\phi(x,t)\,dVdt \qquad (1.1)$$

The combustion instability mode is attributed to various other factors, such as heat release oscillation [6] by the flame vortex and acoustic pressure boundary formation with other space except the combustor, as well as the internal configuration of the combustor [7, 8, 9, 10]. For instance, the Seo-Incheon power plant of Korea Western Power Company, there is one of the latest engines made by the General Electric (GE) Company, called the 7FA+e DLN-2.6, and the fuel staging technique is used to stabilize the combustion as shown in Fig. 1.1. In the initial stage of combustion, a high level of NOx is generated in the section called Mode 3 (10~20 MW), that is, a yellow plume is generated by NO_2 in the chimney and lasts four hours at most., In the section of Mode 6B (20~45 MW), which leads to the maximum output, this has a feature that the engine combustion oscillation (the average pressure inside the combustion chamber is as follows: 15.1 bar, pressure fluctuation: 0.3 bar, about 2% oscillation of the average combustion chamber pressure) is caused by the conversion into the premixed mode. At this moment, through

the frequency of combustion instability, although the combustor temperature increases in proportion to the output increase in speed, there is no change in the instability frequency, and it is sustained as 120 ~ 140 Hz [11] Since the instability frequency does not increase as the temperature of the combustion chamber increases, we discovered that the instability mode, which is appears as an acoustic pressure field, is formed not by the combustor mode but other geometric characteristics [12, 13].

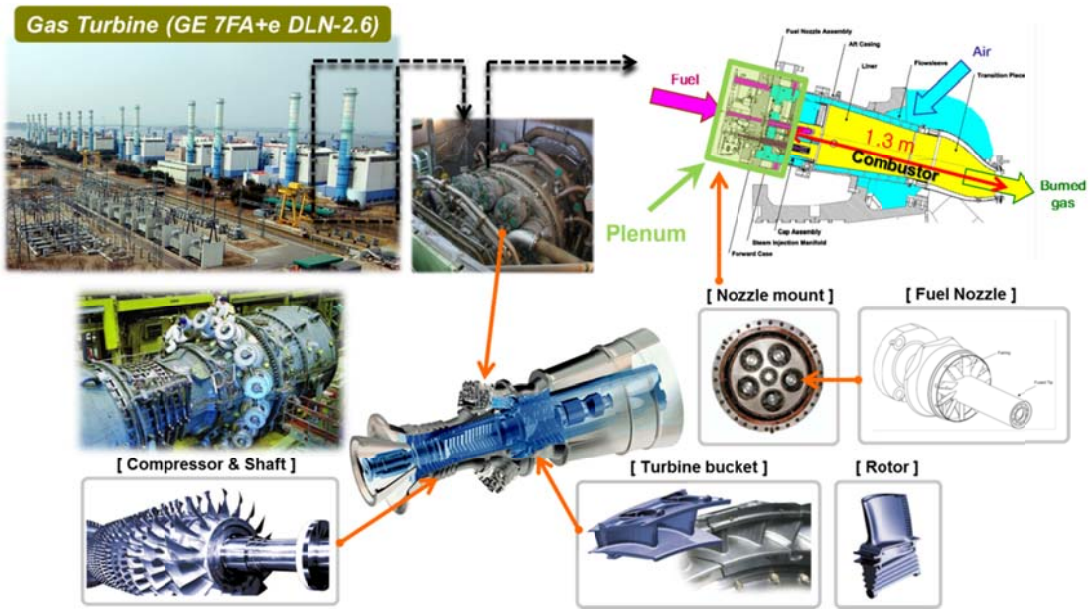

Fig. 1.1 GE 7FA+e DLN-2.6 (DLN : Dry Low NOx) ground state gas turbine engine used for power generation operated by Korea Western Power Co. Ltd. at Seo-Incheon power plant, Incheon, Republic of Korea.

In the past, aero gas turbine engine designers have sacrificed emissions to attain greater flight speeds and altitudes. For today's aero gas turbine engines, it is necessary to reduce these emissions, while at the same time, maintaining these same speeds and altitudes. In some European countries, airlines are being taxed for NOx emissions in their airspace. Concern for pollutant reduction is particularly strong for the next generation of

aircraft, represented by the High Speed Civil Transport, which is being designed to fly at stratospheric altitudes. In the stratosphere, NOx emissions could contribute to ozone depletion [14]. To achieve this reduction in NOx emissions, engine designers have been challenged to evaluate various combustor configurations. One promising configuration is the three-stage RQL combustor as shown in Fig. 1.2.

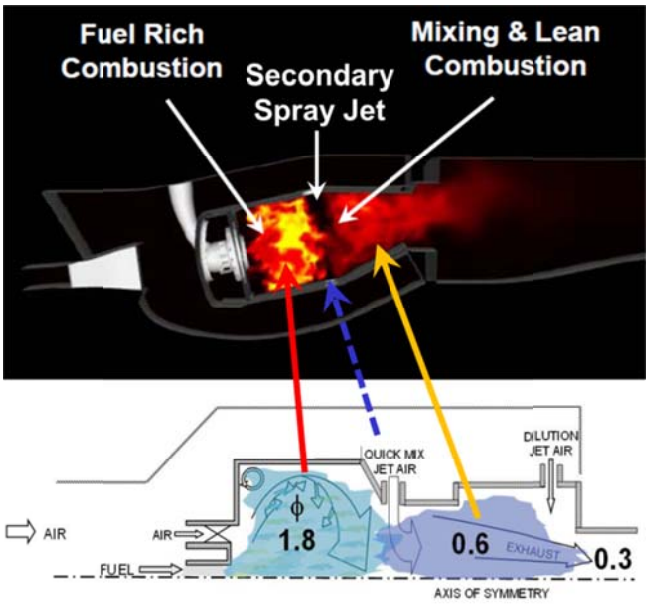

Fig. 1.2 Schematic of RQL (Rich burn - Quick mix - Lean burn) Combustor

(ϕ : *Equivalence Ratio*)

In the RQL (Rich burn - Quick mix - Lean burn) combustor, air is mixed with the fuel in two stages. In the primary zone of the combustor, a fraction of the total air is reacted with the fuel to form a fuel rich combustion mixture. By operating rich of stoichiometery, the flame temperature is reduced and an active pool of hydrocarbon is produced which can reduce NO formed. Downstream, the remaining air is added to the fuel rich product mixture via dilution jets to form a fuel lean mixture in the secondary

zone. Operating lean of stoichiometric keeps the combustion temperature low and also eliminates carbon monoxide (CO) and unburnt hydrocarbons (UHC). To date, the reduction of NOx from staged RQL type combustors operating at atmospheric, low temperature inlet conditions has been well documented. Staged combustion has been demonstrated successful at reducing thermal and fuel NO at atmospheric conditions with no air preheat [15, 16], and at atmospheric conditions with air preheat up to 600 K [17]. However, little information exists for the RQL's low NOx potential when operating at temperatures and pressures that correspond to actual gas turbine engines. A full evaluation of the RQL, for use in stationary and aero applications, requires a systematic study of the effects of current, as well as futuristic, operating conditions on the emissions of NOx and combustion efficiency.

1.2 Historical Overview of Combustion Instability

Historically, the first observation of combustion oscillation was the “singing flame” which was discovered by Higgins in 1777 [18]. This phenomenon caught the interest of several researchers [19, 20] and they described that high levels of sound can be produced by placing a flame, anchored on a small diameter fuel supply tube in a larger diameter tube. The flame was found to excite the fundamental mode or one of the harmonics of the larger tube. The “dancing flame” was discovered later by Le Conte [21] where a flame pulses in sync with the audible beats of music. “It was exceedingly interesting to observe how perfectly even the trills 1 of the musical instrument were reflected on the sheet of the flame. A deaf man might have seen the harmony!”, he quoted. Concomitantly, Rijke [22] showed that sound can be generated in a vertical tube open at both ends by placing a heated metal gauze inside the tube. The sound was heard only when the heating element was placed in the lower half of the tube, specifically at a distance of a quarter the tube length from the bottom. Rayleigh [23] was the first to hypothesize the onset of the instability, and define a criterion for positive coupling based on a phenomenological,

heuristic, description of the instability, his explanation was as follows: *"If heat be periodically communicated to, and abstracted from, a mass of air vibrating in a cylinder bounded by a piston, the effect produced will depend upon the phase of the vibration at which the transfer of heat takes place. If heat be given to the air at the moment of greatest condensation or to be taken from it at the moment of greatest rarefaction, the vibration is encouraged. On the other hand, if heat be given at the moment of greatest rarefaction, or abstracted at the moment of greatest condensation, the vibration is discouraged"*. This can also be compared to a thermodynamic cycle (e.g. the Carnot engine). In a continuous combustion. Fig. 1.3 shows an historical overview of combustion instabilities in devices for propulsion and power generation [24]. Combustion instability was observed in solid rockets in the 1930s, and was a major issue in the development of liquid rocket engines as well as solid rocket motors. A notable instability in liquid-fueled rockets was encountered during the development of the F-1 engine for the Saturn rockets. The F-1 experienced strong instability with oscillation amplitudes up to 100% of the mean pressure (more than 2000 psi) in the combustion chamber at the frequency range of 200 ~ 500 Hz [25, 26]. In developing solid-propellant rockets, combustion instability was observed in the Space Shuttle rocket boosters, Minuteman ICBM, and the decent motors of the Mars Pathfinder [26, 27]. Combustion instabilities in ramjets have been also problematic as they cause strong fluctuations in thrust and/or shock-system oscillations in the inlet diffuser [26, 28]. Similar problems have been experienced in afterburners, where transverse modes as well as axial mode instabilities have damaged engine components such as flame holders and liner sections. In land-based gas turbines, vibrations induced by oscillating pressure and entropy waves in the combustion chambers have given rise to fatigue in combustor liners and turbine blades, which can reduce system lifetimes significantly.

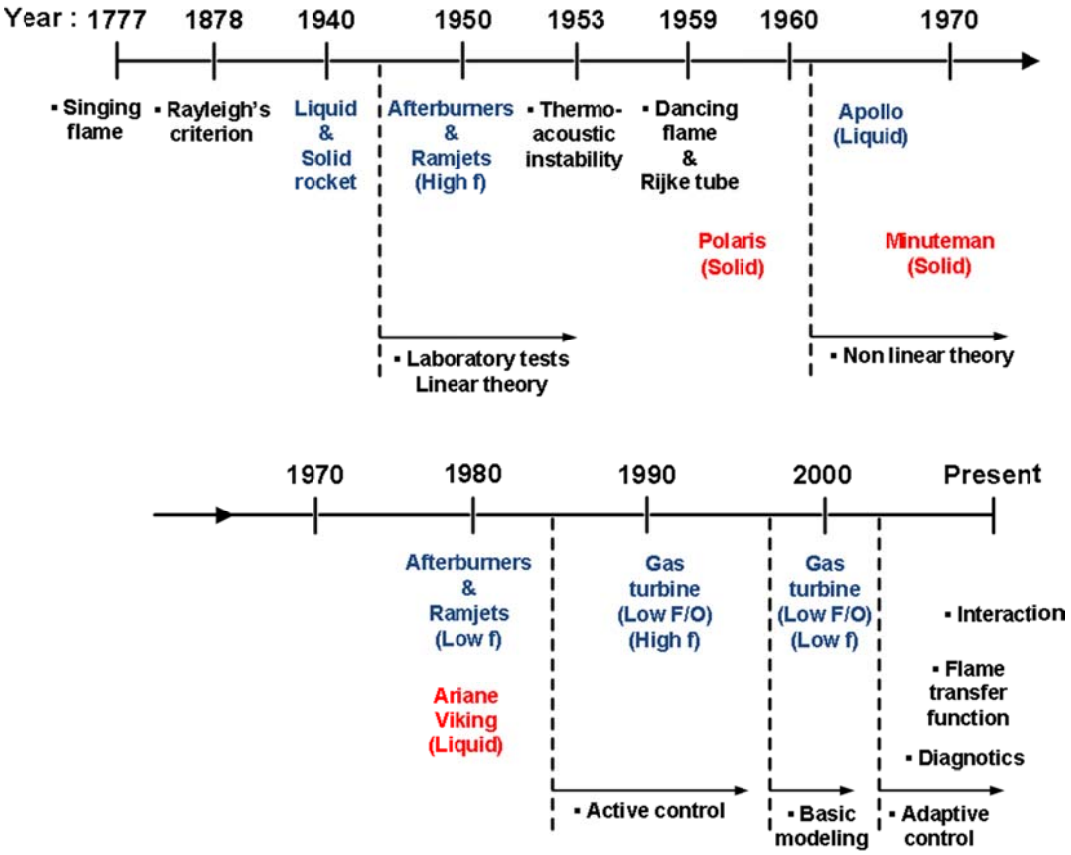

Fig. 1.3 Historical overview of combustion instabilities.

1.3 Mechanism of Combustion Instability

Combustion instabilities, in general, appear as large amplitude pressure oscillations with the natural frequency of the acoustic modes of combustion systems [26]. They are caused by complex, feedback type interactions between periodic flow and combustion processes that produce a periodic heat addition, exciting large amplitude acoustic oscillations in the combustor. An unsteady combustion process generates sound. If the combustion process occurs in a free field, the generated sound simply radiates away. However, if sound is generated in a confined region it can be reflected from the

boundaries, allowing the reflected waves to interact with the combustion process. Since the combustion process is sensitive to these flow field variations, a feedback loop is created and combustion instability can result [29].

Fig. 1.4 shows the feedback processes responsible and driving souses are involved in combustion instability [30]: a driving process and a coupling process. The driving process is the process that leads to the acoustic pressure oscillations due to the rate of heat release fluctuations, while the coupling process is the one that is responsible for the heat release fluctuation caused by the acoustic oscillations. When the two processes interact with a certain phase relationships, they can initiate and amplify combustion instability in a system.

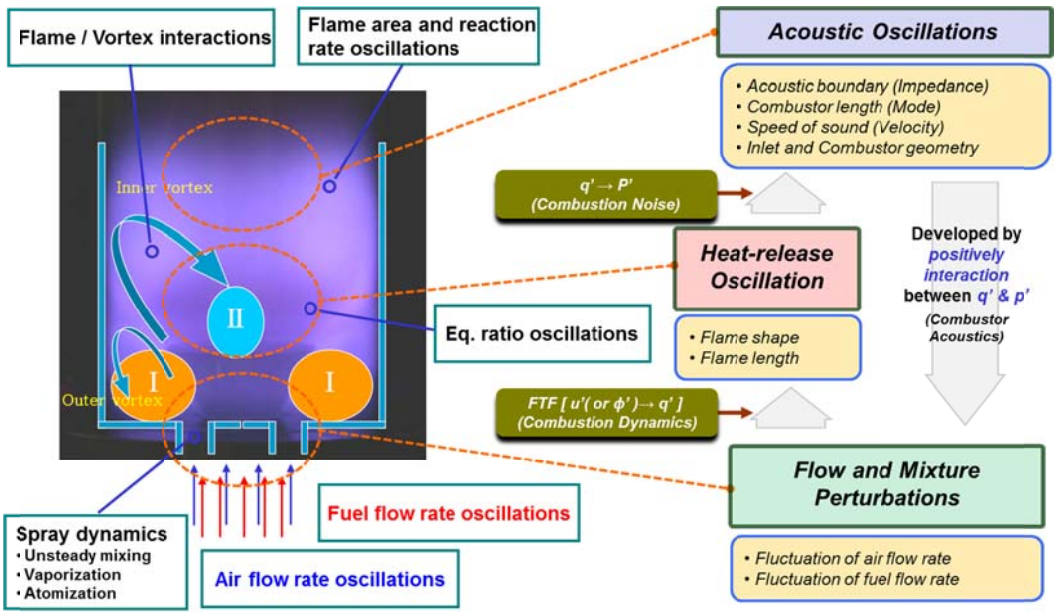

Fig. 1.4 Illustration of feedback loop and generic combustion instability mechanism.

1.4 Objectives and Outline

Optimum designing an advanced low NOx gas turbine combustor requires, essentially, the capability of predicting stability characteristics as a function of combustor operating conditions and geometry. This requires a substantial understanding of the physical processes which generate fluctuations of the rate of heat release and/or acoustic oscillations in lean and rich premixed combustors. Unfortunately, neither the driving nor coupling mechanisms of combustion instability are well enough understood, particularly under realistic combustor, inlet mixing section geometries and operating conditions.

For this purpose, experimental study is conducted to characterize the effects of flame-vortex interactions, fuel air mixture velocities and inlet mixing section geometry on unstable combustion in a swirl-stabilized, laboratory-scale gas turbine combustor. In chapter 2, the acoustic theory for each of the combustion instability mechanisms is presented to lay a theoretical foundation for the experiments. Chapter 3 then presents the experimental facility, including the model gas turbine combustor configuration and measurement techniques. The observed overall instability characteristics for swirl stabilized flame structure and recirculation zone are shown in Chapter 4. Based on the observations in Chapter 4, the combustion instability mechanisms due to flame-vortex interactions of various fuel-air mixture velocities and effect of mixing section geometry discussed in Chapters 5 and 6, respectively. Chapter 7 presents the secondary spray jet mechanism and characteristics of canted injection angles in secondary quick mixing zone for reducing the NOx level. The optimized tuning experience of a GE 7FA+e DLN-2.6 gas turbine combustor is shown in Appendix section. Lastly Chapter 8 presents the conclusions of this study.

CHAPTER 2

EXPERIMENTAL BACKGROUND

2.1 Acoustic Mode and Phase Analysis of Resonance Frequency

The combustion instability characteristics have very complicate mechanism such as flame-vortex and flame-acoustic interaction. This chapter is introduced to fundamental analytic theory for understand the combustion instability mechanism. Fig. 2.1 shows a model gas turbine with a blockage nozzle for turbine section where a flame sits in the main combustor. We can model either cases as a tube hosting a localized heat release zone (the flame), as seen in Fig. 2.2.

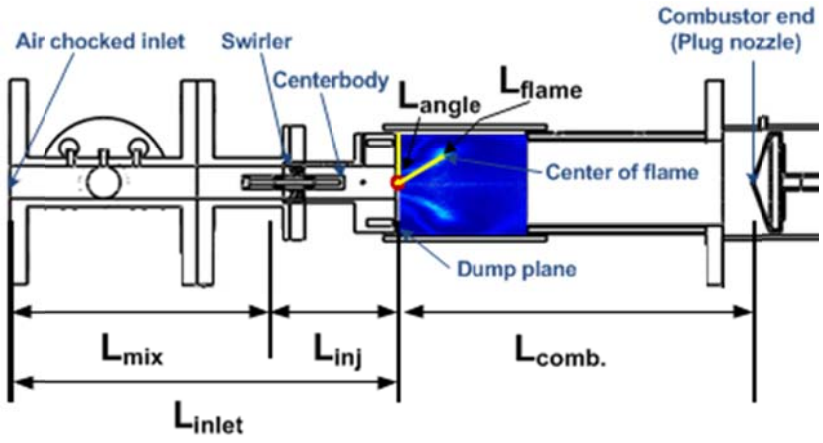

Fig. 2.1 Basic dimensions of model gas turbine combustor.

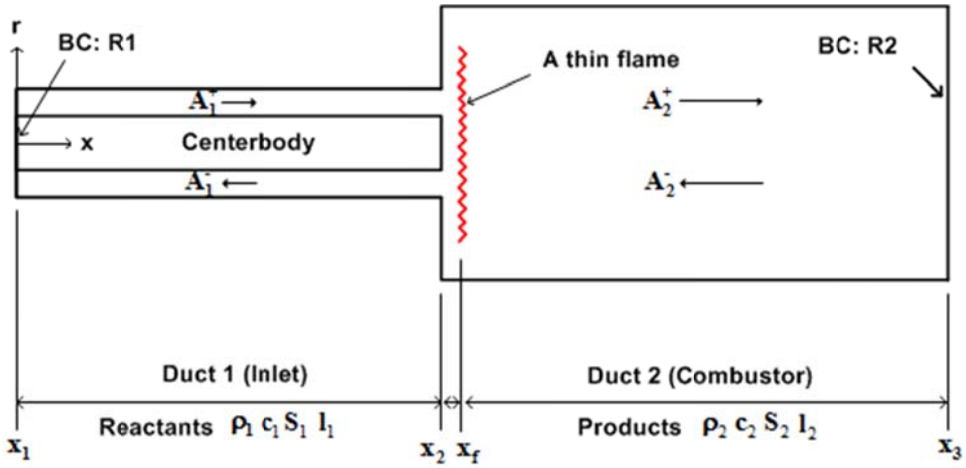

Fig. 2.2 Schematic of one dimensional reacting fluid flow with flame at $x = x_f$.

2.1.1 Acoustic wave equation

The basic assumptions used to derive the conservation equations for the flow in the combustor are: 1) One-dimensional flow, in the longitudinal direction of the combustor. (This is a valid assumption when the acoustic frequencies considered are low with respect of the cut-off frequency of the combustor, and hence waves considered are planar, and all modes are longitudinal), 2) Inviscid flow, i.e. the duct has negligible dissipation effect on the acoustic waves, 3) Negligible thermal conductivity to the surroundings, 4) Perfect gas and 5) Stationary flow.

In this Section, equations governing the acoustic pressure and velocity are obtained in the presence of unsteady heat addition within the field. These are manipulated to get the forced acoustic wave equation which is then reduced to the case when the mean heat release is negligible, i.e., approximately homogeneous field, and when the mean flow is also negligible.

Taking into consideration the three first assumptions above, the reactive-gas dynamics are described using the conservation equations as:

$$\text{Mass continuity}: \quad \frac{\partial \rho}{\partial t} + \frac{\partial (\rho u)}{\partial t} = 0 \tag{2.1}$$

$$\text{Momentum}: \quad \rho \frac{\partial u}{\partial t} + \rho u \frac{\partial u}{\partial x} + \frac{\partial p}{\partial x} = 0 \tag{2.2}$$

$$\text{Energy}: \quad \rho \frac{\partial e}{\partial t} + \rho u \frac{\partial e}{\partial x} = - p \frac{\partial u}{\partial x} + q \tag{2.3}$$

Where, t and x are time and space, respectively, ρ, u, p, and e are the density, velocity, pressure, and specific internal energy respectively, and q is the heat release rate per unit volume. We assume that the gases on both sides of the combustion zone behave as perfect gases, recall the perfect gas state equation Where, R is the gas constant, and T is the absolute temperature.

$$p = \rho R T \tag{2.4}$$

Combining Eq. (2.1), Eq. (2.3) (note, $\rho e = \rho C_v T = C_v \frac{p}{R} = \frac{p}{\gamma - 1}$, where C_v and γ are the constant-volume specific heat and the specific heat ratio, respectively) and Eq. (2.4), we get

$$\frac{\partial p}{\partial t} + u \frac{\partial p}{\partial x} + \gamma p \frac{\partial p}{\partial x} = (\gamma - 1) q \tag{2.5}$$

Since we are only interested in the small perturbation behavior at the onset of the instability, we use the perturbation method to linearize the system. We separate the system variables into their mean (function of space only) and small perturbation (function of space and time) components as follow, where $\overline{()}$ and $()'$ are the mean and the perturbation of a variable, respectively.

$$
\begin{aligned}
p(x,t) &= \overline{p}(x) + p'(x,t)\ ,\ u(x,t) = \overline{u}(x) + u'(x,t) \\
\rho(x,t) &= \overline{\rho}(x) + \rho'(x,t)\ ,\ and\ \ q(x,t) = \overline{q}(x) + q'(x,t)
\end{aligned}
\tag{2.6}
$$

Substituting the flow variable decompositions in Eq. (2.6) in Eqs. (2.2) and (2.5) and neglecting second order terms of the fluctuating components, we obtain the governing linear equations for the perturbations as:

$$
\overline{\rho}\frac{\partial u'}{\partial t} + \overline{\rho u}\frac{\partial u'}{\partial x} + \overline{\rho}u'\frac{d\overline{u}}{dx} + \rho'\overline{u}\frac{d\overline{u}}{dx} + \frac{\partial p'}{\partial x} = 0 \tag{2.7}
$$

$$
\frac{\partial p'}{\partial x} + \overline{u}\frac{\partial p'}{\partial x} + u'\frac{d\overline{p}}{dx} + \gamma\overline{p}\frac{\partial u'}{\partial x} + \gamma p'\frac{d\overline{u}}{dx} = (\gamma - 1)q' \tag{2.8}
$$

We also assume that the flame zone is spatially localized at x_f (see Fig. 2.2), i.e.,

$$
q'(x,t) = q'_f(t)\delta(x - x_f) \tag{2.9}
$$

Where, q'_f denotes the heat release rate per unit area and $\delta(\cdot)$ denotes the Dirac delta function. This implies that the mean variables are essentially constant over the length of the combustor except for a step change at x_f. For low Mach number flows, the effect of the step change in the pressure is negligible compared to the change in the mean velocity or mean density, and the spatial gradient of the mean pressure as well as the mean velocity can be considered small (see Ref. [1] for more details).

If the mean flow Mach number is negligibly small, Eqs. (2.7) and (2.8) can be obviously simplified as

$$
\left(\frac{\partial^2 p'}{\partial t^2} - \overline{c}^2\frac{\partial^2 p'}{\partial x^2}\right) = (\gamma - 1)\frac{\partial q'_f}{\partial t}\delta(x - x_f) \tag{2.10}
$$

$$\frac{\partial p'}{\partial t} + \gamma \bar{p} \frac{\partial u'}{\partial x} = (\gamma - 1) q'_f \delta(x - x_f) \tag{2.11}$$

Equations (2.10) and (2.11) capture the dominant characteristics of the thermoacoustic instability dynamics of the combustor. It should be noted also that the homogeneous form of Eq. (2.10) (i.e., when the RHS equals to zero) becomes the "classical acoustic wave equation". The general solution of the homogeneous wave equation can be represented as [2, 3, 4]:

$$p'(x, t) = \bar{p}\psi(x)\eta(t) \tag{2.12}$$

$$\psi(x) = \sin(kx + \phi_0) \tag{2.13}$$

$$\eta(t) = \sin(k\bar{c}x + \theta_0) \tag{2.14}$$

Where, $\psi(x)$ is called the basis function and describes the spatial component of the solution of the wave equation, and $\eta(t)$ represents the temporal component. k is the wave number, θ_0 is a given phase, and both are determined by the boundary conditions in the field. For example, in a tube open at both sides, the boundary conditions can be described as: $p'(0, t) = p'(L, t) = 0$. Solving Eq. (2.13) with these boundary conditions, we get

$$\phi_0 = 0, \pi, 2\pi... \tag{2.15}$$

$$k = \frac{n\pi}{L},\ n = 1, 2, 3, ... \tag{2.16}$$

We see that there exists an infinite set of discrete values of k, for which p' has non-trivial solutions (eigenvalues). Hence, $\psi(x)$ will represent the modes along the tube (n-modes). In Fig. 2.3, the first three modes for an open-open tube are shown, the points

where $\psi = 0$ are called nodes, and the crests are called anti-nodes [1, 4, 5].

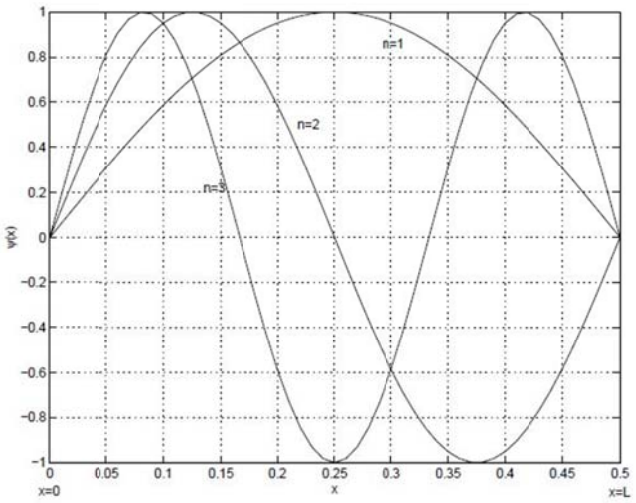

Fig. 2.3 Acoustic longitudinal modes for the open-open ended combustor geometry.

2.1.2 Theory of the Rayleigh criterion

In this section, we will carry out an energy balance of the combustor. We should note that the acoustic field (hosted by the combustor) is the primary energy storage mechanism in the combustor. Increasing or decreasing the storage (or internal) energy of this field can be achieved by exerting work or heating the field. Since, in our case, the flame is considered a localized heat source, only a small control volume in the acoustic field is heated, the small volume expands and in turn exerts work on the field.

The acoustic energy density, e', in a one-dimensional acoustic field can be derived from the unforced conservation equations as (see [2] for more details)

$$e' = \frac{\bar{\rho} u'^2}{2} + \frac{p'^2}{2\overline{\rho c^2}} \tag{2.17}$$

Where, the first term in the RHS is the kinetic acoustic energy and the second is the potential acoustic energy. It is clear that any system that would sustain waves (also, as in many vibration processes) should have these two components of energy, and the periodic conversion from one form to the other sustains the oscillatory behavior.

The temporary, over the period of oscillation, τ, and spatially, over the length of the combustor, L, we get

$$\Delta_\tau \int_0^L e' dx = \frac{(\gamma-1)}{\overline{\rho c}^2} \int_0^\tau \int_0^L p'(x,t) q'(x,t) dx dt - \Delta_L \int_0^L E' dt - \int_0^\tau \int_0^L \phi(x,t) dx dt \tag{2.18}$$

Where, Δ_τ and Δ_L are the changes over time and length, respectively. The LHS of Eq. (2.18) represents the change in the acoustic energy per cross-sectional area of the combustor. The first term in the RHS is the Rayleigh integral (similar to Eq. (1.1)), the second term represents the acoustic energy flux across the control surface of the field and is defined as $E' = \rho' u'$, and the last term quantifies the dissipation in the acoustic field. We can clearly see from the energy balance in Eq. (2.26) that when the Rayleigh criterion is satisfied, i.e. p' and q' become in phase, and the gain of the first term in the RHS is large enough to overcome both the dissipation and the energy flux terms (which are typically small), there will be an increase in the acoustic energy in the combustor, i.e. thermo-acoustic instability will be dominant [6].

The latter can happen when perturbations in the acoustic field affect the inlet conditions of one of the reactants (fuel or air), prior to mixing, and thus causes perturbations in the equivalence ratio which translate into perturbations in the unsteady heat release. This case could happen if the inlet conditions of one of the reactants to the combustor are not choked [7]. In both cases, if these perturbations are such that the phase between p' and q' is $\leq 90^o$, instability will occur.

2.1.3 Standing wave in combustor and inlet mixing section

For definition of the acoustic standing wave and phase analysis, we measured the multi-position dynamic pressure in combustor and inlet mixing section using the 11ea. dynamic pressure sensors. And the combustion instability characteristics in combustor and inlet mixing section are represented by below fundamental equations of acoustic standing wave. At the combustor section ($0 \le x \le L_{comb.}$) can be written as:

$$\text{First of half wave equation} = \frac{A_5}{\cos\left(\frac{\pi X_{D5}}{\lambda}\right)} * \cos\left(\frac{\pi x}{\lambda}\right) \qquad \lambda = L$$

$$\text{Second of half wave equation} = \frac{A_5}{\cos\left(\frac{\pi X_{D5}}{\lambda}\right)} * \cos\left(\frac{\pi x}{\lambda}\right) \qquad \lambda = \frac{L}{2}$$

$$\text{First of quater equation} = \frac{A_5}{\cos\left(\frac{\pi X_{D5}}{\lambda}\right)} * \cos\left(\frac{\pi x}{\lambda}\right) \qquad \lambda = 2L$$

$$\text{Second of quater equation} = \frac{A_5}{\cos\left(\frac{\pi X_{D5}}{\lambda}\right)} * \cos\left(\frac{\pi x}{\lambda}\right) \qquad \lambda = \frac{2L}{3} \tag{2.19}$$

At the inlet mixing section ($L_{inlet} \le x \le 0$) can be written as:

$$\text{First of half wave equation} = \frac{A_4}{\cos\left(\frac{\pi X_{D4}}{\lambda}\right)} * \cos\left(\frac{\pi x}{\lambda}\right) \qquad \lambda = L$$

$$\text{Second of half wave equation} = \frac{A_4}{\cos\left(\frac{\pi X_{D4}}{\lambda}\right)} * \cos\left(\frac{\pi x}{\lambda}\right) \qquad \lambda = \frac{L}{2}$$

$$\text{First of quater equation} = \frac{A_4}{\sin\left(\frac{\pi X_{D4}}{\lambda}\right)} * \sin\left(\frac{\pi x}{\lambda}\right) \qquad \lambda = 2L$$

$$\text{Second of quater equation} = \frac{A_4}{\sin\left(\frac{\pi X_{D4}}{\lambda}\right)} * \sin\left(\frac{\pi x}{\lambda}\right) \qquad \lambda = \frac{2L}{3}$$

(2.20)

2.2 Flow Dynamics of Swirl Injector

The swirling flows have been widely used in practical combustion systems such as industrial burners, furnaces, and gas turbine combustors because they enable high energy conversion in a small volume. Swirl flames exhibit good ignition and stabilization behavior over a wide operating range by promoting rapid mixing, improving flammability limits, shortening flame size, and reducing pollutant emissions [8]. The vast majority of gas turbine systems employ swirl injectors that provide a lot of advantages. Fuel injection and mixing efficiency is a very important factor for combustion emissions and gas turbine efficiency. Nowadays, most gas turbines use swirl injectors. Using this kind of injector affects flame stabilization and mixing quality. A swirl injector is composed of a central recirculation zone and an outer recirculation zone. This central recirculation zone re-circulates combusted hot gas to the nozzle part and it works as a heat source of the combustion and central recirculation zone, making a shear layer of the mixture and re-circulated flow, which will help the mixing efficiency [9].

As mentioned above, a recirculation zone is important for the stabilization of flames, and this is generated by swirl flow. The pressure gradient and distribution inside the combustor is the most important factor in forming a recirculation zone. As the flow passes through the swirl vane, tangential-direction velocity components are generated in the flow, further generating centrifugal force toward the outside of the combustor. A radial-direction pressure gradient is then formed in order to sustain equilibrium with the centrifugal force, which is called simple radial equilibrium flow. The pressure gradient

generated at this time can be calculated through a radial-direction momentum equation [10, 11]. First of all, an assumption can be established for the simple radial equilibrium flow as follows: Both the axial-direction and tangential velocity cannot exist in a steady state condition. Therefore, axial and radial velocities are related to radius functions, axial symmetry and radial-direction velocity. Under this assumption, the axial and tangential direction momentum equations become trivial solutions. The radial-direction momentum equation can be regarded as a governing equation that shows the pressure gradient of swirl flow.

$$\frac{\partial v_r}{\partial t} + (V \bullet \nabla) v_r - \frac{1}{r} v_\theta{}^2 = -\frac{1}{\rho}\frac{\partial p}{\partial r} + g_r + \nu(\nabla^2 v_r - \frac{v_r}{r^2} - \frac{2}{r^2}\frac{\partial v_\theta}{\partial \theta}) \quad (2.21)$$

Reduces to

$$\frac{\partial p}{\partial r} = \rho \frac{v_\theta{}^2}{r} \quad (2.22)$$

Figure 2.4 and Equation (2.22) show that the centrifugal force and the pressure gradient have equilibrium with each other. With this equation simply integrated, it was found that the closer it gets to the combustion chamber, that is, the smaller the radius becomes, the lower the stagnation pressure becomes. Since the tangential velocity component gets damped while moving closer toward the axial direction, the radial pressure gradient disappears in the back of the combustion chamber when it has a sufficient distance toward the axial direction, which indicates an achievement of pressure equilibrium. Therefore, around the combustion chamber wall, whose radius is large, a negative pressure gradient is formed, through which the pressure decreases gradually; meanwhile, in the central part of the combustion chamber, a positive pressure gradient is formed, through which the pressure gradually increases. Due to such a pressure distribution, outside flow comes rolling up the central part of the combustion chamber, enhancing the funnel-shaped recirculation zone existing in the central axis.

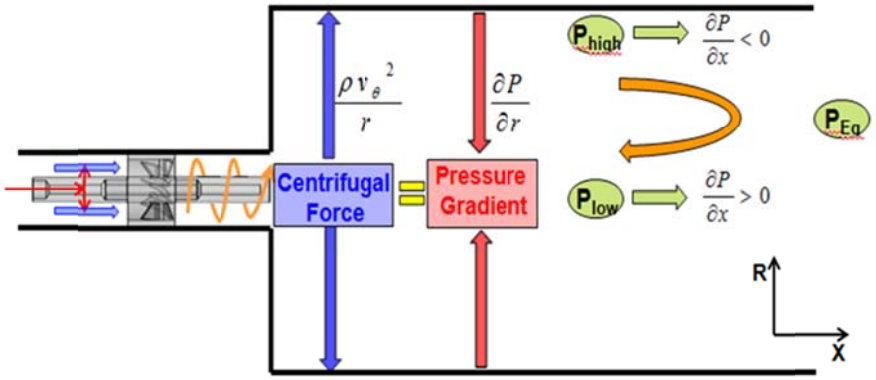

Fig. 2.4 Formation of recirculation zones for simple radial equilibrium flow condition.

2.3 Liquid Jet Column Trajectory

The theoretical expression of the liquid column trajectory shows the trajectory and the breakup point of the liquid column prior to the breakup, under the assumption that the horizontal acceleration is identical to the aerodynamic force acting on the front of the liquid column, as the relation of the momentum flux ratio (q) and the injected fuel jet velocity, the drag coefficient (C_D) and normalized axial (air-stream) distance (x/d), and showed the empirical formula by the injection angle (θ) as the liquid column trajectory equation. Also, using the breakup regime parameter of the time value from the secondary breakup of the spherical droplet, the horizontal and vertical breakup lengths were predicted and its reliability was confirmed by the empirical results in various cases [12, 13].

Under the 90° injection angle(Fig. 2.5(a)), trajectories of a liquid jet transversely injected into crossflows have been studied by numerous researchers. From previous research, it is known that the orifice diameter and liquid/air momentum flux ratio are the most important parameters for the trajectories. Schetz et al. [14] obtained the complete formula including the influence of q, the aspect ratio d_f/d_s of the injector and

injection angle θ as follows:

$$\frac{h}{d_j} = 1.32\ q^{0.5}\ C_d \left(\frac{d_{eq}}{d_f}\right)^{0.5} \left(\frac{d_f}{d_s}\right)^{0.46} \ln\left[1+6\frac{x}{d_j}\right] + \sin\left(\frac{2}{3}\theta\right) \qquad (2.23)$$

Assuming that liquid acceleration was balanced with aerodynamic drag forces and that the liquid column could be modeled as a cylindrical fluid element of the diameter of the nozzle exit. Wu et al. [15] calculated the correlation of the liquid column trajectory before the fracture point as follows:

$$\frac{y}{d} = 1.37\ \sqrt{q\left(\frac{x}{d}\right)} \qquad (2.24)$$

And the below 90° injection angle condition (Fig. 2.5(b)), By introducing an average drag coefficient, C_D, the axial momentum equation can be written as follows:

$$\frac{\pi}{4}\ \rho_f\ d^2\ \ell\ \frac{du_f}{dt} = \frac{1}{2}\ c_o\ \rho_g \left(u_g - u_f\right)\left[\left(u_g - u_f\right)^2 + \left(v_g - v_f\right)^2\right]^{\frac{1}{2}} ld \qquad (2.25)$$

To render the above equation more tractable, the following considerations were made. For the present investigation, $\left(v_g - v_f\right)^2$ was estimated to be considerably less than $\left(u_g - u_f\right)^2$ in most cases and was therefore neglected. In addition, the variation in u_f was, in most cases, very small as compared to u_g, so that the approximation $u_g - u_f \approx u_g - u_j$ could be made. Finally, ρ_g and u_g were presumed constant at their respective free stream values, and ρ_f and u_f were presumed constant at their

respective jet exit values, ρ_j and u_j.

$$u_f = \frac{2C_D}{d\pi}\frac{\rho_\infty}{\rho_j}\left(u_\infty - u_j\right)^2 \tag{2.26}$$

With $u_f = \frac{dx}{dt}$, a second integration with respect to time yields the following equation.

$$x = \frac{C_D}{d\pi}\frac{\rho_\infty}{\rho_j}\left(u_\infty - u_j\right)^2 t^2 + u_j t \tag{2.27}$$

Because the transverse velocity of the liquid column was presumed constant and equal to the transverse component of the jet exit velocity, $u_f = dy \big/ dt = v_j$, so $y = v_j t$ and the trajectory equation could be written as follows:

$$\frac{x}{d} = \frac{C_D}{\pi}\frac{\rho_\infty}{\rho_j}\frac{\left(u_\infty - u_j\right)^2}{v^2{}_j}\left(\frac{y}{d}\right)^2 + \frac{u_j}{v_j}\left(\frac{y}{d}\right) \tag{2.28}$$

With the momentum flux ratio $\overline{q}$ and the injection angle θ, the following equation was derived.

$$\frac{x}{dq} = \frac{1}{\pi}\frac{C_D}{\sin^2\theta}\left(1 - \frac{v_f \cos\theta}{v_a}\right)^2\left(\frac{y}{dq}\right)^2 + \frac{\cos\theta}{\sin\theta}\left(\frac{y}{dq}\right) \tag{2.29}$$

Therefore, the trajectory experimental formula of the liquid column region can be calculated depending on the injection angle that is less than 90° and on the reverse

injection. Here, x indicates the value of the axial distance of the axial (air-stream) direction, y indicates the value of the penetration distance of the penetration direction, d is the diameter of the orifice exit, θ is the injection angle, v_f is the fuel velocity and v_a is the value of the air velocity.

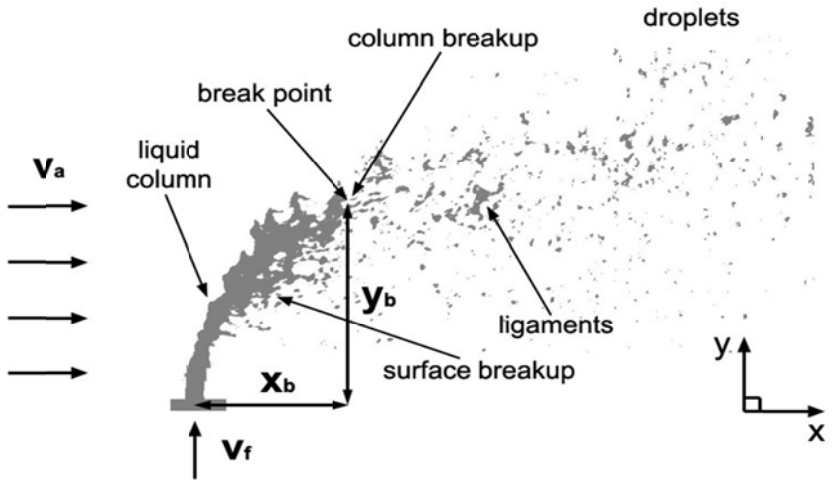

(a)

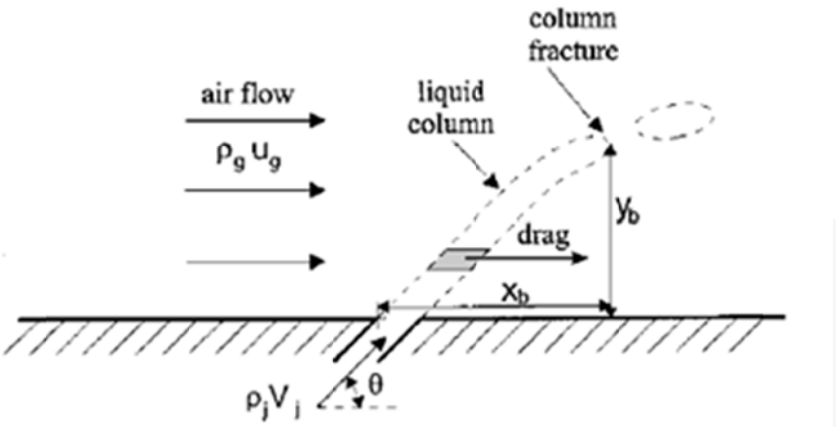

(b)

Fig. 2.5 Force diagram at the transverse liquid spray jet in crossflow; (a) 90° injection, (b) below the 90° injection.

CHAPTER 3

EXPERIMENTAL FACILITY AND TECHNIQUES

3.1 Model Gas Turbine Combustor

The combustor used for this study is a model gas turbine combustor simulating in the 1/3 scale downed of a GE 7FA+e DLN-2.6 gas turbine combustor, characterized with partially premixed and swirl stabilized flame, and the form is as shown in Fig. 3.1.

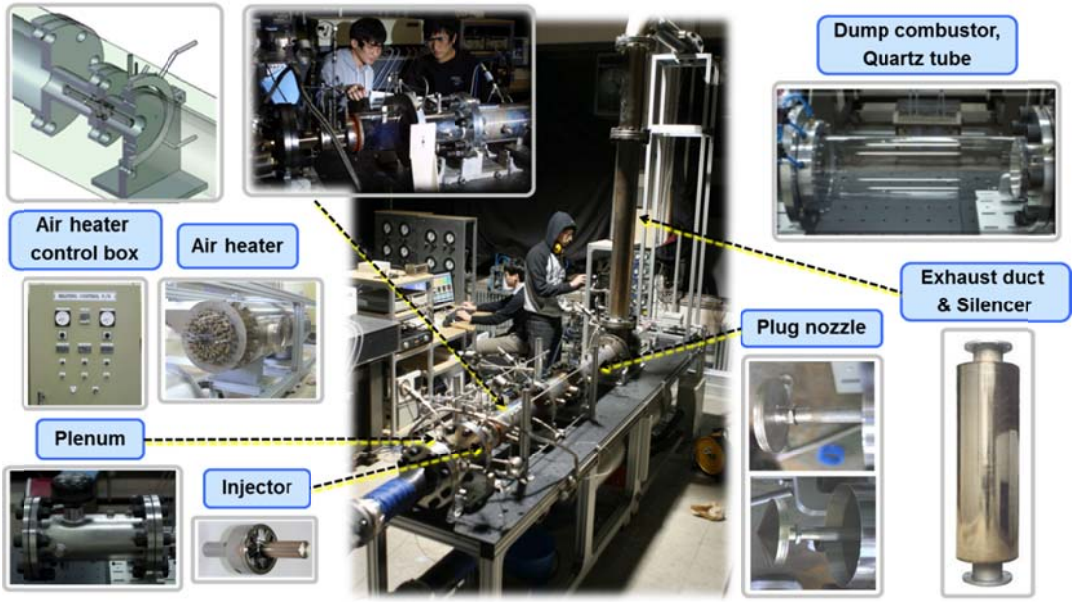

Fig. 3.1 Model dump shaped combustor simulating in the 1/3 scale downed of a GE 7FA+e DLN-2.6 gas turbine combustor and related component.

It is composed of air heating device, air supply lines, fuel nozzles, flame visualization quartz combustor and spike-typed plug nozzle of the exhaust duct for acoustic boundary. The air heating device consists of three 40 KW class electric heating element, functioning to heat the supplied air up to 873K. As shown in Fig 3.2, the

temperature of air supplied during the experiment is controlled within ±1%. And the air temperature is calibrated by K-type thermocouple at all of air velocity experimental conditions.

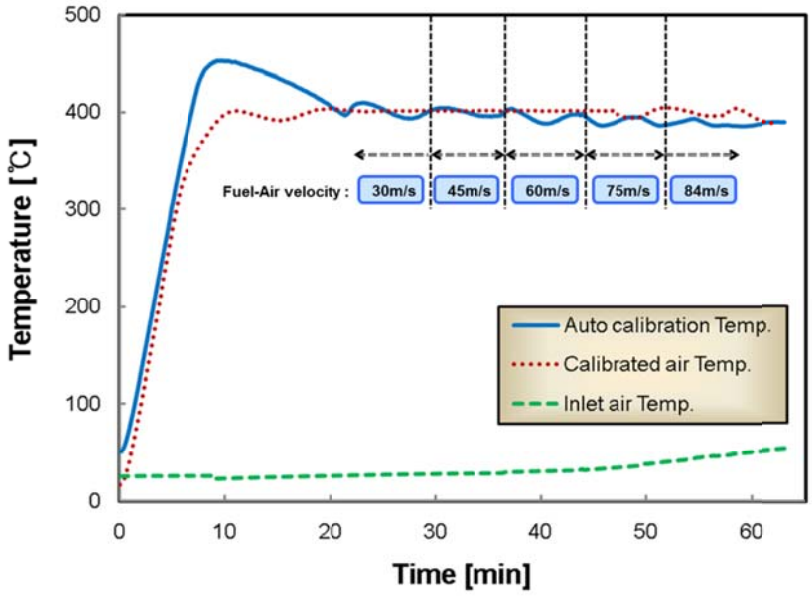

Fig. 3.2 Heated air calibration result of air heater control.

As shown in Fig 3.3, one of the main variables for this experimental study, the fuel-air mixing section was located between the combustor dump-side and the chocking orifice at the back of the air heating device, and there were three kinds in lengths, such as 470 mm, 550 mm and 870 mm, although they were all 40 mm inner diameter. The swirl injector used for this device is an axial-typed injector, and the angle of swirl vanes are 0°, 30° and 45°, and the number of vanes is 10. On the spot of 20 mm in front of the swirl vane, fuel is injected from 10ea nozzles with a 1.2 mm-sized hole, and through the 112 mm-sized mixing length in the back of the swirl vanes, fuel and air get partially premixed. The swirl effect can be expressed in the swirl number, which is the ratio of the tangential momentum and the axial momentum, and it can be approximately calculated through the

following equation [1].

$$S = \frac{2}{3}\left[\frac{1-(d_h/d)^3}{1-(d_h/d)^2}\right]\tan\Phi \approx \frac{2}{3}\tan\Phi \quad (d_h << d) \tag{3.1}$$

According to the above equation, the swirl number of the swirl injector used for this research was about 0.42(30°) and 0.72(45°). A circular stainless steel (@ Chapter 6, case 1, 2) and a quartz tube (@ Chapter 6, case 3 ~ 8) for the flame visualization were alternately used, and the diameter inside the combustor was 120 mm. The plug nozzle placed at the exhaust duct was supposed to function to change the resonant frequency of the combustor by making an acoustic boundary that blocks 91% of the combustor exhaust duct, which was designed to regulate the length of the combustor by 0.1 mm from 800 mm to 1680 mm through the stepper motor located in the exhaust part of model gas turbine combustor.

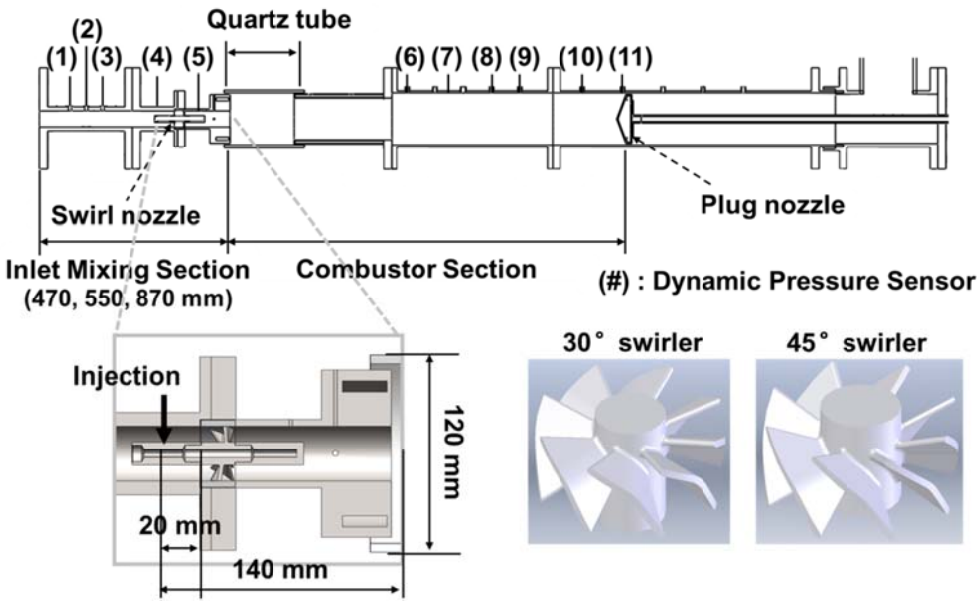

Fig. 3.3 Schematics of model gas turbine combustor and swirl injectors.

Figure 3.4 shows the calibration data and composition of air supply system. Working air was pressurized up to 8.5 bar by air compressor. The ACS100TA2 (Kyungwon compressor) was used for compressing air and it can blow out the air to 12.1 m^3/min. Many instruments, which are some chocked orifices, pressure differential gage and ball valves, were located in air supply line. Pressurized air was stabilized through the chocked orifice and then passed through the pressure differential gage. The air mass flow rate was controlled by ball valve using measured pressure differential gage. In addition, we measured air supply pressures and air temperatures, and these were used to control the air mass flow rate.

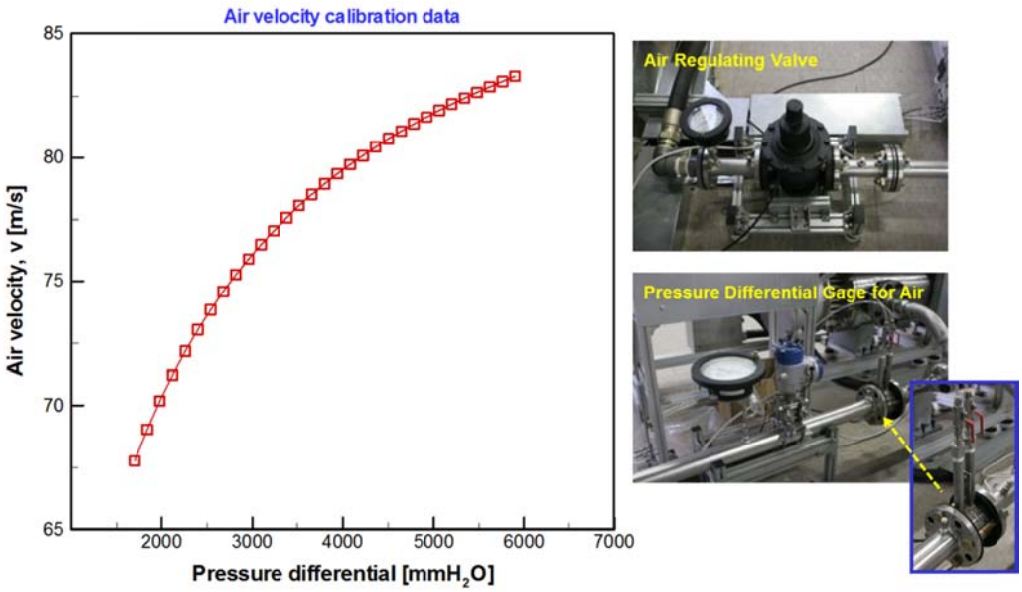

Fig. 3.4 The air calibration data and composition of air supply system.

Figure 3.5 shows the calibration data and composition of fuel supply system. In this experiments, Natural gas (89.4% CH_4, 8.6% C_2H_6, 1.39% C_3H_8, 0.25% i-C_4H_{10}, 0.32% n-C_4H_{10}, 0.04% N_2) was used as the fuel. And it was serviced by Seoul city gas Co., Ltd. (SCG). The fuel chocked orifice was used for precise control of equivalence ratio. In this

experimental study, fuel mass flow rate required about 0.9 ~ 3.5 g/s. So fuel orifice size (1 mm, 2.5 mm, 3 mm and 4 mm) were selected by each test condition for appropriate mass flow rate. And each orifice was calibrated by mass flow meter. The fuel mass flow supplied to the model dump combustor experimental device was measured with an M-1500SLPM-D Mass Flow Meter, made by Alicat Scientific Company. The fuel and air mass flow rate calculated through the flow meter and the differential pressure gauge was finally confirmed through Model 6332D, which is a Hot-wire velocimeter made by KANOMAX, and it was found that the errors of the values calculated and the mixture velocity measured at the combustor exit were within the range of ±3%.

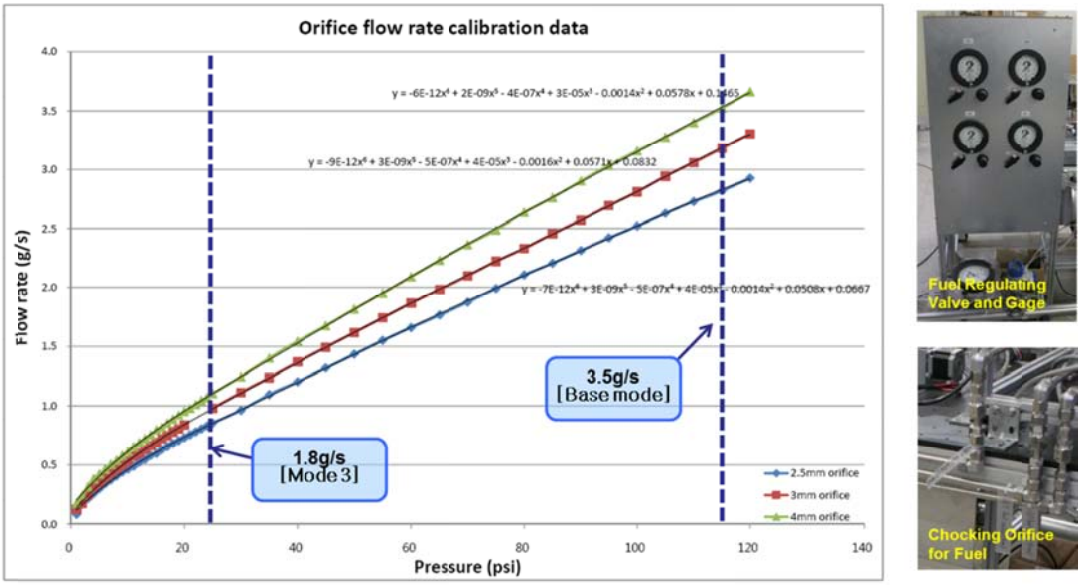

Fig. 3.5 The fuel calibration data and composition of fuel supply system.

Figure 3.6 shows the ignition system consisted of high voltage generator, tungsten wire and ceramic tube. About 18,000 volt was induced by high voltage generator. The tungsten wire was placed inside a ceramic tube for insulation. And the ceramic tube was inserted in a dump surface. Spark was induced by the gap between dump surface and

tungsten wire. The location of pyrotechnic initiator was selected to consider the vortex shedding zone. And the exhaust nozzle, dump surface and combustor were cooled down by water and the outer surface of combustor was cooled down by air.

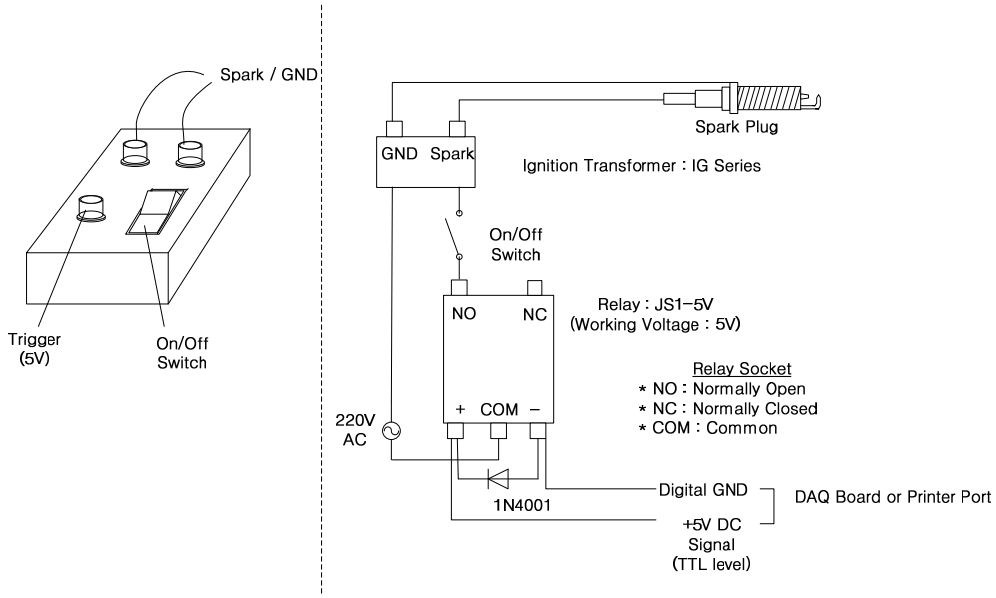

Fig. 3.6 The ignition system consisted of high voltage generator and spark plug.

3.2. Combustion Data Acquisition System

To measure the flow rate of fuel and air, combustion static pressure, exhaust emission and combustion dynamic characteristics of the model dump combustor, this experimental study used various kinds of sensors and a flow-meter to regulate the flow rate. First of all, to control the change of static pressure and the air flow rate before and after the combustion experiment, a total of six static pressure sensors made by Valcom Company were used. A K-type thermo couple was used to measure the temperatures of eight channels in total consisting of the air-supply (3 each), the combustor (4 each), and the exhaust emission sensor location (1 each), as well as the temperature around the

differential pressure gauge for the regulation of the fuel and air flow rate. To observe the oscillation of dynamic pressure occurring during the combustion experiment, we used five 102A05-type dynamic pressure sensors, manufactured by PCB Company, for the inlet mixing section and six for the combustor, as well as infinity probes, which suppress the reflected wave of dynamic pressure [2, 3]. In addition, the sampling rate was observed by receiving 10,000 data per second, and through Fast Fourier Transformation (FFT) techniques, it was possible to analyze them up to 5,000 Hz. The location of each dynamic pressure sensor is shown in Fig. 3.3. Moreover, OH* chemiluminescence was measured from the flame around the dump side. By using a high-speed ICCD camera made by Photron Company, we photographed flames at the speed of 1/6000 fps, and were able to obtain the pressure oscillation and heat release values from the time axis in the same experimental conditions by phase locking the dynamic pressure sensor. Fig. 3.7 indicated that phase locking system in this experimental study.

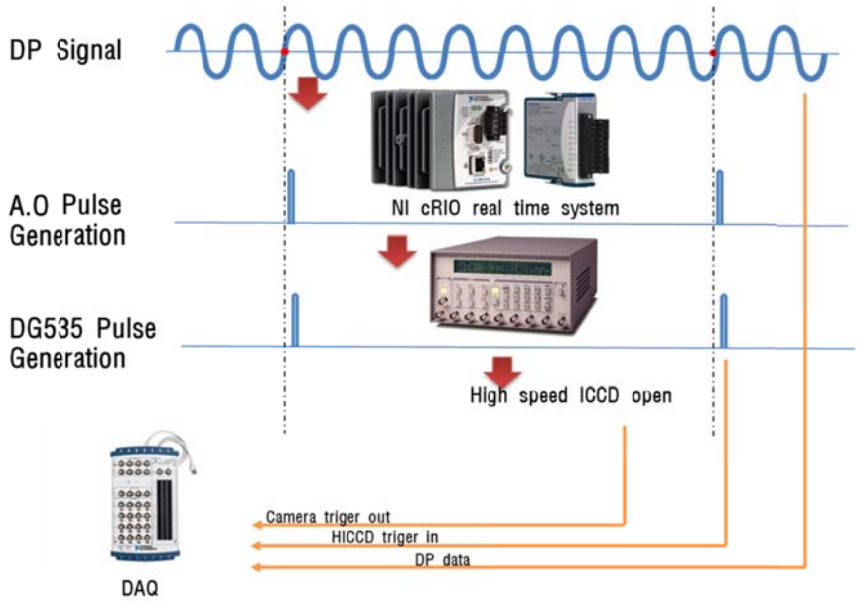

Fig. 3.7 LabView based phase locking system for heat release oscillation.

Data collection of the sensors was conducted with such devices as the C-RIO and DAQ made by National Instrument Company. The processing of the sensor data for the fuel and air mass flow rate control were performed with the use of a LabView-based program as shown in Fig. 3.8. And the heat release oscillation is basic data to be measured in order to understand causes of combustion instability. Thus, this study carried out a chemiluminescence signal measurement research and started photographing spots where – changes to + by observing dynamic pressure information through Nl cRIO. Besides, this study acquired signals that drive high-speed ICCD, signals of photos being taken and dynamic pressure signals by using DAQ and analyzed the flame visualization information and acoustic field oscillation information at the same time, especially about the combustion instability phenomenon, through the process of measuring the results of dynamic pressure and heat release waves in the same time domain.

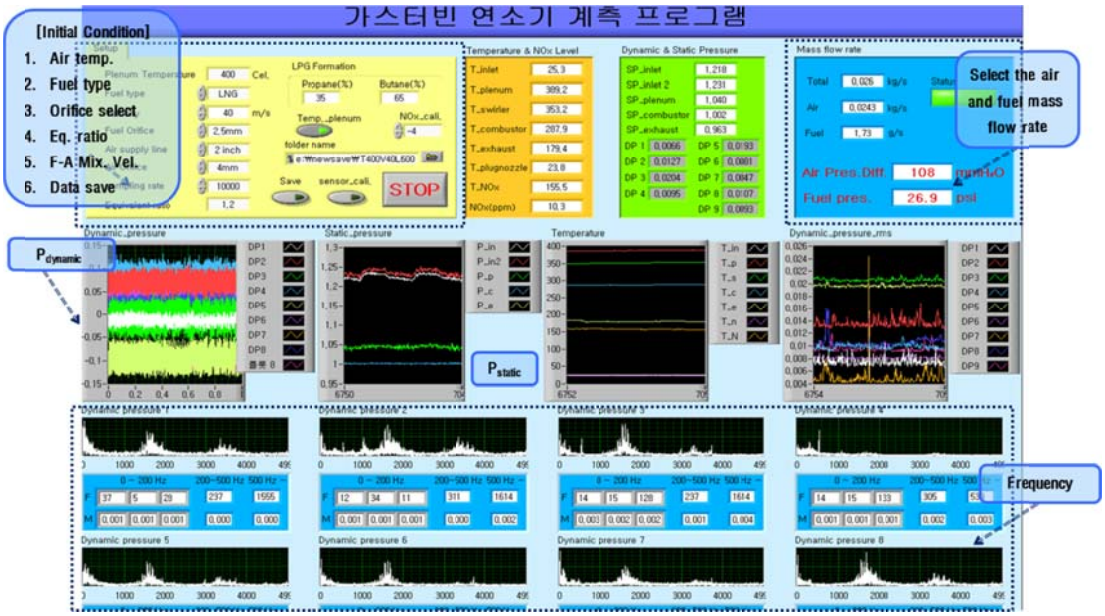

Fig. 3.8 LabView based combustion data collecting system and user interface program.

3.3 Multi-Position Dynamic Pressure Sensing System

To observe the oscillation of dynamic pressure and standing wave form occurring during the combustion experiment, this study used 5ea 102A05-type dynamic pressure sensors, manufactured by PCB Company, for the inlet mixing section, 6ea for the combustor, and the infinity probes that suppress the reflected wave of dynamic pressure [4]. In addition, the sampling rate was observed by receiving 10,000 data points per second. Through FFT, it was possible to analyze up to 5,000 Hz. The location of each dynamic pressure sensor is shown in Fig. 3.9. As aforementioned it, the data collection of the sensors was conducted with such devices as a C-RIO and DAQ made by National Instrument Company. The sensor data processing the fuel and air mass flow rate control were performed through a LabView-based program.

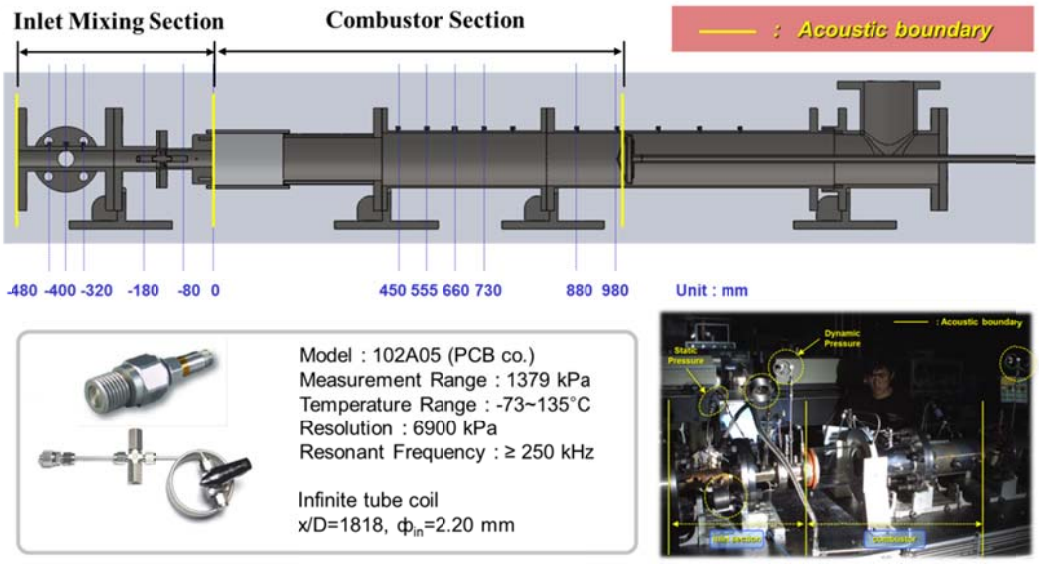

Fig. 3.9 Composition of dynamic pressure sensors and location in model gas turbine combustor.

3.4 Chemiluminescence and Flame Structure Analysis

Chemiluminescence from hydrocarbon flames arises from specific molecules that are lifted to an excited state by exothermic chemical reactions and then subsequently decay back to equilibrium energy levels by emitting a photon. Chemiluminescence emission occurs in specific wavelength bands that are characteristic of the emitting molecules. Because the molecules responsible for the chemiluminescence change for different combustion regimes and types, chemiluminescent emissions can provide information about the nature of the reactions and the fuel/airmixture [5].

Most naturally emitted ultraviolet and visible radiation of flames, called chemiluminescence, is caused by short lived electronically excited intermediate species such as OH*, CH* or C_2* formed during chemical reactions [6, 7]. An example is depicted in Fig. 3.10 (left panel) from a Bunsen burner, operated with a stoichiometric mixture of methane and air. If the radiation emitted by this flame is dispersed in a spectrometer into its wavelength components, spectra can be observed like those shown in Fig. 3.10 (right panel). On recognizes characteristic emission bands originating from the above mentioned species in their respective electronically excited (A) states of OH* (310 nm), CH* (388, 431 nm) und C_2* (473 nm), respectively. It is therefore of interest to investigate if the intensities or spectral shapes of these band systems can provide quantitative information on, e.g., local fuel/air ratios, heat release rate (HRR) or chemical processes of the combustion system investigated. If so, this would be of great importance for technical combustion systems, since detecting chemiluminescence radiation is a cheap and non-intrusive method for monitoring the combustion event in environments such as power plants, waste incinerators or combustion engines [8].

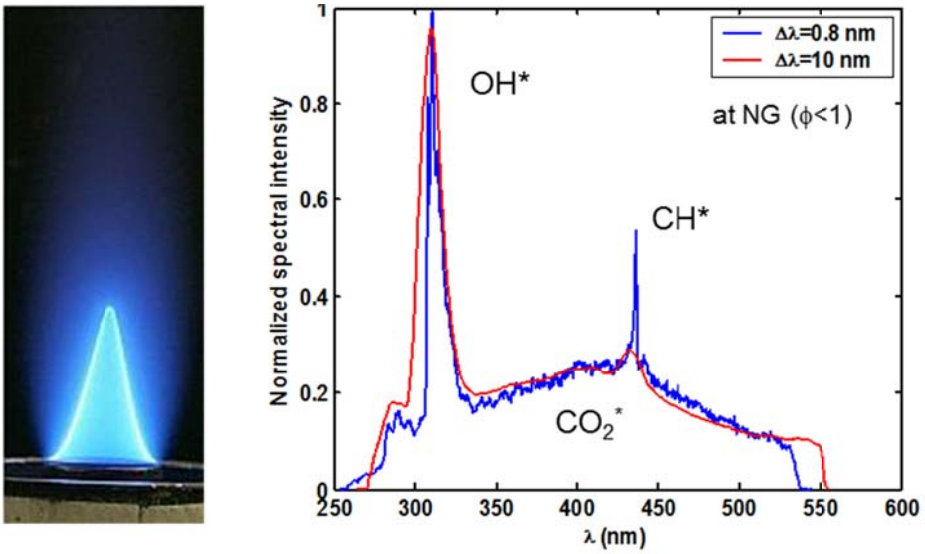

Fig. 3.10 Spectrum of the chemiluminescence radiation emitted from a premixed methane/air flame in Bunsen burner [8].

Abel convolution is one of optical diffraction tomography and integral transform, such as onion pilling method and back-projection algorithm. It is useful to transfer a 3-dimensional line-of-sight image to a 2-dimensional profile [9]. According to Pun et al. [10], light emission measurement of chemiluminescence cannot capture the fine flame structure, because the signal is integrated through the depth of the flame. Therefore, each image was processed with Abel convolution. With Abel inverted images, the time-averaged flame structure profile can be reconstructed, if the flame shape is axisymmetric.

This work is focused on the interpretation of OH and CH chemiluminescence data, because they have been widely employed as a flame marker [11] to study the combustion process by spectral combustion diagnostics [12, 13-18]. A high-speed ICCD Camera was used in this study for recording OH and CH chemiluminescence images of high-frequency instability phenomenon. For synchronization of heat release data from ICCD and dynamic data from PCB dynamic sensor, NI cRIO was used for triggering and NI DAQ was also used for recording data. NI cRIO operates at 40M Hz and has reliable

computation speed; therefore, it was used for detecting the rising edge of dynamic pressure data and triggering at the data changing point, which occurs when the data changes from positive to negative. To quantify the flame structure, the concept of maximum intensity location of the flame was used to calculate the flame center as shown in Fig. 3.11. The flame angle is computed from the intensity center and the center of the dump plane. In other words, the angle between the intensity center and the middle of the dump plane is regarded as the flame angle. Flame angle can demonstrate the axial and radial momentum ratio; a similar concept about flame center is used in the research of Kim et al [19, 20]. There, flame angle is a factor that can represent the flow structure of the flame. This calculation for the flame center is performed in all phases of the Abel-inverted image and shows the flame angle change at each phase.

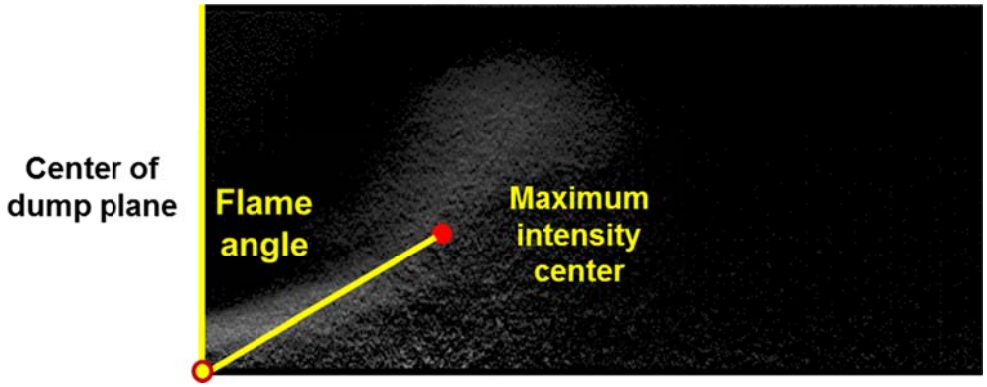

Fig. 3.11 Definition of flame angle and length of maximum intensity location.

3.5 PIV (Particle Image Velocimetry)

Particle Image Velocimetry (PIV) is a quantitative method for measuring 2-D velocity fields instantaneously, using consecutive images of particles illuminated by light sheets. The experimental setup of a PIV system typically consists of several subsystems [21]. Tracer particles have to be added to the flow, and these particles have to be illuminated in a plane of the flow at least twice within a short time interval. The light

scattered by the particles has to be recorded either on a single frame or on a sequence of frames. The displacement of the particle images between the light pulses has to be determined through evaluation of the PIV recordings. For evaluation, the digital PIV recording is divided in small subareas called “interrogation areas”. The local displacement vector for the images of the tracer particles of the first and second illumination is determined for each interrogation area by means of statistical method (auto- and cross- correlation). It is assumed that all particles within one interrogation area have moved homogeneously between the two illuminations. The projection of the vector of the local flow velocity into the plane of the light sheet (2-component velocity vector) is calculated taking into account the time delay between the two illuminations and the magnification at imaging. The process of interrogation is repeated for all interrogation areas of the PIV recording. Fig. 3.12 shows the typical procedures of PIV measurement.

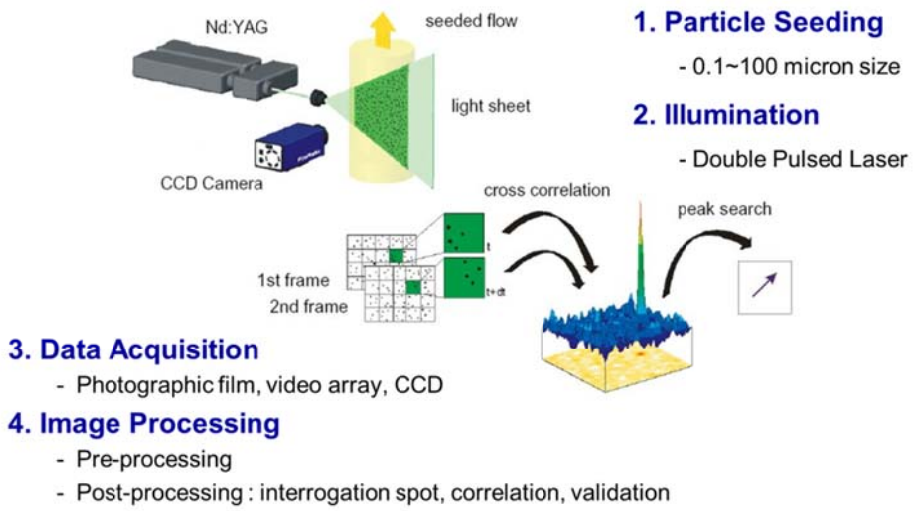

Fig. 3.12 Typical Procedures of PIV measurement.

The correlation function is expressed as follows:

$$h\left(s_x,\ s_y\right) = \int_0^\infty \int_0^\infty f\left(x,\ y\right) h\left(x + s_x,\ y + s_y\right) dxdy \tag{3.2}$$

A correlation method is classified into auto-correlation and cross-correlation according to the number of functions. Auto-correlation is for the case $f\left(x,\ y\right) = g\left(x,\ y\right)$ in Eq. (3.2) and the cross-correlation is the $f\left(x,\ y\right) \neq g\left(x,\ y\right)$ case. Auto-correlation is used when the first image and the second image are recorded in one frame (single frame / double exposure) and cross-correlation is used when the two images are recorded in separate frames (double frame / single exposure). Compared to auto-correlation method, cross-correlation method has some merits: 1) The problem of directional ambiguity is eliminated, 2) The algorithm is simple because there is only one peak as a result of correlation and 3) Dynamic range is relatively large.

3.6 PLLIF (Planar Liquid Laser Induced Fluorescence)

To measure the trajectory and breakup length of the liquid column spray jet, we used the PLLIF (Planar Liquid Laser Induced Fluorescence) technique. Another approach to the patternation of fuel sprays is the use of PLLIF (Planar Liquid Laser Induced Fluorescence). The PLLIF technique is based on the fact that the fluorescence signal intensity of a spray drop is proportional to the concentration of fluorescent molecules (i.e. the volume of the drop) under the condition that the laser light absorption is low enough for the molecules to be uniformly illuminated [22]. The grey level of the *i*-th and *j*-th pixel of the CCD array by the fluorescence signal can be expressed as follows [23]:

$$G\left(i,\ j\right) = CI_0 \sum_k n_k d_k^3 \tag{3.3}$$

Where, C is a constant and I_0, the incident laser beam intensity at the (i, j) pixel, is assumed to be constant within the pixel. Since the drop number density of the k_{th} size class $d_k(n_k)$ is the time-averaged value, the grey level in Eq. (3.3) indicates the total volume of drops which do not pass the unit volume but exist inside the volume during the camera exposure time, i.e. spatial volume (or mass) concentration of the liquid drops. Furthermore, the constant C in Eq. (3.3) is difficult to obtain, so that only the relative distribution of the spray mass concentration can be obtained directly from the PLLIF measurements.

A laser sheet is formed by some combination of cylindrical and spherical optic. A digital camera is used for imaging the energy of interest. Depending upon the information desired, either continuous or pulsed lasers can be employed. If a suitable light source is selected in conjunction with a suitable test fluid, fluorescence can be induced. Fluorescence is dependent upon the concentration of the fluorescing molecules. If a molecule which can be made to fluoresce is present within the test fluid in a homogeneous fashion, then the fluorescence can be related to the volume of material. Some materials may fluoresce naturally (e.g. ringed hydrocarbons), while others may not (e.g. octanes, alchohols, water). In this case, suitable dye can be added to the fluid (e.g. rhodamine, fluorescein). If a dye is added, it can be selected such that is absorption spectra conveniently overlaps with common laser wavelengths.

CHAPTER 4
SWIRL STABILIZED FLAME STRUCTURE AND RECIRCULATION ZONE

4.1 Background and Objectives

At the turn of 21st century, problems related with energy depletion and environmental pollution has become an important issue [1]. Under these circumstances, emission regulations have become more stringent. Many researchers have tried to develop a new type of combustor which burns fuel more efficiently and produces lower emissions [2, 3]. In the context of such efforts, a lean premixed combustor has been introduced and used for power generation all over the world. A lean premixed combustor produces less NOx than conventional gas turbines by burning the fuel at a low temperature. Conventional gas turbines that burning the fuel near stoichiometric condition have some advantages in terms of stability of combustion, but these produce locally high temperature regions which induce large amounts of NOx and soot production. On the other hand, lean premixed combustors can decrease combustion temperature significantly by burning the fuel near lean equivalence ratio conditions [4, 5, 6]. However, combustion instabilities occur under the lean burning conditions where they are designed to operate. To eliminate these instabilities and develop effective approaches for their control, the mechanisms responsible for their occurrence must be understood. The necessary condition for combustion instability was first determined by Lord Rayleigh [7] and can be summarized in the following mathematical expression called the Rayleigh Criterion.

It means that combustion is unstable when the net rate of energy added to the acoustic field exceeds the net rate of damping provided by inherent dissipative processes such as heat and acoustic energy loss. It also shows that combustion instability can occur when the phase between pressure oscillations and heat release oscillations is less than 90°. During the last decade, the underlying mechanisms of combustion instabilities in lean,

premixed gas turbine combustors have been investigated. These involved mechanisms of the combustion instability and the physics of acoustic interactions in premixed gas turbines [8, 9, 10], the flame transfer function measurements and the coupling of combustion instability mechanisms [11, 12, 13, 14], and the dynamics and stability of lean premixed swirl-stabilized combustion [15, 16, 17].

Other groups have investigated flow structures and flame behaviors in lean premixed gas turbine combustors via laser diagnostics. Observations included: flame behavior in a laboratory-scale premixed natural gas turbine combustor from Planar Laser Induced Fluorescence (PLIF) images of OH*, Laser Doppler Anemometry (LDA), and Coherent Anti-stokes Raman Spectroscopy measurements [18, 19], the investigation of flow field, structures, temperature and species distributions of swirl flames in a gas turbine model combustor [20, 21, 22]. Those two research parts have been performed somewhat separately, and studies on flow structures and flame behaviors are not well documented for confined laboratory gas turbine combustors in comparison with studies for unconfined combustors. This chapter has been performed to investigate the flow structure in cold flow and mechanism of the combustion instability in terms of flow structural characteristics. PIV measurements and dynamic pressure measurements were conducted simultaneously to examine the effects of structural characteristics on the combustion instability. The result strongly suggests that the formation of a recirculation zone and its structural characteristics contribute to the occurrence and development of combustion instability.

4.2 Experimental Method and Conditions

The combustor used for this study is a model gas turbine combustor simulating in 1/3 scale a GE 7FA+e DLN-2.6 gas turbine combustor [23], characterized with partially premix and swirl stabilized flame. The form is as shown in Fig. 3.3. It consists of five main parts: an air heater, a fuel-air mixing section, a swirl injector, an optically accessible

quartz combustor section, and a plug nozzle. Regulated inlet air enters the electric air heater and is heated to 673 K. The air heater consists of three heating elements. Each of the elements uses 40 KW power and can be controlled individually. The air heater can maintain the desired temperature throughout the experiments. The heated air enters the mixing section through a chocking plate which is installed at the entrance of the mixing section to prevent mass flow rate oscillations and to provide a well-defined acoustic boundary condition. The mixing section is 550 mm long and has an annular cross section whose diameter is 40 mm. An axial-entry type swirl injector with 30° swirl vane angle was mounted in the mixing section 53 mm upstream of the dump plane. The swirl effect can be expressed by the swirl number, which is the ratio of the tangential momentum and the axial momentum.

As for the working fuel in the model gas turbine combustor, this study used CNG (compressed natural gas) that has 89.4% methane. The fuel is issued from 10 holes located 20 mm upstream of the swirl vanes, and mixed with heated air by passing through the swirl vanes. The combustor consists of a stainless steel dump plane, an optically accessible quartz combustor section with an inner diameter 120 mm, and a length of 200 mm, and a stainless steel variable-length section, which is blocked by a water-cooled plug nozzle. The length of the combustor, which is defined as the distance from the dump plane to the plug, can be continuously varied between 825 mm to 1125 mm by moving the plug nozzle along the axial direction of the combustor. The nozzle not only changes the length of the combustor but also defines the acoustic boundary condition for measurements of self-excited instabilities. The blockage ratio of the plug nozzle is 91%, which is large enough to set a proper acoustic boundary condition. All of the experimental conditions from this study are listed in Table 4.1.

To measure the flow rate of fuel and air, combustion static pressure, exhaust emission and combustion dynamic characteristics of the model dump combustor, this experimental study used various kinds of sensors and a flow-meter to regulate the flow rate. First of all, to control the change of static pressure and air flow rate before and after the combustion experiment, a total of 6 static pressure sensors made by Valcom Company

were used. One was placed in the front and one in the back of the orifice, and two were in the front and back of the swirl injector, and two were in the combustor. A K-type thermo-couple was used to measure the temperature. In all, the temperatures of 8 channels were measured, including air-supply (3ea), combustor (4ea), exhaust emission sensor location (1ea) temperature, and the temperature around the differential pressure gauge for the regulation of fuel and air flow rate.

Table 4.1 Experimental conditions and parameters.

Parameters	**Values**
Fuel type	Natural gas [CH_4(89.4%) + C_2H_6(8.6%) + C_3H_8(1.39%)]
Inlet air temperature [K]	673
Fuel temperature [K]	318
Swirl vane angle	30°, 45° swirler (swirl number = 0.42, 0.72)
Fuel-Air mixture velocity [m/sec]	40, 50, 60, 70
Equivalence ratio (Φ)	Blowout limit ~ 1.2
Inlet mixing section length [mm]	550
Combustor length [mm]	850 ~ 1082
Blockage nozzle [mm]	128 (Blockage ratio : 91%)

In this chapter, flame structures were obtained using Particle Image Velocimety (PIV) and OH* chemiluminescence. PIV is an attractive and useful technique for capturing instantaneous flow fields [24]. PIV is the simultaneous measurement of fluid or particulate velocity vectors at many (e.g. thousands) points, using optical imaging techniques. The measurements are usually made in planar “slices” of the flow field. It is a qualitative visualization method that can instantaneously capture 2-dimensional velocity fields, along with additional information such as turbulent intensity, strain rate, and vorticity. Several processes are required to get useful information, such as adding tracing

particles to the flow, laser illumination with periodic time delay, recording of Mie scattering images, and post-processing of recorded images. Fig. 4.1 shows the configuration of a PIV measurement system in a model gas turbine combustor.

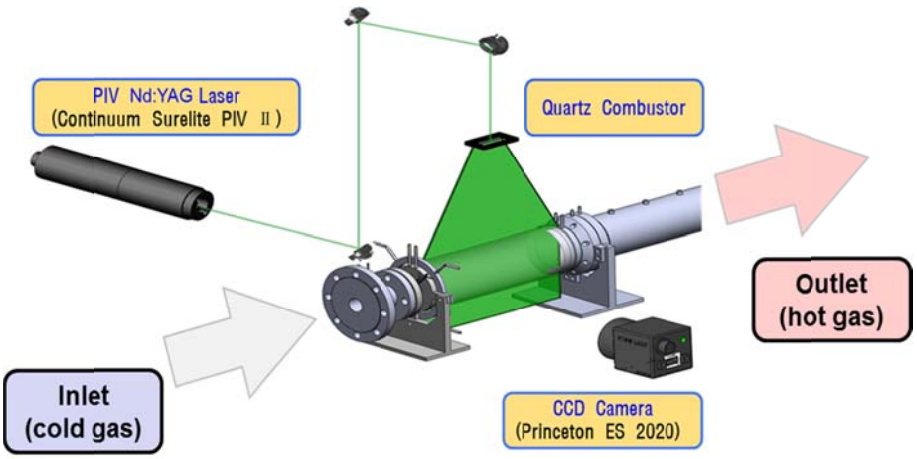

Fig. 4.1 Configuration of a PIV measurement system in a model gas turbine combustor.

A double pulse PIV laser (ND:YAG laser, 532 nm, Max. 3W per one head, 5 ns of laser pulse, 1 mm of laser sheet width, 8μs of double-pulse interval and 10 Hz of PIV repetition rate) was used to illuminate seeding particles, and Mie scattering images were captured by a CCD camera with a pixel resolution of 1600 × 1200 (Princeton ES2020). The size of the test section is 120 mm × 200 mm. Zirconium Oxide was used as a seeding particle, and its' mean diameter was about 1μm. The biggest challenge in applying the PIV technique to velocity measurements in strongly swirling flows is the strong out-of-plane motion decreasing the number of valid particle-pair images within the laser sheet [25]. Therefore, the laser sheet profile, the time interval between laser pulsed, and the seeding density in the flow have to be controlled to obtain valid velocity vectors. The addition of seeding particles to the flow and their contamination of the quartz combustor present an additional challenge in applying the PIV technique. This is extremely serious for the application of PIV and is a main reason for the relatively few publications describing PIV

measurements in gas turbine combustors. However, 2-dimensional images of the instantaneous flow field provide new insights into the dynamics of turbulent swirl-stabilized flames, which are very important for the understanding of combustion instabilities. Moreover, to measure the heat release oscillation of flame under stable and unstable combustion conditions, OH chemiluminescence was measured from the flame around the dump side. By using the high speed ICCD camera made by Photron Company, this study photographed flames at a speed of 6000 fps. This study was able to obtain the pressure oscillation and heat release values from the time axis in the same experimental conditions by linking with the dynamic pressure sensor, while locking the phase.

4.3 Results of Recirculation Zones

Previous researchers have used the size of the recirculation zone to examine the intensity of the recirculation zone which is based on how well recirculation zones move hot gases to the middle of the combustor and down into the ignition zone. Therefore, the intensity of the recirculation zone can be examined in terms of the size and the mass flow rate of hot burnt gases that the recirculation zone provides to the middle of the combustor. The examination of the zero axial velocity and the zero radial velocity helps define recirculation regions. The sizes of the recirculation zones are directly related to the height and width of the zero velocity contours.[26] Based on the size of the recirculation zone and the mass flow rate of hot burnt gases in the recirculation zone, the effect of each operating condition on the formation of recirculation zone was experimented.

4.3.1 Effect of various combustion parameters in cold flow

For the study of recirculation zones in cold flow, numerous experiments were conducted under the various operating conditions: fuel-air mixture velocities, equivalence ratios, and swirl numbers. Fig. 4.2 shows the averaged PIV images at different fuel-air mixture velocity conditions. The recirculation size can be defined by the contours of the zero axial and radial velocity. It is observed that the size of the recirculation zone

increases as the fuel-air mixture velocity increases form 40 m/s (Fig. 4.2 (a)) to 60 m/s (Fig. 4.2 (b)). The position of the vortex core was rarely changed and the magnitude of negative velocity vectors has increased as increase of the fuel-air mixture velocity. The formation of recirculation zones is the pressure gradient in the combustor so the trend with respect to the change of mixture velocities can be explained about the pressure gradient. The magnitude of the tangential velocity component is proportional to that of the axial velocity component determined by the fuel-air mixture velocity. According to Eq. (2.30), the magnitude of the pressure gradient is proportional to that of the square of the tangential velocity component, so the pressure gradient becomes larger as the mixture velocity increases. The pressure gradient disappears gradually along the axial direction because the tangential velocity component decays with axial distance. However, the more time and distance are necessary for the decay of the tangential velocity component under higher mixture velocity conditions, that is, the pressure gradient that is essential to drive the formation of the recirculation zone exist in the further downstream region under higher mixture velocity conditions.

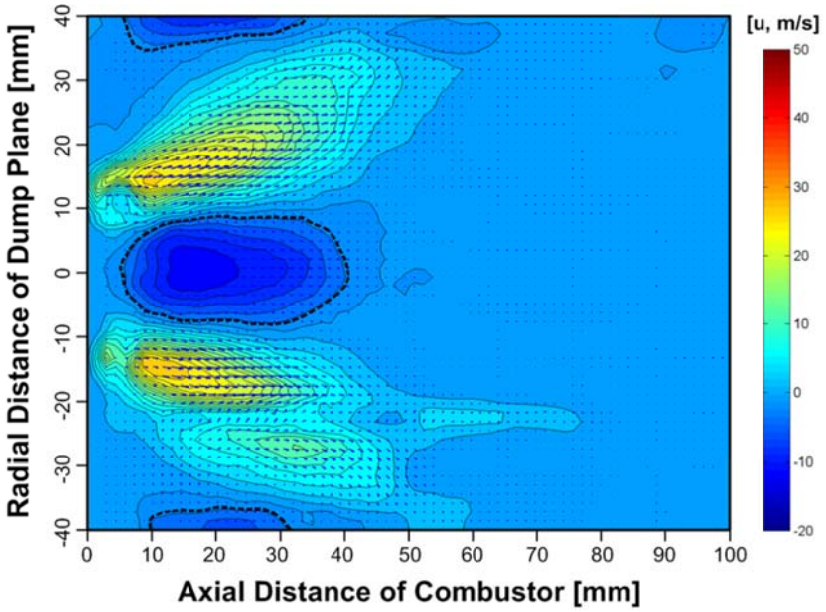

(a)

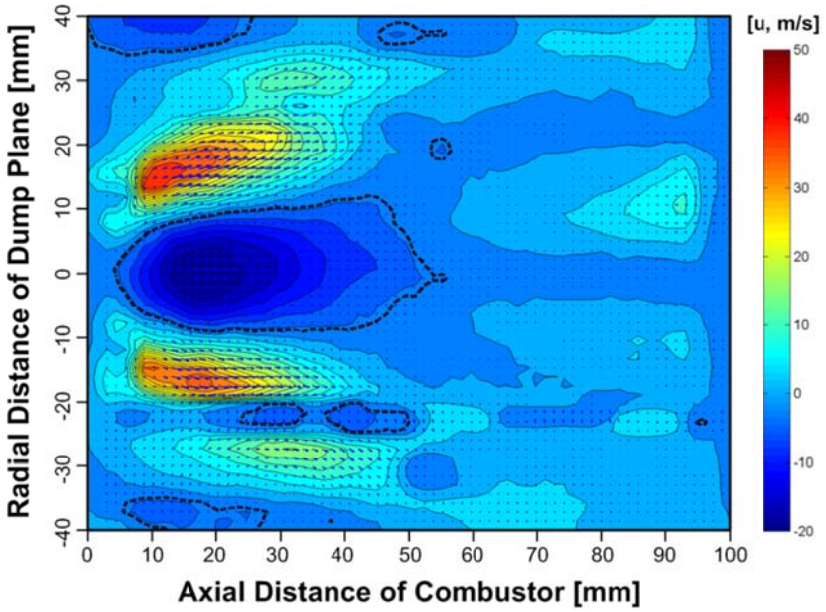

(b)

Fig. 4.2 Averaged PIV images and mean flow structures in a non-reacting flow at $L_{comb.}$ = 1050 mm, Φ = 0.8 and 30° swirl; (a) v_{mix} = 40 m/s, (b) v_{mix} = 60 m/s.

As shown in Fig. 4.3, the equivalence ratio doesn't have any effects on the formation of recirculation zones in a non-reacting flow. Actually, the equivalence ratio is one of the most important parameters that understand and driving issue the combustion dynamics. However, that does not have any influence on the flow structure without the combustion.

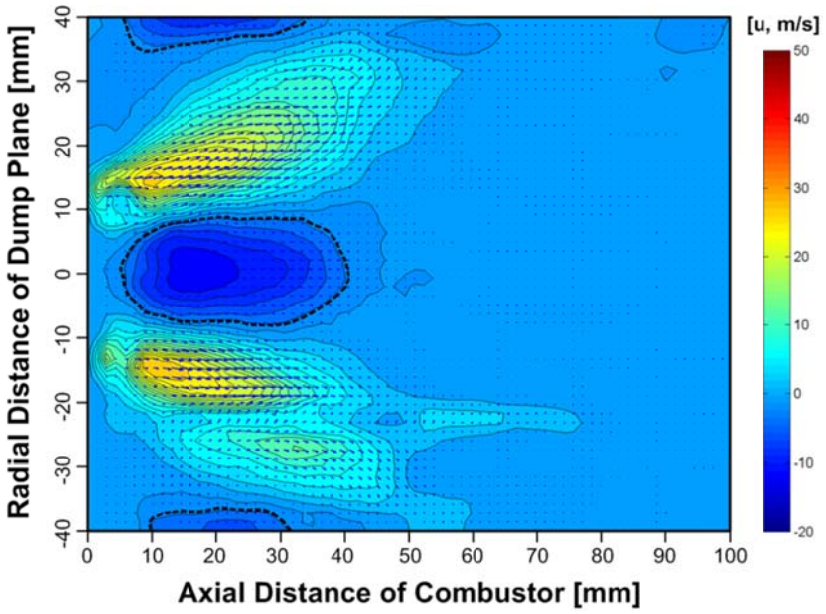

(a)

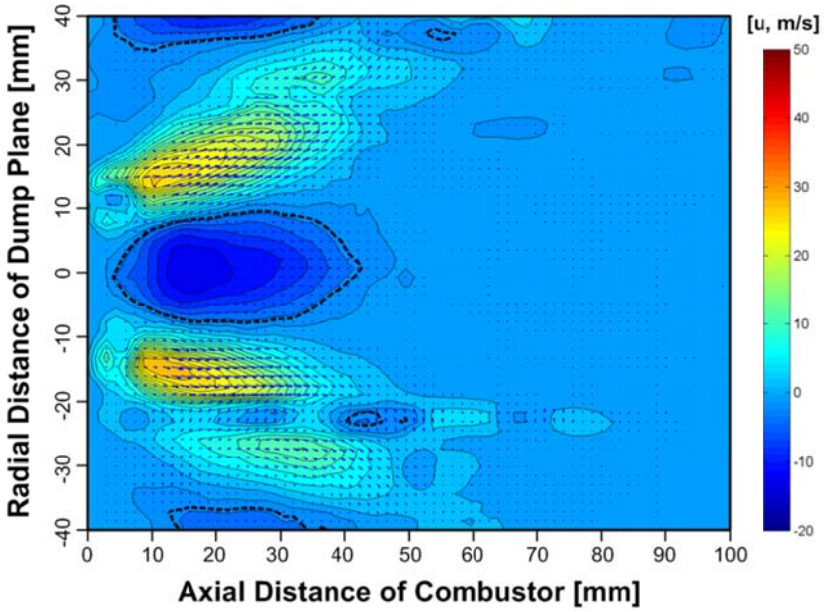

(b)

Fig. 4.3 Averaged PIV images and mean flow structures in a non-reacting flow at $L_{comb.}$ = 1050 mm, v_{mix} = 40 m/s and 30° swirl; (a) Φ = 0.8, (b) Φ = 0.65.

Figure. 4.4 shows the effect of the swirl number on the flow structure result. The swirl number was changed from 0.42 (30°) and 0.72 (45°) by using different swirl vane angles. An increase in the magnitude of the swirl number directly means the increase of tangential velocity components in the flow. According to the governing equation of the swirl flow Eq. (2.30), the pressure gradient becomes stronger as the tangential velocity increases. Consequently, the pressure gradient that drives the formation of recirculation zones can exist over a wider region of the combustor, so the size of the recirculation zone increase. The increase of the swirl number has the same effect with the increase of the mixture velocity on the size of recirculation zones.

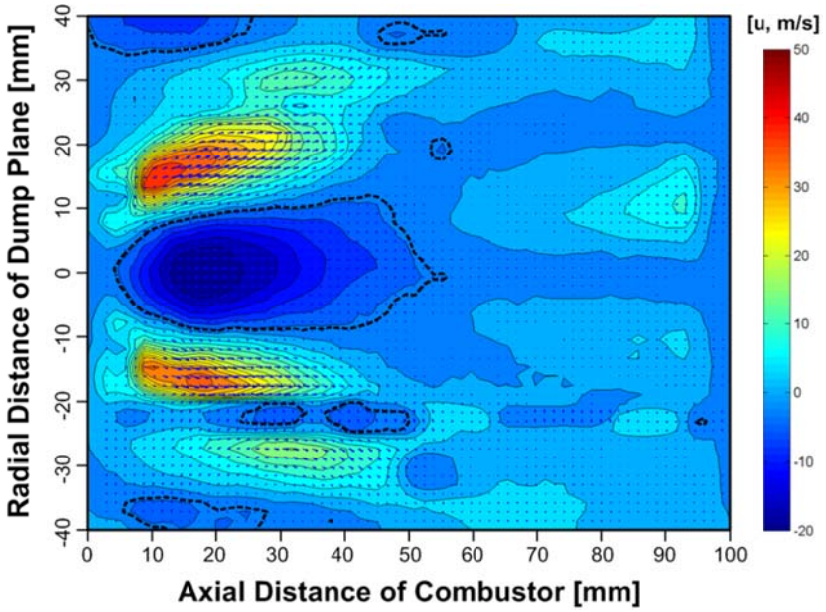

(a)

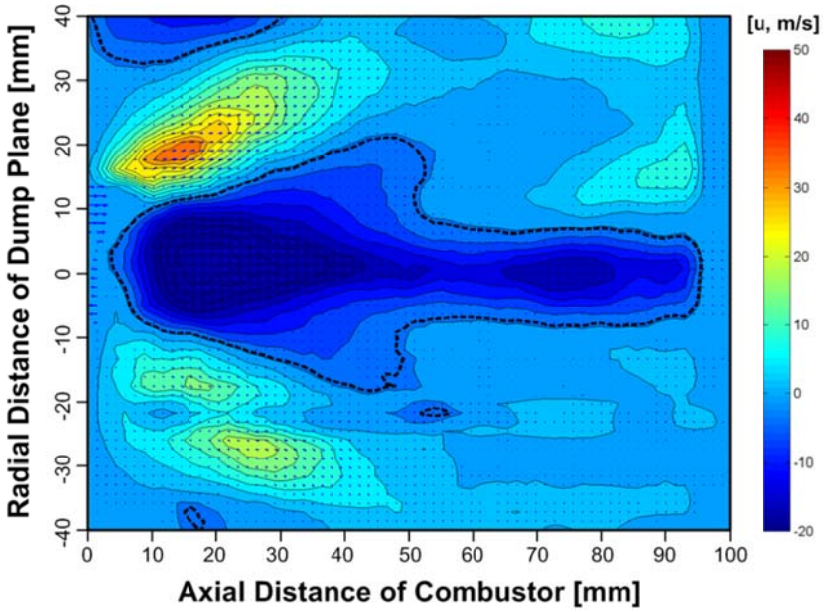

(b)

Fig. 4.4 Averaged PIV images and flow structures in a non-reacting flow at $L_{comb.}$ = 1050 mm, v_{mix} = 60 m/s and Φ = 0.8; (a) 30° swirl, (b) 45° swirl.

4.3.2 Effect of combustion and instability characteristics

Figures 4.5 (a) and (b) show values obtained through PIV measurement in a combustion field. After measuring 600 pairs of instant fields, this study calculated their average, which shows that a recirculation zone is formed in actual combustion conditions. To compare recirculation zone size, many researchers used the height or width of a recirculation zone, with the size of such a recirculation zone defined with borderlines connecting points whose axial-direction velocity and radial-direction velocity are 0 [18]. Fig. 4.5 (a) shows the characteristics of a recirculation zone formed under stable combustion conditions, while Fig. 4.5 (b) shows a recirculation zone formed in unstable combustion conditions. In this section, when combustion instability took place, it was observed that the size of a recirculation zone became remarkably enlarged. This finding indicates that the occurrence of combustion instability has an effect on the formation of a recirculation zone. Fig. 4.6 shows a calculating process used to simply compare the size of volume flux in a recirculation zone. Through this process, this study compared quantitative volume flux in a recirculation zone every moment in the random-phase PIV images in both flame stable and unstable conditions.

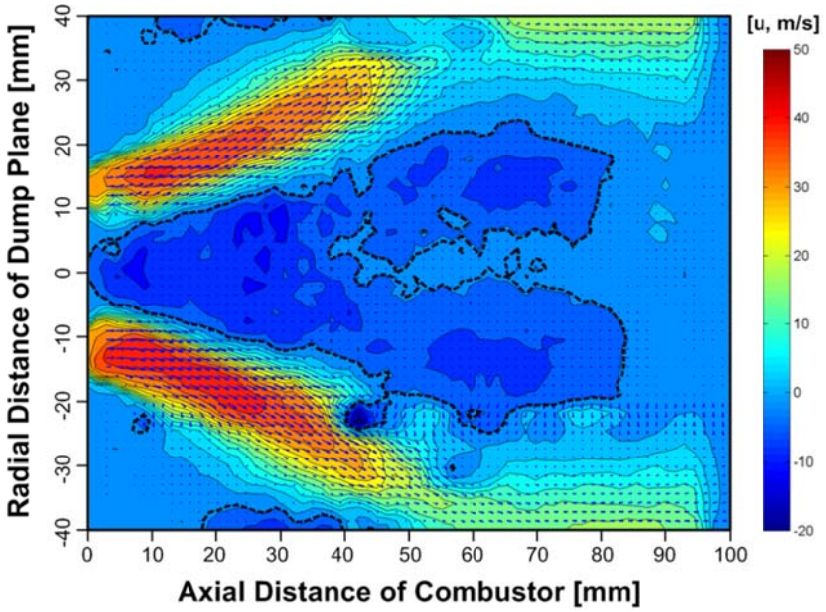

(a)

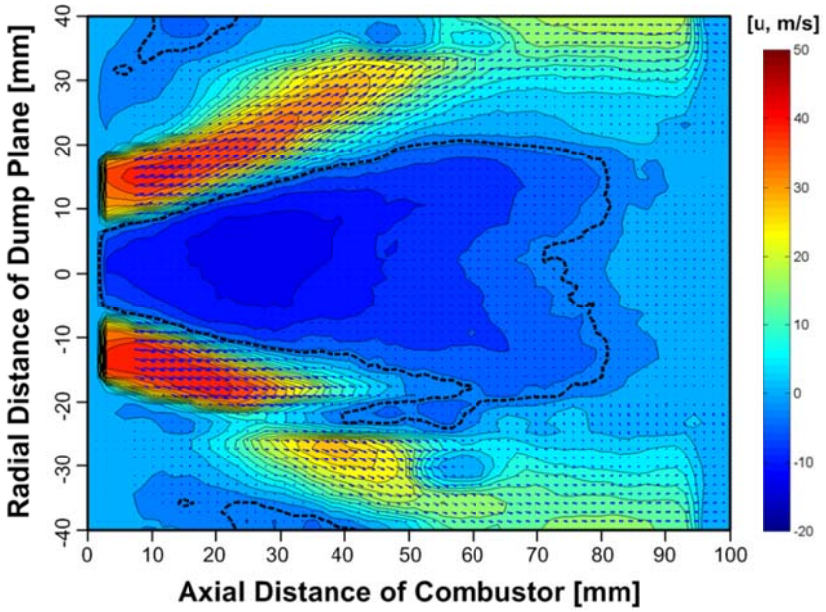

(b)

Fig. 4.5 Averaged PIV images in combustion condition at $L_{comb.}$ = 1050 mm, v_{mix} = 40 m/s and 30° swirl; (a) stable, Φ = 0.65, (b) unstable, Φ = 0.8.

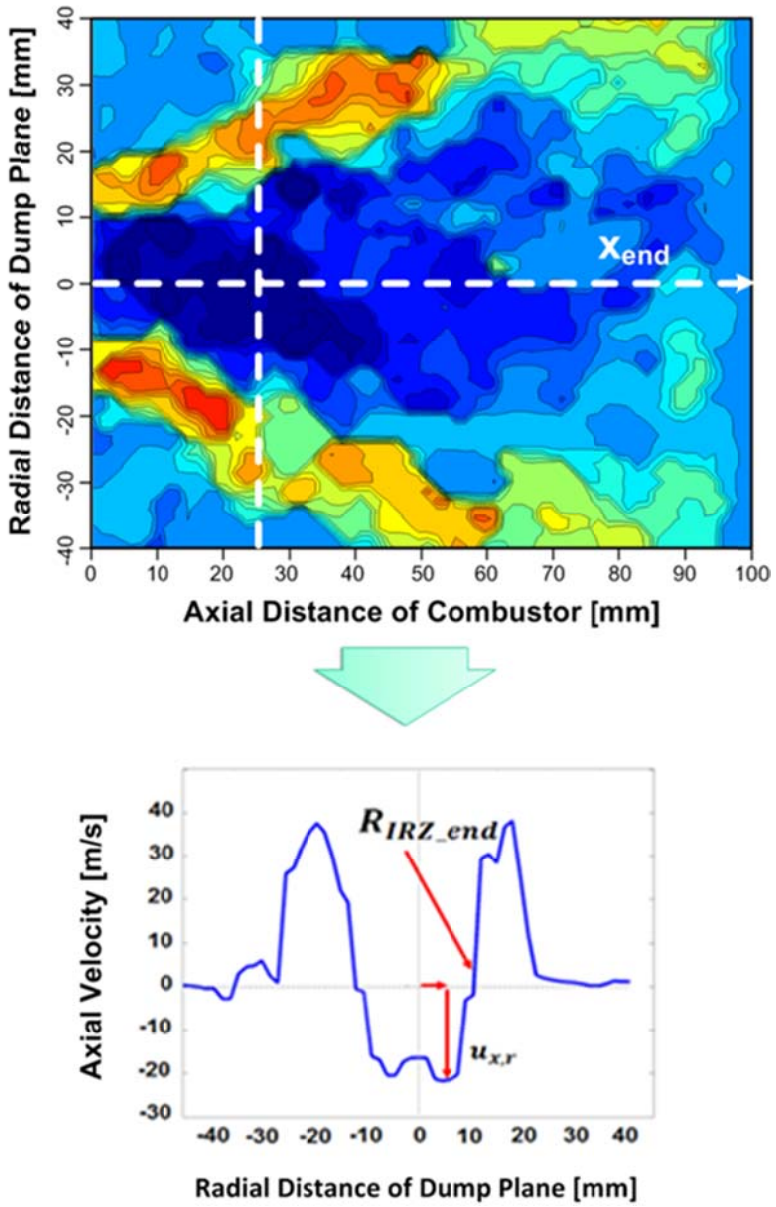

Fig. 4.6 Calculation for volume flow rate of swirling flame zone at 30 mm detached measurement point from the dump plane in stable and unstable conditions.

To find out the relation between the formation of a recirculation zone and combustion instability, this study adopted the PIV measurement technique. As combustion instability is a kind of a dynamic phenomenon, its characteristics are hard to investigate through mean-field images only. In this section, therefore, this study investigated the characteristics of a recirculation zone by using instantaneous images under the condition of combustion instability. Fig. 4.7 (a) shows the 4 cycles of random phase unstable flame images obtained through PIV under combustion instability. The phase of each image is not clear, owing to the phase locking method, but its cycle shows that the recirculation zone vibrates with a main instability frequency. In contrast, Fig. 4.7 (b) shows cycles composed of instantaneous images in stable combustion conditions, through which it was observed that the size of a recirculation zone hardly changed but was sustained almost throughout.

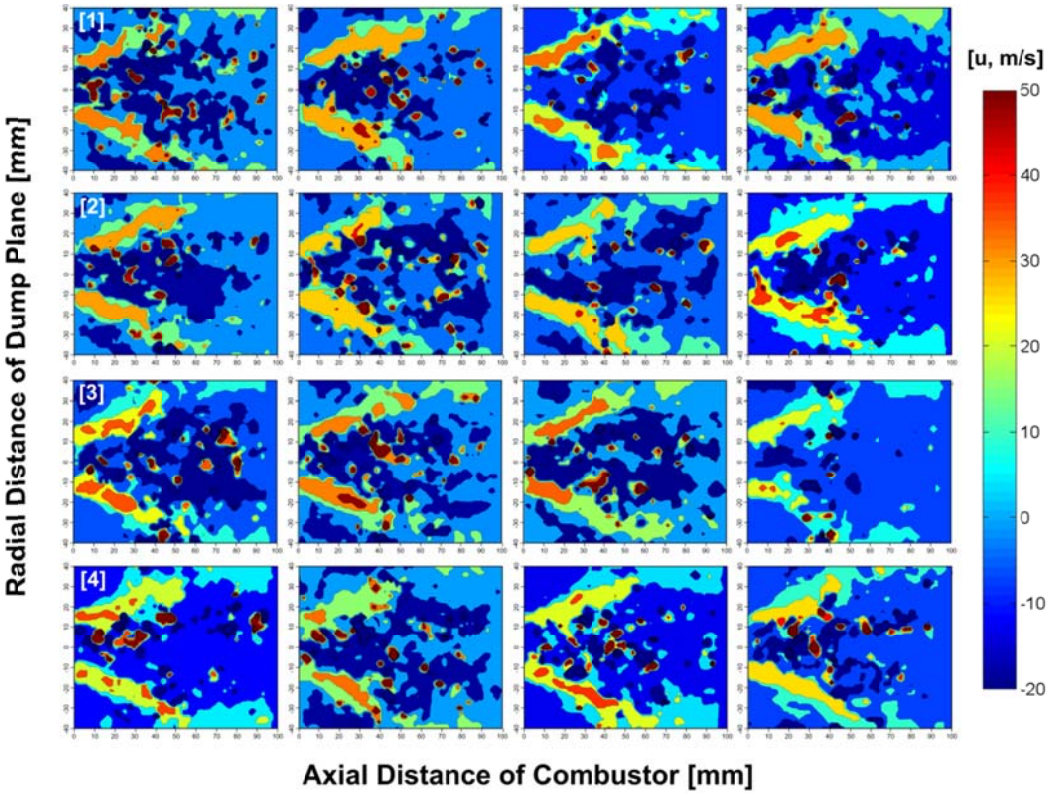

(a)

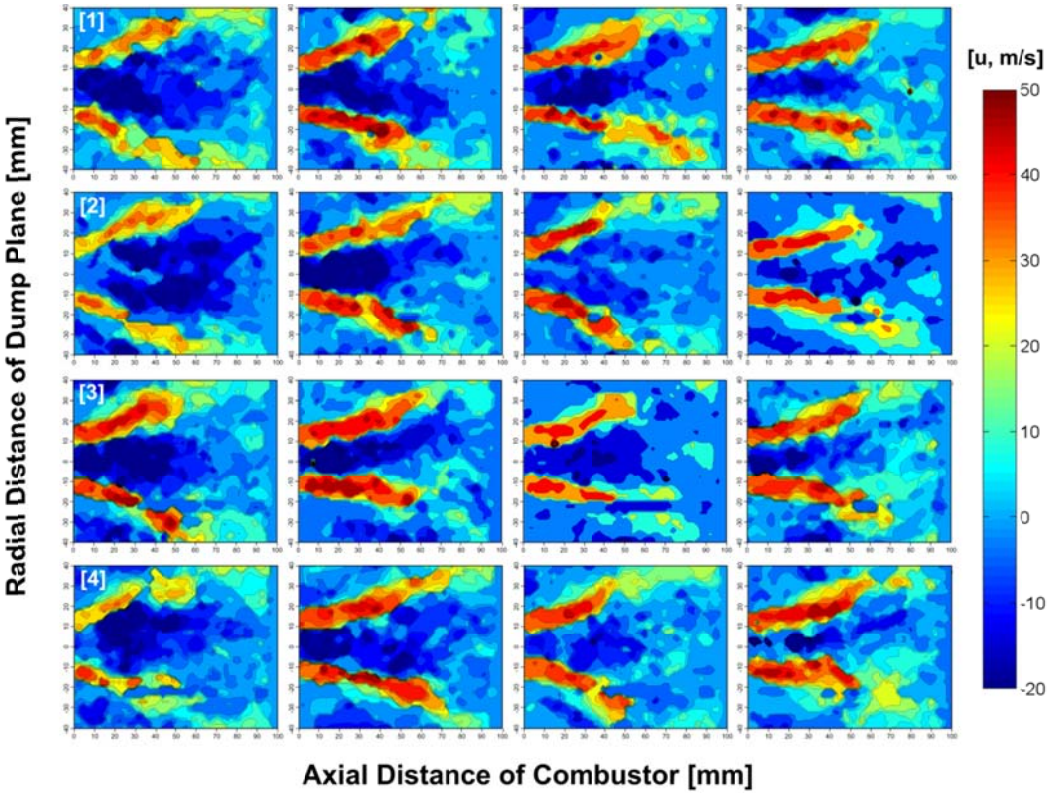

(b)

Fig. 4.7 Instantaneous PIV images in combustion condition at $L_{comb.}$ = 1050 mm, v_{mix} = 40 m/s and 30° swirl; (a) stable, Φ = 0.6, (b) unstable, Φ = 0.8.

Also, this experimental investigation is confirmed by Fig. 4.8 (a) and (b). That figures indicate that the axial velocity profile result of the each instantaneous PIV images at 20 mm detached measurement point from the dump plane in stable and unstable conditions. As mentioned earlier, the recirculation zone contributes to the stability of combustion by moving high-temperature combustion gas to the central part of a combustion chamber and near the fuel-air injected nozzle where ignition takes place. So, the most important assumed item is the volume flux of re-circulated combustion gas and which has almost the same value of flame zone air density. The volume flux can be calculated through the area of a recirculation zone and the size of negative-direction

velocity components. Therefore, the size of a constantly-changing recirculation zone means that the volume flux of recycled high-temperature gas changes as well, which is essential for the stabilization of combustion. Such change of volume flux causes the fluctuation of reaction rate and heat release rate oscillation, ultimately leading to combustion instability.

Unlike a case where stable combustion takes place as usual, it was observed that the size of a recirculation zone constantly changes in a condition of unstable combustion condition. Moreover, when this study examined the sizes of recirculation zones in the last picture in Figs. 4.7 (a) and (b), it was found that the formation was so weak that it contributed nothing to the stabilization of combustion, further causing flame quenching. Also, the fluctuation of a recirculation zone seems to have an effect on the occurrence of combustion instability. For the validation of this experimental study, we found the volume flow rate of a recirculation zone in combustion condition.

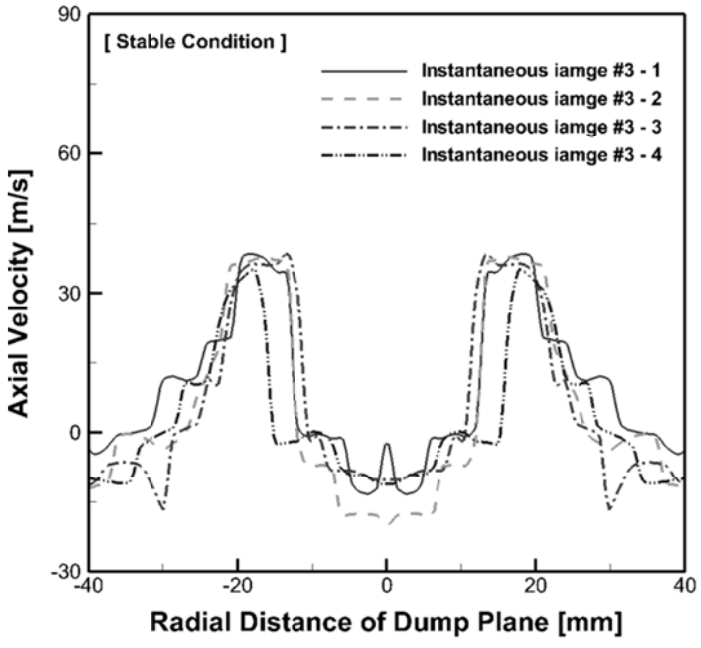

(a)

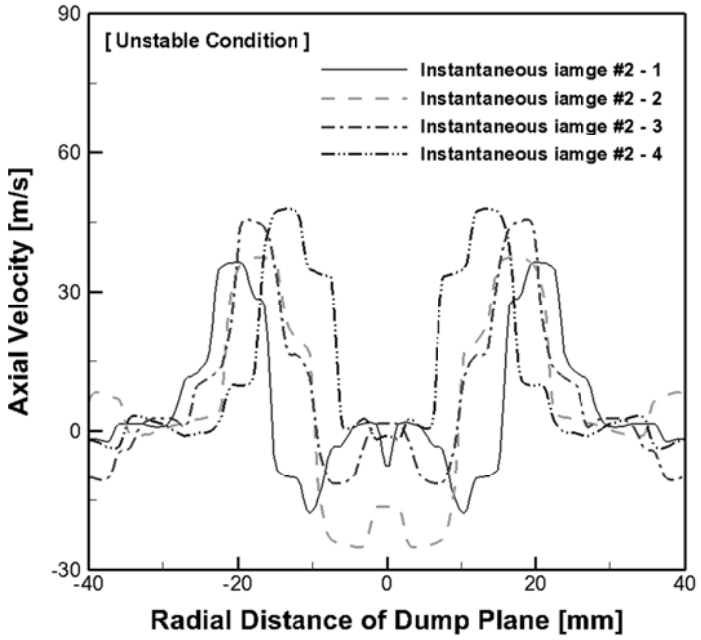

(b)

Fig. 4.8 Velocity profile result of instantaneous PIV images at $L_{comb.}$ = 1050 mm, v_{mix} = 40 m/s and 30° swirl vane angle; (a) stable, Φ = 0.6, (b) unstable, Φ = 0.8.

Figures 4.9 (a) and (b) indicate the result of volume flow rate changing in each random phase conditions through stable and unstable flame conditions. As shown this figure, there have larger volume flow rate region in the recirculation zone and its fluctuation at unstable combustion region than the stable combustion conditions.

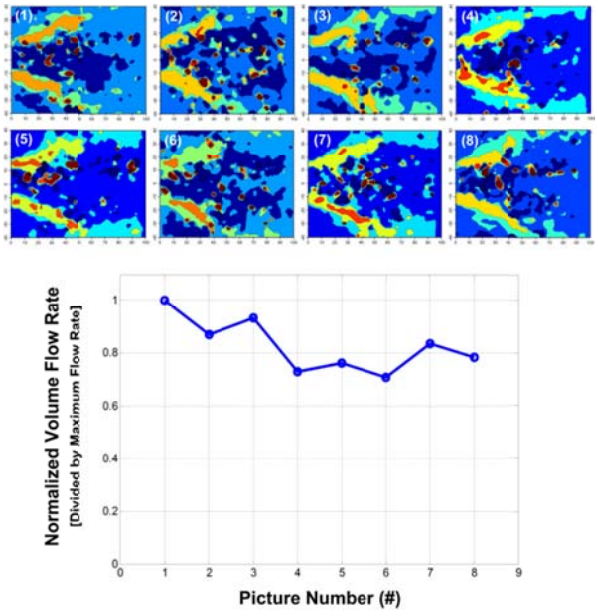

(a)

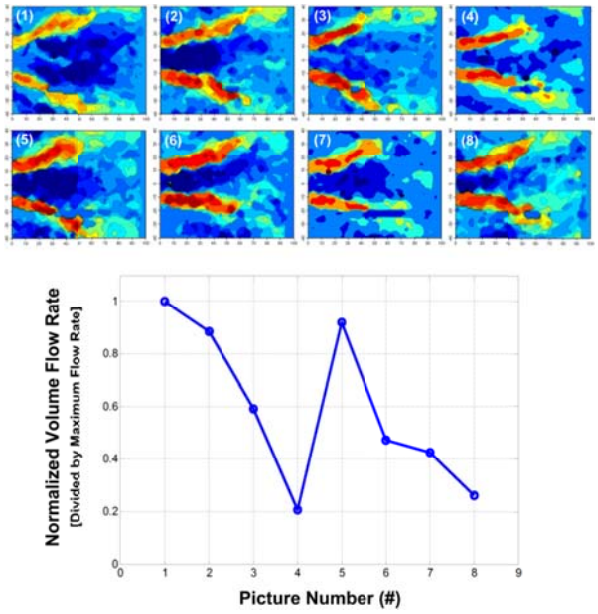

(b)

Fig. 4.9 Result of volume flow rate in each random phase conditions at $L_{comb.}$ = 1050 mm, v_{mix} = 40 m/s and 30° swirl; (a) stable, Φ = 0.6, (b) unstable, Φ = 0.8.

4.4 Analysis of combustion instability frequency

To investigate whether a recirculation zone vibrates cyclically and what that frequency of the vibration means When it occurs, this study measured the OH* chemiluminescence with a high-speed ICCD camera. At each moment, the camera frame speed was set at 2048 Hz. Figs. 4.10(a) and (b) are the results arranged in each phase, which shows that flame vibrates cyclically in conditions of combustion instability (Fig. 4.10(b)). In stable combustion conditions as shown in Fig. 4.10(a), it was observed that there was almost no change in the intensity of chemiluminescence signals, which shows that the form and size of flame were constant.

This study converted the values of intensity of chemiluminescence images obtained in instability conditions to analyze the frequency. Through the sum of them, this study examined the change of intensity by time and performed FFT. As a result, it was found that it vibrated with its natural frequency, 315Hz of combustor longitudinal mode. As a result of FFT with dynamic pressure information obtained during the process of this experiment, the frequency was found to be 313Hz. Furthermore, when theoretical instability modes were calculated with the length of a combustion chamber (1.05 m), and temperature (868 K, the average obtained from 3 points on the combustion chamber) in the closed-closed boundary condition, this study found the natural frequency of combustor at 322 Hz. Since the average temperature of the entire combustion chamber was actually lower than the temperature measured, this study found that the fluctuation of flame, the fluctuation frequency of instability phenomenon, and the theoretically-calculated unstable mode all have very similar values. This result supports the assumption that there is a direct relation between combustion instability and the fluctuation of a recirculation zone.

A theoretical analysis to calculate this phenomenon is shown in Eq. (4.1) and Eq. (4.2). It is assumed that the movement course of energy in a gas turbine combustor is axial direction and the average temperature is constant with 1-D standing waves theory.

$$\text{Quarter wave mode} : f_0 = \frac{(2n-1)c}{4L} \tag{4.1}$$

$$\text{Half wave mode} : f_0 = \frac{nc}{2L} \tag{4.2}$$

$$\left[\textit{where}, n = 1,2,3..., c = \sqrt{\gamma RT} \right]$$

Combustion instability has an essential relation with the fluctuation of a recirculation zone, and it can be explained through procedures shown in Fig. 4.11. When combustion instability takes place, high pressure fluctuation occurs inside the combustion chamber. As mentioned above, the most important factor in forming a recirculation zone is the very formation of a pressure gradient inside the combustion chamber. However, when combustion instability takes place, a pressure gradient is not smoothly formed due to the pressure fluctuation inside the combustion chamber, which is needed for the formation of a recirculation zone. Consequently, the recirculation zone proceeds to vibrate under the influence of instability-caused pressure fluctuation. The vibration of a recirculation zone further causes mass flow rate fluctuation of high-temperature recycled gas needed for stable combustion. It is at this moment that, mass flow late fluctuation in recirculation zone leads to the fluctuation of heat release as one of the factors sustaining and developing combustion instability.

In summary, the fluctuation in a recirculation zone functions as one of several factors causing and developing combustion instability. It can be regarded as an essential accompanying phenomenon when combustion instability takes place.

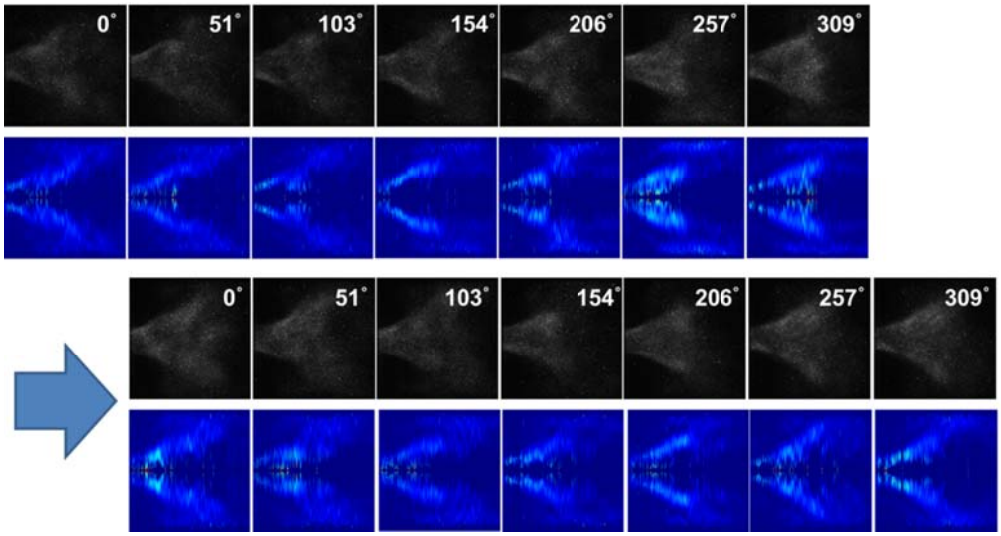

(a)

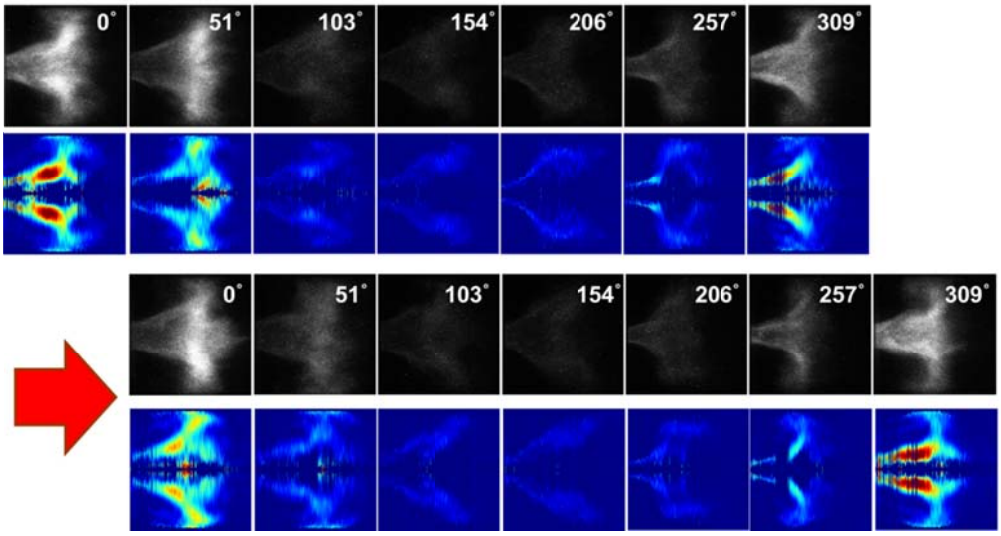

(b)

Fig. 4.10 OH chemiluminescence and abel-inverted images at $L_{comb.}$ = 1050 mm, v_{mix} = 40 m/s and 30° swirl; (a) stable, Φ = 0.6, (b) unstable, Φ = 0.8.

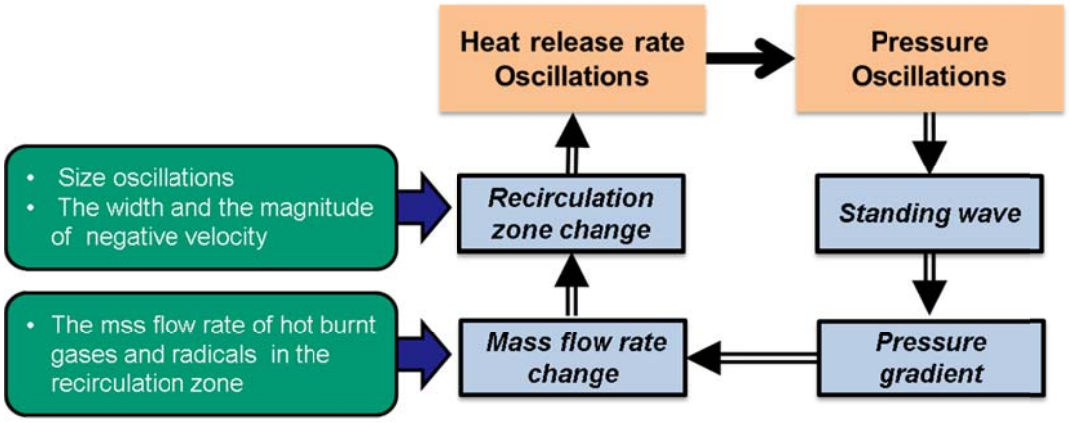

Fig. 4.11 Relation between the recirculation zone oscillation and combustion instability.

CHAPTER 5
EFFECT OF FUEL-AIR MIXTURE VELOCITY

5.1 Background and Objectives

Combustion instabilities occur when different combustion processes combine in such a way that inherent disturbances in the system are self-excited via interactions with the combustion process. These are caused by complex, feedback-type interactions between periodic flow and combustion processes that produce a periodic heat addition, exciting large-amplitude acoustic oscillations in the combustor [1].

In addition, a recent study by Meier et al. [2, 3, 4] has shown the relation between ignition delay time and combustion instability occurrence by CFD and experimental studies using the PIV and PLIF measurements in a model gas turbine combustor. Candel et al. [5, 6] investigated the flame response by measuring the unsteady heat release induced by an imposed velocity perturbation and flame dynamic, which is documented by the calculating the phase averages. As concerns the flame vortex interaction research field, Kim et al. [7] investigated the effects of acoustic forcing on flame length and NOx emission in turbulent hydrogen non-premixed jet flames with coaxial air, which was acoustically forced at the resonance frequency of the combustor. Also, in order to examine mixing and dynamic behaviors during flame-vortex interaction, the local properties on the flame surface were characterized quantitatively. The behavior of the precessing vortex core (PVC) is also significantly altered by combustion heat release and by the system parameters (e.g. swirl number, axial velocity and geometry). Previous studies [8, 9] suggest that the type of combustion (i.e., premixed or non-premixed) can affect the PVC frequency and its intensity.

However, there is no other research about the interaction of vortex structure and combustion instability phenomenon. The flame recirculation zone (flow patterns in combustion region) is very important, as it can modulate the air flow rate at instability condition and may be the source of instability by modulation local equivalence ratio. In

this chapter, we conducted experiments under various fuel-air mixture velocity and operating conditions with a model gas turbine combustor to examine the relation of combustion instability and flame structure using the OH chemiluminescence and multi-channel dynamic pressure sensing system.

5.2 Experimental Method and Conditions

Figure 5.1 shows a schematic of a partially premixed, variable length, model gas turbine combustor (same as facility of Fig. 3.3). It consists of an air heater, an inlet mixing section, which is called the plenum, a swirl injector, an optically accessible quartz combustor section, a steel combustor section, and an exhaust duct. An air heater provides heated air (673K) to a combustor through an air inlet section. There is a choking orifice at the entrance of the air inlet section to provide a well-defined acoustic boundary condition and to protect the fluctuation of inlet air. In the inlet mixing section, the mixing process between the fuel and heated air is done by a swirl injector, which provides a spatially and temporally homogeneous reactant mixture to the combustor. The length of the steel combustor can be varied continuously from 850 mm to 1100 mm by moving a water-cooled plug nozzle along the axial direction of the combustor. The temperature of plug nozzle varies from 350 to 490K, which is based on inlet velocity conditions. PCB 102A05 piezoelectric transducers are used to measure unsteady pressure perturbations in the inlet mixing section and combustor section. Five pressure transducers are installed in the mixing section, and six pressure transducers are installed in the combustor, respectively. Five static pressure sensors made by Valcom inc. are used to measure the combustion static pressure and control the mass flow rate of inlet air and five K-type thermocouples are also used.

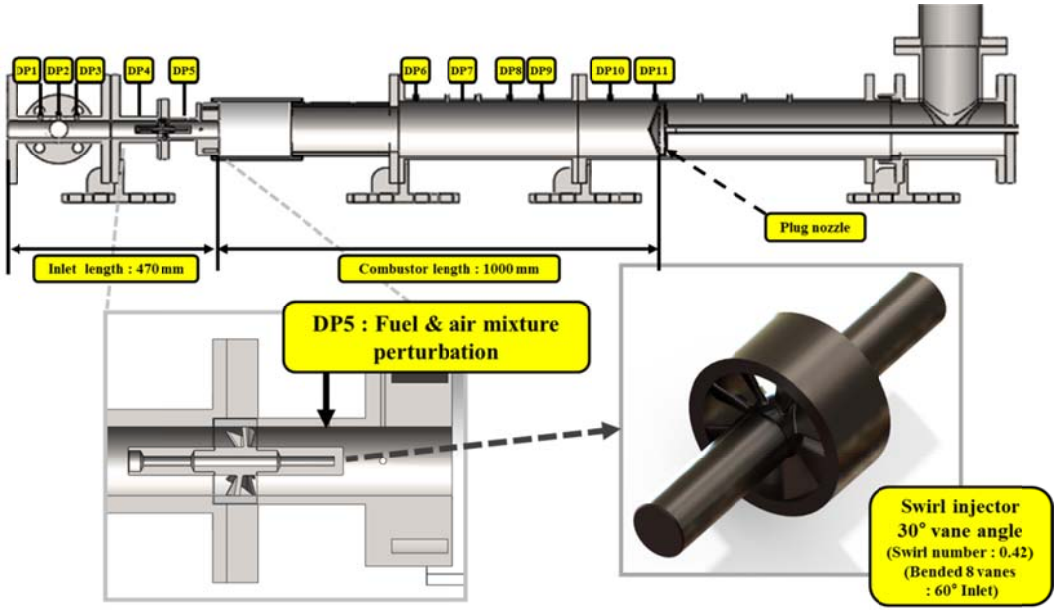

Fig. 5.1 Schematics of model gas turbine combustor for variable fuel-air mixture velocity.

Figure 5.2 shows the stability map of our dump combustor. Changes occur in the combustion instability phenomenon trend, based on inlet mixture velocity, and vary from 30 to 70 m/s. In the low and high fuel-air mixture velocity regions, high-levels of instability occur and the middle of the velocity conditions has a low-level unstable effect. Therefore, inlet mixture velocity was selected as the main variable and other variables, such as combustor length, equivalence ratio, and plenum length were fixed of 470 mm during this study and then flame visualization and dynamic pressure analysis was performed at these conditions as shown in Table 5.1. Since almost same phenomenon occurs at both slightly lean and rich conditions, and rich condition was much easier to maintaining instability conditions, slightly rich condition which means equivalence ratio 1.2 was selected in this study. Through this process, various mixture velocities for the cause of combustion instability and its maintenance process were performed to understand the relevant processes in this study. The velocity variable can be treated as a condition of the burner output and then low velocity conditions when low fuel flow rates

condition. In this experiment, somewhat high instability occurs at low inlet velocity conditions. The mechanism of these results was the subject of the investigation of this study.

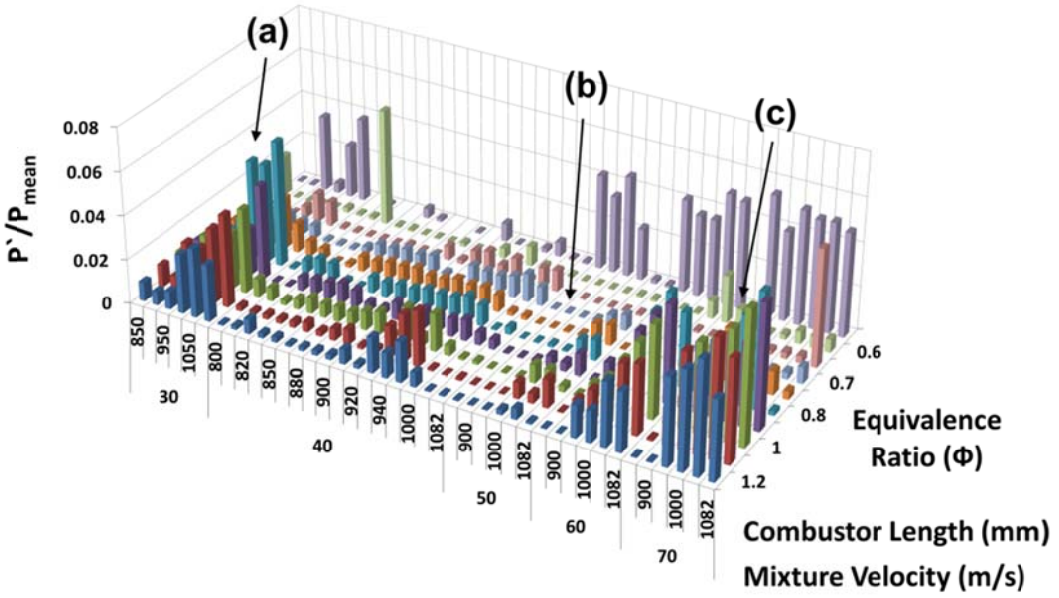

Fig. 5.2 Stability map for all experimental conditions; (a) unstable, v_{mix} = 30 m/s, 370 ~ 390 Hz, (b) stable, v_{mix} = 50 m/s and (c) unstable, v_{mix} = 70 m/s, 340 ~ 360 Hz.

Table 5.1 Experimental conditions.

Parameters	Values
Fuel type	Natural gas [CH_4(89.4%) + C_2H_6(8.6%) + C_3H_8(1.39%)]
Combustor Length [mm]	1000
Inlet Temperature [K]	637
Equivalence Ratio (Φ)	1.2
Swirl Injector	30° swirler (swirl number = 0.42)
Mixture Velocity [m/s]	30, 35, 40, 45, 50, 55, 60, 65, 70

5.3 Flame and Abel-inverted Images

To investigate of flame structure and high-frequency phenomena, high-speed ICCD camera was used in this study. The recorded frame rate was 6000 frame/sec and image size was 512 by 512 pixels. The dynamic pressure sensor and high speed ICCD triggering signal were recorded to measure heat release rate oscillation and dynamic pressure at the same time. These data were also used for phase-locking of the chemiluminescence imaging. The phase-locking process is performed based on 6th dynamic pressure, which was located at the detached section of the existing flame zone. The peak amplitude of 6th dynamic pressure was selected as 0 degree and the OH chemiluminescence image is collected by 12 phases, which means that 30-degree gaps per phase and Abel-inversion was carried out for each averaged picture. Abel-inversion is the process by which 2D images can be reconstructed from an accumulated 3D image [10, 11]. So, that is indicated the analysis of flame structures.

Figure 5.3 shows the three mixture velocity conditions for investigation of flame structure in stable and unstable condition. At 30 and 70 m/s fuel-air mixture velocity conditions, combustion instability took place and the stable condition is 50 m/s. First, a low velocity condition as some flame intensity changes according to phase changes,

however, there have few axial length variations and flame structural changes at the edge of the flame, which indicated vortex-flame interaction zone. Second, the stable conditions (50 m/s) produce no changes in flame length and intensity at each phase of the averaged image. Lastly, high mixture velocity conditions, which means that condition of 70 m/s, shows a drastic change of flame structures, which means length variation, heat release intensity oscillation, and outer recirculation size is changeable, which helps flame stabilization.

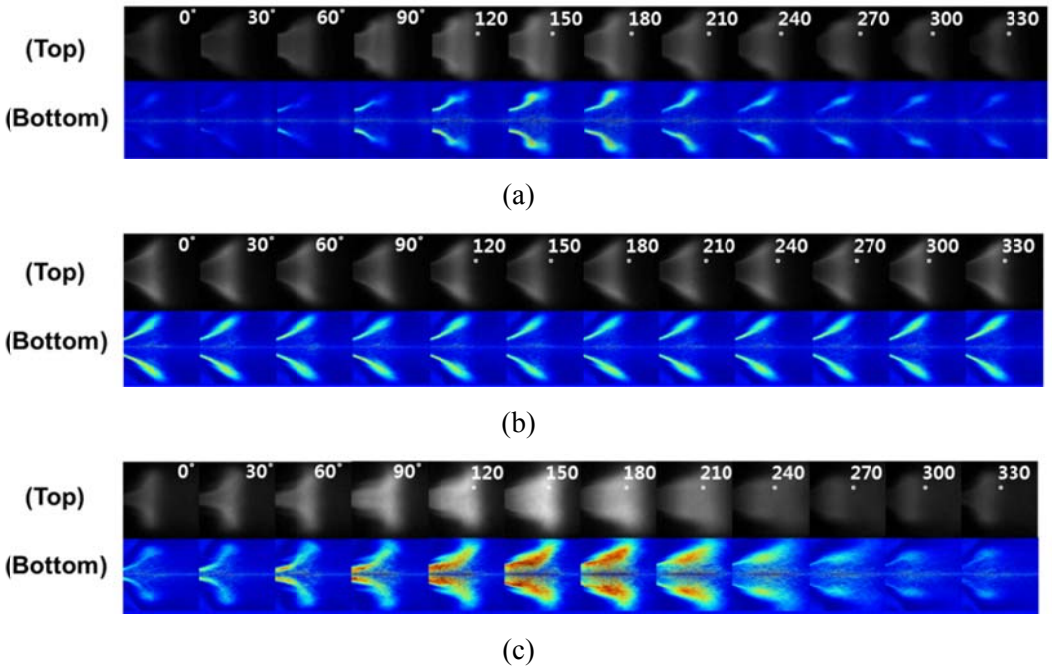

Fig. 5.3 OH chemiluminescence (top) and Abel-inverted images (bottom) at $L_{comb.}$ = 1000 mm, Φ = 1.2 conditions; (a) unstable, v_{mix} = 30 m/s, 370 ~ 390 Hz, (b) stable, v_{mix} = 50 m/s and (c) unstable, v_{mix} = 70 m/s, 340 ~ 360 Hz.

5.4 Main Instability Frequency and Strouhal Number

Figure 5.4 shows the experimental results of combustor temperature and instability frequency relation. There have separated into the three parts of low fuel-air mixture velocity instability region, stable region, and high fuel-air mixture velocity instability regions. The instability frequency and mean temperature of the combustion chamber have a linear correlation because the mean temperature of combustor affects the speed of sound about main combustion fluid and the instability frequency varies the increasing or decreasing temperature conditions. This analytic theory is well matched with the high fuel-air mixture velocity instability conditions from around 55 to 70 m/s. In contrast, at condition of low velocity instability condition about 30 and 35 m/s, combustion zone has much lower temperature zone via a high mixture velocity instability case and have a higher instability frequency. This phenomenon is not a general tendency of acoustic theory. This chapter main investigation is the relation between inlet fuel-air mixture velocity and combustion instability. Also, distinguish the difference between low and high levels of instability. To investigate such a relation, the flame structures during condition of instability will be discussed.

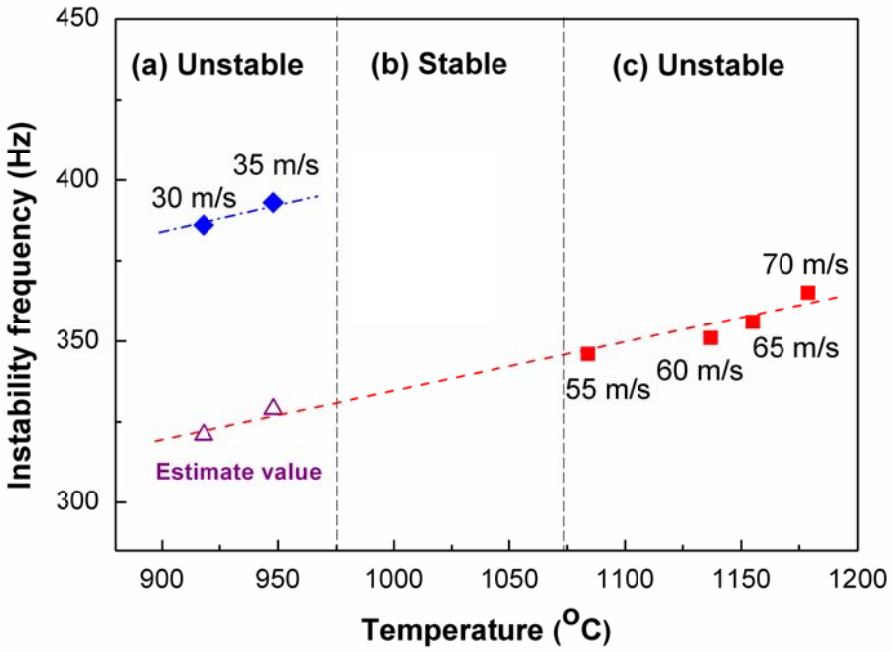

Fig. 5.4 Combustion instability frequency shifting results at various fuel-air mixture velocity conditions; (a) unstable, v_{mix} = 30 m/s, 370 ~ 390 Hz, (b) stable, v_{mix} = 50 m/s and (c) unstable, v_{mix} = 70 m/s, 340 ~ 360 Hz.

So, to examine the flame structure and instability characteristics, we calculated the Strouhal number for each combustion instabilities condition. A Strouhal number is the most famous of dimensionless number describing oscillating flow mechanisms. Instability frequency and inlet mixture velocity were used and characteristic length was replaced as flame length, which was measured by using the flame center with the averaged image. Table 5.2 shows the low mixture velocity (30, 35 m/s) conditions of unstable flame region has a higher Strouhal number than the high mixture velocity instability cases. Further, there is no acoustic boundary build up caused by influence heating flux value on the lower mixture velocity condition. So, very low instability amplitude exists, and the instability mode does not matched with others one.

Table 5.2 Strouhal number calculation for conditions of each fuel-air mixture velocity.

State	Flame shape	Length (mm)	Velocity (m/s)	Frequency (Hz)	Strouhal number
Unstable (@ low velocity)	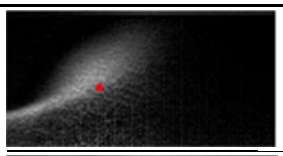	50.72	30	370	0.626
	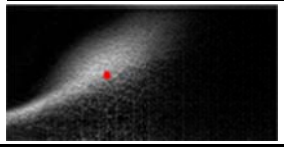	54.64	35	393	0.614
Stable	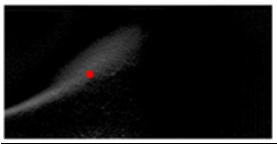	48.52	40	-	-
	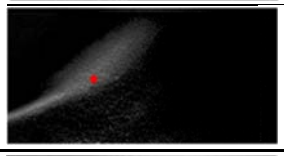	47.42	50	-	-
Unstable (@ high velocity)	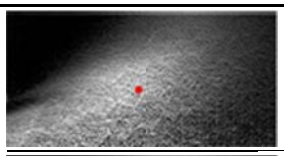	66.13	65	356	0.362
	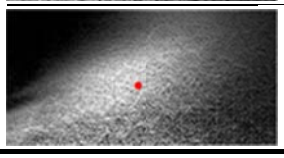	66.53	70	365	0.347

C. Kulsheimer et al.[12] and M. Escudier[13] are suggest that when the Strouhal number is high, the critical pressure for making a vortex shedding structure is less when the Strouhal number is lower condition. Applying that result in this chapter for the low mixture velocity instability case, which shows a high Strouhal number, can more easily generate the vortex structure and, therefore the interaction of this vortex structure with an acoustic wave will be the cause of unstable combustion. When the OH chemiluminescence image has not been averaged, the low velocity condition shows

sharper vortex structures, and these images can help confirm the hypothesis about the origin of frequency shifting at low-speed instability.

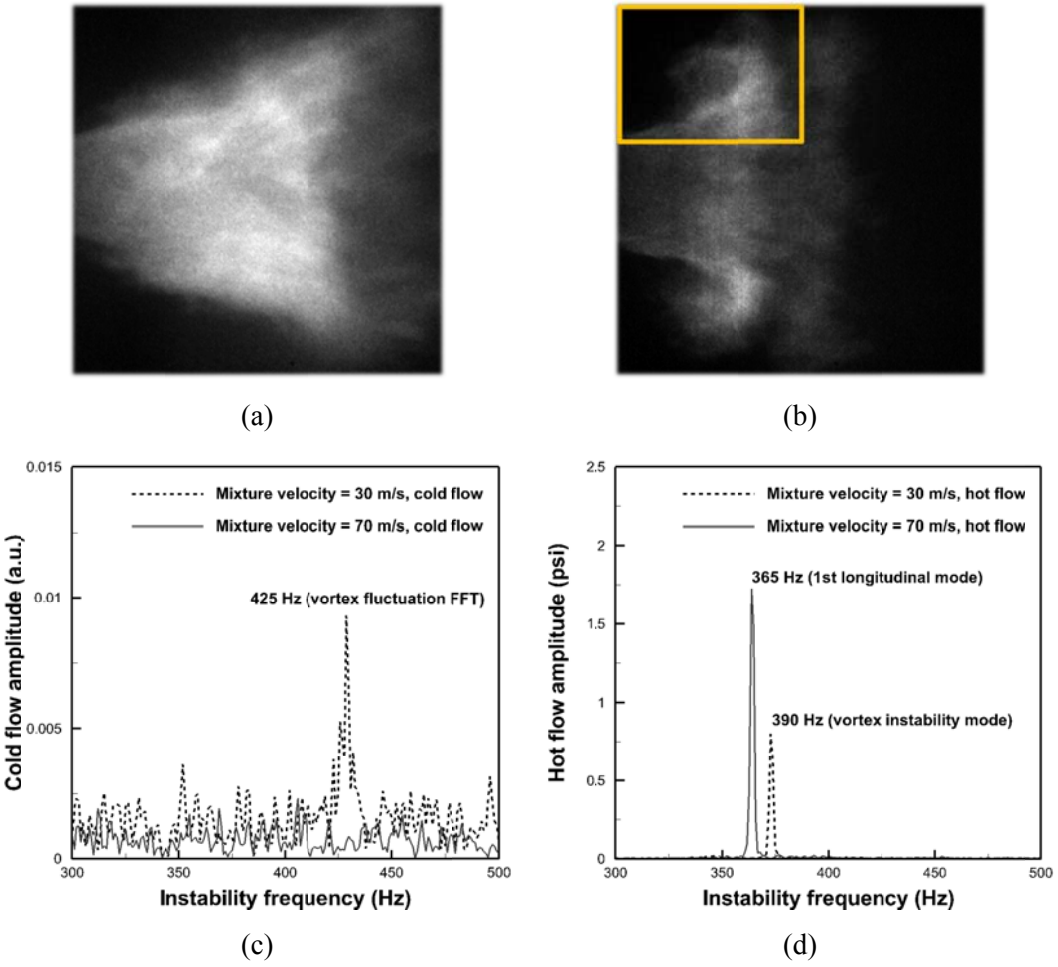

Fig. 5.5 High speed camera instantaneous image and heat release wave FFT analysis in vortex instability region; (a) v_{mix} = 70 m/s, (b) v_{mix} = 30 m/s, (c) FFT analysis of instability intensity fluctuation in cold flow and (d) FFT analysis of instability intensity fluctuation in combustion condition.

Figure 5.5 shows the FFT results, which means the local vortex frequencies in cold and hot flow condition. At cold condition, frequency was detected even though there was no acoustic forcing. This vortex instability frequency which was measured at vortex structure is same as the heat release rate instability frequency of the total flame oscillation (Fig. 5.5 (b), (d)).

5.5 Combustion Instability Mode and Phase Analysis

To analyze the frequency shifting characteristics, we performed a mode and phase analysis using the multi position dynamic sensing system in the flame at conditions of low and high fuel-air mixture velocity instability. First, the dynamic mode analysis was conducted with dynamic pressure sensors (#5) to confirm the instability mode at 30, 70 m/s mixture velocity conditions. We assumed that both the combustor and the inlet mixing section have closed-closed acoustic boundary conditions which one-dimensional acoustic wave condition and constant temperature condition in each combustor and inlet mixing sections. Fig. 5.6(a) and 5.7(a) show the result of dynamic pressure mode analysis. Dots indicate experimental data obtained by dynamic pressure sensor and the mean pressure amplitudes at each position. Black dotted lines indicate the acoustic boundary of the inlet section and combustor. Solid lines indicate ideal standing waves of ideal acoustic boundary. The result of mode and phase analysis represents the longitudinal mode of the inlet mixing section and combustion chamber. Experimental data follow the ideal standing wave and are quite well matched which means that the mode of instability is the first half wave longitudinal mode of the combustor for all of fuel-air mixture velocity conditions. This means that no change in instability mode occurs during inlet velocity variation. In other words, frequency jumping is not the result of a change in instability mode. Second, we investigated the heat release and dynamic pressure sensor data which are located near the combustion section to use phase locking each other. At conditions of high mixture velocity instability as shown Fig. 5.6(b), there is an in-phase of heat release

and dynamic pressure sensor #5. There are combustion instabilities caused by the coupling between pressure oscillations and heat release oscillations and the necessary condition for sustaining the combustion unstable is explained by Rayleigh's Criterion. But, at a low velocity instability condition as shown Fig. 5.7(b), heat release and pressure wave phase are delayed at around 130 degrees, in other words, the out-of-phase phenomenon occurs. This means that at conditions of low velocity instability there is another reason for the occurrence of combustion instability, except for the coupling of heat release and pressure perturbation waves. Conclusively, we found the frequency-shifting phenomenon during a variety of inlet mixture velocity conditions. Based on mode analysis and heat release, as well as dynamic pressure data, there is no reason for the 30 m/s mixture velocity case leading to the arising of combustion instability except the Rayleigh Criteria. From the Strouhal number result and direct images of the conditions of instability, it seems that fluid dynamic instability and vortex structure interactions are the main causes of frequency shifting during low fuel-air mixture velocity instability.

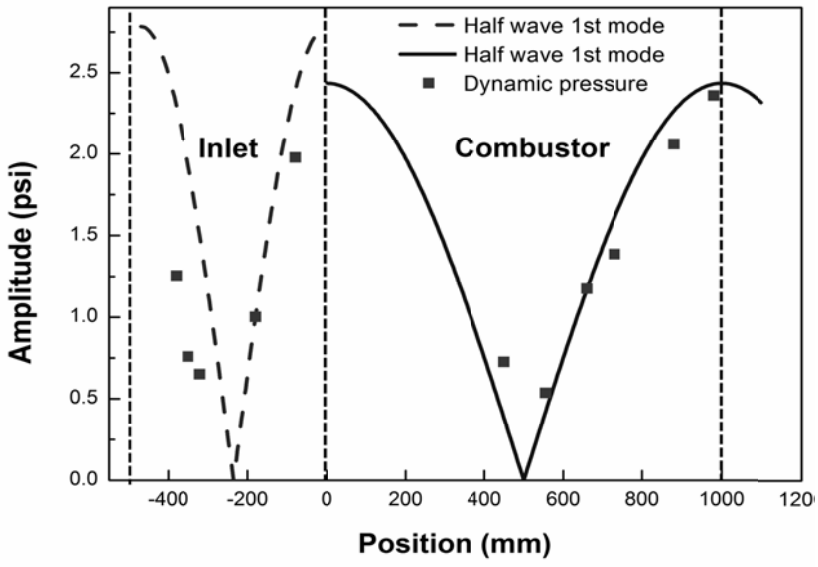

(a)

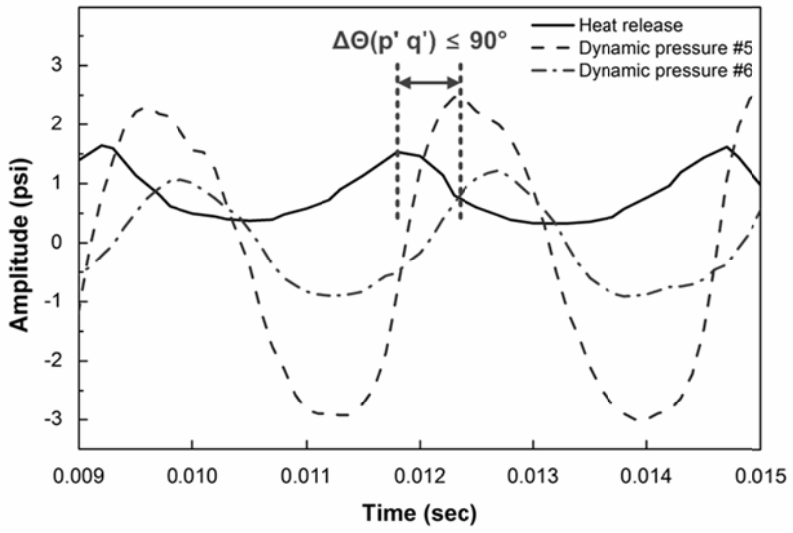

(b)

Fig. 5.6 Dynamic pressure results at fuel-air mixture velocity of 70 m/s conditions; (a) acoustic standing mode, (b) phase difference.

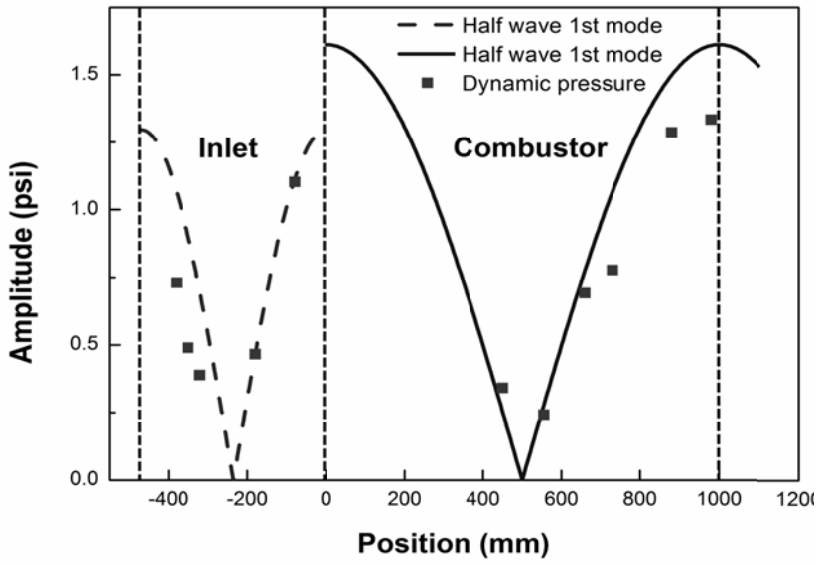

(a)

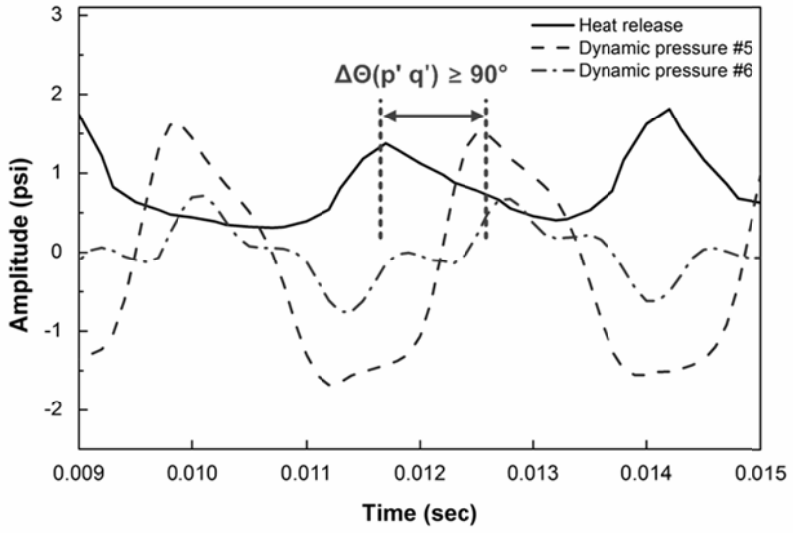

(b)

Fig. 5.7 Dynamic pressure results at fuel-air mixture velocity of 30 m/s conditions; (a) acoustic standing mode, (b) phase difference.

5.6 Dynamic Pressure Gradient Variation

An analysis was conducted on the basis of a phase-averaged, Abel inversion transform image as identified above, and the structural change in flame according to the unstable phenomenon was largely analyzed into two types – changes in flame angle and flame length. A study was carried out on the pressure gradient that is formed inside of the combustion chamber and change in the flame structure based on dynamic pressure fluctuations inside the combustion chamber. For the pressure gradient, the information concerning the dynamic pressure on no.5 sensor at the front of the combustion chamber (fuel-air nozzle exit) and on no.6 sensor closest to the combustion chamber from the exhaust exit was used.

It was confirmed through measuring that the unstable flame under high fuel-air mixture velocity conditions showed a higher value in the constant pressure at the front end of the combustion chamber than the exhaust duct. Looking into the phase 120° ~ 270° zone showing an increase in the dynamic pressure at the front end, as shown in Fig. 5.8(a), the pressure at the front of the combustion chamber increase as much as dynamic pressure, with the exhaust duct also showing an increase, but the growth rate is expected to be relatively small. That is, the mass flow rate is expected to increase by the pressure gradient relatively getting greater and this phenomenon can be confirmed through a substantial change in length and brightness of the flame. On the contrary, checking the area where the pressure at the front of the combustion chamber decreases more than the exhaust duct pressure brings an expectation that the dynamic pressure at the front of the combustion chamber is relatively reduced more than the dynamic pressure at the back, which would lead to a relative decline in pressure gradient formed inside the combustion chamber. That is, the overall flow is expected to be less and this phenomenon can be confirmed through the phase-averaged OH chemiluminescence images. The unstable flame under fuel-air mixture velocity conditions, shown in Fig. 5.8(b), is confirmed to have a different behavior from the flame under high fuel-air mixture velocity conditions. When the constant pressure was first measured, the pressure difference between front and

rear of the combustion chamber was almost constant. Therefore, it is expected that the flame will be retarded in an area where the dynamic pressure at the front of the combustion chamber relatively gets smaller than the rear, that is, in an area where the pressure gradient relatively gets lowered. Unlike the fact that the brightness of flame under high fuel-air mixture velocity conditions is reduced, it is possible to check that the brightness of flame becomes brighter than the flame of low mass flow rate on average. Besides, it was possible that the vortex structure developed at the flame edge and the vortex structure developed this way was pushed backward while gradually losing the flame brightness by the rise in mass flow rate in an area where the pressure at the front of the combustion chamber increases. In other words, an explanation can be presented as to changes in flame length through the pressure gradient formed of combustor inside. Especially the flame under low fuel-air mixture velocity conditions was confirmed to reveal characteristics different from the flame under high fuel-air mixture velocity conditions such as forming the vortex structure at the flame edge.

We conducted an analysis on the basis of variation in flame angle, illustrating a graph through the flame angle for each phase and the OH chemiluminescence intensity. Fig. 5.9 could check out change in flame angle and heat emissions, and that the behavior of the 5th dynamic pressure sensor closest to the combustion chamber displays a small phase difference and issues a sequential vibration. That is, it can be confirmed that this does meet the Rayleigh's criterion that causes combustion thermo-acoustic instability. On top of this, it is possible to confirm that the fluctuations caused by heat release rate oscillation through the phase difference in each data are propagated to the upper class and that such a fluctuation in pressure waves causes a change in flame angle. The paper of Candel et al. [14, 15] once reportedly says the pressure fluctuations change the swirl number of a swirler to bring change to the flame structure. This means that the flame structures are influenced by mixture perturbation and this oscillation changes the flame angles.

$$\frac{S-\overline{S}}{S}=\frac{S'}{\overline{S}}=\alpha\left[\exp i\left(\frac{\omega}{\overline{u}_2}x\right)-\exp i\left(\frac{\omega}{\overline{c}}x\right)\right]\exp i\left(-i\omega t\right) \tag{5.1}$$

Equation (5.1) shows that velocity fluctuation results in swirl number perturbation and dynamic pressure oscillation. Therefore during at instability conditions when pressure oscillation occurs, it results in swirl number perturbation and this phenomenon has an effect on flame stability and fluctuation of heat release. As identified in Fig. 5.10, a difference is created if the identical analysis is performed in instability under low fuel-air mixture velocity conditions. The order of generating heat release rate oscillation wave and pressure fluctuations and change in flame angle is consistent, but its phase difference can be confirmed to be over 90° or close to 90°.

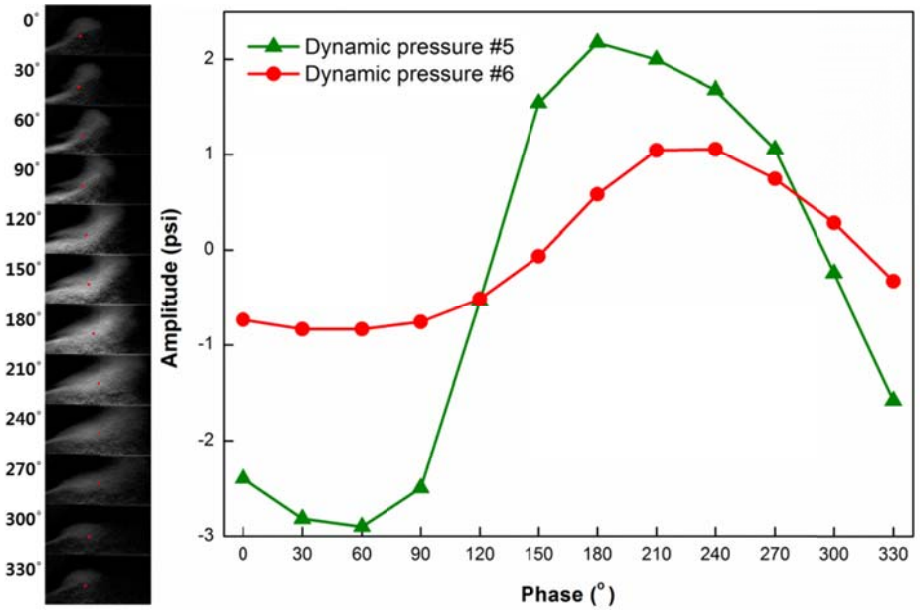

(a)

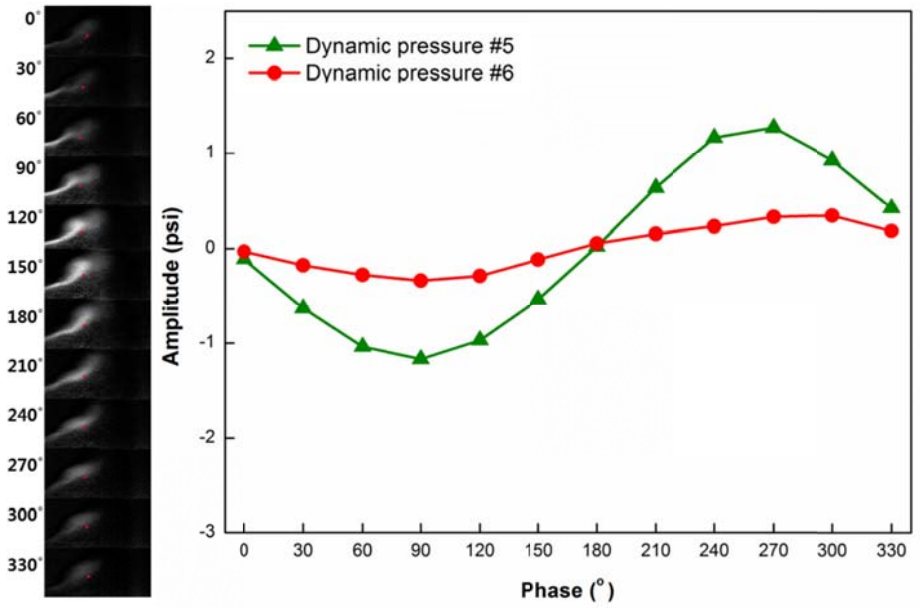

(b)

Fig. 5.8 Dynamic pressure gradient variation and flame structure results at various fuel-air mixture velocity conditions; (a) v_{mix} = 70 m/s, (b) v_{mix} = 30 m/s.

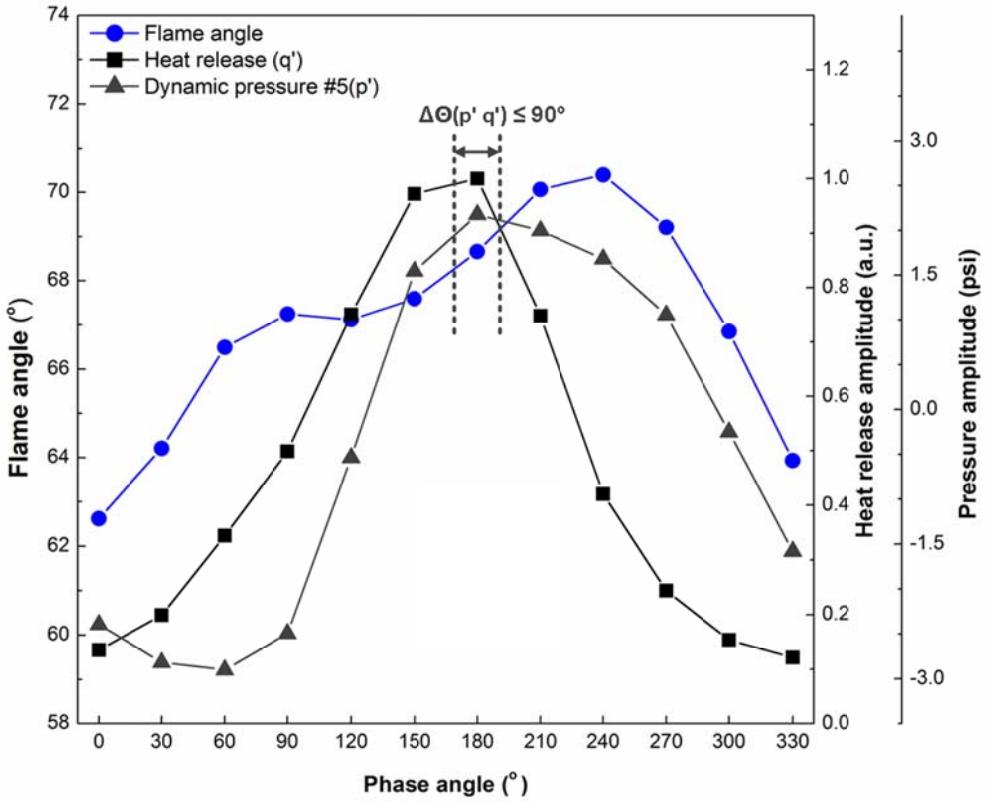

Fig. 5.9 Heat release, dynamic pressure, and flame angle change results at 70 m/s fuel-air mixture velocity conditions.

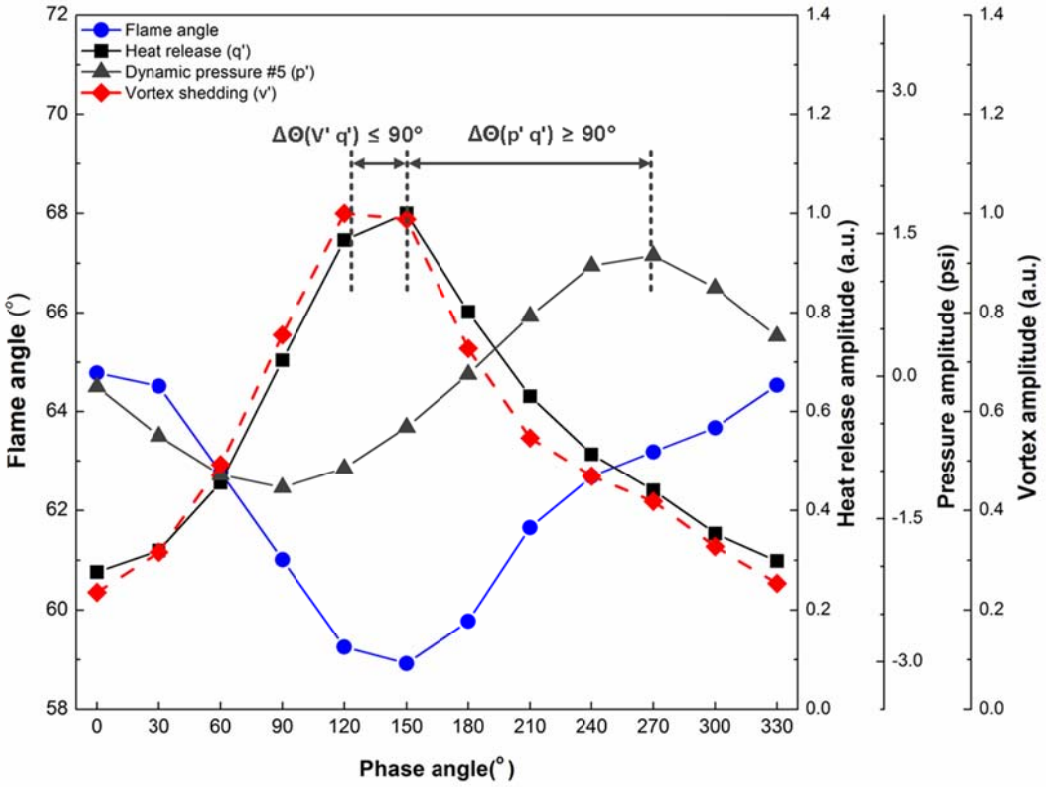

Fig. 5.10 Heat release, dynamic pressure, and flame angle change results at 30 m/s fuel-air mixture velocity conditions.

CHAPTER 6
EFFECT OF FUEL-AIR MIXING SECTION

6.1 Background and Objectives

This chapter is focused on studies of combustion instability characteristics relate with the model combustor length and inlet mixing section geometry. Previous studies were conducted to observe the phenomenon of combustion instability and flame structure [1, 2] in the combustor having a simple fuel nozzle with the swirl effect and to investigate a method of analyzing the cause and mode of combustion instability [3, 4]. Based on the results of the previous studies, however, this chapter observed the phenomenon of combustion instability by changing the combustor length and its fuel-air mixture velocity to discover the characteristics of the combustion instability mode and their kinds in a combustor simulating an actual gas turbine for power generation. At this point, this study of fuel-air mixing section geometry confirmed the conditions of heat release oscillation by changing the fuel-air mixture velocity and equivalence ratio and verified the exact causes of combustion instability by analyzing the instability modes and phases appearing during the combustion instability by multi-channel dynamic pressure sensing measurement [5] in both the combustor and the inlet mixing section.

6.2 Experimental Method and Conditions

The combustor used for this study is a 1/3 scale model gas turbine combustor simulating the GE 7FA+e DLN-2.6 gas turbine combustor, which is characterized with premix and a swirl-stabilized flame as shown in Fig. 6.1. The model is composed of an air-heating device, air supply lines, fuel nozzles, a flame visualization quartz combustor and a spike-typed plug nozzle for the exhaust duct as an acoustic boundary. As one of the main variables for this experimental study (as shown in Table 6.1.), the fuel-air mixing section was located between the combustor dump-side and the choking orifice at the back

of the air-heating device, which came in three lengths, 470 mm, 550 mm, and 870 mm, although all inlet mixing section had an inner diameter of 40 mm as shown in Fig. 6.2. Table 6.2 shows the experimental conditions of this chapter. A swirl injector used for this device is an axial-typed injector, which has 10 swirl vanes set at the angles of 0° and 30°. Fuel is injected at 20 mm detached spot from the swirl vane, 10 nozzles, each of which has a 1.2 mm-sized hole, and is pre-mixed with air through the 140 mm-sized mixing length. The swirl number of the swirl injector used for this research was about 0.42. A circular stainless steel (@ case 1, 2) and a quartz tube (@ case 3 ~ 8) for the flame visualization were alternately used, and the diameter inside the combustor was 120 mm. The plug nozzle placed at the exhaust duct was supposed to function to change the resonant frequency of the combustor by making an acoustic boundary that blocks 91% of the combustor exhaust duct, which was designed to regulate the length of the combustor by 0.1 mm from 800 mm to 1680 mm through the stepper motor located in the exhaust part of model gas turbine combustor.

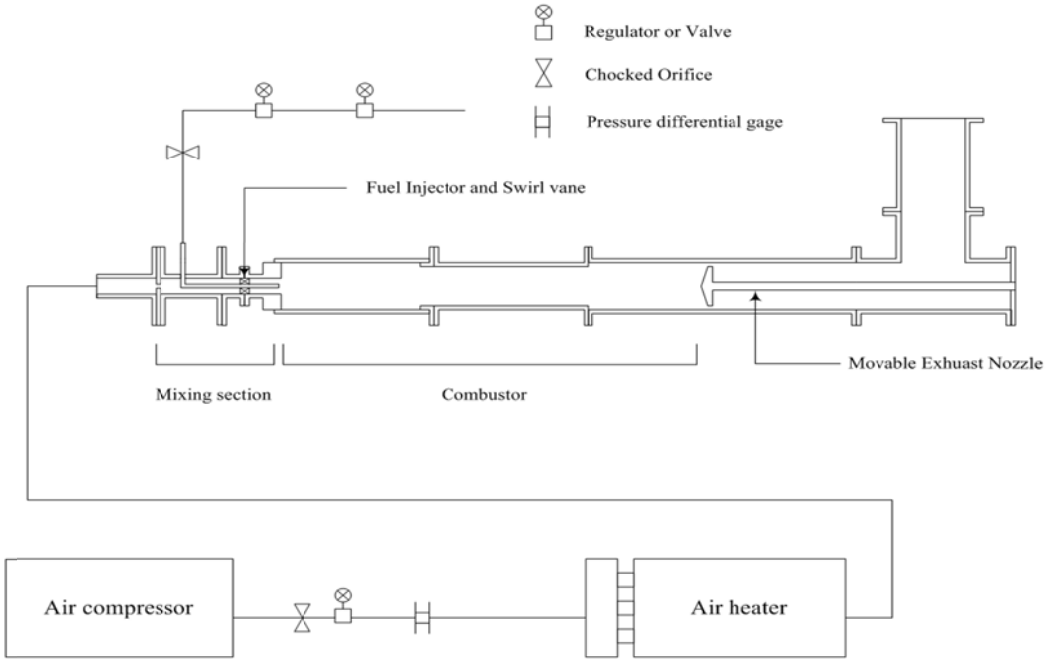

Fig. 6.1 Schematics of a model dump shaped gas turbine combustor simulating in the 1/3 scale downed of a GE 7FA+e DLN-2.6 gas turbine combustor.

Table 6.1 Experimental cases for various combustion instability conditions.

Test case	Injector type	Combustion instability mode	Inlet length [mm] (Plenum)	Combustor length [mm]	Mixture velocity [m/sec]	Equivalence ratio (Φ)
Case 1	No swirl	1L	470	1000	70	0.9
Case 2	No swirl	2L	470	950	70	1.1
Case 3	30° swirl	1L	470	1000	70	1.1
Case 4	30° swirl	2L	470	950	40	1.2
Case 5	30° swirl	1L	550	1050	70	1.0
Case 6	30° swirl	2L	550	950	40	1.1
Case 7	30° swirl	1L	870	1650	60	1.1
Case 8	30° swirl	2L	870	1650	70	0.8

Table 6.2 Experimental conditions.

Parameters	Values
Fuel type	Natural gas [CH_4(89.4%) + C_2H_6(8.6%) + C_3H_8(1.39%)]
Inlet air temperature [K]	673
Fuel temperature [K]	318
Swirl vane angle	No swirl, 30° swirl (swirl number = 0.42)
Mixture velocity [m/sec]	30, 40, 50, 60, 70
Equivalence ratio (Φ)	Blowout limit ~ 1.2
Inlet mixing section length [mm]	470, 550, 870
Combustor length [mm]	800 ~ 1680
Blockage nozzle [mm]	128 (Blockage ratio : 91%)

To observe the oscillation of dynamic pressure occurring during the combustion experiment, we used five 102A05-type dynamic pressure sensors, manufactured by PCB Company, for the inlet mixing section and six for the combustor, as well as infinity probes, which suppress the reflected wave of dynamic pressure [6, 7]. In addition, the sampling rate was observed by receiving 10,000 data per second, and through Fast Fourier Transformation (FFT) techniques, it was possible to analyze them up to 5,000 Hz. Moreover, OH* chemiluminescence was measured from the flame around the dump side. By using a high-speed ICCD camera made by Photron Company, we photographed flames at the speed of 1/6000 fps, and were able to obtain the pressure oscillation and heat release values from the time axis in the same experimental conditions by phase locking the dynamic pressure sensor.

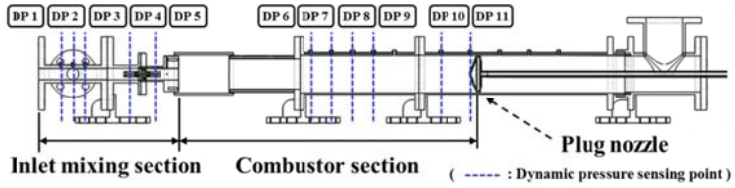

(a)

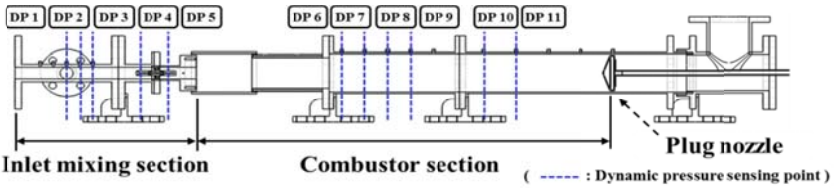

(b)

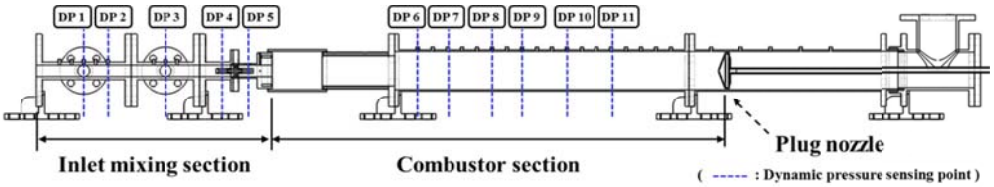

(c)

Fig. 6.2 Location of dynamic pressure sensors in fuel-air mixing section and combustor; (a) L_{inlet} = 470 mm, (b) L_{inlet} = 550 mm and (c) L_{inlet} = 870 mm conditions.

To understand the combustion instability origin mode, we measured the heat release oscillation as shown in Fig. 6.3. Furthermore, this study acquired signals that drive the high-speed ICCD camera, signals of photos being taken and dynamic pressure signals by using DAQ and analyzed the flame visualization information and acoustic field oscillation information at the same time. This was especially the case for combustion instability phenomenon, which was accomplished the process of measuring the results of dynamic pressure and heat release waves in the same time domain.

(a)

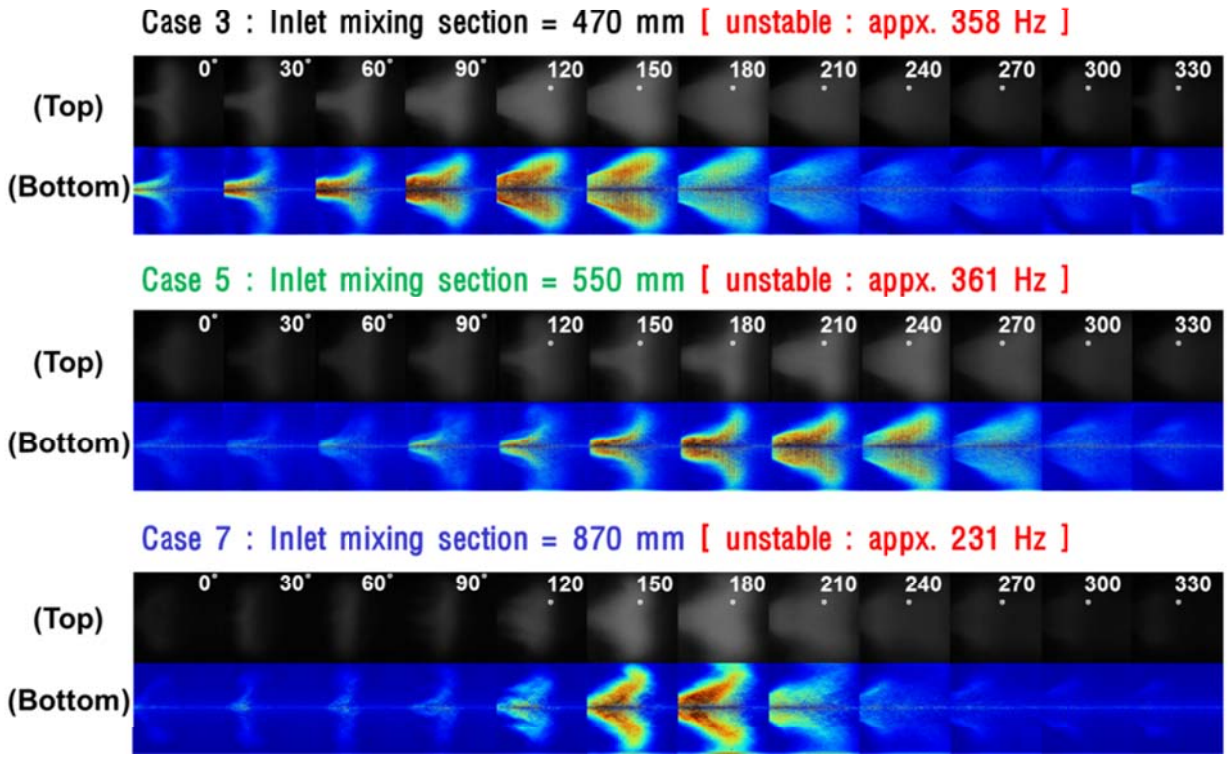
Case 3 : Inlet mixing section = 470 mm [unstable : appx. 358 Hz]
(Top)
(Bottom)
0° 30° 60° 90° 120 150 180 210 240 270 300 330
Case 5 : Inlet mixing section = 550 mm [unstable : appx. 361 Hz]
(Top)
(Bottom)
0° 30° 60° 90° 120 150 180 210 240 270 300 330
Case 7 : Inlet mixing section = 870 mm [unstable : appx. 231 Hz]
(Top)
(Bottom)
0° 30° 60° 90° 120 150 180 210 240 270 300 330

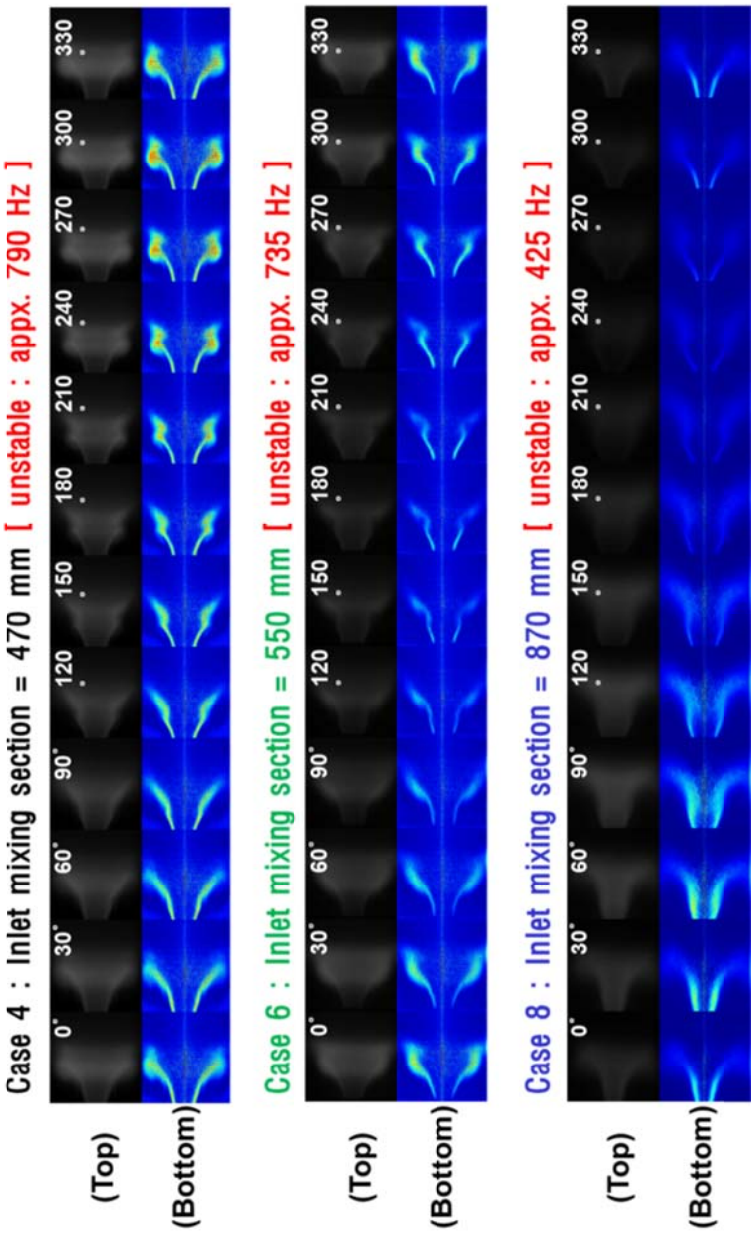

(b)

Fig. 6.3 OH chemiluminescence (top) and abel-inverted (bottom) images at 30° swirl effect; (a) 1st longitudinal instability mode, (b) 2nd longitudinal instability mode.

6.3 Stability Map

By conducting a combustion experiment in different experimental conditions with a model gas turbine combustor, this study conducted an experiment to confirm the flame stability map. Fig. 6.4 is a graph showing the dynamic pressure values observed in all the experimental conditions when the angle of swirl was 0° and the length of the fuel-air mixing section was 470 mm. At this point, the 4th dynamic sensor detached from the dump plane was used as the standard dynamic pressure point. As shown in the graph, as the mixture velocity increased, the combustion tended to be unstable, and especially the combustion generally appeared unstable when the fuel-air mixture velocity was 70 m/s. In conditions where the fuel-air mixture was higher in the velocity region, the modes of combustion instability were divided into two kinds, depending on the combustor length and the equivalence ratio. Also, in the sections where the fuel-air mixture was lower in the velocity region, an insufficient supply of heat energy led to unclear acoustic boundaries, as well as failing to cause the phenomenon of thermo-acoustic instability. Also, it was found that instability did not occur under all of the conditions of the combustor length but in specific conditions of the combustor length, between 950 to 1050 mm. In other words, in the condition of combustor resonant frequencies calculated on the assumption that the combustor is a closed boundary condition, combustion instability took place by coupling with heat release oscillation, through which the combustion length was verified as an important variable causing combustion instability [8, 9, 10].

Figure 6.5 is a graph showing the dynamic pressure values observed in all the experimental conditions when the fuel-air mixing section length was 470 mm with conditions of the 30° swirl effect. At this point, 6th dynamic sensor detached from the dump plane was used as the standard point. In the graph with a 470 mm inlet mixing section with a length condition of 30 m/s in the mixture velocity, another kind of combustion instability phenomenon occurred. This is caused by the flame vortex, which in turn result from a low mixture velocity according to the geometric condition of a provided dump combustor. This, in turn is, not a phenomenon of thermo-acoustic

instability caused by the heat release oscillation of the combustor and flame [11, 12]. In an experimental condition in which fuel and air mixed relatively well, when the mixture velocity was 40 m/s and the length of the fuel-air mixing section was 470 mm, the acoustic boundary of the inlet mixing section was established as a closed-open boundary [13, 14] since the fuel-air mixture should be delivered to the combustor, and it was found that combustion instability was well matched with the mode when resonant frequencies of the 2nd mode of the closed-closed boundary occurred in the combustor. Thus, this study found that the length of the fuel-air mixing section in the driving part of the combustor is an important variable causing combustion instability, which will be verified by analysis of the mode and phase from the results values on the next section and the multi-channel dynamic pressure sensing system.

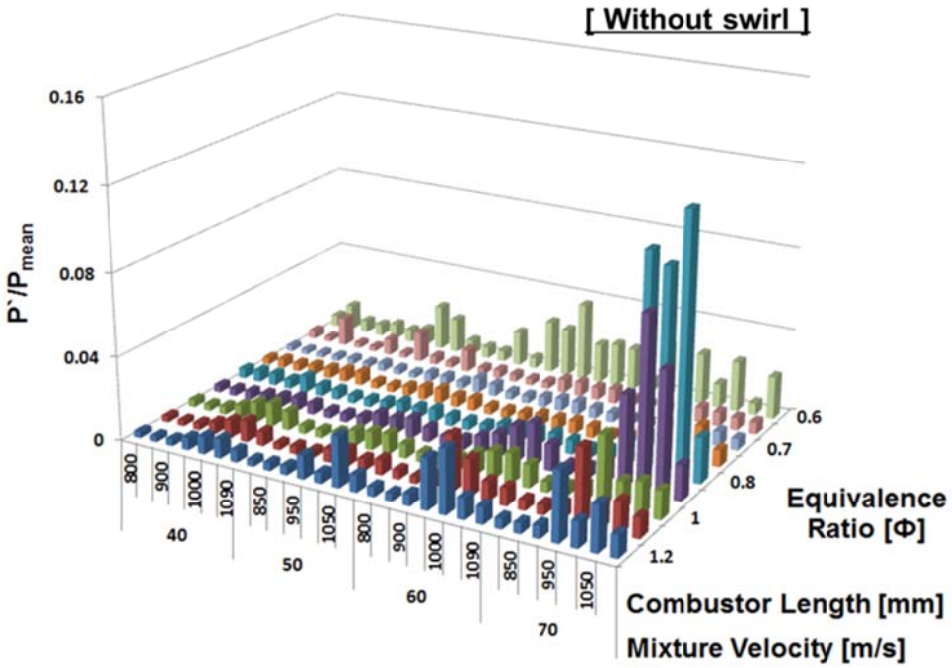

Fig. 6.4 Stability map for all of the experimental conditions at no swirl effect and L_{inlet} = 470 mm (case 1, case 2) conditions.

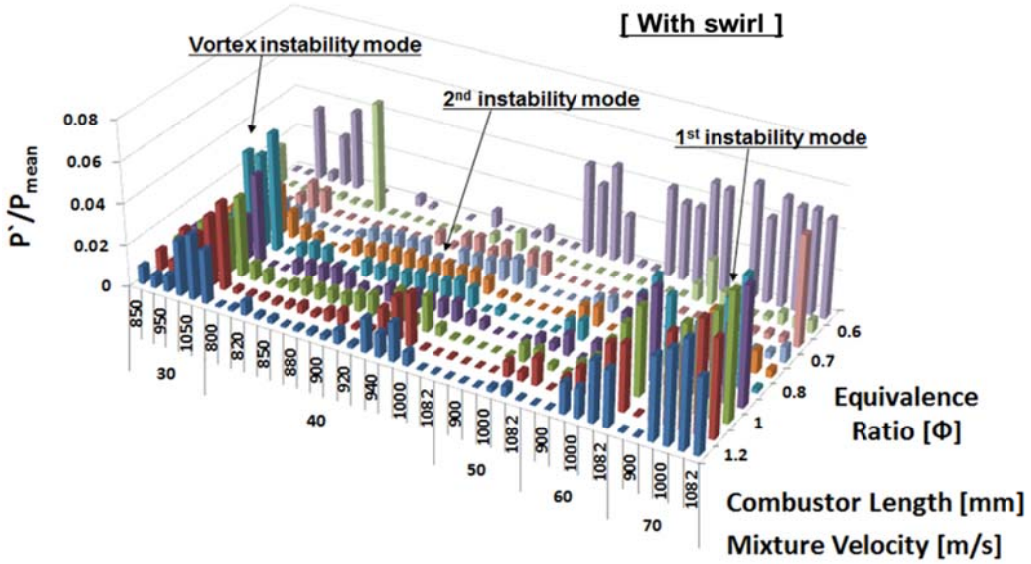

Fig. 6.5 Stability map for all of the experimental conditions at 30° swirl effect and L_{inlet} = 470 mm (case 3, case 4) conditions.

And, it was found that instability did not occur under all of the conditions of the combustor length but in specific conditions of the combustor length, between 950 to 1050 mm, as shown in Fig. 6.6 for example of no swirl, inlet mixing section is 470 mm conditions.

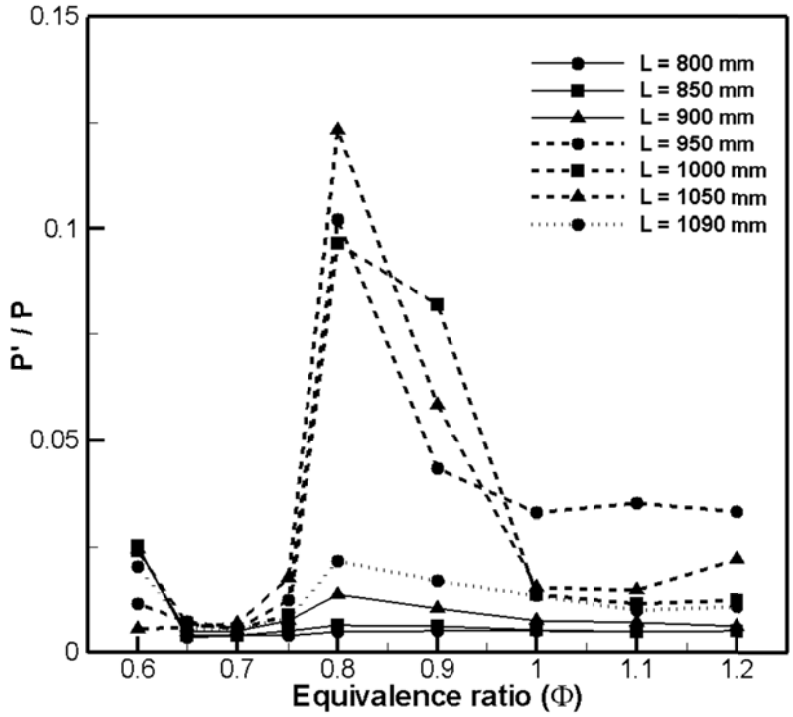

Fig. 6.6 Combustion instability results for various combustor length conditions at no swirl effect and L_{inlet} = 470 mm (case 1, case 2) conditions.

Figures 6.7 and 6.8 is a graph showing the dynamic pressure values observed in all the experimental conditions when the angle of swirl was 30° and the length of the fuel-air mixing section was 550 and 870 mm. Thus, this study found that the length of the fuel-air mixing section in the driving part of the combustor is important variable causing combustion instability, which will be verified by analyzing mode and phase analysis from the result values on next section and multi position dynamic pressure sensing system. To find out if the specific combustion instability characteristics of 2^{nd} longitudinal mode (2L), appeared in another experimental condition, it was tested in different lengths of the mixing section, such as 550 mm and 870 mm. When the length of the mixing section was 550 mm as shown in Fig. 6.7, the flame stability map, combustion instability characteristics were found to occur in all the mixture velocity conditions as well. As a result, it was clear that in the mixture velocity condition related to the mixing section length where fuel and air get mixed well with about 0.42 swirl number, combustion instability characteristics existed as well. As result from previous section, however, it was confirmed that the combustion instability phenomenon doesn't appear in all the combustion chamber length conditions, but instability characteristics became stronger as the combustion chamber became longer in length. When the mixing section length was 870 mm as shown Fig. 6.8, this experimental study attempted to find out if the instability frequency of 2L mode occurs in other frequency band domains, not in such similar conditions as 470 and 550 mm in the length of the mixing section. Therefore, by changing the mixing section length, this experiment provided a flame stability map by confirming all the experimental variable conditions. As shown in the picture, as the higher mixture velocity condition into the combustion chamber, heat flux energy increases as well, leading to confirming that combustion instability characteristics also increase. Besides, it was also found that combustion instability characteristics occurred in a specific length of the combustion chamber through the coupling of heat release and acoustic oscillation energy.

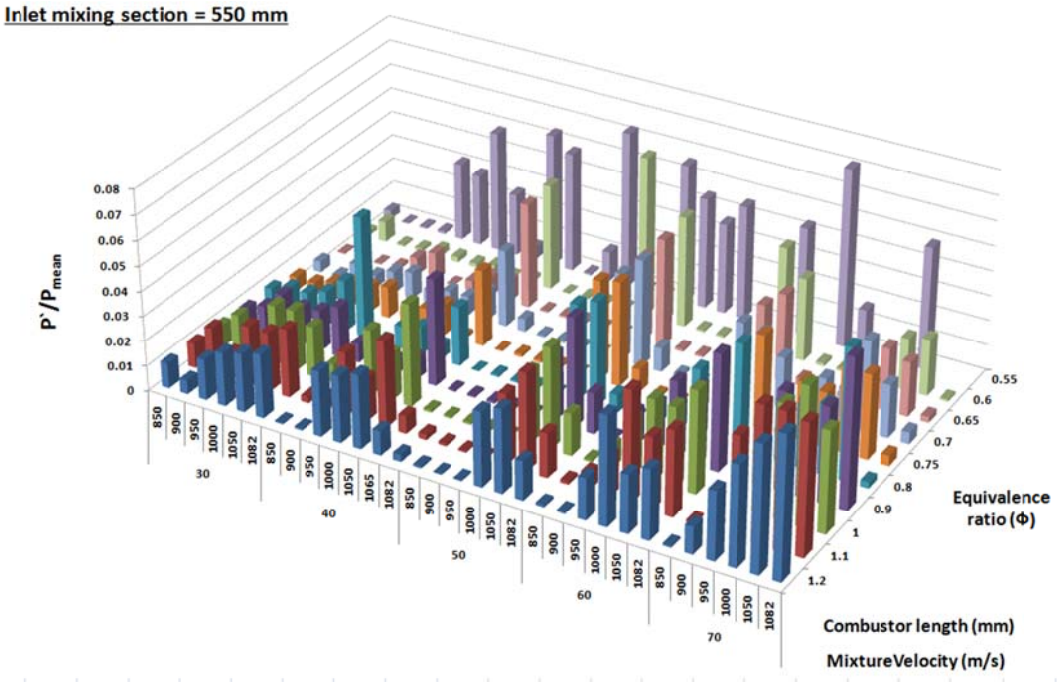

Fig. 6.7 Stability map for all of the experimental conditions at 30° swirl effect and L_{inlet} = 550 mm (case 5, case 6) conditions.

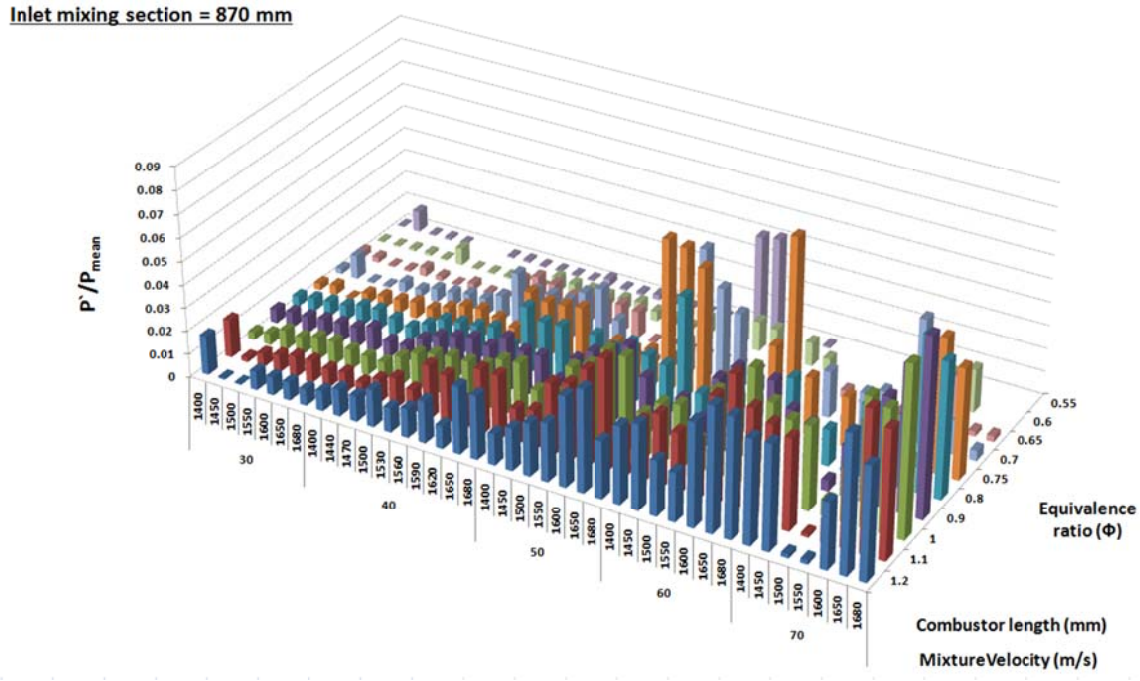

Fig. 6.8 Stability map for all of the experimental conditions at 30° swirl effect and L_{inlet} = 870 mm (case 7, case 8) conditions.

6.4 Main Instability Frequency Analysis

Figure 6.9 shows details about the intensity of each frequency obtained through the FFT analysis of dynamic pressure data in comparison with the all of experimental conditions about no swirl effect of 470 mm inlet mixing section. According to the experiment conducted by Lee et al. [15, 16], when the FFT intensity analysis was conducted on the dynamic pressure data measured in various experimental conditions, it was observed that the maximum intensity appeared in 1 or 2 specific frequency bands in case that combustion instability phenomenon took place. In this study, the combustion instability phenomenon was observed to occur in such frequency bands as 367 ~ 404 Hz and 820 ~ 850 Hz. At this point, when the combustion chamber length was 800 ~ 1090 mm, the combustion chamber temperature appeared in the range of about 1200 ~ 1500K.

To analyze the combustion instability frequency, on the assume that acoustic waves occurring inside the combustion chamber was a 1-dimentional acoustic wave and the temperature was constant value in the combustion chamber, the resonant frequency of the combustion chamber was predicted. The predicted frequency of longitudinal mode (n=1) of the combustion chamber had a range of about 330 ~ 490 Hz, but in this study, it was found that the combustion instability characteristic mostly appeared in an experimental condition where the longitudinal mode was in the frequency band of 367 ~ 404 Hz. This experiment also found that when the resonant frequency of the combustion chamber, calculated by the length and temperature of a combustion chamber, accorded with a specific frequency, a strong combustion instability phenomenon appeared. Also, there have different of secondary instability mode around 829 Hz. This instability frequency indicated that second half wave mode of combustor and quarter wave mode of inlet mixing section acoustic boundary which is related to closed-closed acoustic boundary condition of combustor and closed-opened boundary condition of plenum. And this experimental study has been almost same combustion instability characteristics in another inlet mixing section length conditions.

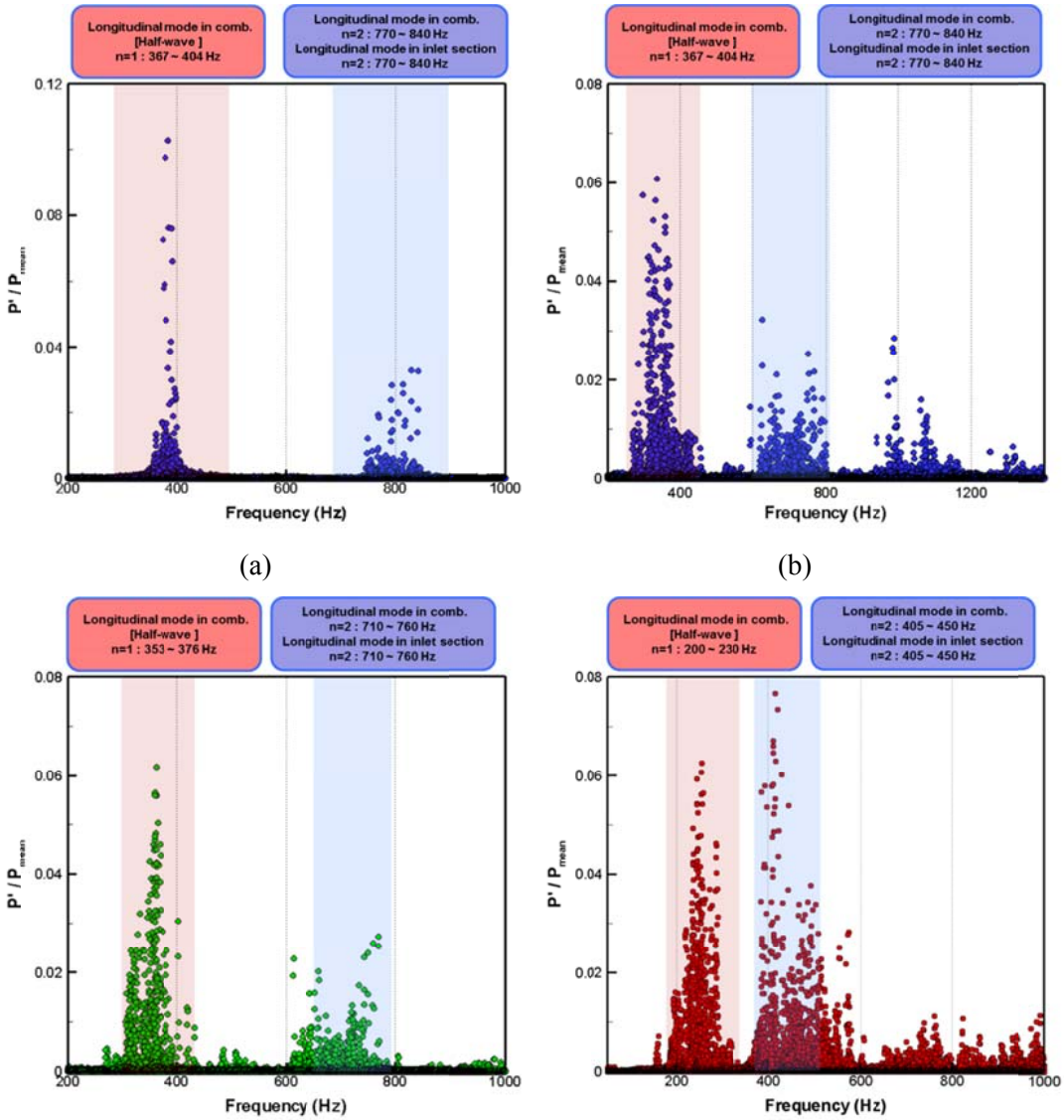

Fig. 6.9 Combustion instability frequency distribution for all of the experimental conditions; (a) no swirl effect and L_{inlet} = 470 mm (case 1, case 2), (b) 30° swirl effect and L_{inlet} = 470 mm (case 3, case 4), (c) 30° swirl effect and L_{inlet} = 550 mm (case 5, case 6) and (d) 30° swirl effect and L_{inlet} = 870 mm (case 7, case 8) conditions.

When the inlet mixing section length changed to 470, 550, and 870 mm, the FFT spectrum of the main frequencies of combustion instability was affected by the change of the equivalence ratio, which is shown in Fig. 6.10. When the circumstances of the inlet mixing section length were 470 mm with a combustor length condition of 1000 mm without a swirl effect and the fuel-air mixture velocity was 70 m/s, the equivalence ratio was 0.9 and 1.2 respectively, and the combustion instability appeared strongest when the equivalence rate was 0.9. At this point, the combustion instability frequency was 375 Hz. That is, a phenomenon was found in which the frequency of combustion instability changed by the combustor length, and when it was outside of the specific instability frequencies, the combustion instability phenomenon disappeared. When the equivalence ratio was 1.2 and the length of a combustor was 950 mm, the combustion instability phenomenon appeared at the strongest. Also, when the combustor length tuned where a specific frequency of, 829 Hz, and the acoustic mode of a combustion chamber accorded with each other, a strong combustion instability phenomenon appeared. Furthermore, when the inlet mixing section length was 550 mm and the equivalence ratio was 1.0, the combustion instability mode occurred relative to the 1st longitudinal mode (1L) of the combustion chamber while the length of the combustion chamber was changing to 1050 mm. In the case when the equivalence ratio of 1.1 became larger, an instability mode occurred related to the inlet mixing section length. Likewise, even when the inlet mixing section length was 870 mm, the instability mode changed as the equivalence ratio changed. In consequence, we discovered, the phenomenon in which the average temperature changes as the inlet mixing section mixture velocity and the equivalence ratio change, further changing the instability frequency, and the combustion instability mode suddenly changes by the matching of the lengths of the combustion chamber and the inlet mixing section.

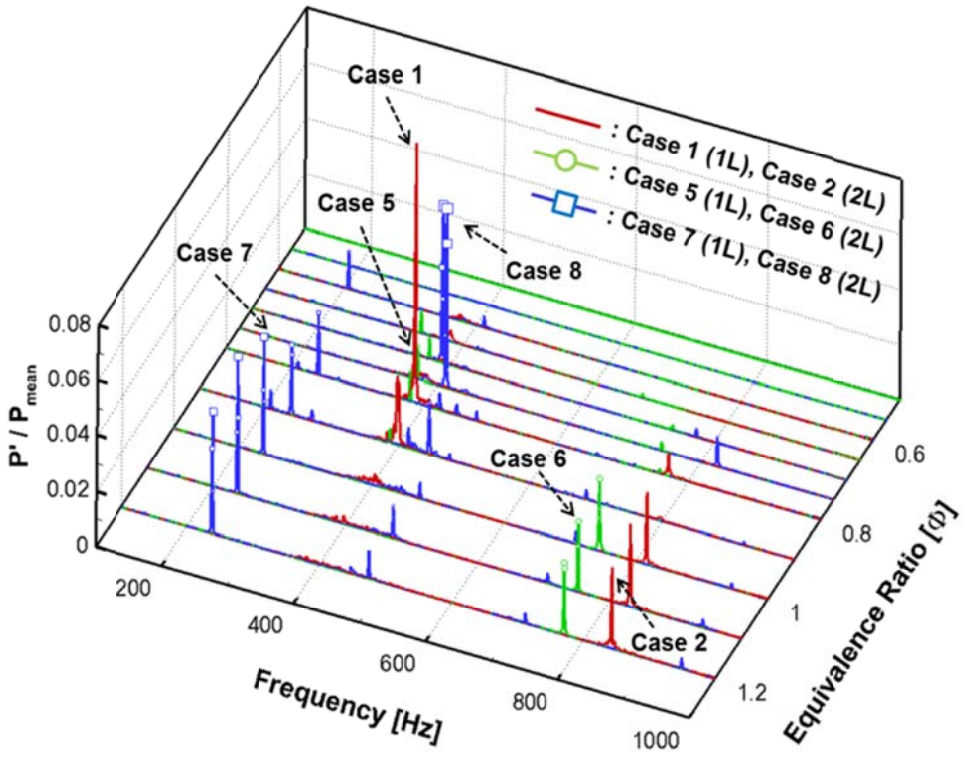

Fig. 6.10 Instability frequency FFT spectrum results for various inlet mixing section conditions.

Figures 6.11(a) and (b) are graphs showing how instability frequencies of half wave mode and quarter wave mode, which occur in the combustion chamber of a model gas turbine combustor related to the various equivalence ratio and its inlet mixing section, occurred as main modes. As shown in the picture below, the instability of an injector without swirl effect has higher instability frequencies and larger sizes than that with swirl effect. Unlike the diffusion flame without swirl effect, the premixed flame with swirl effect causes the combustor average temperature to decrease relatively, which corresponds with a theoretical ground that holds that instability frequencies of the combustion chamber are formed at low temperatures. Moreover, it was also found that as the combustor length and its inlet mixing section increase, the instability frequency

decreases, and the result of the 1L mode shows the combustion instability characteristics in conditions related to the inlet mixing section length of an injector group having swirl effect. Also, it was found that as the equivalence ratio increases, the heating energy of the combustion chamber increases as well, leading to thermal choking. Then, the acoustic boundary of the combustion chamber became clearer, which made it possible to see the size of the increase in combustion instability.

As shown in Fig. 6.11(b), where the inlet mixing section length was in a short condition (470, 550 mm), that is, in the section where the 2L mode changed to high frequencies, since the temperature and length of the combustion chamber accorded with those of the fuel-air mixing section, the combustion instability of the 2L mode was suitable for the inlet mixing section and combustor lengths in the section over 1.0 of the equivalence ratio, and as the energy dispersion into surrounding areas became larger than the case of the 1L mode, the size of the instability was found to be smaller by about on half. On the contrary, in the section where the frequency of the 2L mode was in the low instability frequency region with 870 mm in the length of the fuel-air mixing section, the 2L mode occurred when the equivalence ratio was low. It was also found that in a condition where the equivalence ratio was high, the 1L mode occurred. This was because in a flame condition where the combustion chamber temperature became suitable to accord with the frequency, the relevant combustion instability phenomenon occurred as well. A theoretical analysis likely to calculate this phenomenon is as shown in Eq. (4.1) and (4.2). And it is assumed that the movement course of energy in a gas turbine combustor is in the axial direction and the average temperature is constant with 1-D standing waves theory.

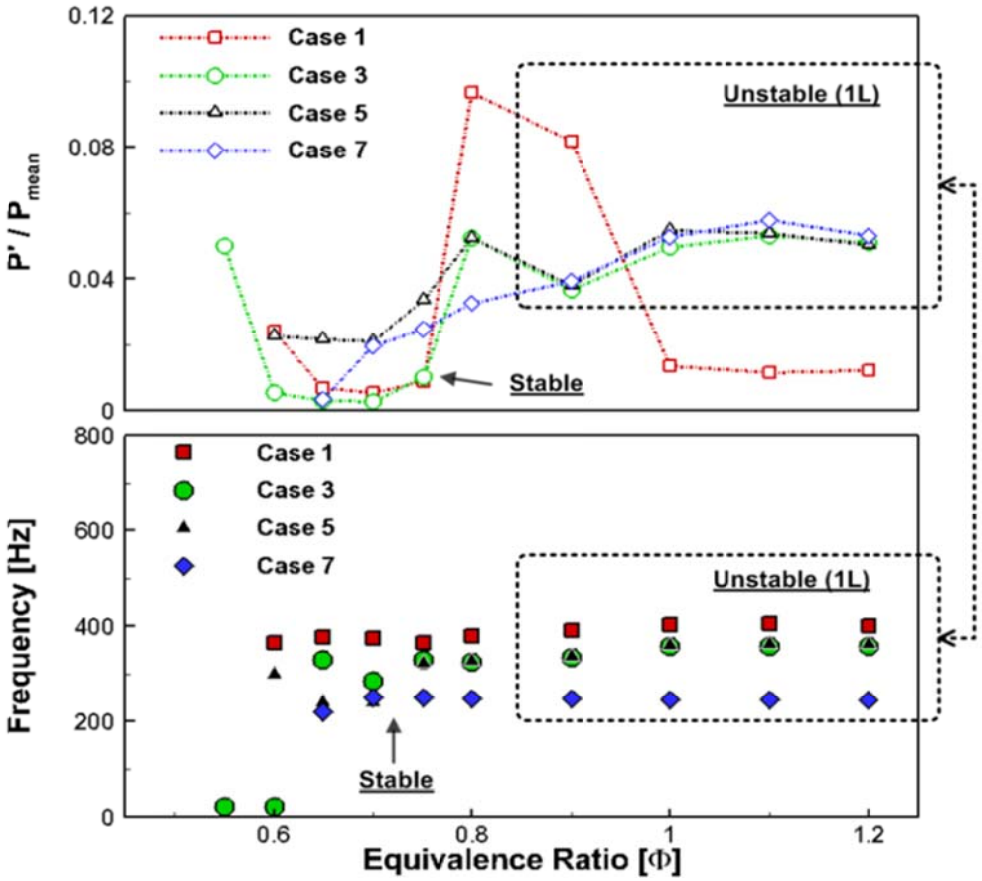
0.12
0.08
0.04
0
P' / P mean
Case 1
Case 3
Case 5
Case 7
Unstable (1L)
Stable
800
600
400
200
0
Frequency [Hz]
Case 1
Case 3
Case 5
Case 7
Unstable (1L)
Stable
0.6
0.8
1
1.2
Equivalence Ratio [Φ]

(a)

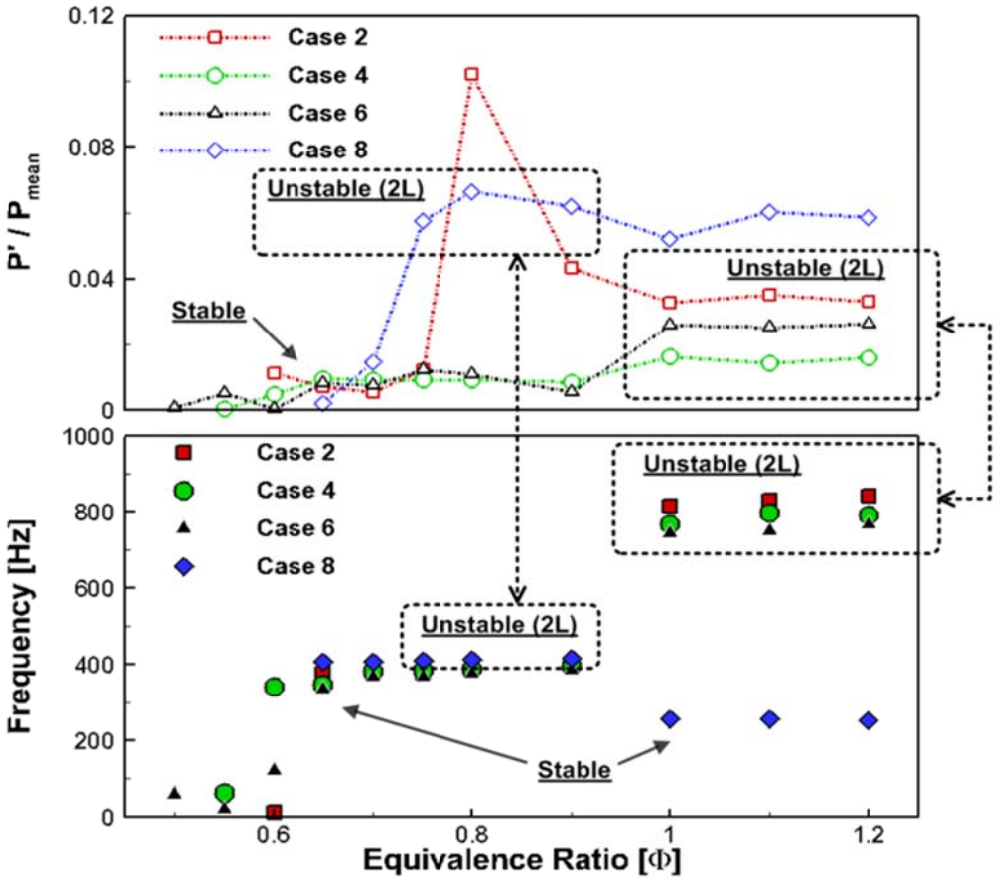

(b)

Fig. 6.11 Combustion instability characteristics for the equivalence ratio conditions; (a) 1st longitudinal instability mode, (b) 2nd longitudinal instability mode.

Figure 6.12 shows the combustion instability characteristics depending on the change of the combustor length. As explained earlier, the reason why the 1L and 2L modes have main combustion instability is not because of the conditions related to the combustor length condition but because of the conditions related to specific combustion chamber lengths. Especially, in an instability case where the 2L mode occurred, it was found that instability modes appear when the acoustic boundary of the inlet mixing section accords with the frequency corresponding to the second quarter wave mode. All of the experimental results from this study are listed in Table 6.3.

Table 6.3 Experimental results for various combustion instability conditions.

Test case	**Plenum temperature [K]**	**Combustor temperature [K]**	**Main instability frequency [Hz]**	**Main instability magnitude (p'/p_{mean})**	**Estimate value of plenum [Hz] (Quarter wave mode)**	**Estimate value of combustor [Hz] (Half wave mode)**
Case 1	397	1150	378	0.1242	276	375
Case 2	398	1268	829	0.0351	829	827
Case 3	395	1126	358	0.0531	264	353
Case 4	396	1068	790	0.0189	791	785
Case 5	401	1116	361	0.0548	237	360
Case 6	403	995	735	0.0253	712	750
Case 7	385	1050	231	0.0578	144	225
Case 8	388	950	425	0.0673	432	442

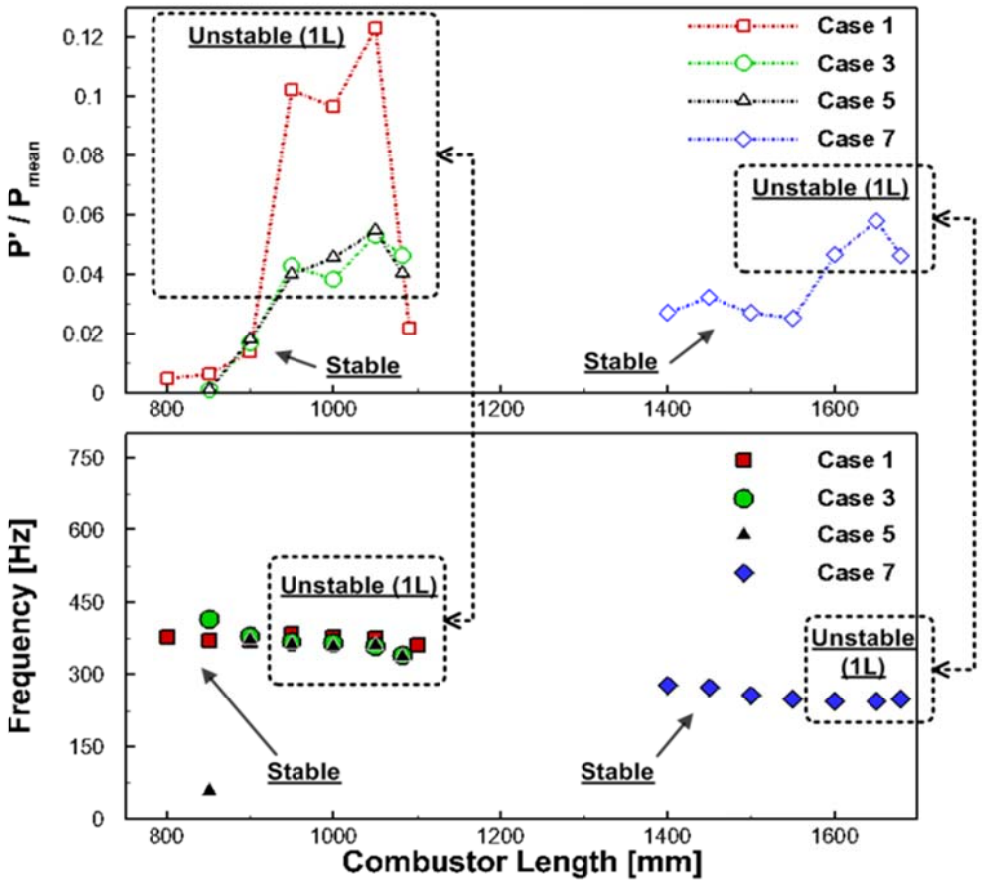
Unstable (1L)
Case 1
Case 3
Case 5
Case 7
Unstable (1L)
Stable
Stable
P' / P mean
0.12
0.1
0.08
0.06
0.04
0.02
0
800
1000
1200
1400
1600
Case 1
Case 3
Case 5
Case 7
Unstable (1L)
Unstable (1L)
Stable
Stable
Frequency [Hz]
750
600
450
300
150
0
800
1000
1200
1400
1600
Combustor Length [mm]

(a)

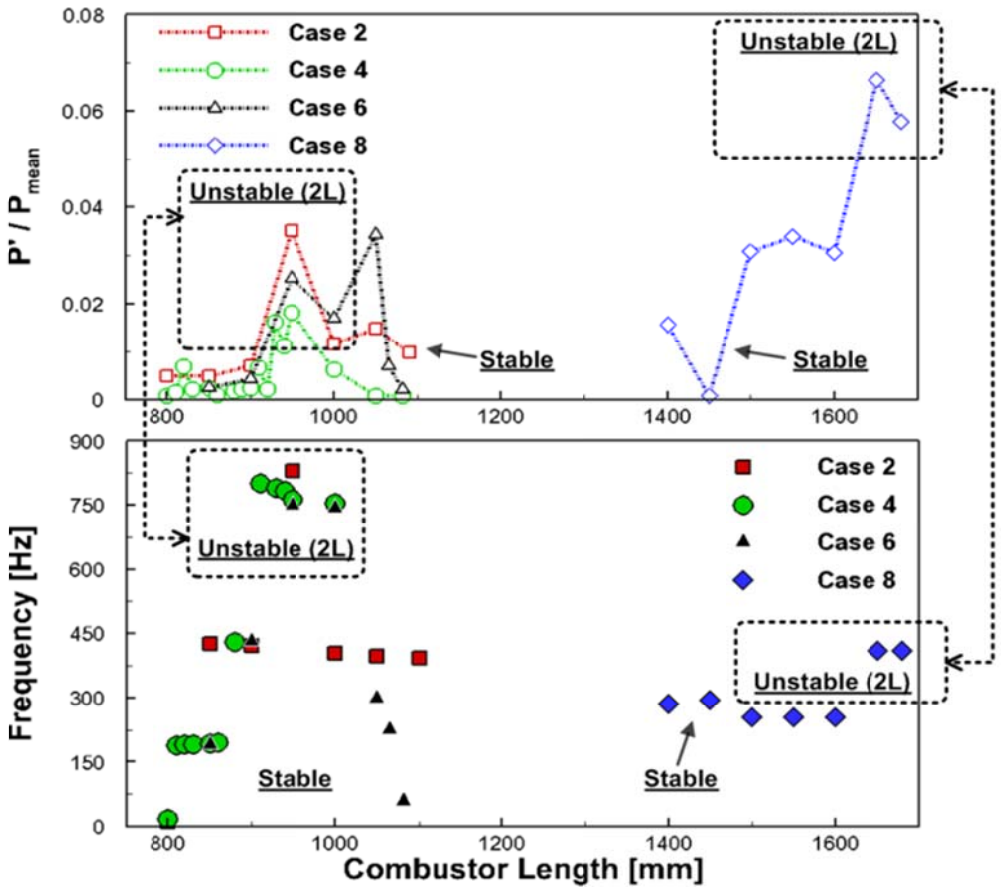

(b)

Fig. 6.12 Combustion instability characteristics for various combustor length conditions; (a) 1st longitudinal instability mode, (b) 2nd longitudinal instability mode.

6.5 Combustion Instability Mode and Phase Analysis

For the combustion instability phenomenon to take place in a model gas turbine combustor, acoustic waves and heat release waves, which are likely to appear due to the form of the combustion chamber, are required to interact with each other. Basically, therefore, combustion instability frequencies are generated by the acoustic wave from the combustion chamber or the fuel-air mixing section connected to it. Fig. 6.13(a), 6.14(a), 6.15(a) and 6.16(a) show the results of the combustion instability of the 1L mode having frequencies between 240 and 350 to 400 Hz occurring in specific combustion chamber lengths, fuel-air mixture velocities, and equivalence ratio conditions and also show the pressure oscillation magnitude and phase differences observed from 11 dynamic sensors installed in the fuel-air mixing section and the combustor section. The lines in the graphs show the estimated values of dynamic pressure in each location of the combustion chamber, and the round red dots show the values of dynamic pressure measured in each location. As shown in the graphs, most of the dynamic pressure values obtained from each location are almost the same value as the estimated ones, but there was a slightly different value in the dynamic pressure data from the end of the combustor because of the lower temperature around the blockage nozzle located at the back of the combustion chamber. In the case that the length of the inlet mixing section with no swirl effect was 470 mm, as the sensor located in the air supply device got closer to the combustion chamber, the phase difference got smaller, further having almost the same phase and oscillation in the combustor. This is well described with square-shaped black dots indicating phase differences from the standard dynamic sensing point. Likewise, from such different length conditions as 470, 550, and 870 mm along with a 30° swirl effect, the same experimental results can be obtained. Furthermore, based on the middle location of the combustion chamber where the pressure node is located, it was found that there was a phase difference of about 180° in the values of dynamic sensors in the front and in the back of the combustion chamber. This can be explained by reference to the response characteristics of a flame, as described in a recently conducted research titled “Flame

Transfer Function" [17, 18]. Specific frequency bands where combustion instability appears strong are determined by the combustor length, the location of a fuel injector, and the type of fuel-air mixing. When a combustion instability, the pressure oscillation from the combustion chamber appears stronger than that from the air supply line, through which the flame response function of a combustor used for the related experiment can be obtained, thus predicting that the band of 240 Hz and between 350 and 400 Hz can be the maximum frequency band by which the flame is affected by acoustic waves around the 1L mode, depending on the length conditions of the inlet mixing section.

Figures 6.13(b), 6.14(b), and 6.15(b) show the amplitudes and phase differences of the pressures measured when the combustion instability phenomenon takes place mainly in a higher equivalence ratio between 1.0 and 1.2. At this point, the acoustic wave of the combustor was assumed to be in the half-wave mode, and for the inlet mixing section, it was assumed to be in the quarter-wave mode. The lines in the graph show the expected values of the longitudinal mode (n = 2) of the combustion chamber, while the dashed lines show the expected values of the longitudinal mode (n = 2) of the fuel-air mixing section. Each dot shows the pressure amplitude measured from the dynamic sensors in each position. In addition, the fifth dynamic sensor is the one located after the swirler and was found to be greatly affected by the pressure field of the combustor section. Like the previous results, most of the dynamic pressure values tend to be almost the same as the expected values, and in a condition in which the combustion instability phenomenon appears, which corresponds to the longitudinal mode (n = 2), the same results can be observed. Square-shaped black dots show the phase difference between dynamic pressure sensors, and in a spot between 1/3 and 2/3 of the combustion chamber, the pressure node appears, and it was found that the phase difference of dynamic pressure sensors in the front and in the back of the spot was about 180°, through which it was possible to confirm the combustion instability of the 2L mode connected with the combustion chamber and the fuel-air mixing section that are assumed above. Unlike the 1st longitudinal mode (n = 1), which is describe in the previous results above, the pressure value measured from a pressure sensor located in the inlet mixing section was a little higher than that measured

from the combustion chamber. Therefore, when such a combustion instability phenomenon takes place, the pressure oscillation occurring in the inlet mixing section has large values around 10%, compared to the average static pressure, through which the combustion instability phenomenon of the 2L mode has an effect on the acoustic pressure field occurring in the inlet mixing section and even on the oscillation of the supplied fuel-air mixture. In this experiment, when the combustion instability phenomenon takes place in each frequency band, the fluctuation of the equivalence ratio due to the oscillation of the supplied fuel-air mixture can be regarded as combustion instability caused by a relatively strong pressure oscillation from the inlet mixing section, rather than being amplified through interaction with acoustic waves. When such a phenomenon of combustion instability appears, not only the resonant frequency of a combustion chamber but the resonant frequency appearing in the inlet mixing section are calculated as values similar to the frequency of combustion instability.

In a condition where there is no swirl effect as shown in Fig. 6.13(b), the frequency of combustion instability obtained from this experiment was found to be 829Hz, and the resonant frequency of the fuel-air mixing section, which was calculated by 1-D acoustic wave theory, was found to be 829 Hz and the resonant frequency of the combustion chamber was 827 Hz. This appeared equal in the various other inlet mixing section experimental conditions, and, depending on the mean temperature conditions of the combustion chamber and its inlet mixing section, the instability frequency became a little lower. However, given the results of this research on the modes and phase differences of dynamic pressure, this study verified the validity. It is the same in the condition as shown in Fig. 6.16(b), where the equivalence ratio was formed to the contrary, and it was found that when the combustion instability phenomenon of the 2L mode with relatively high frequencies actually took place, the form of the fuel-air mixing section is greatly affected.

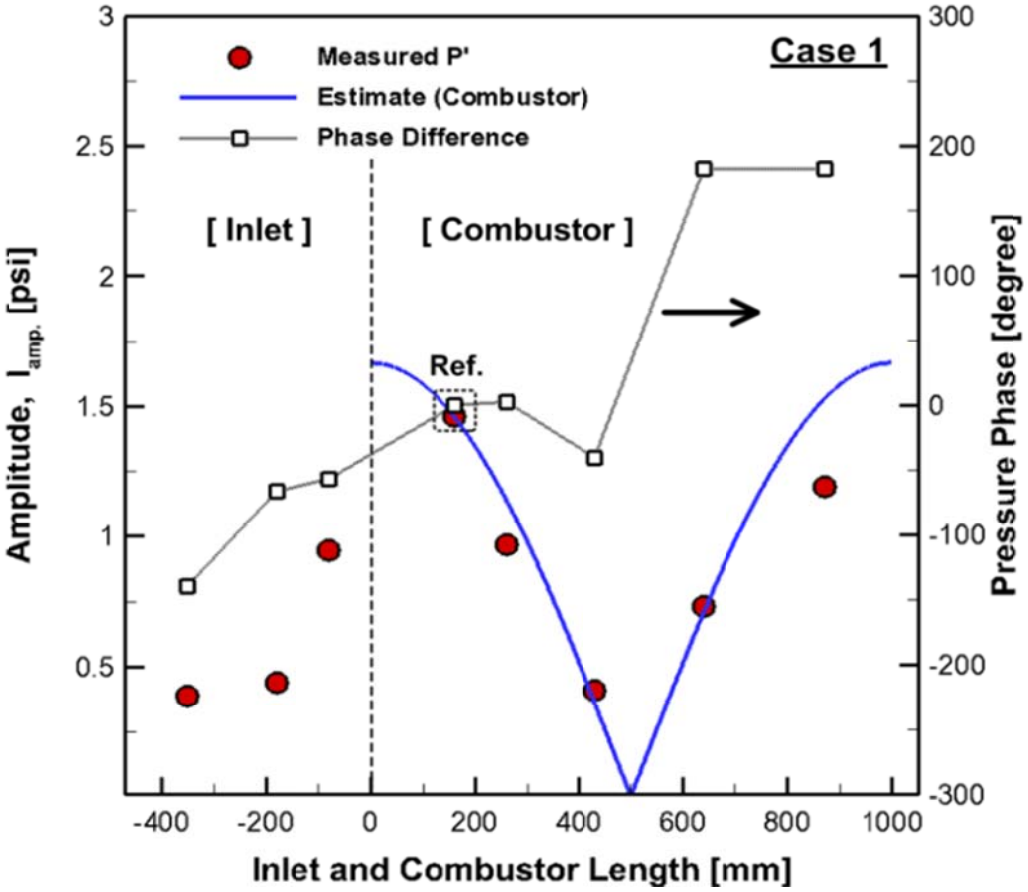
Measured P'
Estimate (Combustor)
Phase Difference
Case 1
[Inlet]
[Combustor]
Ref.
Amplitude, $I_{amp.}$ [psi]
Pressure Phase [degree]
Inlet and Combustor Length [mm]
3
2.5
2
1.5
1
0.5
300
200
100
0
-100
-200
-300
-400
-200
0
200
400
600
800
1000

(a)

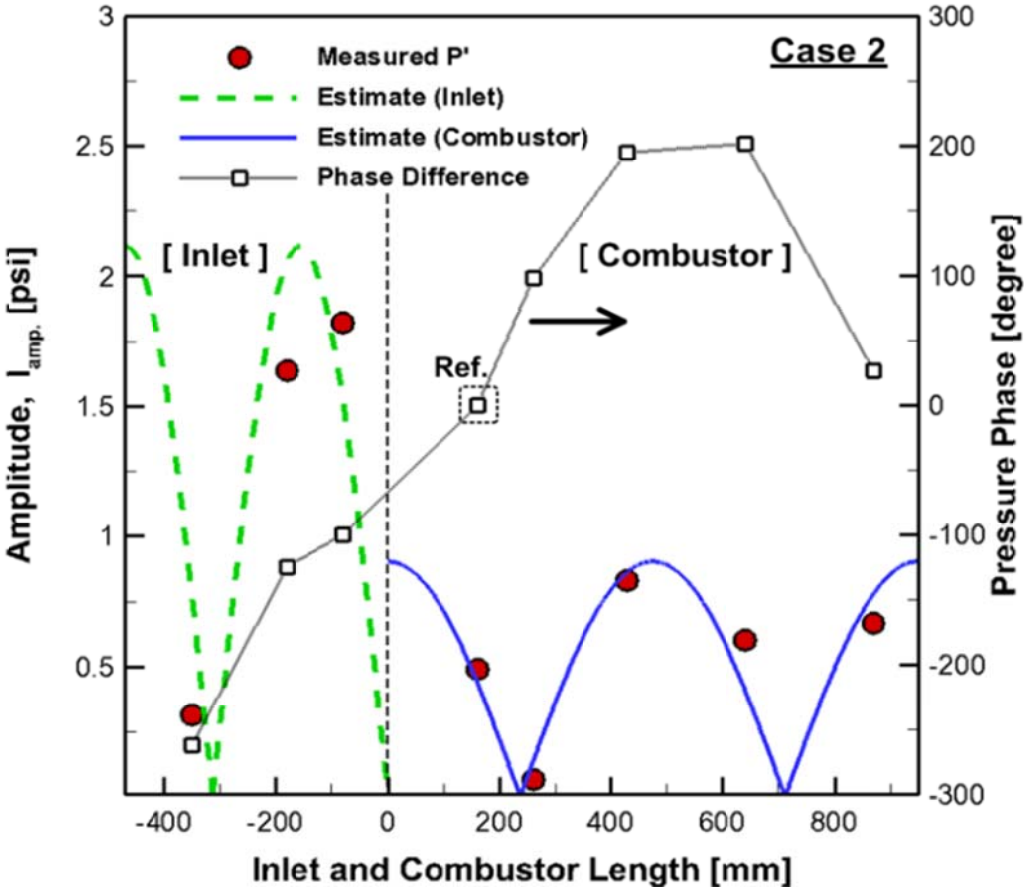

(b)

Fig. 6.13 Dynamic pressure amplitude and phase difference between each sensor at no swirl condition and L_{inlet} = 470 mm; (a) 1st longitudinal instability mode, $L_{comb.}$ = 1000 mm, Φ = 0.9, v_{mix} = 70 m/s, case 1, (b) 2nd longitudinal instability mode, $L_{comb.}$ = 950 mm, Φ = 1.1, v_{mix} = 70 m/s, case 2.

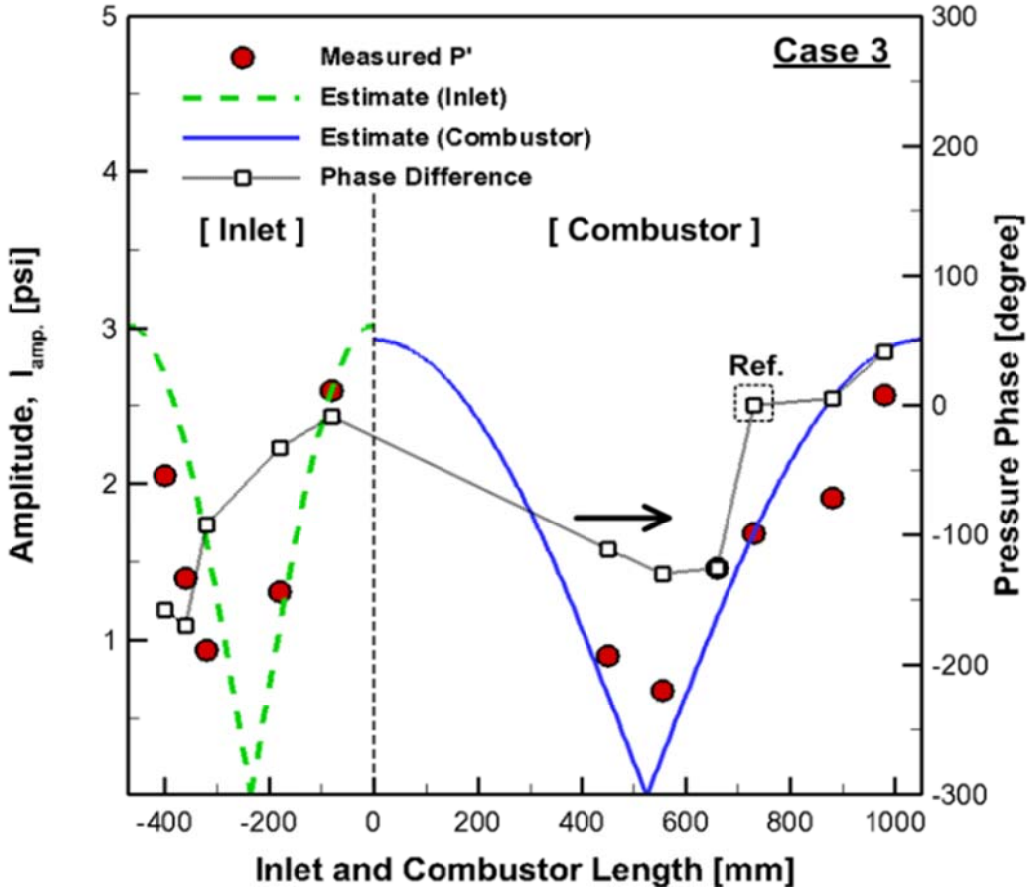
Case 3
Measured P'
Estimate (Inlet)
Estimate (Combustor)
Phase Difference
[Inlet]
[Combustor]
Ref.
Amplitude, $I_{amp.}$ [psi]
Pressure Phase [degree]
Inlet and Combustor Length [mm]
5
4
3
2
1
300
200
100
0
-100
-200
-300
-400
-200
0
200
400
600
800
1000

(a)

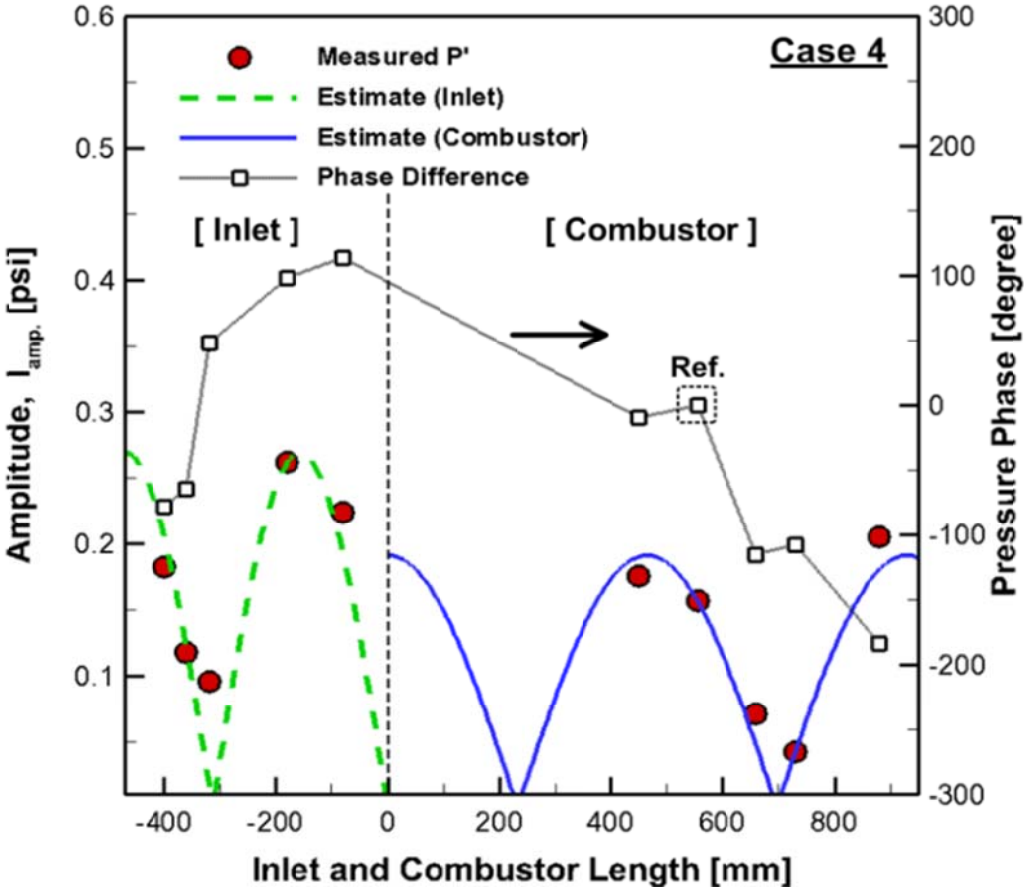

(b)

Fig. 6.14 Dynamic pressure amplitude and phase difference between each sensor at 30° swirl condition and L_{inlet} = 470 mm; (a) 1st longitudinal instability mode, $L_{comb.}$ = 1050 mm, Φ = 1.1, v_{mix} = 70 m/s, case 3, (b) 2nd longitudinal instability mode, $L_{comb.}$ = 930 mm, Φ = 1.2, v_{mix} = 40 m/s, case 4.

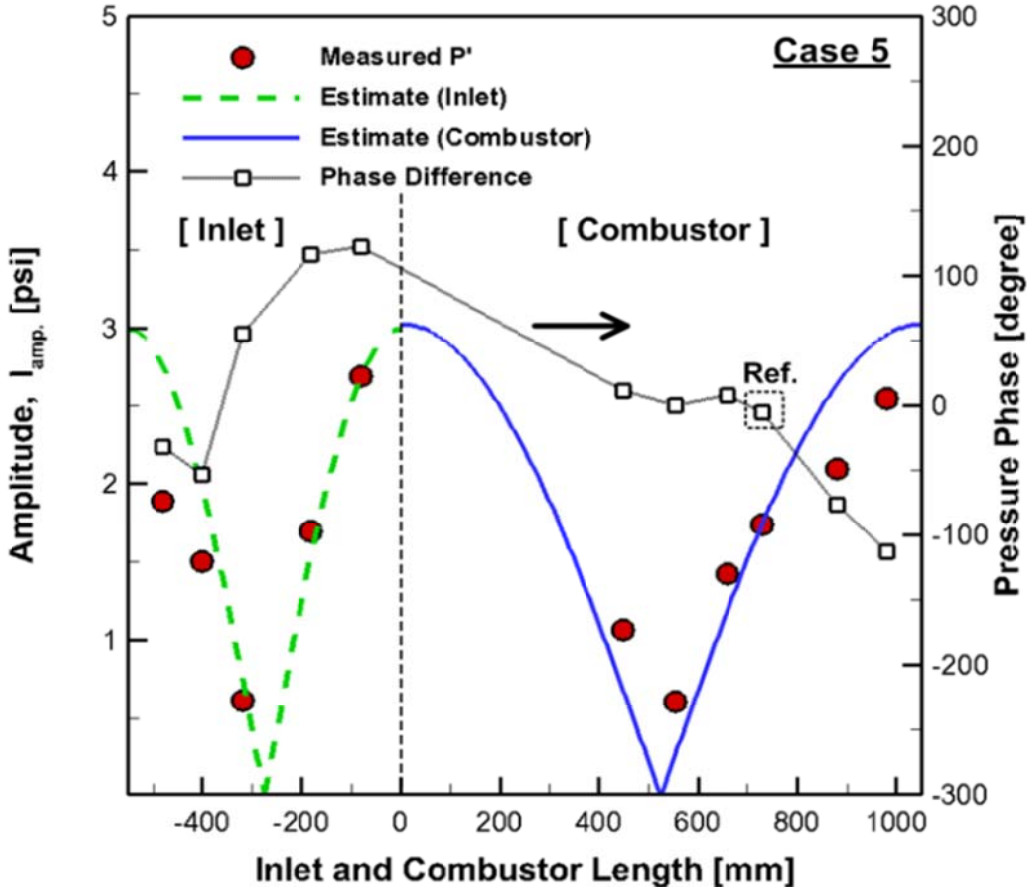
Case 5
Measured P'
Estimate (Inlet)
Estimate (Combustor)
Phase Difference
[Inlet]
[Combustor]
Ref.
Amplitude, $I_{amp.}$ [psi]
Pressure Phase [degree]
Inlet and Combustor Length [mm]
5
4
3
2
1
300
200
100
0
-100
-200
-300
-400
-200
0
200
400
600
800
1000

(a)

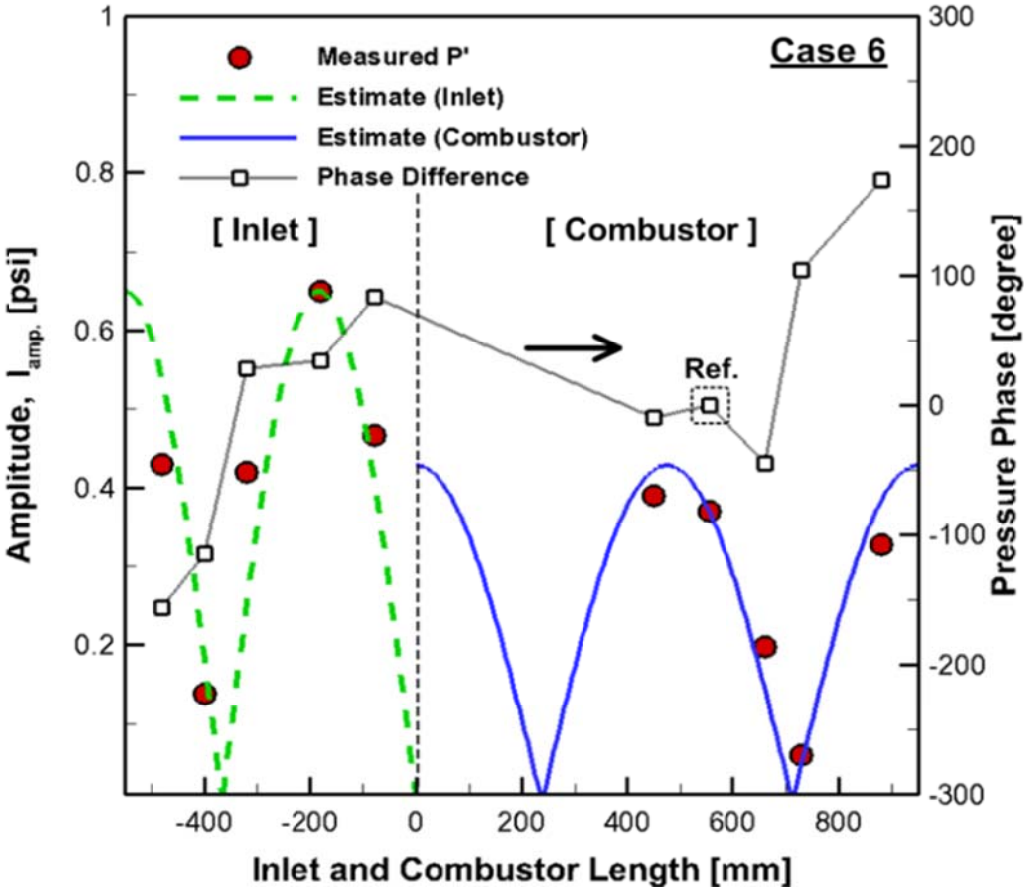

(b)

Fig. 6.15 Dynamic pressure amplitude and phase difference between each sensor at 30° swirl condition and L_{inlet} = 550 mm; (a) 1st longitudinal instability mode, $L_{comb.}$ = 1050 mm, Φ = 1.0, v_{mix} = 70 m/s, case 5, (b) 2nd longitudinal instability mode, $L_{comb.}$ = 950 mm, Φ = 1.1, v_{mix} = 40 m/s, case 6.

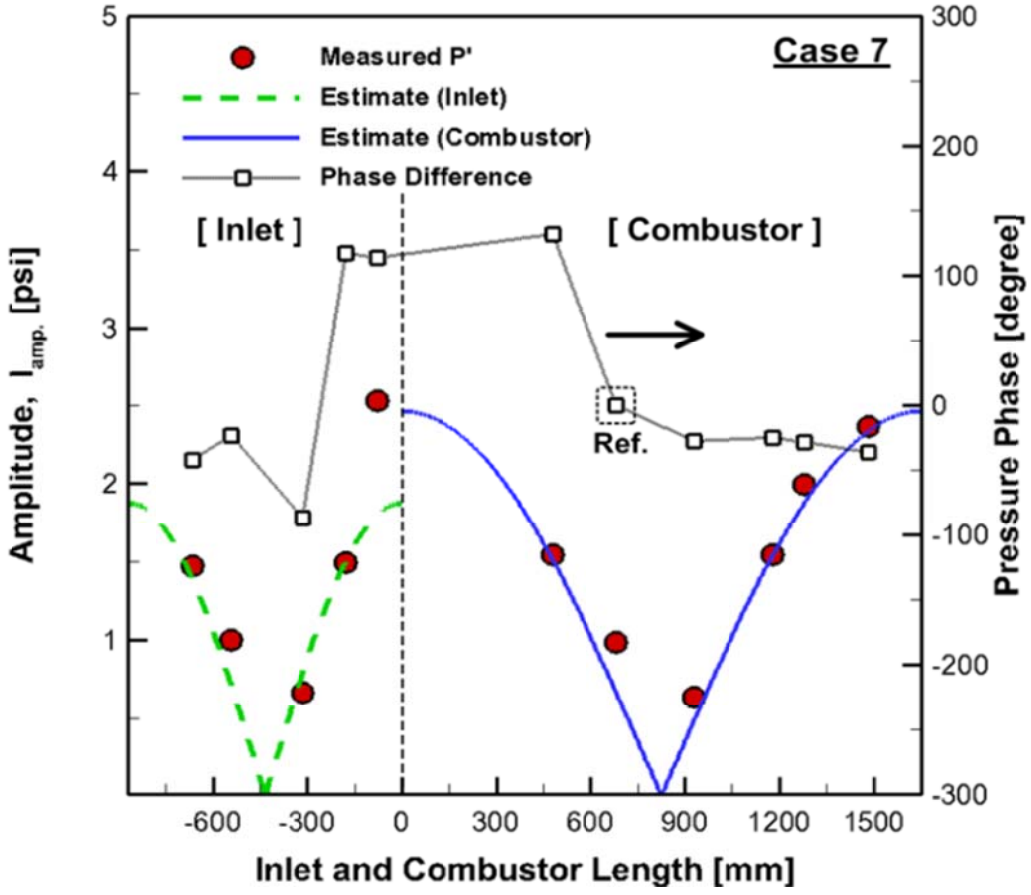
Case 7
Measured P'
Estimate (Inlet)
Estimate (Combustor)
Phase Difference
[Inlet]
[Combustor]
Ref.
Amplitude, $I_{amp.}$ [psi]
Pressure Phase [degree]
Inlet and Combustor Length [mm]
5
4
3
2
1
300
200
100
0
-100
-200
-300
-600
-300
0
300
600
900
1200
1500

(a)

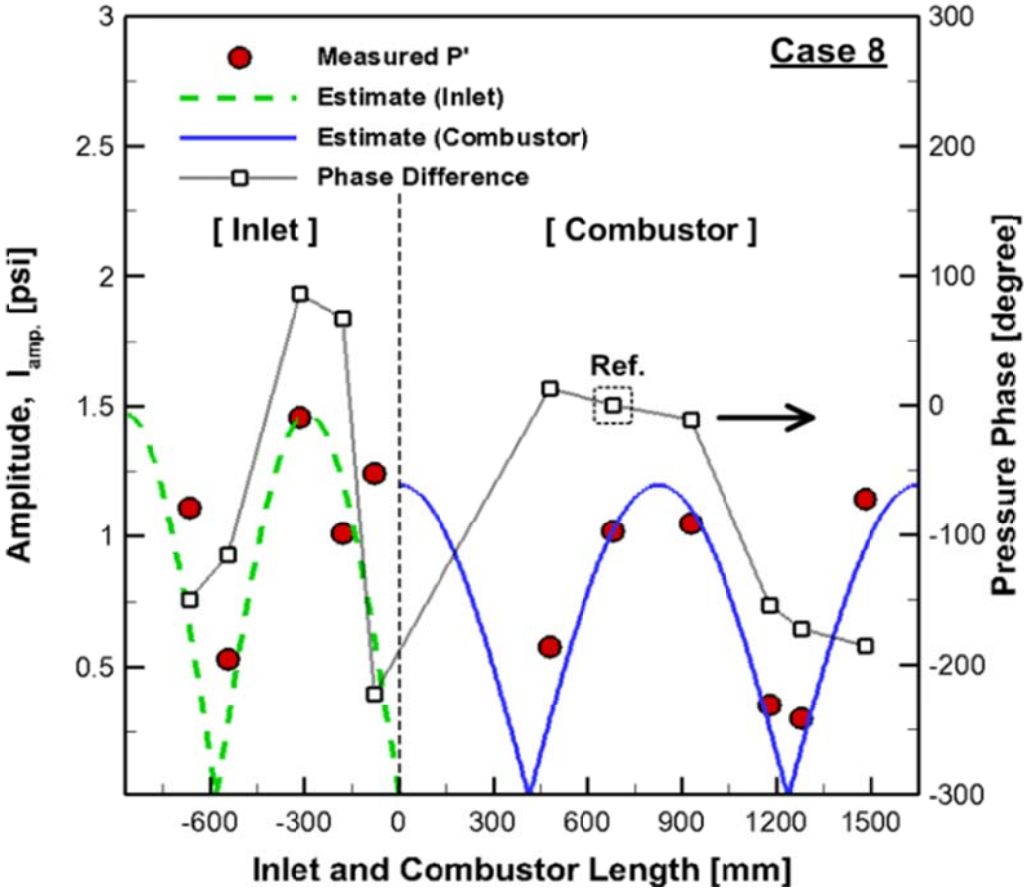

(b)

Fig. 6.16 Dynamic pressure amplitude and phase difference between each sensor at 30° swirl condition and L_{inlet} = 870 mm; (a) 1st longitudinal instability mode, $L_{comb.}$ = 1650 mm, Φ = 1.1, v_{mix} = 60 m/s, case 7, (b) 2nd longitudinal instability mode, $L_{comb.}$ = 1650 mm, Φ = 0.8, v_{mix} = 70 m/s, case 8.

CHAPTER 7
SPRAY CHARACTERISTICS OF CANTED INJECTION ANGLES

7.1 Background and Objectives

The liquid spray jet, which injects perpendicularly into the crossflow, is used as the fuel, air and steam injection device for propulsion units. These units then take the air as the oxidizer, such as the secondary injection for RQL burner, liquid ramjet engine, running on the power obtained through the combustion of the mixture of the air and the fuel, or the after-burner of the gas turbine engine. In addition to these propulsion and power devices, it is also used in the flow control for the aircraft engine performance enhancement and stability, the film-cooling of the turbine blades, and, recently, the second fuel injectors to actively control the combustion instability of the liquid ramjet engine or the gas turbine engine. As shown in Fig. 7.1 the injection structures of the vertical spray jet are generally defined according to three types: the liquid column region which is maintained in proportion to the size of the injector exit immediately after the initial injection; the liquid clumps (ligaments) region where the droplets are bigger than the droplets of the wake flow due to the start of the division generated by the injection velocity of the fluid and the drag of the air-flow field and later on, the spray plume region (droplet region) where the atomization into tiny droplets occurs as it proceeds to the wake flow.

Also, the trajectories of the test spray jets are classified into two types: the trajectory of the liquid column region which is the liquid column of the test fuel immediately after the initial injection and that of the spray plume region formed by the small droplets after the breakup point. Each of the spray jet trajectories infers the exiting distance of the flames as being mixed with the cold air or hot one, decides the shape of the combustion chamber depending on the design of the injector, and can decide mixing time of the fuel

and the air and the evaporation of the droplets prior to the ignition of the fuel. It also decides the location of the second injection for the control of combustion instability, and infers a factor for the flame transfer function of the active control by the presumption of the delay time. Therefore, the combustor designed through the research on the inaccurate fuel injection trajectory can cause performance degradation and flame instability and have a great impact on the performance of the combustor. Research on the injections that perpendicularly spray into the crossing air-flow has already been experimentally conducted along with theoretical research through the proper modeling by a number of researchers.

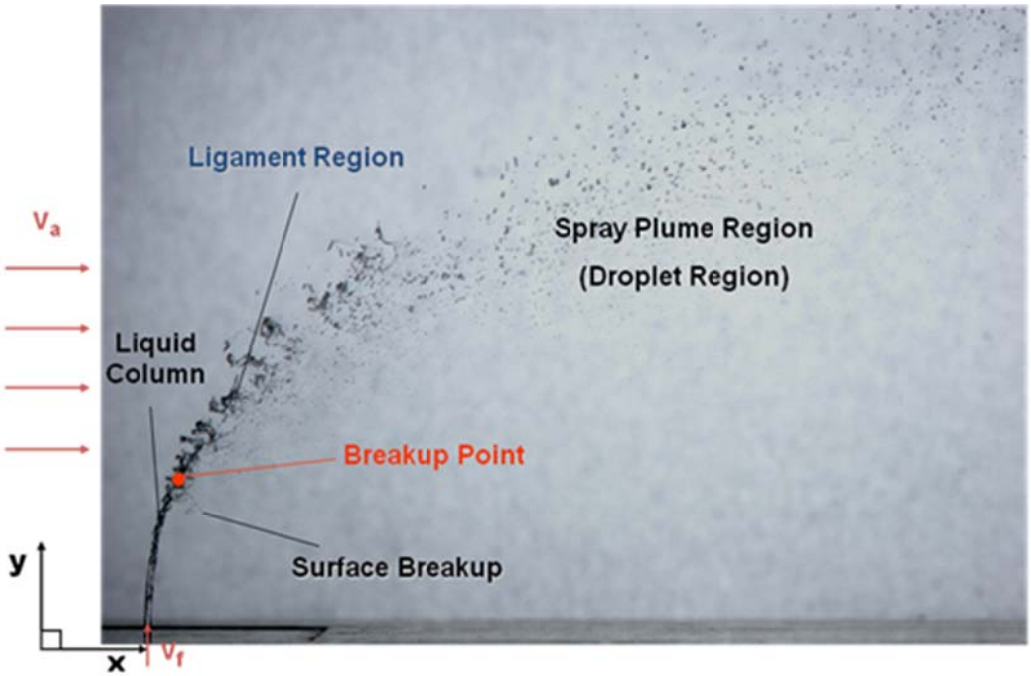

Fig. 7.1 Typical breakup process image of spray jets in subsonic crossflow.

For the experimental methodologies, research has been conducted on the spray structure, the penetration length and the breakup of the liquid column using Schlieren, Mie scattering, direct photography and PDA (Phase Doppler Anemometry), etc. The

representative research on the trajectory of the vertical injection, whose fuel injection angle with the crossflow of the air is 90°, is as follows; Schetz and Padhye et al. [1] suggested that the maximum penetration height is the distance required to turn the momentum flux of the liquid jet injection into the air flow direction. They stated that the penetration height is approximately ~6.25 times the nozzle diameter and that it relates to the liquid/gas momentum flux ratio. Wu et al. [2] derived the spray trajectory and the breakup point of the liquid column region from the free-body diagram of the force equilibrium [3, 4]. Nguyen and Karagozian et al. [5] predicted the trajectories under the combustion condition and the non-reaction condition by converting the interaction between the crossflow and the fuel injection liquid column into a numerical modeling method. Tamaki et al. [6] performed a study on the spray injection and breakup characteristics of the cavitation phenomena decided by the internal shape of the orifice. Song et al. [7] found that cavitation or hydraulic flip effect has an influence on trajectory and Sauter Mean Diameter (SMD) of spray plume region. An introduction of effective jet diameter and effective jet velocity with various spray conditions was proposed.

For the research on the spray whose injection angle is less than 90°, Fuller et al. [8] suggested the liquid column trajectory relation at the injection jet using the same method as Wu et al. Also, the research on the liquid column location defines the breakup regime parameter in proportion to the aerodynamic breakup, which breaks due to rapid air-flow depending on each injection condition and spray angle, and the non-aerodynamic breakup, which in turn breaks due to the inertia and the turbulent forces that the jet itself has without getting influenced much by the air, and deprives the relation to the breakup point through the experiments. Also, Costa et al. [9] confirmed that the liquid column region trajectory relation of the injection is influenced more by the injection velocity than the crossing air velocity, and analyzed the phenomena using the SMD by the fuel injection angle, through the research on the injection angle of less than 90°.

Therefore, this research suggests the relation between the liquid column trajectory and the distance to the breakup point at various forward injections through high resolution direct photography technique [10, 11, 12] and PLLIF (Planar Liquid Laser Induced

Fluorescence), which is an applied measurement technique, conducts the comparison analysis with the prior research findings and additionally aims to confirm the relation to the reverse injection.

7.2 Experimental Methods

7.2.1 Design of angle injectors

The exit diameter of the injector (d) was fixed at 0.5 mm, and the internal structure of the injector was formed by the orifice and the chamber. The diameter of the chamber (D) is 12 mm and here, the type of internal flow is decided depending on the ratio of the orifice length (L) and diameter (L/d), and it is known that hydraulic flip occurs generally when $L/d \leq 8$ [6] and in other cases, instead cavitation phenomena occur. Also, the flow with or without cavitation is decided by the curvature of the inner chamber and orifice. Since this research did not consider the phenomenon of the internal flow of the injector by the cavitation or hydraulic flip, the curvature was set as $R/d = 1$, which indicates that the inlet radius (R) and the orifice diameter are the same. It is known that when $R \geq 0.14d$, normally the vena-contracta does not form and coordinately the cavitation does not occur either [6]. Fig. 7.2 is a picture of the injector shape used for this research. For the study of injection characteristics according to injection angle, we were manufactured the orifices of the various injection angles such as 30°, 45°, 60°, 75°, 90°, 105°, 120°, 135° and 150°.

Table 7.1 Experimental conditions.

Parameters	**Values**	
Air velocity [m/s]	60	
Air temperature [K]	300	
Fuel temperature [K]	318	
Fuel (Mixture ratio)	Water + Ethanol Water : Ethanol = 4 : 1 (Ethanol 20%)	
Orifice diameter [mm]	0.5	
Orifice shape	Inner round edged (L/d=20)	
Pressure Differential [ΔP, bar]	1, 2, 3, 4, 5	
x/d (Normalized Transverse Distance)	40, 60, 80, 100, 120	
Injection angle (Normalized Transverse Distance)	30°, 45°, 60°, 75°, 90° (Forward injection)	105°, 120°, 135°, 150° (Reverse injection)

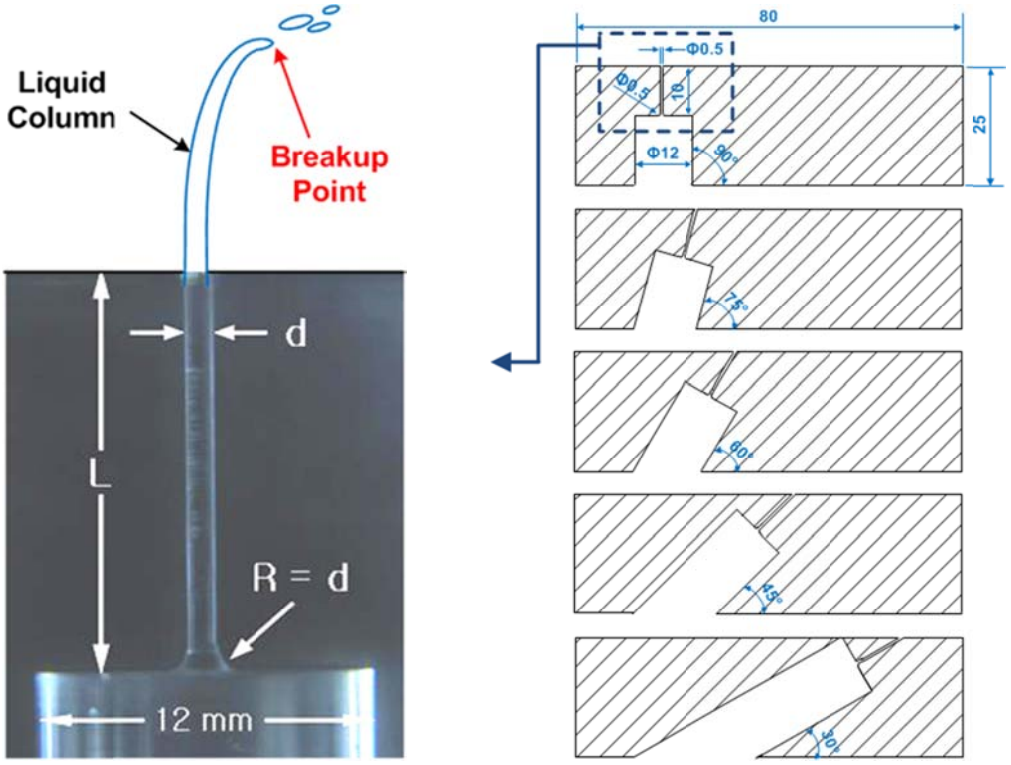

(a) (b)

Fig. 7.2 Angled injector shape; (a) round-edge orifice (L/D = 20), (b) angled orifices.

7.2.2 Experimental apparatus and conditions

The liquid column trajectory of the injection and the breakup length, for the forward injection whose injection angles are 30°, 45°, 60°, 75° and 90°, and on the reverse injection whose injection angles are 105°, 120°, 135° and 150°, was measured. First, for the direct photography technique, the photos for the liquid column trajectory were taken with a Canon EF 100mm f/2.8 Macro USM lens which supports high resolution photography. And the liquid breakup distances were taken with a Canon MP-E 65mm f/2.8 1-5x Macro Photo lens. The photos were taken by synchronizing the digital camera (Canon EOS 20D) and the stroboscope, the light source; the expansion ratio per pixel is

about 2~10㎛. About 2000~3000 photographs for each experimental case of the trajectory and the breakup point of the liquid column region were taken to maintain the experimental error range within 5% [13]. Also, the injection structure was observed using the PLLIF technique, which is capable of measuring the intensity values of the fluorescence signal and the scattering signal for the comparison analysis with the present experimental results of the trajectories and the breakup length obtained by direct photography technique.

Figure 7.3 shows the experimental devices for PLLIF and the direct photography techniques. The mixture of water and ethyl alcohol (of volumetric ratio 4:1) was used as working fuel, and the fluorescent ($C_{20}H_{12}O_5$, Aldrich F245-6) of 30 mg was dissolved into the simulant working fuel of 1 liter. Because of the fluorescent absorbs light in the wavelength range from 400 to 530 nm, and the experiment fuel was heated to 318 K to obtain the non-cavitation flow. For the specific gravity of the experiment working fuel, the fuel similar to that of the previous research result was used, and the working fluid similar to the fuel specific gravity at the real combustor was used. The size of the visible area is 50 mm x 50 mm x 330 mm, air with a velocity of 60 m/s was blown in by the 20 hp blower, and the stabilized air in the settling chamber was supplied to the test section after passing through the honeycomb for the uniform air-flow.

For the LEXEL's, an argon-ion laser was used, and for the major beam, Dantec's fiber-optics were used to convert into the planer beam. The fluorescence signal and the scattering signal obtained by PLLIF were installed into the digital camera Canon EOS D30 with the 28-105mm standard lens, and the 2X Vivitar enlargement lens was installed so that the image could be enlarged and taken. The high-pass filter that detects the 550 nm wavelengths and the band-pass filter that detects the 514±5 nm wavelengths were installed into both cameras to obtain the fluorescence signal and the scattering signal. It was possible to obtain the experimental values by scanning the picture gained by the PLLIF scattering signal through the image processing and by considering the point where the lights are rapidly scattered as the breakup point.

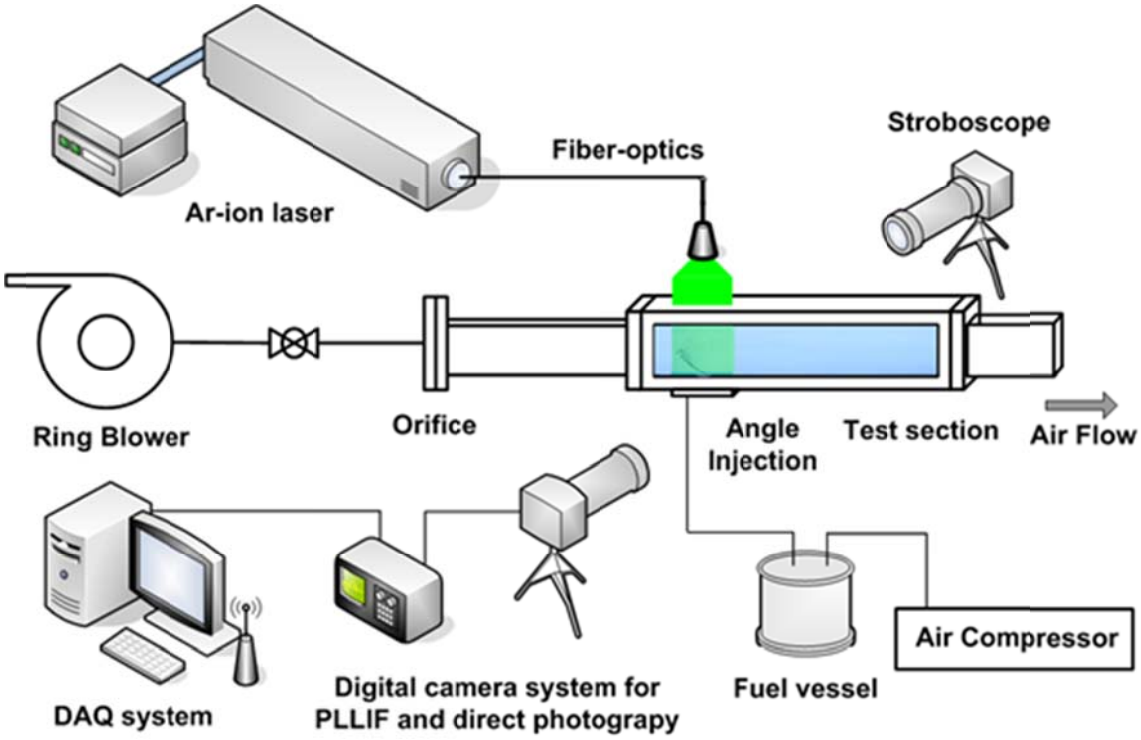

Fig. 7.3 Experimental setup for direct photography and PLLIF measurement.

7.3 Canted Injection Characteristics

The air velocity of the experiment was fixed at 60 m/s, and the injection characteristics of the liquid column region and the droplet region of the injection jet were studied by changing the injection pressure differential of the fuel (water + ethanol) to 1~5 bar; in other words, by varying the values of fuel/air momentum flux ratio, q($\rho_f u_f^2 \ / \ \rho_g u_g^2$) as 21~105, to identify the characteristics of the fuel velocity. This is the value of the momentum flux ratio in the prior research that can be compared with this study. Fig. 7.4 is a direct photography and Fig. 7.5 shows the PLLIF images of the vertical injection with the angles of 30°, 60°, 90°, 120°, 135° and 150° from the datum of the nozzle exit at the normal flow injector group without any cavitation or hydraulic flip

effects, under the normal injection conditions that the fuel injection pressure differential is 3 bar and that the momentum flux ratio is 65.

In the forward injection whose angle is less than 90° and in the reverse injection, as the fuel velocity q increases, the jet velocity increases accordingly so that it can be confirmed that the penetration distance of the crossflow into the air-flow field also increases. As shown in the following Fig. 7.4, in the area with the injection angle of less than 90°, as the injection angle decreases, the liquid column gets straighter and the penetration distance becomes decrease than the injections with other angles. Therefore, since the shear stress on the liquid column surface decreases, the atomization performance degrades compared to the cases with other angles injection. And since the velocity of the injection jet with the 30° injection angle processes is almost the same as the value of the velocity of the blowing air compared with the other injection angle conditions. The breaking forces due to the effects of the wavelengths caused by the free vibrations and the power of inertia, the own turbulence effect of the liquid column becomes bigger than the breakups caused by the air. Fuller at el. [8] mentioned that the factors that decide the penetration distance of the vertical injection jet are the injection angle and fuel/air momentum flux ratio (q) and also mentioned that in the low fuel/air momentum flux ratio (q) region, the liquid column has big waves. Furthermore, they state that due to this phenomenon, the surface of the liquid column gets distorted and breaks up due to the kink phenomenon. Chigier and Reitz et al. [14] mentioned that this is the fiber-type breakup.

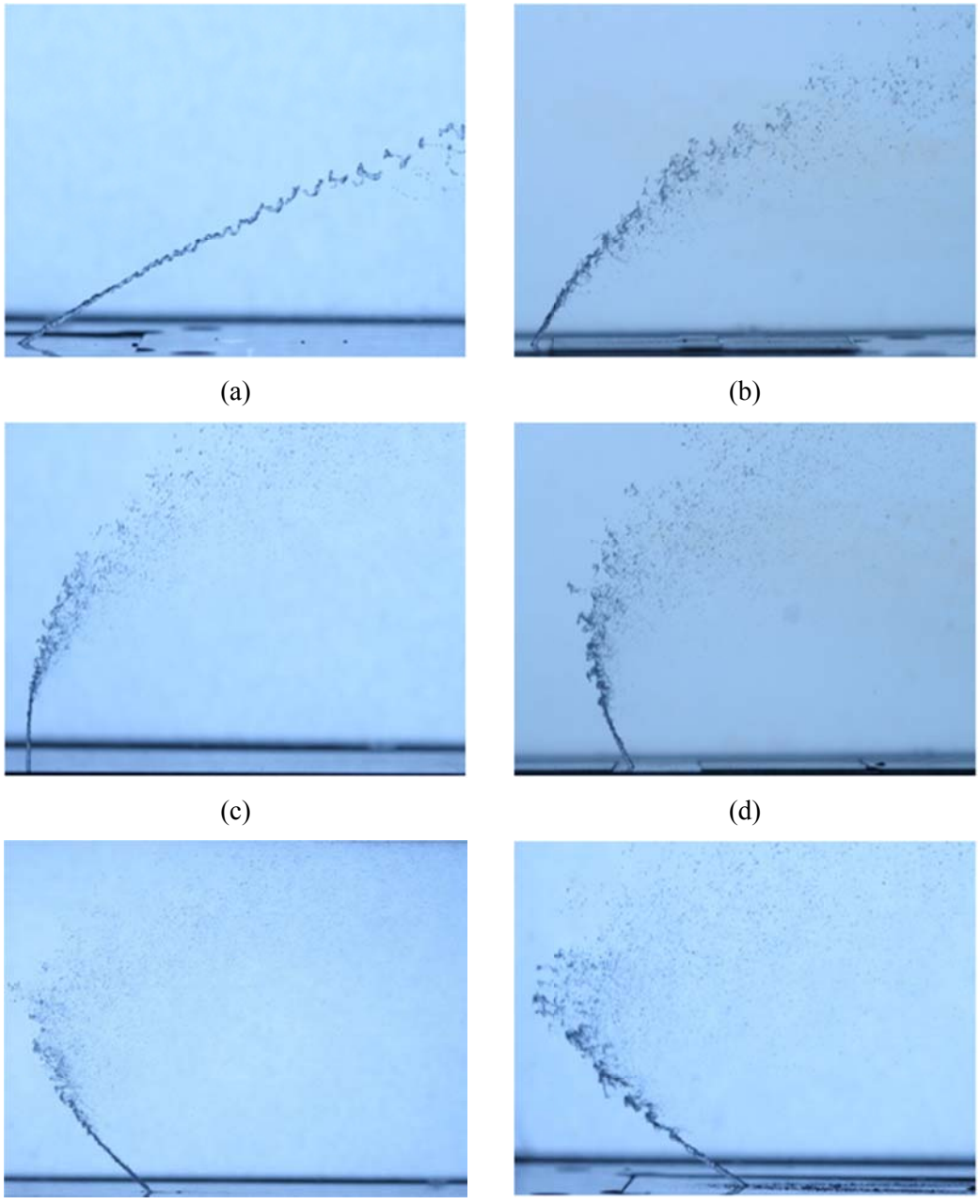

Fig. 7.4 Spray patterns at variously angled injections (ΔP = 3 bar, q = 65); (a) 30°, (b) 60°, (c) 90°, (d) 120°, (e) 135° and (f) 150°.

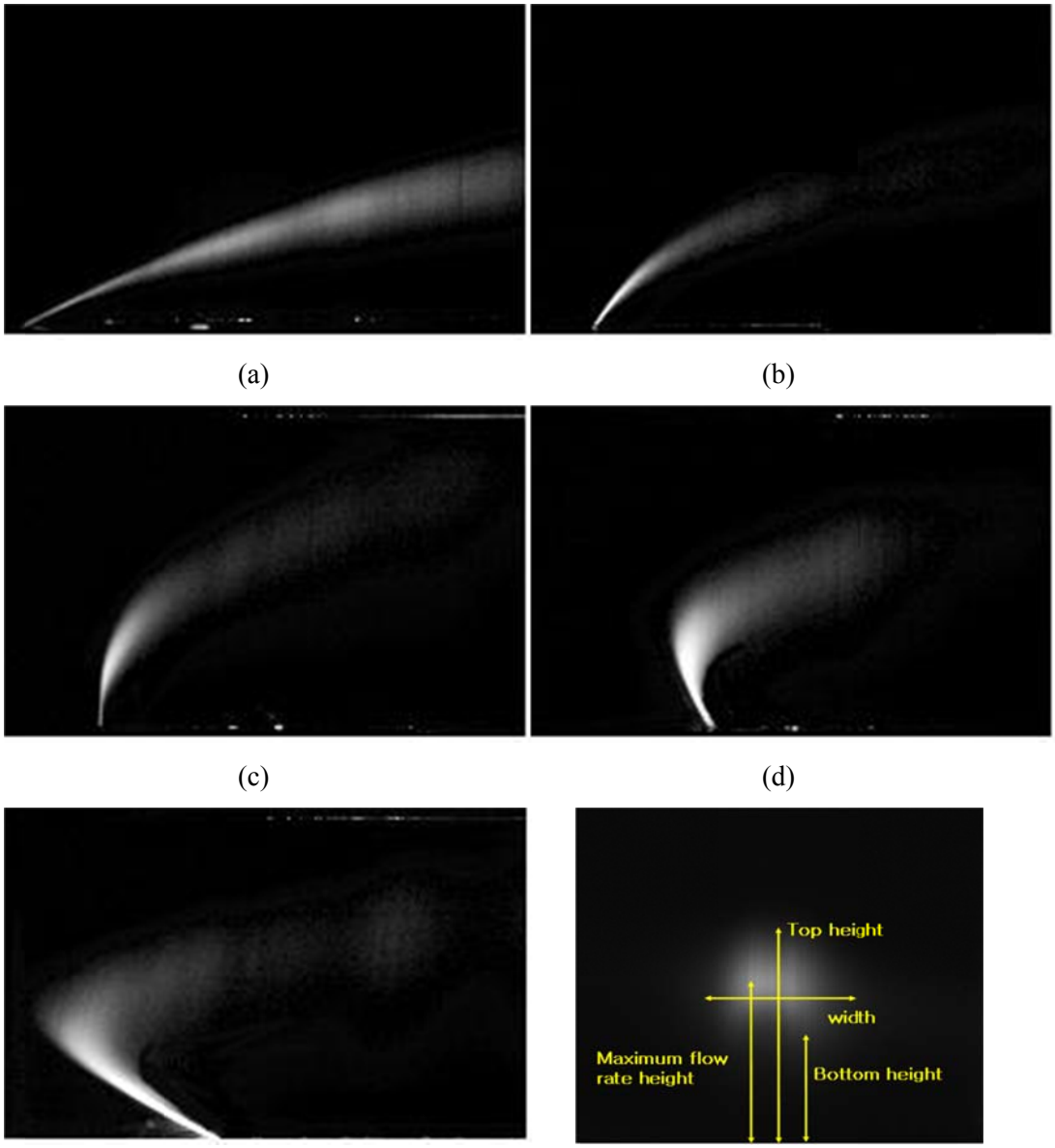

Fig. 7.5 LIF images by PLLIF measurement (ΔP = 3 bar, q = 65); (a) 30°, (b) 60°, (c) 90°, (d) 120°, (e) 150° injections and (f) spray plume structure.

7.4 Liquid Column Trajectory in Forward and Reverse Injections

Therefore, the trajectory experimental formula of the liquid column region can be calculated depending on the injection angle that is less than 90° and on the reverse injection. Here, x indicates the value of the axial distance of the axial (air-stream) direction, y indicates the value of the penetration distance of the penetration direction, d is the diameter of the orifice exit, θ is the injection angle, v_f is the fuel velocity and v_a is the value of the air velocity.

The liquid column trajectory is decided by the drag coefficient, and Fuller et al. [8] defined the drag coefficient value of the sections where the experimental values of this study fit smoothly into the comparison with the theoretical value obtained by the equation derived of the experimental results with less than 90° and the force equilibrium. By the empirical formulas about liquid column trajectory of Fuller et al. [8], the error range was set within about 30% across the entire experiment, and the drag coefficient (C_D) was obtained 4.4. Fig. 7.6 (a) shows the drag coefficient values through the comparison between the experimental and the theoretical value of the liquid column trajectory whose injection angle is less than 90° in this experiment, and this coefficient result was compared to the previous research result. In this research, the drag coefficient value, gained within a 3% error range across the entire experiment of 30°, 45°, 60°, 75° and 90° injection conditions was obtained as 1.3. Wu et al. [2] computed the drag coefficient value 1.7 based on the liquid column trajectory, obtained by taking the variables of the fuel type, injector exit diameter, air velocity, etc.

The result of this experiment shows a good match with the experiment of Wu et al. [2] more than the drag coefficient value that Fuller et al. [8] suggested. This can be explained as the q condition of this experiment and the fuel type used in the experiment involving the mixed fuel of water and ethanol are similar to Wu's experiment, resulting in a similar coefficient value. Also, it was detected that the drag coefficient value showed its difference caused by the errors of each experimental environment, the injector manufacturer, the orifice passage length, and the thickness difference of the liquid column.

In this experiment, the Reynolds number (Re) value for the liquid column region is as follows: 5000≤Re≤15000 [15]. This matches to a certain degree with the approximate drag coefficient value for the smooth circular cylinder, which remains as 1~1.5. Fig. 7.6 (b) is the graph that decides the drag coefficient of the trajectory equation for the liquid column region. The drag coefficient was decided as 0.2 through the comparison between the experimental value, which was obtained for the reverse injection and for the theoretical value of the Eq. (7.1).

$$\frac{x}{dq} = \frac{1}{\pi}\frac{C_D}{\sin^2\theta}\left(1-\frac{v_f\cos\theta}{v_a}\right)^2\left(\frac{y}{dq}\right)^2 + \frac{\cos\theta}{\sin\theta}\left(\frac{y}{dq}\right) \tag{7.1}$$

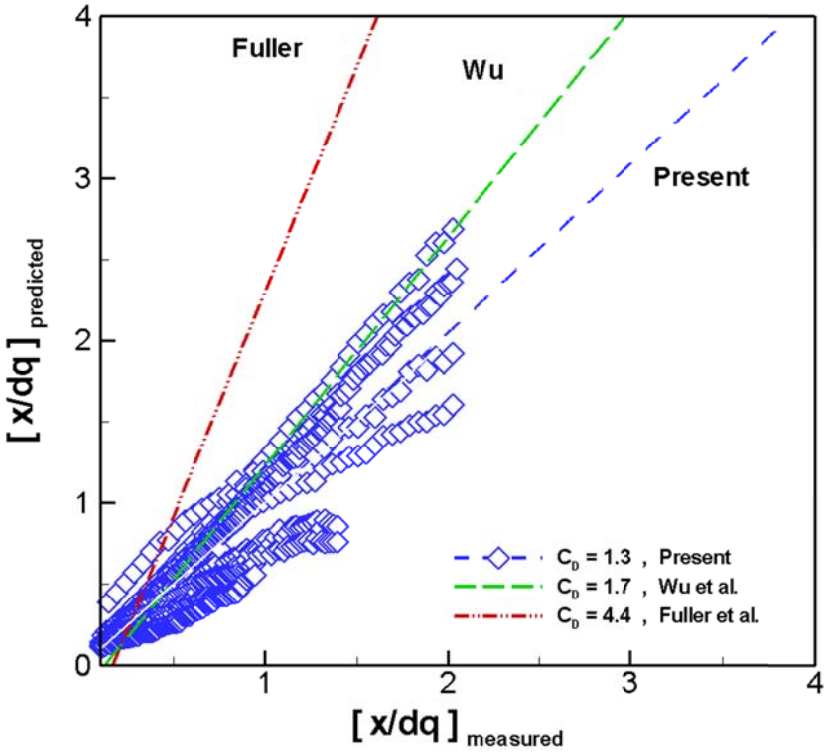

(a)

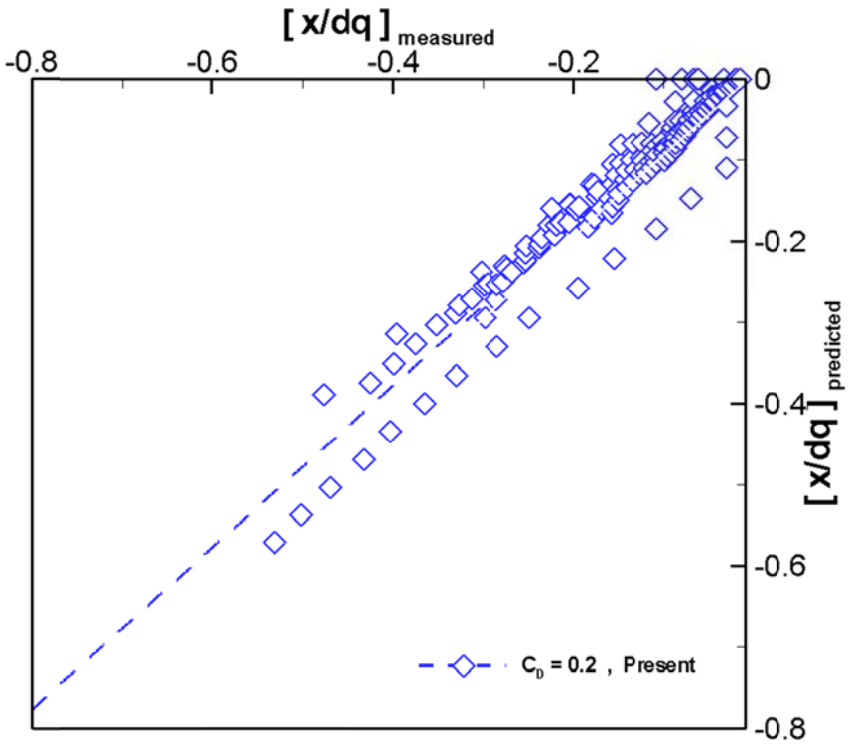

(b)

Fig. 7.6 Drag coefficient for all of experimental cases (C_D); (a) forward injection (Θ = 30°, 60°, 90°), (b) reverse injection (Θ = 120°, 150°).

7.5 The Verification of Liquid Column Trajectory

The trajectories of the liquid column region obtained by the experiment were compared with the previous research to verify the trajectory, and then an analysis was conducted as to whether it validated all injection angle cases. Fig. 7.7 is a graph of the comparison of the experimental values compiled by direct photography at 30°, 60°, 90° of the injection angle, and the figure also shows the results of the PLLIF technique presented by Wu et al. [2] and Fuller et al. [8]. It is clear that in the cases of 30° and 60° in the following Fig. 7.7, the drag coefficient result is different from that of Fuller et al. [8], and

it could be suggested that this was due to the differences in the proportion of the working fluid according to the Eq. (7.1), the experimental conditions and the drag coefficient which were used in the previous experiment. Fig. 7.7(c) is the graph that compares the measured experimental values in the injector group with the 90° injection angle and the previous research results.

Likewise, the present study shows the different drag coefficient (C_D) results from the studies by Wu et al. [2] and Fuller et al. [8]. This research derived the trajectory of the liquid column by the each injection angle, maintaining the error range of the experimental value and the theoretical value, through the experiment result with various injection angles condition provided than the previous research result, within 3%. Also, the drag coefficient for the 90° injection result has a similar value with Wu's drag coefficient, and its reliability was confirmed since the experimental conditions that were formerly mentioned were similar. It was verified that the case with the forward injection angle showed differences due to the experimental condition and due to the experimental fluid in the prior experimental result. Fig. 7.8 shows a graph that compares the empirical formula of the liquid column trajectory obtained from the reverse injection experiment of the 120° and 150° injectors with the data categorized according to each angle. In the case of the experimental equation of the reverse injection, it can be verified that the reverse injection result matches the experimental value when the drag coefficient is 0.2. Moreover, it was confirmed that the drag coefficient of reverse injection matched in all regions with the results of additional experiments involving angles of 105°, 135° and others.

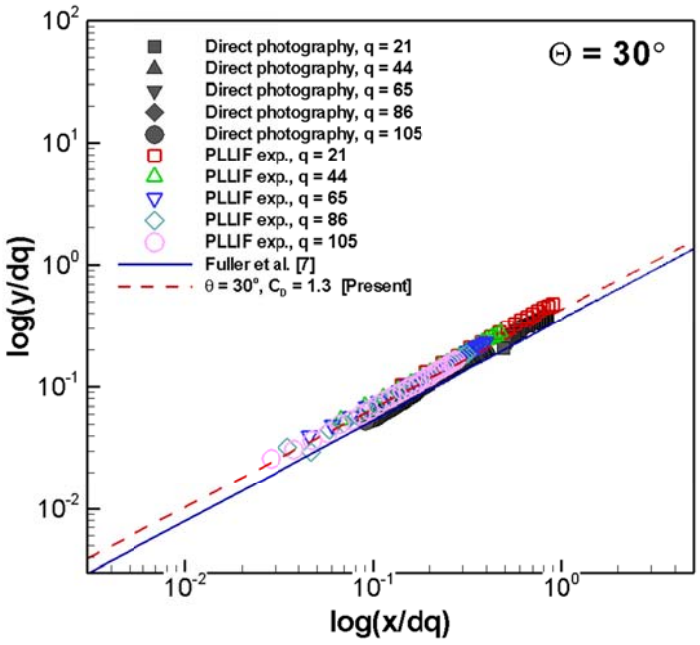
Direct photography, q = 21
Direct photography, q = 44
Direct photography, q = 65
Direct photography, q = 86
Direct photography, q = 105
PLLIF exp., q = 21
PLLIF exp., q = 44
PLLIF exp., q = 65
PLLIF exp., q = 86
PLLIF exp., q = 105
Fuller et al. [7]
θ = 30°, C0 = 1.3 [Present]
Θ = 30°
log(y/dq)
log(x/dq)

(a)

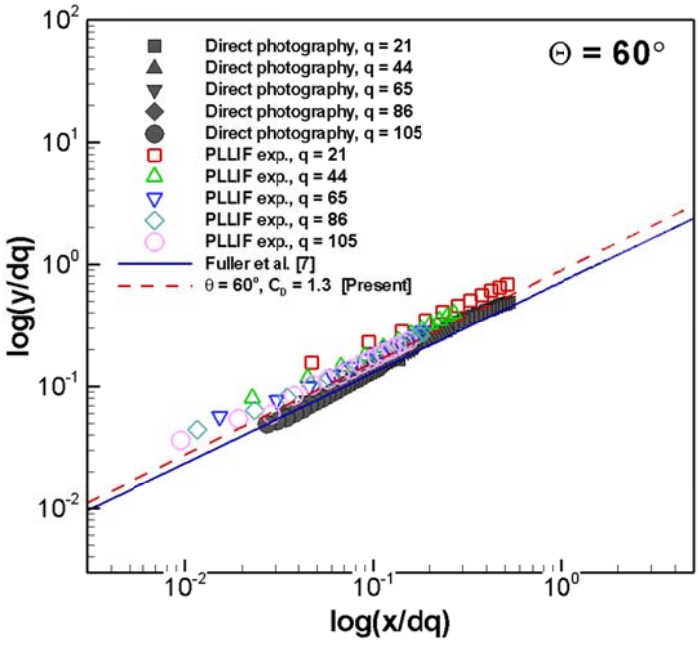
Direct photography, q = 21
Direct photography, q = 44
Direct photography, q = 65
Direct photography, q = 86
Direct photography, q = 105
PLLIF exp., q = 21
PLLIF exp., q = 44
PLLIF exp., q = 65
PLLIF exp., q = 86
PLLIF exp., q = 105
Fuller et al. [7]
θ = 60°, C0 = 1.3 [Present]
Θ = 60°
log(y/dq)
log(x/dq)

(b)

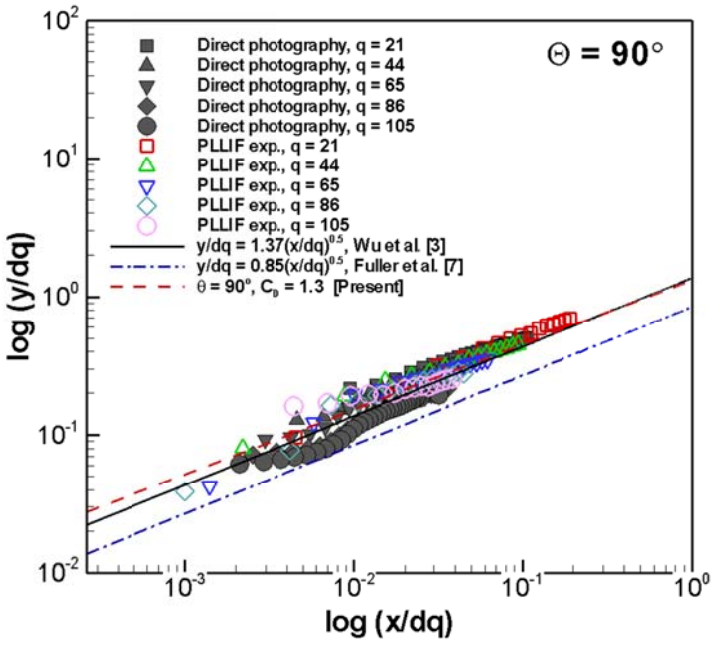

(c)

Fig. 7.7 Comparison with previous and present correlated liquid column trajectory results at forward injection ($\Theta \leq 90°$); (a) 30°, (b) 60° and (c) 90° injection.

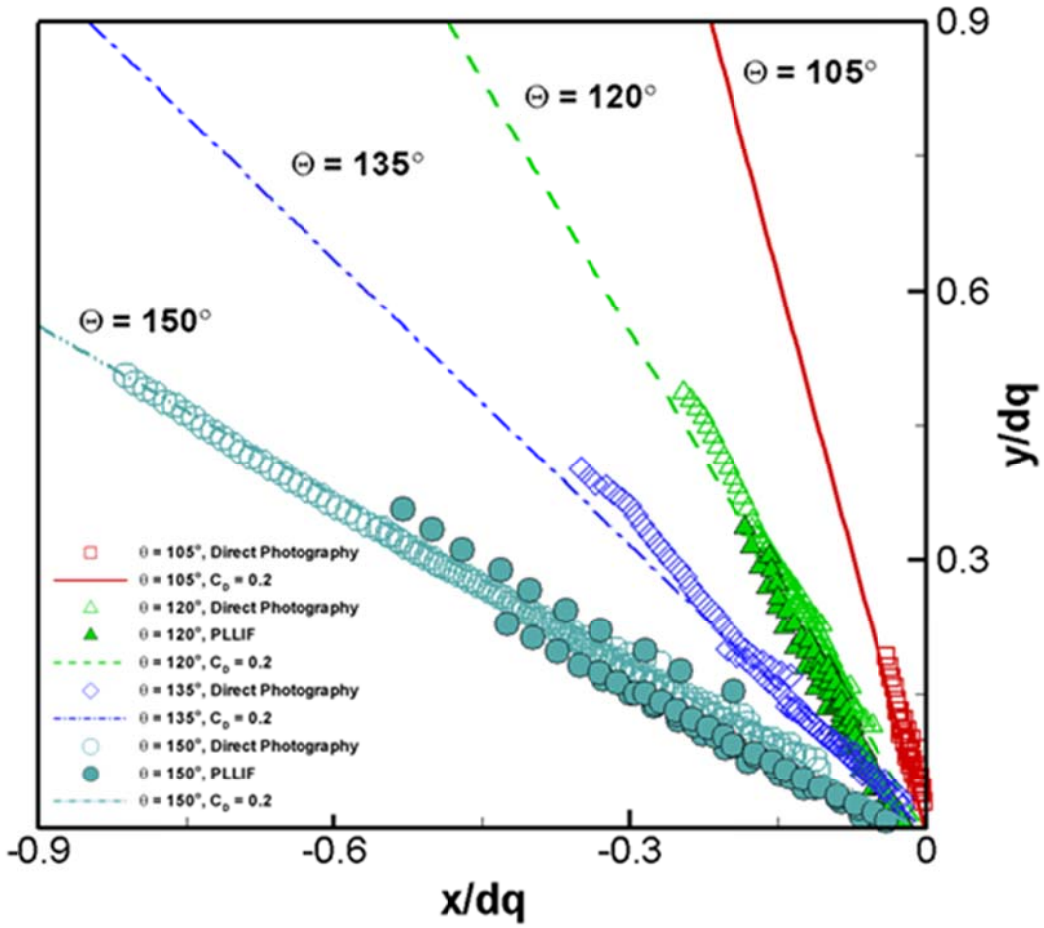

Fig. 7.8 Correlated liquid column trajectory in reverse injection (Θ > 90°) injection.

7.6 Spray Breakup Characteristics

Figure 7.9 shows a graph that expresses the distance to the breakup point, which is the border of the liquid column region and the droplet region of the spray experiments with the various injection angles. In the case of the reverse injection, spray in the reverse direction from the datum of the injector exit. Therefore, the measured distance to the breakup point was taken and compared with the results of the other injection angles in

this experiment. Wu et al. [2] found out the relation of axial distance with respect to the wake flow to the breakup point (*x*-direction) and the penetration distance (*y*-direction) through the experiment.

In the case of the 90° injection, it could be verified that most of the results of this research match with Wu's equation because the drag coefficient value was similar in the trajectory result. Fig. 7.9(a) shows a graph of the axial direction breakup of the air-flow. The cases of 60°, 75°, 105°, 120° injection, which are similar to the 90° injection, show that the breakup points in the forward direction are similar. However, in the case of the reverse injection where it injects in the opposite of the proceeding direction, since the injection occurs in the opposite direction of the rapid airflow intake, it was identified that the distance to the breakup point becomes shorter due to aerodynamic forces.

In the cases of the 30° and 150°, the axial breakup distance has the bigger value than in the cases of the rest of the injection angles where it similarly injects into the vertical plane of the flow field. This is considered since it indicates the tendency of it to breakup due to the power of the liquid jet rather than breaking up due to the air. The distance to the breakup point in the proceeding direction has somewhat larger value than the other injector group. In the case of the 150° reverse injection, the value is than 30° since it penetrates in the opposite direction of the air-flow direction. However, in case of 150°, in spite of the fact that it is a reverse injection, the axial distance to the breakup point shows similar results with the 30° injection. This is because as the q value increases, also for the reversed injection, the penetration distance remains constant to a certain degree. Furthermore, when it passes the maintained penetrated distance, rapid atomization is observed. Fuller et al. [8] suggested that in case of the injection with lesser angles, the penetration distance influences the injection velocity more than the breakup due to the air velocity, and the larger injection angles condition has shorten the axial direction distance to the breakup point in the experimental result performed to the range of 90°. It was shown that in the 90° case, the result showed a similar tendency with the breakup equation suggested by Wu et al. [2], and for the lesser angles, the contents were well matched with the findings by Fuller et al. [8] Finally, the distance to the breakup point

shortens as it injects closer to the vertical plane of the air-flow direction regardless of the normal injection or of the reverse injection.

Figure 7.9 (b) shows the result related to the distance to the breakup point of the penetration direction. Since the injectors with the angle of less than 90° in the result of the graph have the relatively smaller penetration distance, their distances to the breakup point of the penetration direction become shorter than those of the injectors with other given angles. It was also verified that if the injection pressure differential increases, the penetration distance increases generally and so the breakup point lengthens.

In the case of 30° injection, the flow velocity of the air and the velocity of the jet are almost identical. Also, in the case of 30° injection, compared to the other angled injections, the large scale atomization performance cannot occur. Therefore, it was identified that the distance to the breakup point of the penetration direction remains almost constant. In the case of 150° reverse injection, the distance to the breakup point of the proceeding direction is similar to the case of 30°, but as the trajectory wraps upwards by the characteristic of the reverse injection, the distance to the breakup point of the penetration direction gains a relatively bigger value.

Also, in the cases of 60° and 120°, the distance to the breakup point of the penetration direction remains similar regardless of whether it is the reverse injection or the normal injection. And it was verified that in the region where the injection pressure is low, there is no difference in the breakup lengths, but in the region where the injection pressure differential is high, there are different breakup length scale effects. It could also be identified that the distance to the breakup point of the penetration direction shortens in cases of 75°, 90° and 105° injection whose direction is close to the vertical plane of the air flow direction regardless of the normal injection or the reverse injection.

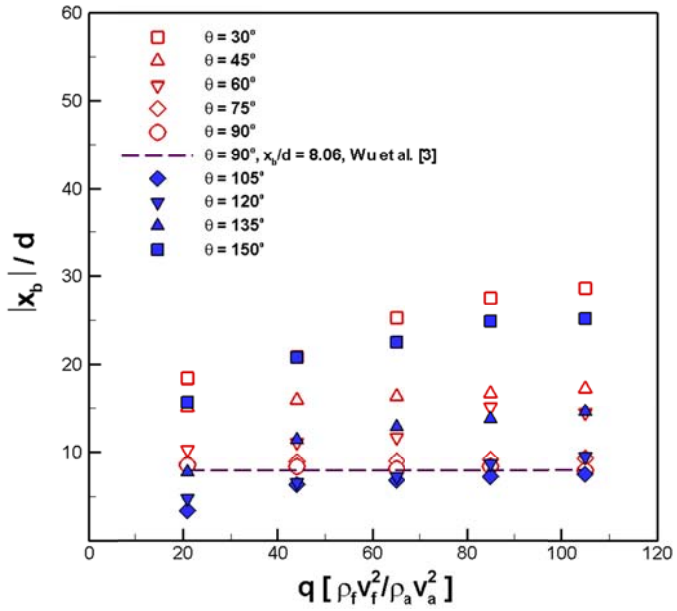

(a)

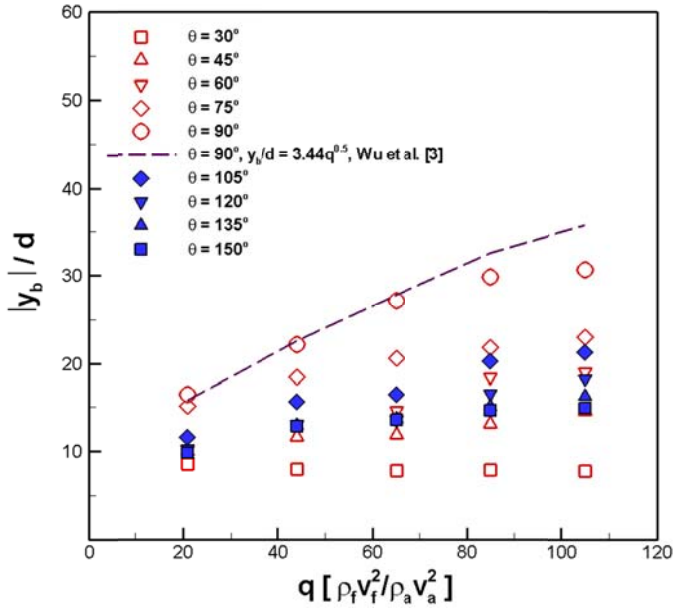

(b)

Fig. 7.9 Breakup length characteristics; (a) axial distance (*x*-direction), (b) penetration distance (*y*-direction).

Figure 7.10 is the result of the ratio of the proceeding direction of the fluid and the distance to the breakup point of the penetration direction. Except the 30° injection which has the breakup characteristic due to the velocity of the liquid jet rather than the effect of the aerodynamic drag, each of the experimental results maintained almost constant values. Thus, this study could suggest an empirical formula for the airstream direction of the sprays in all injection angles and the distance to the breakup point of the penetration direction as in the following

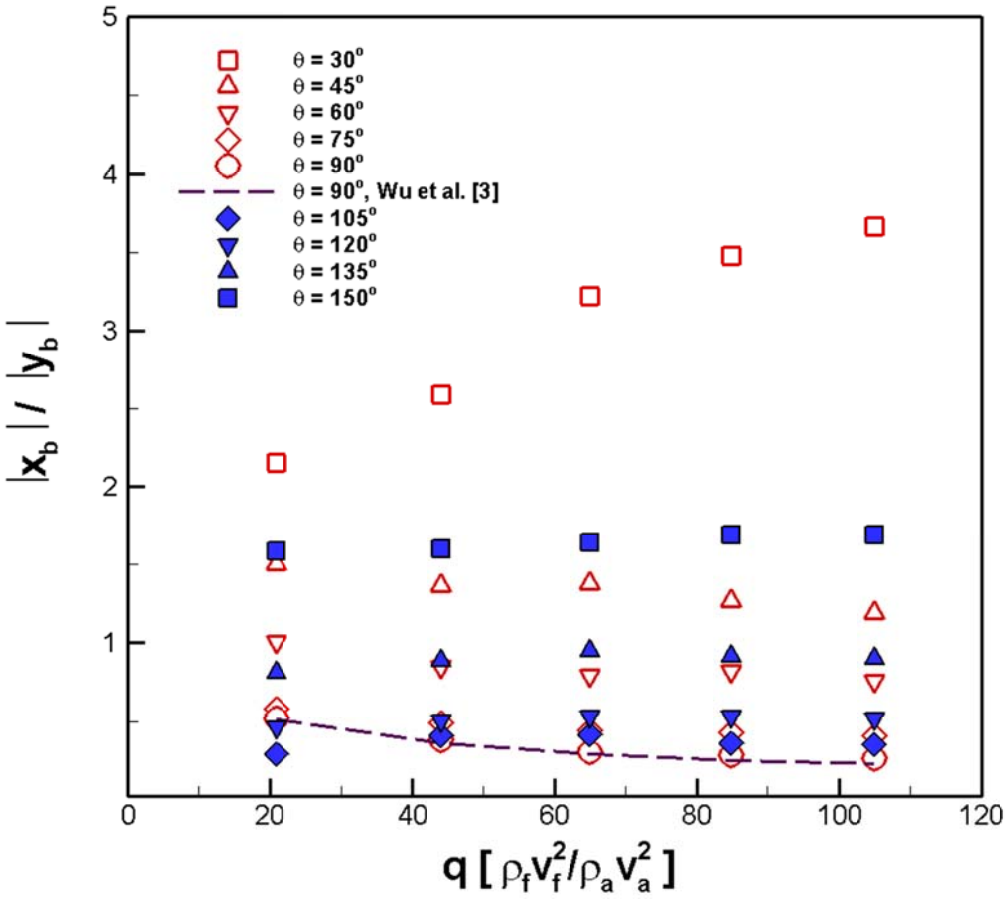

Fig. 7.10 Ratio of liquid column breakup length with normalized axial and penetration distances.

Figure 7.11 shows the empirical formula for the distance to the breakup point derive as Eqs. (7.2), (7.3), (7.4) and (7.5). It was demonstrated that the relation of the proceeding direction of the air flow and the breakup distance of the penetration direction varies depending on the forward injection or the reverse injection.

Forward injection cases :

$$\left.\frac{|x_b|}{d}\right|_{\theta \le 90^o} = \frac{6.34\, q^{0.07}}{\sin^2 \theta} \tag{7.2}$$

$$\left.\frac{|y_b|}{d}\right|_{\theta \le 90^o} = 6.33\, q^{0.314} \sin^2 \theta \tag{7.3}$$

Reverse injection cases :

$$\left.\frac{|x_b|}{d}\right|_{\theta > 90^o} = \frac{1.14\, q^{0.39}}{\sin^2 \theta} \tag{7.4}$$

$$\left.\frac{|y_b|}{d}\right|_{\theta > 90^o} = 4.64\, q^{0.317} \sin^{0.5} \theta \tag{7.5}$$

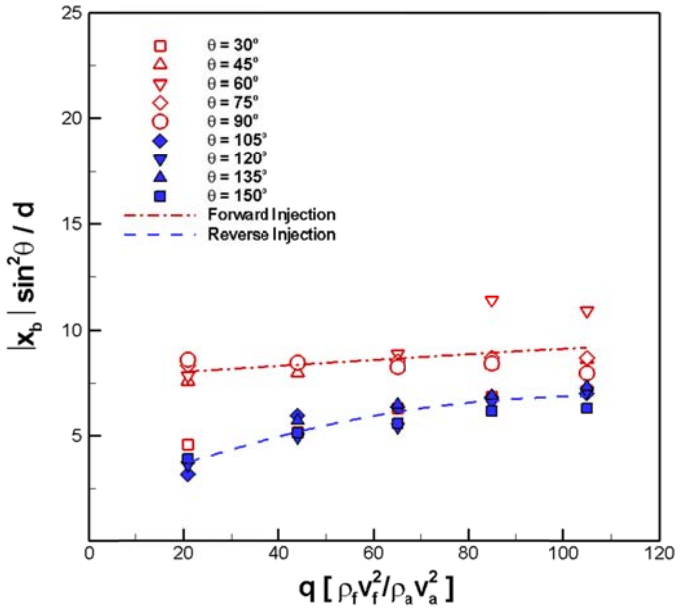

(a)

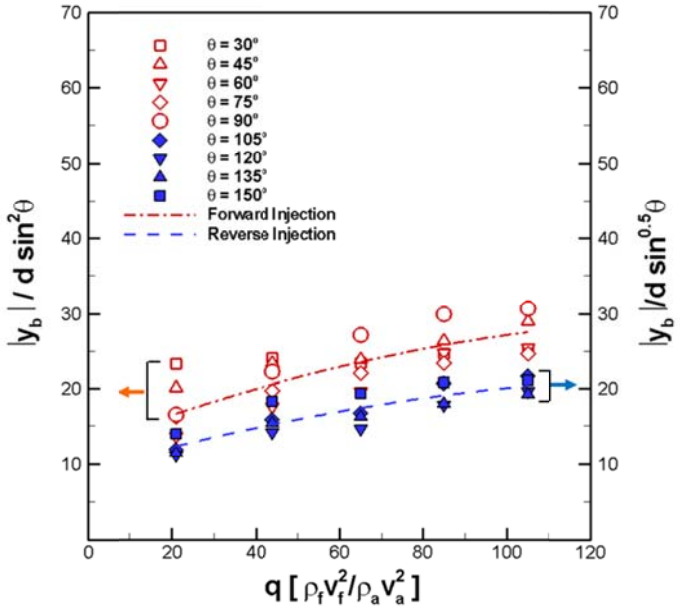

(b)

Fig. 7.11 Empirical formula of liquid column breakup length; (a) axial distance (*x*-direction), (b) penetration distance (*y*-direction).

CHAPTER 8
CONCLUSION

Experimental investigations were performed on the flame structure and combustion instability characteristics of model gas turbine combustor for low NOx combustion. Also, secondary spray jet mechanism and the optimum combustion tuning method were conducted on model and stationary gas turbine combustor for validation of this experimental study. This study carried out a research on the combustion dynamic characteristics of partially premixed flame by changing the combustor length, the equivalence ratio, and the fuel-air mixture velocity of nozzle exit and depending on the length of the fuel-air mixing section length. The fuel-air mixture velocity and equivalence ratio were confirmed to be main variables for the phenomenon of combustion instability as they changed the response characteristics of flame and the average temperature conditions in the combustion chamber, and in such a condition as a diffusion flame without swirl effect, there was a higher dynamic perturbation value during combustion instability than in the condition of more premixed type flame, causing a 30° swirl effect. In addition, it was found that larger combustion instability took place in the section where the fuel-air mixture velocity was high.

This study also investigated the relation between the combustion instability phenomenon and the formation of a recirculation zone through the PIV measurement technique. Although there has been considerable research on the mechanism of flame stabilization, the results mostly cover the closed-open boundary of combustors. This study, however, observed the structural characteristics of swirl-stabilized flame in a limited combustor through the PIV technique, and associated the results with thermo-acoustic instability characteristics. This study observed that when combustion instability occurred, flame vibrated cyclically, accompanied with the fluctuation of a recirculation zone. The fluctuation frequency of the recirculation zone was the same as the frequency of combustion instability, through which the fluctuation of the recirculation zone was

generated under combustion instability. It also was found that such a fluctuation in the recirculation zone causes fluctuations in the rate of mass flow and heat release within the recirculation zone, further functioning to generate and reinforce combustion instability.

Experimental results of the relation between inlet velocity and combustion instabilities in model gas turbine combustor. In our experimental conditions, two dominant mechanisms affect the rising combustion instability. Structural change is mainly related with mixture fluctuation and this is proven by the changing of flame angles. As a result, the combustion instability mechanism was specified in two ways: one is swirl number perturbation and the other is flame length fluctuation based on pressure gradient variation. Swirl number perturbation was experimentally proven by OH chemiluminescence results and the change in flow rate was well matched with the pressure gradients of the combustor. These two dominant mechanisms work to amplify heat release fluctuation and this feedback loop maintains combustion instability. It was also found that frequency shifting occurs in conditions of low fuel-air mixture velocity condition. Therefore, we performed mode and dynamic pressure analysis, and consequently we estimate that at condition of low velocity, there is another reason for the occurrence of combustion instability. This is because of phase delay of heat release and dynamic pressure in low fuel-air mixture velocity conditions. Therefore, we calculated Strouhal number and found a difference in those conditions. We concluded that fluid dynamical vortex frequency has major effects on the combustion of low velocity conditions, making it unstable.

From the results of inlet mixing section characteristics, this experiment observed two different modes of strong combustion instability frequencies, and it was found that both the frequency bands had a relation with the acoustic mode (Longitudinal mode, n = 1, 2) caused by the combustor length through amplitudes and phases measured by dynamic sensors located in the combustion chamber. Since a specific instability band frequency in which that combustion instability actually appears existed and since either the 1L or 2L modes were bands of acoustic mode likely to appear in case of combustion instability, it was found that the mean temperature (or equivalence ratio) and length of a combustion

chamber, which determine the acoustic frequency inside the combustion chamber, had an important influence on the phenomenon of combustion instability. The combustion instability phenomenon of the 1L mode observed in this experiment had a relation with the longitudinal mode of the combustor, and such a phenomenon of combustion instability is caused by the flame response characteristics while being coupled with heat release oscillation. This is also described in the previous researches on the existing gas turbine combustion instability. In the case of the combustion instability phenomenon where an instability mode is transited into a higher instability frequency, this experiment confirmed that it was a mode generated by the combination of the longitudinal mode of the combustor and the longitudinal mode of the inlet mixing section. When both the inlet mixing section and the combustion chamber had similar acoustic frequency domains, which correspond to n = 2 of the acoustical longitudinal mode, the combustion instability phenomenon was caused by the related frequency. It was also found that this phenomenon was more affected by the pressure oscillation from the fuel-air mixing section than from the combustion chamber.

The findings as follows were achieved through experimental research on the spray injection characteristics depending on the injection angle (forward, reverse) within the jets in a subsonic crossflow field of RQL combustor for reducing the NOx emissions. Through the experimental studies on canted injection, it was identified that the trajectory and the distance to the breakup point of the liquid column region are the function of the fuel/air momentum flux ratio (q), injection angle (θ), axial distance, penetration distance and the drag coefficient (C_D). The empirical formula of the trajectory and breakup length in the liquid column region by the injection angle was derived, and there generated the differences at constant value, the drag coefficient between the experimental equation of the liquid column trajectory on the forward injection which has a matching direction with the normal air-flow direction and that of the reverse injection.

These experimental results make it possible to infer that when an actual gas turbine is optimum designed. The combustion values such as v_{mix}, Φ, fuel and air mass flow rate are very important factor for study of combustion instability mechanism. Also, the swirl

vane angle, combustor and inlet mixing section geometries of a gas turbine should be optimally designed in addition to the optimal design of a combustion chamber by the flame oscillation. On the contrary, when combustion instability takes place, the combustor and inlet mixing section geometries are possible to create optimum control of combustion instability modes through the tuning of plenum or transient piece devices. Fig. 8.1 shows the relation between combustion instability mechanism and each chapter result of this study.

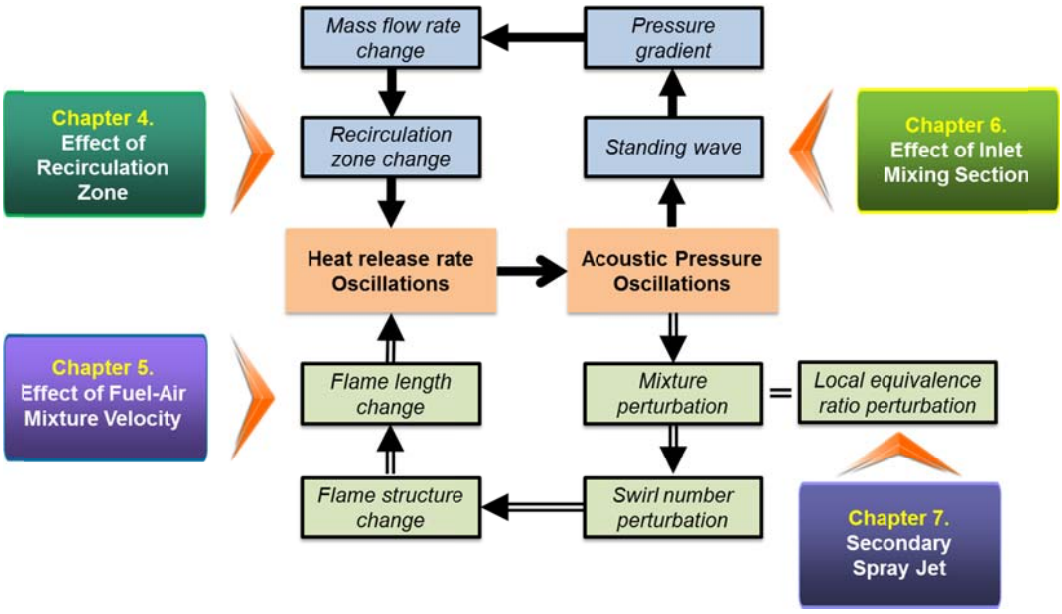

Fig. 8.1 Mechanism of combustion instability results from this study.

APPENDIX A

GE 7FA+e DLN-2.6 GAS TURBINE COMBUSTOR

A.1 Introduction of DLN-2.6 Combustor

The new utility gas turbine (GT) that often require compliance with NOx emissions as low as 2.5 ppm (5 mg/Nm^3) based on a combination of 9-ppm (18 mg/Nm^3) DLN technology coupled with 75% reduction Selective Catalytic Reduction (SCR) [1, 2, 3]. To suppress NOx levels to 9 ppm DLN combustors of many modern GTs must operate in lean premix mode near the lean blowout (LBO) limit, where the quantity of fuel in the air/fuel mix at the burner is barely sufficient to sustain combustion at low flame temperatures. The safe and reliable operation of modern combustors near the LBO requires a number of vital elements: (1) an in-depth understanding of the mechanisms that promote combustion stability at these extremely low fuel equivalence ratios, (2) precise manufacturing of key components with narrow design tolerances, (3) a reliable monitoring system to detect onset of instabilities in individual combustors and (4) protective passive or active control hardware and systems that can implement corrective actions such as changes in fuel splits or, in case of emergencies, Protective Load Shedding (PLS) or turbine trip. Obviously, PLS and turbine trips are not desirable events. Thus, operators often need to remain proactive in preventing onset of excessive pressure oscillations and combustion-induced vibrations and flame instabilities. The phenomenon of combustion instability has afflicted a wide range of ultra-low-NOx machines for a variety of reasons, including GE 7F, ABB 13E2 and GT24 and GT26, Siemens/Westinghouse 501F, and Siemens V64.3 and V84.3. Today, combustion instability is viewed as the major challenge facing the gas turbine industry.

The GE 7FA+e is a high-performance gas turbine for a power generation that has been developed by General Electric and has the generating capacity (P_{out}) of 180 MW. This gas turbine engine is composed of an Inlet Guide Vane (IGV) to control air flow rate, a 15-stage compressor, a 14 can-type combustor, and a 3-stage turbine. For a combined-

cycle thermal power generation, the GE 7FA+e gas turbine engine operates in connection with a starting motor, heat exchanger (heat-recovery steam generator or HRSG), and steam turbine. A Seo-Incheon power plant is located in the west side of Incheon city, South Korea. This electric power plant is a subsidiary company of WP (Korea Western Power Company) and operates 8ea GE 7FA+e gas turbines for a combine-cycle power generation. To reduce maintenance costs, the company is attempting to reduce NOx emission levels (involving a yellow plume; NO_2 flue gas) during the start-up mode and combustion vibration during the loading mode for the GE 7FA+e DLN-2.6 gas turbine combustor.

A.2 Operating Combustion Conditions of a DLN-2.6 Combustor

The GE 7FA+e gas turbine is controlled by a microprocessor-based MARK-Ⅵ as an operating system. For power generation, the gas turbine mode changes during a mode transfer operation from the starting mode (Mode 1) to the base mode (Mode 6AQ) at the speed of up to 3600 rpm of a turbine shaft rotation. However, the combustor has a critical operating section with high NOx levels and a high degree of combustion oscillation. At the beginning of operation at P_{out} = 20 ~ 45 MW (Mode 3), the NOx level increases, while at P_{out} = 40 ~ 45 MW (Mode 6B), the combustion vibration increased with the increase of output power. Both problems are minimized by optimizing the mode transfer. The main idea of GT tuning is to control the amount of fuel and air mass flow rate entering the combustors. Fuel to the DLN-2.6 combustor is staged to operate the machine over the entire load range. Burners are brought on in stages, starting at Full Speed No Load (FSNL) with the center burner only and turning on additional burners as load is increased. The staging is accomplished by using four fuel systems. Each fuel system consists of a different number of nozzles coupled together via a common manifold. These systems are used alone or in combination with one another to maintain fuel / air ratio within a desirable range in the reaction zone. The mode names reflect the number of

burners that are being fueled in that mode. The suffix Q in mode 6Q reflects the fact that quaternary fuel may be in use. Mode 6Q spans the load range for 9/9 ppm NOx / CO operation. The machine lights on the PM2 and PM1 circuits. Following ignition, the PM1 nozzles are turned off and the PM2 nozzles support combustion while the unit ramps to 95 percent speed. At 95 percent speed, the unit transfers from mode 2 to mode 1 for continued acceleration to full speed no load (FSNL) and leading to synchronization. At approximately 10 percent load, the PM2 manifold is turned back on (3 nozzles = mode 3) and continues until 25 percent load. At this transfer point, the PM2 manifold is switched off, with the PM3 manifold turned on for operation in mode 4 to 50 percent load. All nozzles are turned on to enter mode 6 or 6Q with quaternary. Originally, the system also used modes 5 or 5Q with the five outer nozzles in operation. However, this mode was eliminated to simplify the staging and controls strategies [4]. Fig. A.1 shows the strategy of fuel staging and the process of mode transfer from Mode 3 to Mode 6AQ in a GE 7FA+e gas turbine. Fig. A.2 shows the DLN2.6 fuel nozzle end cover downstream face with partial fairings. The nozzle has a plane orifice-type hole in a swirl vane and on the top of the nozzle. The choke orifice hole acts as an injector and acoustic barrier that prevents both the flow-oscillation effect on fuel injection and distribution in delivery lines and external disturbances from a reaction zone. The compressed air was supplied to a nozzle mount, and become partially premixed with fuel after delivery along the swirl vanes before combustion.

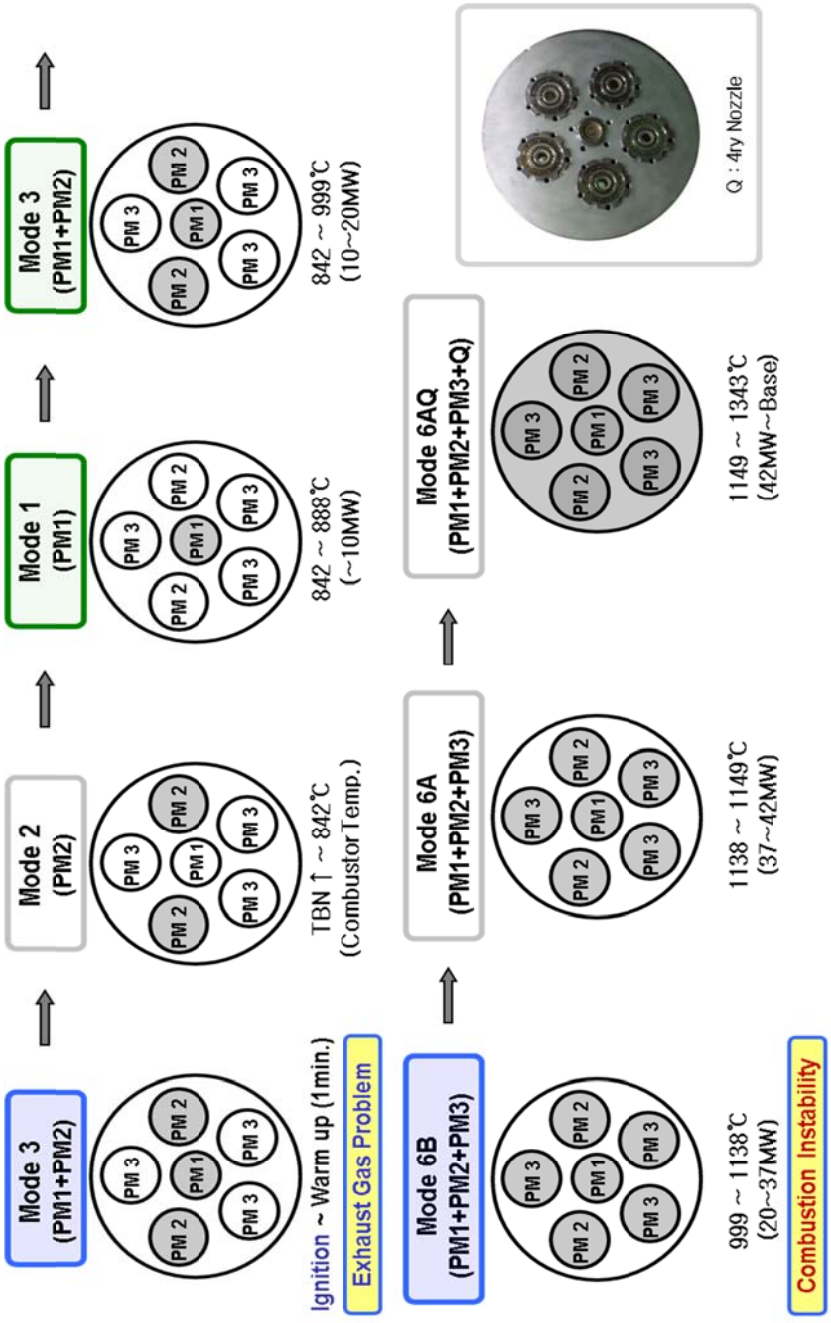

Fig. A.1 Fuel staging methods in GE 7FA+e DLN-2.6 combustor.

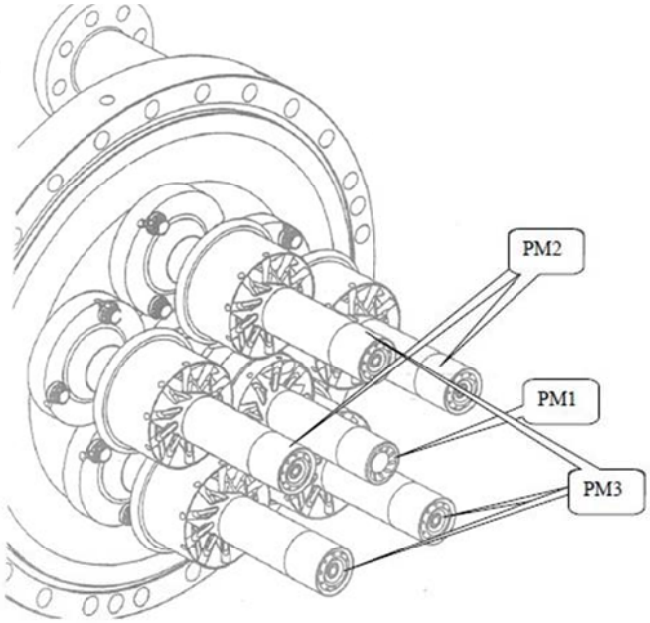

Mode 3:	PM1+PM2	Ignition to 18% speed
Mode 2:	PM2	18% to 95% speed
Mode 1:	PM1	95% speed to 10% load
Mode 3:	PM1+PM2	10% load to 25% load
Mode 4:	PM1+PM3	25% load to 50% load
(Originally, Mode 5:	PM2+PM3	transfer mode on start)
Mode 6 or 6Q:	PM1+PM2+PM3+(quaternary)	50% to 100% load

Fig. A.2 GE 7FA+e DLN 2.6 fuel nozzle end cover downstream face with partial fairings.

A.3 Measurement of Combustion Values

The main control elements of the GE DLN-2.6 gas turbine is the air mass flow rate affected by the opening of FSRSEL (Fuel Stroke Reference Selection) and IGV (Inlet Guide Vane) getting into each fuel nozzle at the time of changing the mode [5]. Therefore, MARK VI enables checking air and fuel mass flow rate by the desired output net power. All gas turbine plants in Korea Western Power Co. Ltd. at Seo-Incheon power plants were used to measure the property of a combustion value, dynamic pressure and exhaust

emission (NOx) levels while changing their outputs by 5～10 MW unit within the range of 20～60 MW. The total amount of fuel in the mode transfer varies linearly for outputs and the fuel quantity in each nozzle is known to be changed mainly by PM1 in Mode3, PM3 in Mode 6B, PM2 and 3 in Mode 6AQ. It is thought that such fuel quantities as PM1 in Mode3, PM3 in Mode 6B, and PM2/3 in Mode 6AQ will work as main elements to fit the optimum dynamic pressure and exhaust emission levels when tuning the burner.

A.4 Combustion Instability and NOx Emission Characteristics

EINOx (Emission Index of NOx) depends on the fuel-mass flow rate and the residence time for exposure to hot flow of more than 1800K, as exposure time is proportional to the flame volume and length [6]. To understand the optimum tuning of gas turbine, the exhaust emissions and frequency spectrum of dynamic pressure measured along with fluctuations in value of control constants per output. First, we identified characteristic growth of the quantity of thermal NOx formed by higher temperatures at the combustion chamber in Mode 3 than in other Modes. The dynamic pressure had a higher level in Mode 6B (30～45 MW) than in other Modes, and the characteristic frequency was close to 140Hz, outputs being kept at a 35～45MW range, with the magnitude of dynamic pressure reaching approximately 0.6 psi. This feature comes up as the fuel quantity in PM3 fuel nozzle shows a rapid change, and given that almost no change in characteristic frequency according to turbine exit temperature is made, dynamic pressure is regarded to have the reflection of the cold flow prior to combustion and the characteristics of the chamber geometry near the nozzle, instead of the impact of the combustion field. This constant frequency is evidence that the flow is not affected by combustion. In addition, the fuel mass flow rate for nozzle PM3 is significantly changed in Mode 6B (P_{out} = 40 ~ 45 MW). Therefore, the pressure fluctuation may be caused by cold flow, and occur in the plenum chamber between the compressor outlet and the combustor inlet. The peak frequency of 140 Hz is therefore thought to be revealed as a

resonance frequency for the plenum chamber of nozzle PM3.

The equation for bulk or Helmholtz mode is as follows;

$$f_H = \frac{c}{2\pi} \cdot \sqrt{\frac{A}{L_n \cdot V_p}} \qquad \left(where,\ c = \sqrt{\gamma RT}\right) \tag{A.1}$$

Where, A is the nozzle neck area, L_n is the nozzle neck length, and V_p is the plenum chamber volume [7]. Hubbard and Dowling [8] used a numerical calculation to study the acoustic resonances effect on an industrial gas turbine combustion system. These researchers reported that the resonance in a plenum chamber or in the delivery lines affects the local mixture of fuel and air around nozzles. The oscillation of the local mixture fraction influences the turbulent burning velocity and becomes one cause of combustion instability [9]. The plenum resonance frequency can be reduced by a Helmholtz resonator attached to a plenum chamber; this is a significant factor to keep in mind when designing a combustion system.

APPENDIX B
DEVELOPMENT OF DYNAMIC PRESSURE TOOLKIT

The main purpose of a stationary gas turbine is to generate power, and diagnostics will only be implemented when they are absolutely necessary for reliable power production. That is why optical access is only available as a safeguard to check for the presence of the flame, and not for detailed study. However, monitoring of the combustion process and related phenomena in large gas turbines though still limited is increasingly being recognized as a necessary part for safely operating ultra-low-NOx power turbines.

Because of cost and other maintenance needs, combustion dynamic sensors are typically mounted on modern GE, Alstom, and S/W gas turbines only when required for intermittent measurement and burner tuning. GE performs tuning in the commission stage and after a major overhaul. For these intermittent tuning requirements, a permanent monitoring system may not be required. However, GE also offers remote monitoring, diagnostic and tuning of modern DLN 2.6 combustors with the permanent installation of a monitoring system. In most large Siemens and Alstom gas turbines, on-line dynamic pressure transducers are employed to generate an alarm if acoustic amplitudes exceed a preset limit, thus preventing damage to structural components. For purpose of completeness, this subsection presents technically available options to monitor combustion instabilities, although the industry relies almost exclusively on piezo-electric pressure transducers, which can pick up pressure pulsations over a wide range of frequencies pertinent to GT combustors. Sensors available to monitor flame stability under extreme lean combustion conditions can be divided into three main groups. Pressure sensors that monitor the frequency and amplitude of pressure pulsations caused by unstable combustion in enclosed chambers. These are Piezo-resistive transducers, piezo-electrical transducers and accelerometers [10].

Figure B.1 shows the dynamic pressure sensor module for GE stationary gas turbine

combustor. To measure combustion vibration, we developed a dynamic pressure measurement device which was composed of a sampling probe, pressure transducer (102A05, PCB Piezotronics Co., Depew, NY, USA), a signal conditioner (482A22, PCB Piezotronics Co.), and a data acquisition (DAQ) board (USB-6218, NI Co., Austin, TX, USA).

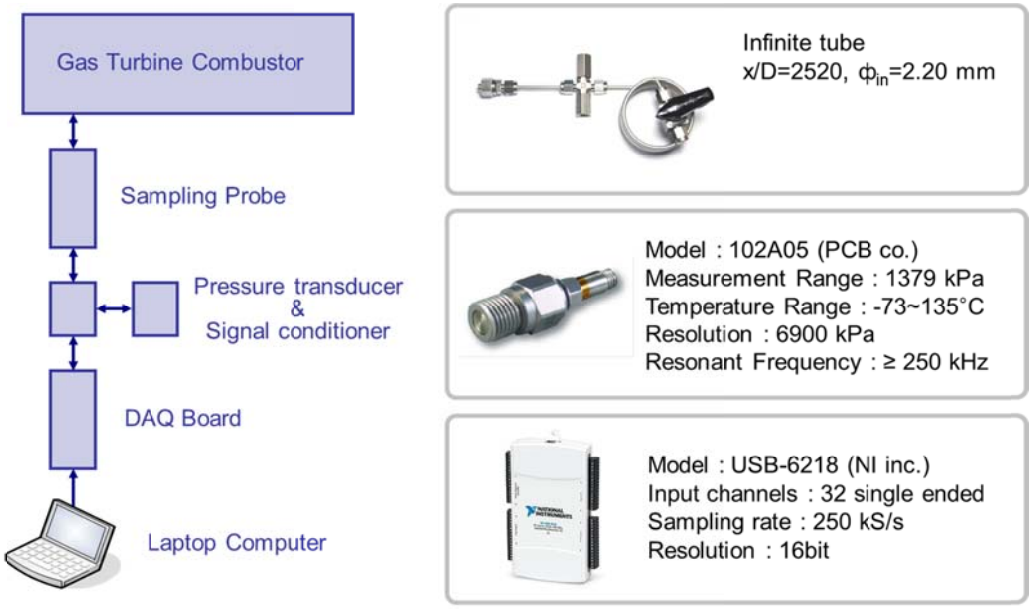

Fig. B.1 Dynamic pressure sensor module for GE stationary gas turbine combustor.

Fig. B.2 shows the experimental setup for the measurement of dynamic pressure at GE stationary gas turbine. The measurement system could detect dynamic pressure in a range of 10~10000 Hz by connecting with a gas turbine combustor. The sampling tube was designed as an infinite cylindrical tube to minimize the dynamic pressure loss at a certain frequency; this tube acts as a Helmholtz resonator [11]. The ratio of length (l) to inner diameter (d) for a long-tube type of probe was greater than l/d = 2500 ~ 3000, providing the advantage of reduction of wave reflection and interruption. To make the size compact, the probe end was rolled as a pig tail. In addition, the transducer was

mounted on the side of the infinite tube and located as close as possible near a combustor wall to maximize the signal intensity. According to Rea et al. [12], because of the acoustic cavity effect, the location of l/d = 20 from a combustor wall is suitable for the dynamic pressure measurement.

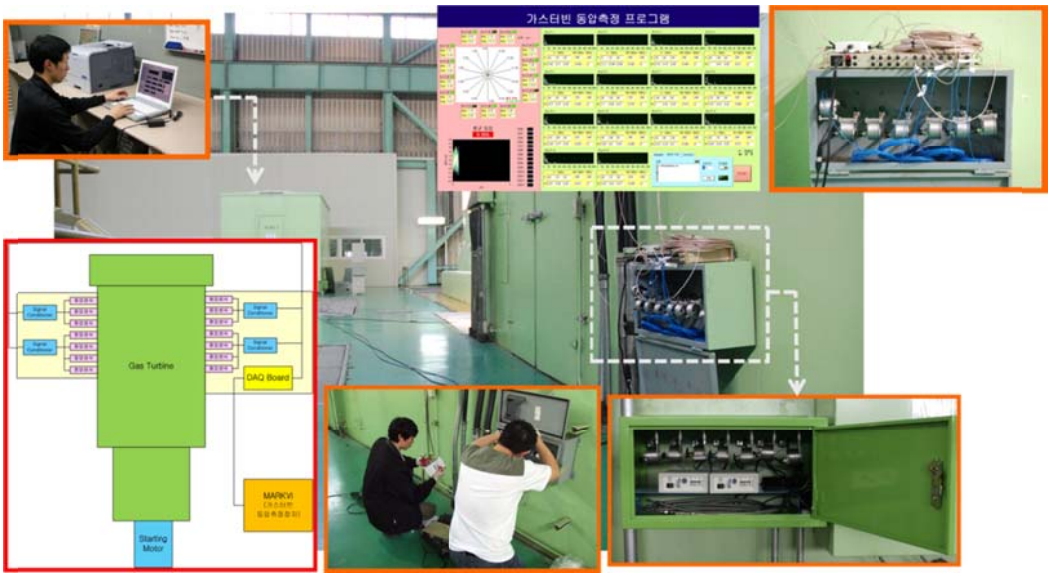

Fig. B.2 Experimental setup for the measurement of dynamic pressure at GE stationary gas turbine.

Appendix C
OPTIMUM COMBUSTION TUNING

It is helpful for a more fundamental understanding of combustion conditions to check out the equivalence ratio in each nozzle (PM 1, PM 2, PM 3, Quaternary) along with the trends in the dynamic pressure distribution per output and exhaust emissions in DLN-2.6. If the Φ is 1, complete combustion takes place as it gets close to the theoretical air-fuel ratio. And if below 1, lean combustion takes place as the fuel gets a smaller portion in the fuel-air mixture, and conversely, rich combustion occurs as the fuel gets a higher portion. Table C.1 represents the variation in the control constant of a fuel nozzle changed in each mode as the combustion temperature shows an increase. This way, the fluctuations in flow rate of a fuel nozzle in each mode were able to be identified and a flame structure could be predicted. Table C.1 could identify that in Mode 3 the Φ was relatively high near the PM1 fuel nozzle, enough to impose impacts on the characteristics of exhaust emissions. In Mode 6B the equivalence ratio near the PM3 fuel nozzle noticeably dropped to induce heat release fluctuations by lean burn and caused combustion instability to occur in the combustion chamber. In general, the reactant attains complete combusting at a stoichiometric conditions (Φ = 1). However, from the point of view NOx emissions, the thermal NOx production is maximized due to the combustion temperature approaching adiabatic temperature [13]. In Φ < 1, the flame utilizing lean premixed fuel has the advantage of low NOx production, and the disadvantage of conferring a potential risk for combustion instability. At Φ > 1, the rich premixed-flame is available for flame stabilization, while it is disadvantageous to NOx reduction. So, The fuel rate of PM1 nozzle decrease as the NOx emissions level was decrease around 25 ppm in GE combustor. Hence, in Mode3 with a problem of exhaust emissions when tuning the burner, the fuel nozzle constant dropped by 25～30 ppm, and in Mode 6B the pressure amplitude was reduced by about 52% compared to the existing one as the PM 2 constant value shows an increase, which leads to experiencing the optimal combustion control.

Table C.1 Tuning the equivalence ratio of each fuel nozzle.

Combustion mode	Nozzle / Power	PM1	PM2	PM3	Quat.	Total
Mode 3	Negative (5)	**0.487**	0.359	0	0	0.196
	20 MW	**0.509**	0.345	0	0	0.195
	Positive (5)	**0.538**	0.329	0	0	0.195
	Negative (5)	**0.621**	0.370	0	0	0.222
	30 MW	**0.643**	0.352	0	0	0.220
	Positive (5)	**0.700**	0.337	0	0	0.223
Mode 6B	Negative (5)	0.378	0.399	**0.102**	0	0.247
	40 MW	0.380	0.386	**0.119**	0	0.252
	Positive (5)	0.379	0.383	**0.123**	0	0.252
	Negative (5)	0.373	0.416	**0.120**	0	0.261
	45 MW	0.372	0.389	**0.148**	0	0.266
	Positive (5)	0.375	0.360	**0.155**	0	0.260
Mode 6AQ	Negative (5)	0.373	**0.115**	0.346	0.016	0.273
	50 MW	0.375	**0.119**	0.347	0.013	0.276
	Positive (5)	0.376	**0.124**	0.347	0.016	0.277
	Negative (5)	0.385	**0.176**	0.338	0.019	0.292
	60 MW	0.386	**0.174**	0.340	0.017	0.292
	Positive (5)	0.383	**0.170**	0.338	0.013	0.290

Prepared was the optimal combustion control program able to analyze real-time data by each mode from the gas turbine engine showing a rise in output up to the base mode through the real-time receipt of the data on the combustion property of MARK VI in GE 7FA+e DLN-2.6, and through the researchers added who got the values of dynamic pressure variation in measurement module for dynamic/static pressure. (See Fig. C.1) [14] The empirical equation for combustion control constants was obtained through the connection with the constant value of fuel nozzles for optimal combustion control using the combustion property values acquired from the tuning experiment (about 50 times) with several gas turbine burners. This program presents the user friendly combustion environments where the combustor can operate under optimal conditions, by conducting a swift analysis into the equivalence ratio, exhaust emissions, dynamic pressure and control constants in the troubled mode. This program also enables providing types of fuel nozzles to control in each mode and optimal constant values. Furthermore, it can also present how the gas turbine combustor is operating in each situation by monitoring the combustion conditions across the mode area.

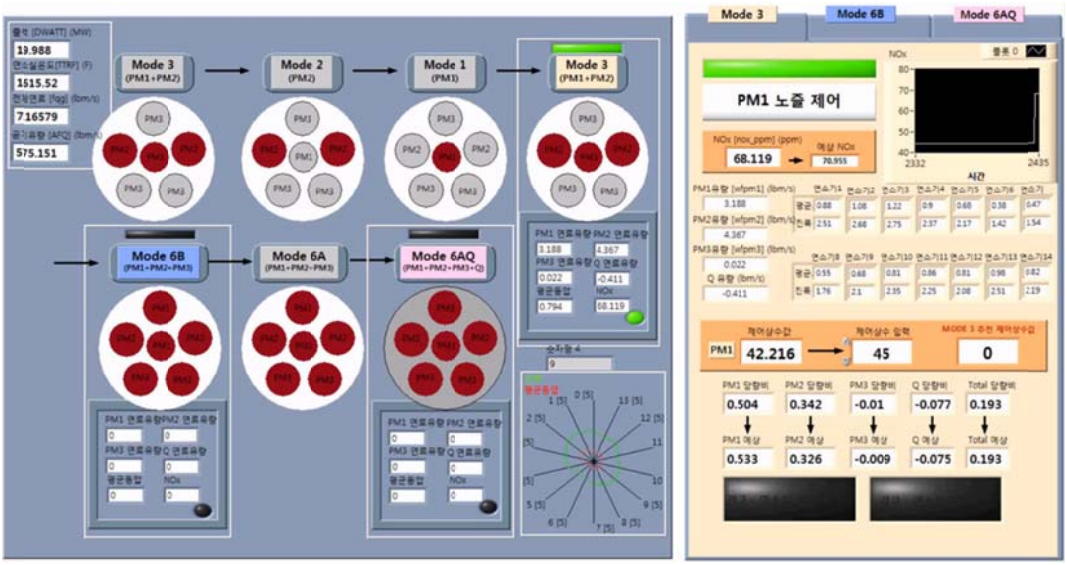

Fig. C.1 Optimum combustion control program in GE gas turbine combustor.

BIBLIOGRAPHY

Chapter 1 Introduction

[1] M.P. Boyce, Gas Turbine Engine, Handbook-3rd ed., Gulf Professional Publishing, New York, 2001, pp. 47.

[2] T.C. Lieuwen, Investigation of Combustion Instability Mechanisms in Premixed Gas Turbines, PhD. thesis, Georgia Institute of Technology, USA, pp. 1-52. 1999.

[3] A.H. Lefebvre, Gas Turbine Combustion-2nd ed., Taylor and Francies, USA, 1999, pp. 364.

[4] C.O. Peterson, W.A. Sowa, G.S. Samuelsen, Performance of a Model Rich Burn-Quick Mix-Lean Burn Combustor at Elevated Temperature and Pressure, NASA Report CR-2002-211992, University of California, USA, pp. 1-19, 2002.

[5] J.W.S. Rayleigh, The Theory of Sound, Nabu Press, New York, Vol. 2, 1945, pp. 226.

[6] N. Syred, J.M. Beer, Combustion in Swirling Flows. A Review, Combust. Flame, 22(2) (1974) 143-201.

[7] T. Poinsot, C.L. Chatellier, S. Candel, E. Esposito, Experimental Determination of the Reflection Coefficient of a Premixed Flame in a Duct, J. Sound Vib., 107 (1986) 265–278.

[8] C. Paschereit, E. Gutmark, W. Weisenstein, Excitation of Thermo-acoustic Instabilities by the Interaction of Acoustics and Unstable Swirling Flow, AIAA J. 38 (2000) 1025–1034.

[9] N. Tran, S. Ducruix, T. Schuller, Damping Combustion Instabilities with Perforates at the Premixer Inlet of a Swirled Burner, Proc. Combust. Inst., 32 (2009) 2917–2924.

[10] M.R. Bothien, J.P. Moeck, A. Lacarelle, C.O. Paschereit, Time Domain Modelling and Stability Analysis of Complex Thermo-acoustic Systems, J. Power and Energy, 221(5) (2007) 657-668

[11] J. Oh, M.-K. Kim, Y. Yoon, The Tuning Methodology of a GE 7FA + e DLN-2.6 Gas

Turbine Combustor, Appl. Therm. Eng., 36 (2012) 14-20.

[12] T. Schuller, D. Durox, S. Candel, Self-induced Combustion Oscillations of Laminar Premixed Flames Stabilized on Annular Burners, Combust. Flame, 135 (2003) 525–537.

[13] N. Noiray, D. Durox, T. Schuller, S. Candel, Self-induced Instabilities of Premixed Flames in a Multiple Injection Configuration, Combust. Flame, 145 (2006) 435–446.

[14] H. Johnston, Reduction of Stratospheric Ozone by Nitrogen Oxide Catalysts from Supersonic Aircraft Exhaust, Science, 173 (1971) 517-521.

[15] K. Yamagishi, M. Nozawa, T. Yoshie, T. Tokumoto, Y. Kakegawa, A Study of NOx Emissions Characteristics in Two-Stage Combustion, 15th Symposium on Combustion, The Combustion Institute, 15(1) (1975) 1157-1166.

[16] J.M. Beer, M.T. Jacques, W.F. Farmayan, A.K. Gupta, S. Hanson, Reduction of NOx and Solid Emissions By Staged Combustion of Coal Liquids Fuels, 19th Symposium on Combustion, The Combustion Institute, (1982) 1301-1309.

[17] M. Sadakata, Y. Fujioka, D. Kunii, Effects of Air Preheating on Emissions of NO, HCN, and NH_3 from Two-Stage Combustion, 18th Symposium on Combustion, The Combustion Institute, (1981) 65-72.

[18] J. Tyndall, Sound, Appleton & Company, New York, 1915

[19] G.J. Bloxsidge, A.P. Dowling, N. Hooper, P.J. Langhorne, Active Control of an Acoustically Driven Combustion Instability, Journal of Theoretical and Applied Mechanics, 6 (1987) 161-175.

[20] A.A. Putnam, Combustion Driven Oscillations in Industry, American Elsevier Publishing Company, USA, 1971.

[21] A.P. Dowling, Nonlinear Self-excited Oscillations of a Ducted Flame, J. Fluid Mech., 346 (1997) 271−290.

[22] G.J. Bloxsidge, A.P. Dowling, N. Hooper, P.J. Langhorne, Active Control of Reheat Buzz, AIAA J., 26 (7) (1989) 783-790

[23] J.W.S. Rayleigh, The Explanation of Certain Acoustical Phenomena, Nature, 18(455) (1878) 319-321.

[24] F.E.C. Culick, Combustion Instabilities in Liquid Rocket Engines : Fundamentals and Control, ONERA, 2002.

[25] J.C. Oefelein, V. Yang, Comprehensive Review of Liquid-Propellant Combustion Instabilities in F-1 Engines, Journal of Propulsion and Power, 9 (1993) 657-677.

[26] B.T. Zinn, T.C. Lieuwen, Combustion Instabilities : Basic Concepts - Combustion Instabilities in Gas Turbine Engines : Operational Experience, Fundamental Mechanisms, and Modeling, Progress in Aeronautics and Aeronautics Series, AIAA 210 (2005) Chapter1.

[27] F.S. Blomshield, Historical Perspective of Combustion Instability in Motors: Case Studies, AIAA J., (2001) 2001-3875

[28] F.E.C. Culick, Combustion Instabilities in Liquid-Fueled Propulsion Systems - An Overview, AGARD 72B Specialists' Meeting of the Propulsion and Energetics Panel AGARD CP 450, 1977.

[29] K.R. McManus, T. Poinsot, S.M. Candel, A Review of Active Control of Combustion Instabilities, Progress in Energy and Combustion Science, 19(1) (1993) 1-30.

[30] S. Ducruix, T. Schuller, D. Durox, S. Candel, Combustion Dynamics and Instabilities : Elementary Coupling and Driving Mechanisms, Journal of Propulsion and Power, 19(5) (2003) 722-734.

Chapter 2 Experimental Background

[1] A.M. Annaswamy, M. Fleifil, J.P. Hathout, A.F. Ghoniem, Impact of Linear Coupling on the Design of Active Controllers for Thermoacoustic Instability, Combustion Science and Technology, 128 (1997) 131-180.

[2] A.P. Dowling, J.E. Efowcs, Sound and Sources of Sound, Ellis Horwood Limited, West Sussex, England, 1983.

[3] A.D. Pierce, Acoustics : An introduction to Its Physical Principles and Applications, McGraw-Hill, USA, 1981.

[4] L. Debnath, Nonlinear Partial Differential Equations for Scientists and Engineers,

Birkhauser, USA, 1997.

[5] B.T. Zinn, Pulsating Combustion : Advanced Combustion Methods, Academic Press Inc. LTD., England, 1986.

[6] M. Fleifil, A.M. Annaswamy, Z. Ghoniem, A.F. Ghoniem, Response of a Laminar Premixed Flame to Flow Oscillations : A Kinematic Model and Thermoacoustic Instability Result, Combustion and Flame, 106 (1996) 487-510.

[7] A.A. Peracchio, W. Proscia, Nonlinear Heat Release/Acoustic Model for Thermoacoustic Instability in Lean Premixed Combustors, In ASME Gas Turbine and Aerospace Congress, Sweden, 1998.

[8] P.M. Anacleto, E.C. Fernandes, S.I. Shtork, Swril Flow Structure and Flame Characteristics in a Model Lean Premixed Combustor, Combust. Sci. and Tech., 175(8) (2003) 1369-1388.

[9] Y. Huang, V. Yang, Dynamics and Stability of Lean-Premixed Swirl-Stabilized Combustion, Progress in Energy and Combustion science 35(4) (2009) 293-364.

[10] E.M. Greitzer, C.S. Tan, M.B. Graf, Internal Flow : Concepts and Applications, Cambridge University Press, England, 2004.

[11] R.L. Murray, Laser Doppler Anemometry measurements in a Turbulent, Premixed, Natural Gas/Air combustor, Brigham Young University, USA, 1998.

[12] P.-K. Wu, K.A. Kirkendall, R.P. Fuller, A.S. Najad, Spray Structures of Liquid Jets Atomized in Subsonic Crossflows, J. Propul. Power 14(2) (1998) 173-182.

[13] R.P. Fuller, P.-K. Wu, K.A. Kirkendall, A.S. Najad, Effects of Injection Angle on Atomization of Liquid Jets in Transverse Airflow, AIAA Journal 38(1) (2000) 64-72.

[14] J.A. Schetz, E.A. Kush, P.B. Joshi, Wave Phenomena in Liquid Jet Breakup in a Supersonic Crossflow, AIAA Journal, 18(7) (1980) 774-778.

[15] P.-K. Wu, K.A. Kirkendall, R.P. Fuller, A.S. Najad, Breakup Processes of Liquid Jets in Subsonic Crossflows, J. Propul. Power 13(1) (1997) 64-73.

Chapter 3 Experimental Facility and Techniques

[1] N. Syred, J.M. Beer, Combustion in Swirling Flows : A Review, Combust. Flame, 22(2) (1974) 143-201.

[2] R.S.S. James, On-line Cmbustion Mnitoring on Dry Low NOx Industrial Gas Turbines., Measurement Science & Technology, 14(7) (2003) 1123-1130.

[3] H. Zinn, M. Habermann, Developments and Experiences with Pulsation Measurements for Heavy-Duty Gas Turbines, ASME Paper, 1 (2007) 639-648.

[4] Min-Ki Kim, Jisu Yoon, Youngbin Yoon, Method of analyzing combustion state, Patent, NO.12-101799. Republic of Korea, 2012.

[5] A.G. Gaydon, The Spectroscopy of Flames, Springer, Halsted Press, USA, 1974.

[6] P.H. Paul, H.N. Najm, Planar Laser-Induced Fluorescence Imaging of Flame Heat Release, Proc. Combust. Inst., 27 (1998) 43-50.

[7] B.D. Stojkovic, T.D. Fansler, M.C. Drake, V. Sick, High-Speed Imaging of OH* and Soot Temperature and Concentration in a Stratified-Charge Direct-Injection Gasoline Engine, Proc. Combust. Inst. 30 (2005) 2657-2665.

[8] A.G. Gaydon, The Spectroscopy of Flames 2nd ed., Campman and Hall, UK, 1974, pp. 1-13.

[9] A.G. Gaydon, H. G. Wolfhard, Flames : Their Structure, Radiation, and Temperature, Chapman and Hall, London, 1978.

[10] W. Pun, S.L. Palm, F.E.C. Culick, Combustion Dynamics of an Acoustically Forced Flame, Combust. Sci. Tech. 175 (2003) 499-521.

[11] K.H. Yu, A.C. Trouve, J.W. Daily, Low Frequency Pressure Oscillations in a Model Ramjet Combustor, J. Fluid Mech. 232 (1999) 47−72.

[12] J.P. Hathout, A.M. Annaswamy, M. Fleifil, A.F. Ghoniem, Model-Based Active Control Design for Thermoacoustic Instability, Combustion Science and Technology, 132 (1998) 99-138.

[13] H.N. Najm, P.H. Paul, C.J. Mueller, P.S. Wyckoff, On the Adequacy of Certain Experimental Observables as Measurements of Flame Burning Rate, Combust. Flame,

113 (3) (1998) 312-332.

[14] N. Docquier, F. Lacas, S. Candel, Closed-loop Equivalence Ratio Control of Premixed Combustors using Spectrally Resolved Chemiluminescence Measurements, Proc., Combust. Inst., 29 (1) (2002) 139-145.

[15] V.N. Nori, J.M. Seitzman, CH∗ Chemiluminescence Modeling for Combustion Diagnostics, Proc., Combust. Inst., 32(1) (2009) 895-903.

[16] P.G. Aleiferis, Y. Hardalupas, A.M.K.P. Taylor, K. Ishii, Y. Urata, Flame Chemiluminescence Studies of Cyclic Combustion Variations and Air-to-Fuel Ratio of the Reacting Mixture in a Lean-Burn Stratified-Charge Spark-Ignition Engine, Combust. Flame, 136(1-2) (2004) 72-90.

[17] T.M. Muruganandam, B.-H. Kim, M.R. Morrell, V. Nori, M. Patel, B.W. Romig, J.M. Seitzman, Optical Equivalence Ratio Sensors for Gas Turbine Combustors, Proc., Combust. Inst. 30(1) (2005) 1601-1609.

[18] C.S. Panoutsos, Y. Hardalupas, A.M.K.P. Taylor, Numerical Evaluation of Equivalence Ratio Measurement using OH* and CH* Chemiluminescence in Premixed and Non-Premixed Methane-Air Flames, Combust. Flame, 156(2) (2009) 273-291.

[19] K.T. Kim, J.G. Lee, H.J. Lee, B.D. Quay, D.A.Santavicca, Response of Partially Premixed Flame to Acoustic Velocity and Equivalence Ratio Perturbations, Combust. Flame 157(9) (2010) 1731-1744.

[20] D. Kim, J.G. Lee, B.D. Quay, D.A. Santavicca, Effect of Flame Structure on the Flame Transfer Fuction in a Premixed Gas Turbine Combustor, J. Eng. Gas Turb Power, 132 (2010) 021502-1-021502-7.

[21] M. Raffel, C.E. Willert, J. Kompenhans, Particle Image Velocimetry, Springer, USA, 1998.

[22] P. Le Gal, N. Farrugia, D.A. Greenhalgh, Laser Sheet Dropsizing of Dense Sprays, Opt. Laser Technology, 31 (1999) 75-83.

[23] D.G. Talley, T.S. Thamban, V.G. McDonell, G.S. Samuelsen, Laser Sheet Visualization of Spray Structure Recent Advances in Spray Combustion : Spray

Combustion Measurements and Model Simulation, Progress in Astronautics and Aeronautics, 2 (1995) 113-141.

[24] K. Jung, H. Koh, Y. Yoon, Assessment of PLLIF Measurement for Spray Mass Distribution of Like-Doublet Injector, Measurement Science and Technology, 14(8) (2003) 1387-1395.

Chapter 4 Swirl Stabilized Flame Structure and Recirculation Zone

[1] Y.S.H. Najjar, Efficient use of Energy by Utilizing Gas Turbine Combined Systems, Appl. Therm. Eng., 21 (2001) 407-438.

[2] G. Kelsall, C. Troger, Prediction and Control of Combustion Instabilities in Industrial Gas Turbines, Appl. Therm. Eng., 24 (2004) 1571-1582.

[3] N.H. Afgan, M.G. Carvalho, P.A. Pilavachi, A. Tourlidakis, G.G. Olkhonski, N. Martins, An Expert System Concept for Diagnosis and Monitoring of Gas Turbine Combustion Chambers, Appl. Therm. Eng., 26 (2006) 766-771.

[4] T.J. Poinsot, A.C. Trouve, D.P. Veynante, S.M. Candel, E.J. Esposito, Vortex-Driven Acoustically Coupled Combustion Instabilities, J. Fluid Mech., 177 (1987) 265−292.

[5] T. Lieuwen, K. McManus, That Elusive Hum, Mechanical Engineering, 2002.

[6] A.H. Lefebvre, Gas Turbine Combustion-2nd ed, Taylor & Francies, Philadelphia, 1999, pp.364

[7] P. Palies, D. Durox, T. Schuler, S. Candel, Acoustic–Convective Mode Conversion in an Aerofoil Cascade, J. Fluid Mech. 672 (2011) 545−569.

[8] A. Huber, W. Polifke, Dynamics of Practical Premixed Flames, part II : Identification and Interpretation of CFD Data, Int. J. Spray Combust. Dynamics, 1 (2009) 229−249.

[9] T. Lieuwen, B.T. Zinn, The Role of Equivalence Ratio Oscillations in Driving Combustion Instabilities in Low NOx Gas Trubines, Proc. Combust. Inst., 27 (1998) 1809-1816.

[10] K.K. Venkataraman, D.A. Satavicca, Mechanism of Combustion Instability in a Lean Premixed Dump Combustor, J. Propul. Pow., 15(6), (1999) 909-918.

[11] K.T. Kim, S. Hochgreb, The Nonlinear Heat Release Response of Stratified Lean-Premixed Flames to Acoustic Velocity Oscillations, Combust. Flame, 158 (2011) 2482−2499.

[12] N.A. Worth, J.R. Dawson, Cinematographic OH-PLIF Measurements of Two Interacting Turbulent Premixed Flames with and Without Acoustic Forcing, Combust. Flame, 159 (2012) 1109−1126.

[13] T. Lieuwen, Y. Neumeier, Nonlinear Pressure Heat Release Transfer Function Measurement in a Premixed Combustor, Proc. Combust. Inst., 29 (2002) 99-105.

[14] B.D. Bellows, M.K. Bobba, A. Forte, J.M. Seitzman, B.D. Bellows, T.Lieuwen, Flame Transfer Function Saturation Mechanisms in a Swirl-Stabilized Combustor, Proc. Combust. Inst., 31 (2007) 3181-3188.

[15] C. Paschereit, E. Gutmark, W. Weisenstein, Excitation of Thermo-acoustic Instabilities by the Interaction of Acoustics and Unstable Swirling Flow, AIAA J., 38 (2000) 1025–1034.

[16] T. Schuller, D. Durox, S. Candel, Self-induced Combustion Oscillations of Laminar Premixed Flames Stabilized on Annular Burners, Combust. Flame., 135 (2003) 525–537.

[17] A. Birbaud, S. Ducruix, D. Durox, S. Candel, The Nonlinear Response of Inverted “V” Flames to Equivalence Ratio Nonuniformities, Combust. Flame, 154 (2008) 356−367.

[18] A.X. Sengissen, J.F. Van Kampen, R.A. Huls, G.G.M. Stoffels, J.B.W. Kok, T.J. Poinsot, LES and Experimental Studies of Cold and Reacting Flow in a Swirled Partially Premixed Burner with and Without Fuel Modulation, Combust. Flame, 150(1) (2007) 40−53.

[19] U. Stopper, M. Aigner, M. Stohr, I.S. Kim, Flow Field and Combustion Characterization of Premixed Gas Turbine Flames by Planar Laser Techniques, J. Eng. Gas Turb. Power., 131(2) (2009) 021504-1-021504-8.

[20] P.M. Anacleto, E.C. Fernandes, S.I. Shtork, Swirl Flow Structure and Flame Characteristics in a Model Lean Premixed Combustor, Combust. Sci. and Tech., 175(8)

(2003) 1369-1388.

[21] P. Weigan, W. Meier, Investigations of Swirl Flames in a Gas Turbine Model Combustor Internal Flow Field, Structures, Temperature, and Species Distributions, Combust. Flame., 144 (2006) 225-236.

[22] P. Petersson, J. Olofsson, C. Brackman, H. Seyfried, J. Zetterberg, M. Richter, M. Aldén, M.A. Linne, R.K. Cheng, A. Nauert, D. Geyer, A. Dreizler, Simultaeous PIV/OH-PLIF, Rayleigh Thermometry/OH-PLIF and Stereo PIV Measurements in a Low-Swirl Flame, Applied Optics., 46(19) (2007) 3928-3936.

[23] J. Cho, T. Lieuwen, Laminar Premixed Flame Response to Equivalence Ratio Oscillations, Combust. Flame, 140 (2005) 116−129..

[24] D.G. Lilley, Swil Flows in Combustion: A Review, AIAA J., 15(8) (1977) 1063-1078.

[25] M. Raffel, C.E. Willert, J. Kompenhaus, Partcle Image Velocimetry: A particle Guide. Springer-Verlag Berlin Heidelberg, Germany, 1998, pp.3-8.

[26] P.O. Hedman, T.H. Fletcher, G.W. Timothy, Observation of Flame Behavior in a Laboratory-scale Premixed Natural Gas/Air Gas Turbine Combustor from Planar Laser Induced Fluorescence Measurements of OH, Laser Doppler Anemometer Velocity Measurements, and Coherent Anti-stokes Roman Spectrometer Temperature Measurements, J. Eng. Gas Turbines Power., 127 (2005) 724-739.

Chapter 5 Effect of Fuel-Air Mixture Velocity

[1] R. Balachandran, B. Ayoola, C. Kaminski, A. Dowling, E. Mastorakos, Experimental Investigation of the Nonlinear Response of Turbulent Premixed Flames to Imposed Inlet velocity Oscillations, Combust. Flame, 143 (2005) 37−55.

[2] M. Stohr, I. Boxx, C. Carter, W. Meier, Dynamics of Lean Blowout of a Swirl-Stabilized Flame in a Gas Turbine Model Combustor, Proc. Combust. Inst., 33 (2011) 2953-2960.

[3] A.M. Steinberg, I. Boxx, M. Stohr, C. Carter, W. Meier, Flow-Flame interactions causing Acoustically Coupled Heat Release Fluctuations in a Thermo-Acoustically

Unstable Gas Turbine Model Combustor, Combust. Flame, 157 (2010) 2250-2266

[4] M. Stohr, R. Sadanandan, W. Meier, Experimental Study of Unsteady Flame Structures of an Oscillating Swirl Flame in a Gas Turbine Model Combustor, Proc. Combus. Inst., 32 (2009) 2925-2932

[5] P. palies, D. Durox, T. Schuller, S. Candel, The Combined Dynamics of Swirler and Turbulent Premixed Swirling Flames, Combust. Flame, 157(9) (2010) 1698-1717.

[6] P. palies, D. Durox, T. Schuller, P. Morenton, S. Candel, Dynamics of premixed Confined Swirling Flames, C.R.Mecanique, 337 (2009) 395-405

[7] M. Kim, Y. Choi, J. Oh, Y. Yoon, Flame-Vortex Interaction and Mixing Behaviors of Turbulent Non-Premixed Jet Flames under Acoustic Forcing, Combust. Flame, 156(12) (2009) 2252-2263.

[8] D.G. Lilley, Swil Flows in Combustion: A Review, AIAA J., 15(8) (1977) 1063-1078.

[9] N. Syred, J.M. Beer, Combustion in Swirling Flows. A Review, Combust. Flame, 22(2) (1974) 143-201.

[10] N. Bouvet, C. Chauveau, I. Gökalp, S.Y. Lee, R.J. Santoro, Characterization of Syngas Laminar Flames using the Bunsen Burner Configuration, Int. J. Hydrogen Energy, (36) (2011) 992-1005.

[11] C.J. Dasch, One Dimensional Tomography : a Comparison of Abel, Onion-Peeling, and Filtered Back Projection Methods, Applied Optics, 31(8) (1992) 1146-1151.

[12] C. Külsheimer, H. Büchner, Combustion Dynamics of Turbulent Swirling Flames, Combust. Flame, 131(2) (2002) 70-84.

[13] M. Escudier, Prog. Vortex Breakdown: Observation and explanations, Prog. Aerosp. Sci. 25 (1988) 189-229.

[14] V.K. Khanna, A Study of the Dynamics of Laminar and Turbulent Fully and Partially Premixed Flames, Ph.D. Dissertation, Dept. of Mechanical Engineering, The Virginia Polytechnic Institute and State University, Blacksburg, VA, USA, 2001.

[15] J.P. Hathout, M. Fleifil, A.M. Annaswamy, A.F. Ghoniem, Heat Release Actuation for Control of Mixture-Inhomogeniety-Driven Combustion Instability, Proceedings of the Combustion Institute, 28 (2000) 721-730.

Chapter 6 Effect of Fuel-Air Mixing Section

[1] T. Lieuwen, B.T. Zinn, The Role of Equivalence Ratio Oscillations in Driving Combustion Instabilities in Low NOx Gas Trubines, Proc. Combust. Inst. 27 (1998) 1809-1816.

[2] T. Gabrielson, Acoustic Data Measurements and Analysis, Lecture Notes, Graduate Program in Acoustics, The Pennsylvania State University, University Park, PA, 2009.

[3] W. Meier, X.R. Duan, P. Weigand, Reaction Zone Structures and Mixing Characteristics of Partially Premixed Swirling CH_4/air Flames in a Gas Turbine Model Combustor, Proc. Combust. Inst., 30(1) (2005) 835–842.

[4] M. Stohr, I. Boxx, C. Carter, W. Meier, Dynamics of Lean Blowout of a Swirl-Stabilized Flame in a Gas Turbine Model Combustor, Proc. Combust. Inst., 33 (2011) 2953-2960.

[5] M.K. Kim, J. Lee, S. Park, J.G. Lee, Y. Yoon, An Experimental Study of Instability Mode Analysis in a Model Gas Turbine Combustor, J. KOSCO, 15(1) (2010) 12-21.

[6] R.S.S. James, On-line Cmbustion Mnitoring on Dry Low NOx Industrial Gas Turbines., Measurement Science & Technology, 14(7) (2003) 1123-1130.

[7] H. Zinn, M. Habermann, Developments and Experiences with Pulsation Measurements for Heavy-Duty Gas Turbines, Proceedings of ASME Turbo Expo, (2007) GT2007-27475.

[8] K.K.Venkataraman, D.A. Satavicca, Mechanism of Combustion Instability in a Lean Premixed Dump Combustor, J. Propul. Pow., 15(6) (1999) 909-918.

[9] M.P. Auer, C. Hirsch, T. Sattelmayer, Influence of Air and Fuel Mass Flow Fluctuations in a Premix Swirl Burner on Flame Dynamics, Proceedings of ASME Turbo Expo, (2006) GT2006-90127

[10] G. Kelsall, C. Troger, Prediction and Control of Combustion Instabilities in Industrial Gas Turbines, Appl. Therm. Eng., 24 (2004) 1571-1582.

[11] Y. Huang, V. Yang, Dynamics and Stability of Lean-premixed Swirl-stabilized Combustion, Prog. Energy Combust. Sci., 35(4) (2009) 293-364.

[12] A. Toffolo, M. Masi, A. Lazzaretto, Low Computational Cost CFD Analysis of Thermoacoustic Oscillations, Appl.Therm.Eng., 30 (2010) 544-552.

[13] T. Schuller, D. Durox, P. Palies, S. Candel, Acoustic Decoupling of Longitudinal Modes in Generic Combustion Systems, Combust. Flame, 159(5) (2012) 1921-1931.

[14] S. Candel, Combustion dynamics and control: Progress and challenges, Proc. Combust. Inst., 29(1) (2002) 1-28.

[15] J.G. Lee, D.A. Santavicca, Experimental Diagnostics for the Study of Combustion Instabilities in Lean Premixed Combustors, Journal of Propulsion and Power, 19(5) (2003) 735-750.

[16] J.G. Lee, K.T. Kim, D.A. Santavicca, Measurement of Equivalence Ratio Fluctuation and Its Effect on Heat Release during Unstable Combustion, Proceedings of the Combustion Institute, 28(2000) 415-421.

[17] K.T. Kim, J.G. Lee, B.D. Quay, D.A. Santavicca, Spatially Distributed Flame Transfer Functions for Predicting Combustion Dynamics in Lean Premixed Gas Turbine Combustors, Combust. Flame 157 (2010) 1718−1730.

[18] K.T. Kim, J.G. Lee, B.D. Quay, D.A. Santavicca, Reconstruction of Heat Release Response of Partially Premixed Flames, Combust. Sci. Tech. 183 (2011) 122−137.

Chapter 7 Spray Characteristics of Canted Injection Angles

[1] J.A. Schetz, A. Padhye, Penetration and Breakup of Liquids in Subsonic Airstreams, AIAA Journal, 15 (1977) 1385-1390.

[2] P.-K. Wu, K.A. Kirkendall, R.P. Fuller, A.S. Nejad, Breakup Processes of Liquid Jets in Subsonic Crossflows, J. Propul. Power, 13(1) (1997) 64-73.

[3] T.F. Fric, A. Roshko, Vortical Structure in the Wake of a Transverse Jet, J. Fluid Mech., 279 (1994) 1-47.

[4] T. Oda., H. Hiroyasu, Breakup Model of Liquid Jet Across a High-Speed Air Stream, Proceeding of the 9th Annual Conference on Liquid Atomization and Spray Systems, San Francisco, CA, USA, 1996, pp. 99-103.

[5] T.T. Nguyen, A.R. Karagozian, Liquid Fuel Jet in Subsonic Crossflow, J. Propul. Power, 8(1) (1992) 21-29.

[6] N. Tamaki, M. Shimizu, K. Nishida, H. Hiroyasu, Effects of Cavitation and Internal Flow on Atomization of a Liquid Jet, Atomization and Sprays, 8 (1998) 179-197.

[7] J. Song, K. Ahn, M.-K. Kim, Y. Yoon, Effects of Orifice Internal Flow on Liquid Jets in Subsonic Crossflows, J. Propul. Power, 27(3) (2011) 608-619.

[8] R.P. Fuller, P.-K. Wu, K.A. Kirkendall, A.S. Nejad, Effects of Injection Angle on Atomization of Liquid Jets in Transverse Airflow, AIAA Journal, 38(1) (2000) 64-72.

[9] M. Costa, M.J. Melo, M.M. Sousa, Y. Levy, Spray Characteristics of Angled Liquid Injection into Subsonic Crossflow, AIAA Journal, 44(3) (2006) 646-653.

[10] T. Inamura, N. Nagai, Spray Characteristics of Liquid Jet Traversing Subsonic Airstream, J. Propul. Power, 13(2) (1997) 250-256.

[11] T. Inamura, Trajectory of a Liquid Jet Traversing Subsonic Airstreams, J. Propul. Power, 16(1) (2000) 155-157.

[12] N.S. Jacob, J.G. Lee, D.A.Santavicca, Penetration of Liquid Jets in a Crossflow, Atomization and Sprays, 16(8) (2006) 887-906.

[13] A.H. Lefebvre, Atomziation and Sprays, Hemisphere, New York, USA, 1989.

[14] N. Chigier, R.D. Reitz, Regimes of Jet Breakup and Breakup Mechanisms, Recent Advances in Spray Combustion : Spray Atomization and Drop Burning Phenomena, edited by K. Kuo AIAA , 1996.

[15] J. Vennard, Elementary Fluid Mechanics 3rd ed., Wiley, New York, USA, 2008, pp. 216-219.

Appendix A, B, C

[1] F.A. Williams, Combustion Theory 2nd ed., Benjamin Cummings Publishing Company (Pearson), San Francisco, USA, 1985.

[2] L.B. Gary, W.R. Kenneth, Combustion Engineering, 1st edition, McGraw-Hill, New York, 1998.

[3] A.S. Morgans, S.R. Stow, Model-based control of combustion instabilities in annular combustors, Combust. Flame, 150 (2007) 380-399.

[4] L.B. Davis, S.H. Black, Dry Low NOx Combustion Systems for GE Heavy-Duty Gas Turbines, GE Power Systems, GER-3568G, 2010.

[5] J. Oh, M.K.Kim, Y. Yoon, The tuning methodology of a GE 7FA + e DLN-2.6 gas turbine combustor, 36 (2012) 14-20.

[6] J. Oh, J. Hwang, Y. Yoon, EINOx Scaling in a Non-Premixed Turbulent Hydrogen Jet with Swirled Coaxial air, Int. J. Hydrogen Energy, 35 (16) (2010) 8715-8722.

[7] E. Kinsler, A.R. Frey, Fundamentals of Acoustics 2nd ed., John Wiley and Sons, Hoboken, NJ, USA, 1990.

[8] S. Hubbard, A.P. Dowling, Acoustic Resonances of an Industrial Gas Turbine Combustion system, J. Eng. for Gas Turbines Power 123 (2001) 766-773.

[9] S. Candel, Combustion Dynamics and Control; progress and challenges, Proc. Combust. Inst., 29 (2002) 1-28.

[10] N. Docquier, S. Candel, Combustion Conrtrol and Sensors - A Review, Progress in Energy and Combustion Science, (28) (2002) 107-150.

[11] D.R. Englund, W.B. Richards, The Infinite Line Pressure Probe, Thirty-ninth International Instrumentation Symposium, Denver, Colorado, USA, 1984.

[12] S. Rea, S. James, C. Goy, M.J.F. Colechin, On-Line Combustion Monitoring on Dry Low NOx Industrial Gas turbines, Meas. Sci. Technol., 14 (2003) 1123-1130.

[13] S.R. Turns, An Introduction to Combustion, 2nd ed., McGraw Hill, New York, USA, 2000.

[14] J. Sewell, P. Sobieski, C. Beers, Application of Continuous Combustion Dynamics Monitoring on Large Industrial Gas turbines, Proceedings of the ASME Turbo Expo (2004) GT2004-54310.

초 록

본 연구는 친환경 저 NOx 가스터빈 연소기의 최적설계 인자 도출에 대한 연구이며 항공용 및 발전용 가스터빈에서 사용되는 예혼합 연소기에서의 연소 동특성에 대한 실험적 결과를 제시한다. 가스터빈 연소기의 설계 인자인 연료-공기 혼합기 속도, 당량비, 연료노즐 전의 연료-공기 혼합부의 공간 (plenum) 및 연소실의 길이 등의 변화에 따른 화염안정화 지도를 작성하였고, PIV (Particle Image Velocimetry), OH 자발광, He-Ne 레이저 광산란 기법 등을 동압과 위상동기화 하여 안정 및 불안정한 화염의 구조를 분석하였으며, 자체 개발한 다체널 동압측정 시스템을 이용하여 전체 연소기에서 구간별 동압을 실시간으로 측정하여 연소실에서 발생하는 불안정 특성의 원인을 파악하였다. 열방출의 섭동과 11개의 동압센서에서 측정되는 동압의 모드와 위상차 분석을 통하여 연소불안정의 원인을 정확히 파악할 수 있었고, 연료-공기 혼합기의 내제적 불안정에 의해 발생되는 화염의 와동구조 불안정과 연료-공기의 혼합부의 길이가 연소불안정에 크게 영향을 미치는 것을 확인하였다. 이를 통해서 친환경 가스터빈 연소기 제작을 위한 설계 인자를 명확히 확인하였다. 또한 RQL 연소기에서 사용되는 2차 산화제의 빠른 혼합을 유도하는 분무의 분사각도별 액주의 궤적과 분열거리를 측정하여 실험으로 인한 경험식을 도출하였다.

부분 예혼합 연소기와 30도 각도의 스월러를 가진 천연가스 연료분사기에서 발생한 화염구조와 재순환 영역의 형성이 연소불안정에 미치는 영향에 대하여 실험적으로 연구한 부분에서는 PIV 계측기법으로 연소장에서의 화염의 안정화 그리고 불안정한 영역에서 유동장을 확인해 보았다. 스월러에 의한 재순환 영역은 화염의 안정화 및 난류의 강도뿐만 아니라 재순환 영역의 크기에 따른 화염 재점화에도 영향을 주었고, 연소불안정으로 인한 연소기 내부의 압력구배에 의하여 중앙 재순환 영역에서 유입되는 연소가스의 질량유량의 변동

이 화염의 각도와 모양을 변경시키고 이것이 열방출 섭동을 발생시켜 연소불안정 발생의 주요 원인이 되고 있음을 확인하였다.

연료-공기 혼합기 속도에 의한 연소불안정과 화염구조와의 상관관계에 대한 연구에서는 당량비 1.2 조건에서 연료-공기 혼합기 속도를 30 ~ 70 m/s까지 다양한 실험조건에서 수행하였다. 이를 통하여 연소불안정 현상이 낮은 혼합기 속도조건과 높은 혼합기 속도조건에서 발생하는 것을 확인할 수 있었고, 낮은 혼합기 속도조건의 불안정에서는 화염의 끝단의 와동구조가 연소불안정 현상에 영향을 끼친다는 것을 확인할 수 있었다.

모형 가스터빈의 연소실과 연료-공기 혼합부의 공진모드의 관계가 연소불안정에 어떤 영향을 미치고 있는지에 대하여 실험적으로 확인한 연구에서는 다체널 동압측정을 통하여 각각 위치에서 동압의 모드와 각 센서들간의 phase를 분석하여 연소불안정의 원인을 규명하였다. 연소실의 길이 (800 ~ 1800 mm)와 혼합부의 길이 (470, 550, 870 mm)를 음향학적 경계로 일치시켜 연소불안정 특성을 확인해 보았을 때 두가지 서로 다른 연소불안정 모드를 확인할 수 있었는데 저주파 연소불안정 특성은 화염의 열방출 섭동과 연소실의 공진모드에 기인하며, 고주파 영역대의 연소불안정 현상은 혼합부의 길이를 변경하였을 때 발생하는 또 다른 불안정 현상임을 실험적으로 확인할 수 있었다.

친환경 연소기 설계에 있어서 이차분무 연구의 일환으로 분사각도에 따른 산화제 분무특성에 대한 실험적 연구를 수행하였다. 여기서 액주영역의 궤적과 분열지점까지의 거리는 연료분사 속도, 공기의 속도에 의한 연료/공기 모멘텀 플럭스와 분사각도, 항력계수의 함수임을 확인하였다. 분사각도에 의한 액주영역의 궤적 및 분열길이에 대한 실험식을 도출하였으며, 일반적인 공기유동 방향과 일치하는 정방향 분사와 반대방향으로 분사되는 대향분사 액주궤적 실험식과는 항력계수의 차이가 발생하는 것을 확인하였다.

마지막으로 첨부자료에서는 앞에서 소개된 연소불안정 현상에 영향을 미치는 인자들을 고려하여 실제 서인천 복합화력 발전소에서 운용중인 발전용 GE 7FA+e DLN-2.6 연소기에 적용하여 연소최적 튜닝에 대한 결과와 실시간으로 최적제어가 가능하며, 튜닝 대상의 연료노즐과 상수를 제시하고 연소상태를 모니터링 할 수 있는 프로그램을 개발한 내용을 소개하였다.

중심어: 가스터빈 연소기, 연소불안정, 와류화염구조, 중앙재순환영역, 연료-공기 혼합부, 다체널 동압측정 시스템, 분사각도, 액주분무궤적, 분열길이, 최적연소튜닝

학 번: 2005-20996